Superconductivity of Strontium Titanate in Reduced Dimensions

by

Yun-Yi Pai

Bachelor of Science, National Taiwan University, 2010

Master of Science, Cornell University, 2014

Submitted to the Graduate Faculty of

the Dietrich School of Arts and Sciences in partial fulfillment

of the requirements for the degree of

Doctor of Philosophy

University of Pittsburgh

2020

UNIVERSITY OF PITTSBURGH

DIETRICH SCHOOL OF ARTS AND SCIENCES

This dissertation was presented

by

Yun-Yi Pai

It was defended on

January 31, 2020

and approved by

Jeremy Levy, Department of Physics and Astronomy

Michael Hatridge, Department of Physics and Astronomy

David Pekker, Department of Physics and Astronomy

Ayres Freitas, Department of Physics and Astronomy

David Waldeck, Department of Chemistry

Dissertation Director: Jeremy Levy, Department of Physics and Astronomy

Superconductivity of Strontium Titanate in Reduced Dimensions

Yun-Yi Pai, PhD

University of Pittsburgh, 2020

In this thesis, I will summarize my work on mesoscale devices created at the heterointerface between complex oxides lanthanum aluminate and strontium titanate ($LaAlO_3/SrTiO_3$). In chapter I, the relevant advances in the field of $SrTiO_3$ as well as $LaAlO_3/SrTiO_3$ is reviewed. In chapter II, I will briefly describe relevant experimental setups and techniques, from transport at milliKelvin (mK) temperatures to our efforts on mK scanning probe and mK optical characterization of the system. In chapter III, I will summarize our observation of 1D nature of the superconductivity at $LaAlO_3$ /$SrTiO_3$. In chapter IV, results from 1D zigzag superconducting nanowires are summarized. In chapter V, I will summarize our simulation work on phase field modeling $SrTiO_3$, followed by future works and outlook for this field in chapter VI.

Table of Contents

List of Tables

List of Figures

Preface

It's 2016 June 28, 5AM. I came to lab to test the electron waveguide I wrote and cooled down the night before. It's finally a good waveguide, with no backscattering and tunability from 0 to more than 40 e^2/h. 2016 Nov. 4, after replacing the burnt 3-phase power cords to the scroll module of the Cryomech compressor, I powered the compressor on. The weird sound it was making made me realize something was wrong. 2016 Dec. 24, I came to lab to finish the section on Shubnikov de Haas oscillation for our review article. There are so many moments of this kind that spanned the past 5 years I can still viscerally remember. There are also countless hours with Asylum MFP3D, Adixen ASM 340 leak detector, wirebonder, and some 300 helium transfers. And now finally I am typing the acknowledgement of this thesis. Over the past few years I have received help from many persons. I start in reverse chronological order:

I want to thank my supervisor Benjamin Lawrie and Ho-Nyung Lee at Oak Ridge National Laboratory. I want to thank Claire Marvinney, Matthew Feldman, Chengyun Hua, Eugene Dumitrescu, Brian Williams, Brian Lerner, Jie Zhang, Lason Lapano, Jason Dark, Zac Ward, Gyula Eres, Jong-Mok Ok, Matthew Brahlek, Haoxiang Li, Rob Moore, Alex Belianinov. I want to thank Chang-Beom Eom and his group members for samples. I want to thank Long-Qing Chen, Xiaoxing Cheng, Jianjun Wang for the wonderful collaboration on phase-field modeling strontium titanate. It is incredibly wonderful to be able to have this chance to learn and use phase-field modeling to study $SrTiO_3$. I want to thank my committee members, Ayres Freitas, Michael Hatridge, David Pekker, David Waldeck. I want to thank Leyla Hirschfeld, Barbara DelRaso, Chandralekha Singh, Laura Provost, Arthur Kosowsky, Hector Martinez Rodrigues, Jonathan Beaumarriage, Richard Sherman, Ashley Bakaitus.

I want to thank Patrick Irvin, Megan Briggeman for all kind of trainings since I joined the lab. I want to thank Arthur Jianan Li. I can still rember how many sample tests we do per a day summer 2016. I want to thank Yuhe Tang, Guanglei Cheng, Lucy Chen, Qing Guo, Anil Annadi, Mengchen Huang, Bi Feng, Jen-Feng Hsu, Wu Hao, Po Zhang. I want to thank our RF team members Muqing Yu and Dengyu Yang. I want to thank Aditi Nethwewala

for taking good care of CF and MFP3D. I want to thank Joe Albro. I want to thank Jeff Sicher, Tom Gasmire, Shawn Artman, Bill Strang, Jeff Tomaszewski.

I want to thank my advisor Jeremy Levy, for not only the support but also believing in me. I will never forget the life lessons I learned in this research group. I hope that I will be able to pass these lessons down to the future generations.

I want to thank my family for unconditioned love and support.

I. The Physics of $SrTiO_3$-based Heterostructures

The contents of this chapter represent part of the collaborative work published in Yun-Yi Pai, Anthony Tylan-Tyler, Patrick Irvin, Jeremy Levy, *Reports on Progress in Physics* **81** (3), 036503 (2018) [1] and Yun-Yi Pai, Anthony Tylan-Tyler, Patrick Irvin, Jeremy Levy, Vol. 2, Ch.12, in *Spintronics Handbook, Second Edition: Spin Transport and Magnetism, 2nd ed.*, CRC Press 2019 [2].

A. Relevant Properties of $SrTiO_3$

Strontium titanate ($SrTiO_3$) is one of the most fascinating materials ever to exist. It can be used to make synthesized diamond jewelry, solid oxide fuel cell, and quite surprisingly, doped into superconducting at extremely low temperature (0.3 Kelvin). The superconductivity of $SrTiO_3$ is first reported by the research group led by James Schooley in 1964 [3]. The discovery of the superconductivity in $SrTiO_3$ was truly marvelous. No one expected this transparent oxide would ever superconduct. The discovery immediately initiated the search for a whole new class of superconductors, and later a family of the so-called high-transition temperature (T_c) superconductors were discovered. For conventional superconductors, the weak attraction that glues the electrons into pairs is their electron-phonon interaction, as stated by the celebrated BCS theory. However, more than 50 years since the discovery of the superconductivity in $SrTiO_3$, the mechanism, remains a mystery. We know that $SrTiO_3$ is a complicated multiferroic material: it has coupled ferroelectric (and quantum paraelectric), (weak) ferromagnetic, ferroelastic, charge, defect, orbital, and superconducting degree of freedom. The interaction between any two of the above degree of freedom is not well understood [1]. It is really unsurprising at all that the pairing mechanism for $SrTiO_3$ has remained elusive. Outside of the field of low temperature electronic transport, $SrTiO_3$ has many applications from dielectric material, water-splitting catalyst, solid oxide fuel cell, and sensors [4].

1. Structural Distortion, Quantum Paraelectricity and Antiferrodistortion

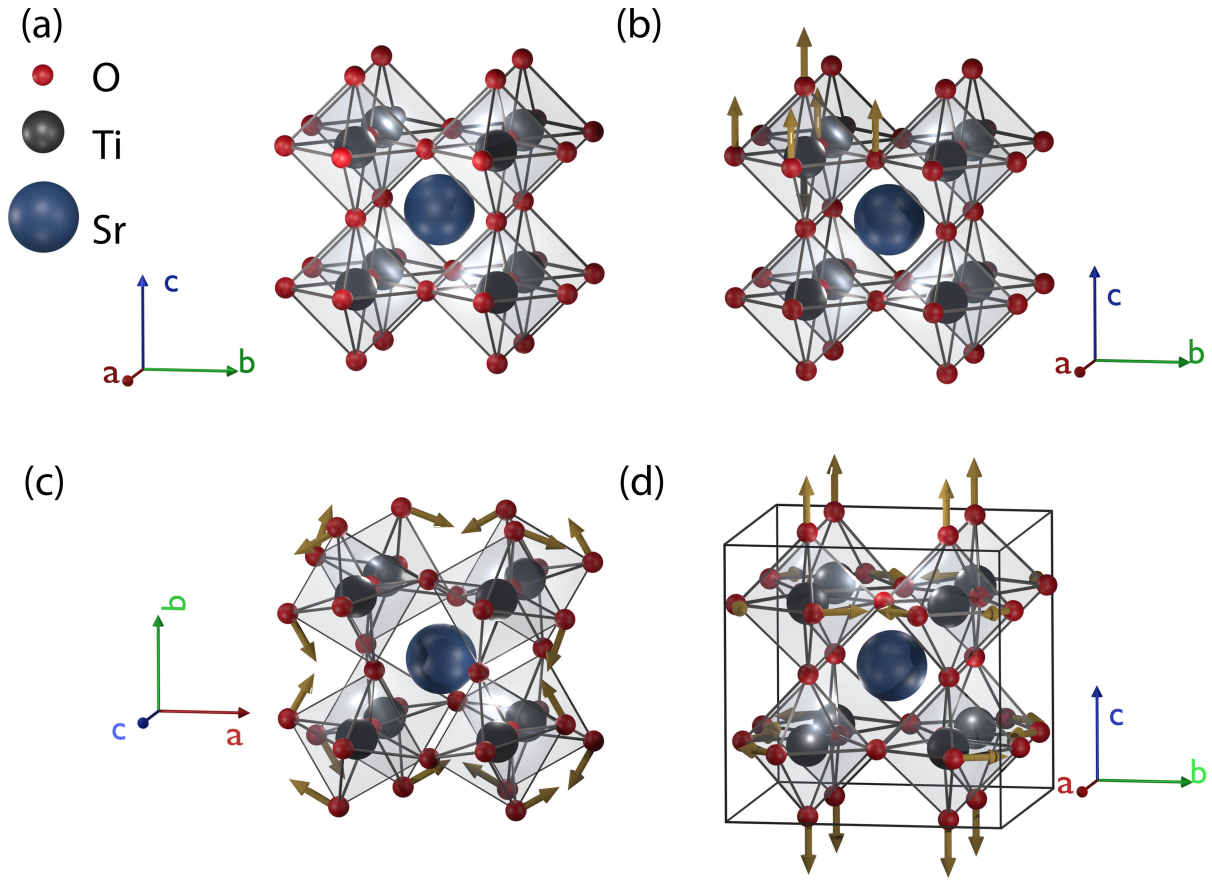

Figure 1: Structure of $SrTiO_3$

At room temperature, $SrTiO_3$ is considered an idealized cubic structure (space group $Pm3\bar{m}$) with lattice parameter $a = 0.3905$ nm [5]. Each Sr atom is surrounded by four TiO_6 octahedra (Figure 1 (a)). Under stress or change of temperature, the $SrTiO_3$ lattice can deform from the ideal cubic structure. The most relevant distortions for $SrTiO_3$ are: (1) Ferroelectric-type (FE) displacement: polar displacement between cations and anions, resulting a built-in polarization (Figure 1 (b)); (2) Antiferrodistortive (AFD) rotation: antiphase rotation of neighboring oxygen TiO_6 octahedra (Figure 1 (c)). Generally, for each perovskite ABO_3, the Goldschmidt tolerance factor ($t = \frac{r_A+r_O}{\sqrt{2}(r_B+r_O)}$ [6]), where r_A, r_B, and r_O are the ionic radii of A-site cation, B-site cation, and oxygen, respectively) provides a reasonably accurate guideline in identifying whether FE displacement or AFD rotation is

more likely to occur [7]. Perovskites with larger Goldschmidt tolerance factors ($t > 1$), such as $t = 1.063$ for $BaTiO_3$, favor FE displacement and are often found to be ferroelectric. On the other hand, perovskites with smaller tolerance factors ($t < 1$), such as t=0.946 for $CaTiO_3$, favors AFD rotation. The tolerance factor for $SrTiO_3$ is found to be very close to unity (t=1.00 in [8, 9, 10]). It is not surprising that both FE and AFD are relevant in the phase diagram of $SrTiO_3$. FE and AFD would compete with each other. Aschauer et al. [11] predicted that AFD and FE compete against each other when the AFD rotation angle $\alpha < 6^\circ$ and cooperate with each other when the AFD rotation angle $\alpha > 6^\circ$.

Experimentally, de Lima et al. [12] reported that both AFD and FE are enhanced after Ca-substitution. Macroscopically, as temperature decreases, $SrTiO_3$ undergoes a cubic-to-tetragonal, ferroelastic, AFD phase transition at around $T_{AFD} = 100 - 110$K [13, 14, 15, 16, 17, 18]. The cubic-to-tetragonal transition is triggered by the AFD rotation (Figure 1 (d)) NOTE: For ferroelectric perovskites such as $PbTiO_3$, the cubic-to-tetragonal structural transition is due to the FE displacement. This AFD transition has a rotation angle (Glazer classification [19] $a^0a^0c^-$) $\alpha = 2.1^\circ$, and the resulting distortion changes the c/a ratio (1.00056) [14], reducing the symmetry of the crystal structure from cubic to tetragonal. The R_{25} phonon condenses at 105 K on the Brillouin zone boundary [17]. Ferroelastic domains with different rotation axes form below the AFD transition temperature [18]. These domains disappear as the sample is warmed above T_{AFD}, and typically form a different domain pattern upon temperature cycling [18]. The cubic-to-tetragonal transition can occur at room temperature if 5-6 GPa of pressure is applied [20, 21]. Theoretically, by applying pressure, Hachemi et al. [22] predicted that $SrTiO_3$ can undergo a chain of thermodynamically continuous structural transitions: cubic $\rightarrow$ tetragonal$\rightarrow$ orthorhombic$\rightarrow$ monoclinic. ($Pm3\bar{m}$ (O_h^1, no.221) $\rightarrow$ $I4/mcm$ (D_{4h}^{18} or D_{4h}^1, no.140) $\rightarrow$ $Cmcm$ (D_{2h}^{17}, no.63) $\rightarrow$ $P2_1/m$ (C_2h^2, no.11)). However, the structural phase transition beyond tetragonal phase is not well established. For example, a second structural transition from tetragonal to possibly orthorhombic or trigonal is reported by Grzechnik et al. [23] and Cabaret et al. [24], but a null result is reported by Guennou et al. [25]. Guennou et al. [25] saw no structural transition up to 53 GPa, far above the 24 GPa for orthorhombic to monoclinic predicted by Hachemi et al. [22]. Besides temperature and pressure, the structural transition can also be affected by defects [26] and

isovalent doping [12].

$SrTiO_3$ is one of the few materials known to be intrinsically quantum paraelectric [27, 28] a phase in which quantum fluctuations between degenerate lower symmetry configurations suppresses ferroelectric ordering. At room temperature, the static dielectric constant of $SrTiO_3$ is large ($\epsilon_r \approx 300$). As the temperature decreases, ϵ_r increases, saturating at $T =$ 4K at $\epsilon_r \approx$ 10,000-24,000, depending on the strain, field, and sample quality. The polar transverse optical soft mode for $SrTiO_3$ scales approximately as $\omega_{TO}^2 \propto (T - T_c)$ for T > T_c, with $T_c = 35$K [27, 28]. For a regular ferroelectric material, the phonon frequency softens at T_c [29]. However, for $SrTiO_3$, as T approaches T_c from above, ω_{TO}^2 starts to deviate from (T- T_c) and eventually levels off at low temperature [30].

While the bulk is paraelectric, the surface of $SrTiO_3$ may be ferroelectric. Bickel et al. [31], using, low-energy electron diffraction (LEED) at $T = 120$ K , found that the surface layer has significant puckering (oxygen ions pulled out of the surface). Later theoretical work by Ravikumar et al. [32] suggests that the surface can be ferroelectric if the surface is SrO-terminated (but not for TiO_2-terminated surface). The structure of $SrTiO_3$ in the polar ferroelectric phase is in fact still under debate [33]. Furthermore, Bussmann-Holder et al. [34] argued that the ferroelectric phase does not possess true long-range order, and consists of coexisting ordered-disordered micrograins. Besides the ferroelectricity of bulk, ferroelectricity in $SrTiO_3$ films [35, 36, 37, 38], and flexoelectricity [39] have also been reported.

Below is a list of experimental variables that are known to be able to drive paraelectric $SrTiO_3$ into a ferroelectric phase, or otherwise impact the ferroelectric transition:

I. **Electric field**. By applying electric field strength greater than 2×10^5 V/m, $SrTiO_3$ becomes ferroelectric at $T \sim 20$ K[40]. The dielectric constant ϵ_r decreases rapidly with applied electric field [41]. Electric field also induces Raman-active odd parity phonons [42, 43].

II. **Stress or strain**. A ferroelectric phase can be triggered by stress on the order of 0.5 GPa at $T = 2$ K [44, 45]. The stress forces the domains with polarization parallel to the stress direction to switch to the perpendicular direction. Notably, the sample must be warmed above T_{AFD}=110 K to remove any remnant ferroelectric polarization. This observation indicates a possible interplay between the AFD transition and the

ferroelectric phase. Thanks to the advances of thin-film growth technologies and the development of suitable substrates [46], $SrTiO_3$ films can be grown under substrate-derived strain. Room temperature ferroelectricity has been reported for $SrTiO_3$ film grown on $DyScO_3$ [36], and later at even higher temperature $T = 400$ K for $SrTiO_3$ film grown on silicon [47].

III. **Cation substitution**. Substituting the Sr atoms with other cations such as Ca, Pb, or Ba can induce ferroelectricity. The critical substitution fraction x_c is different for each material: $x_c = 0.0018$ for $Sr_{1-x}Ca_xTiO_3$ [48, 49], x_c=0.002 for $Sr_{1-x}Pb_xTiO_3$[50], x_c=0.035 for $Sr_{1-x}Ba_xTiO_3$[51].

IV. **Isotope substitution**. Itoh et al. [52] reported that, by substituting ^{16}O with heavier ^{18}O, at x_c=0.33 [53], $SrTiO_3$ develops ferroelectricity at $T_c = 23$ K. The explanation is that the heavier ^{18}O atoms suppress quantum fluctuations. Stucky et al. [54] found that this isotope substitution can also raise the superconducting transition temperature of $SrTiO_3$, indicating that the superconductivity and the ferroelectricity of $SrTiO_3$ may be related. (See Section I.A.4)

V. **Point defects**. Several reports suggest that Sr-vacancy-related defects or oxygen vacancies may be responsible for the observed ferroelectricity in $SrTiO_3$ films, for example, Sr-O-O [55] $V_{Sr} - I_{Ti}$ (Sr-vacancy adjacent to interstitial Ti) [56], antisite detects such as Ti_{Sr} or Sr_{Ti} [57], or oxygen vacancies [58]. However, the detailed mechanism for the defect-driven ferroelectricity is not well understood. Scenarios such as defect-increased tetragonality [58, 59], and electric dipole of V_{Sr}-related defect center, have been considered [55, 56].

2. Electronic Structure of $SrTiO_3$

$SrTiO_3$ is a band insulator, and can be n-type doped with Nb, La, or oxygen vacancies. It has an indirect bandgap 3.25 eV and a direct bandgap 3.75 eV, experimentally determined from valence electron-energy loss spectroscopy (VEELS) [63]. The primary contribution of the valence band is the 2p orbitals of oxygen atoms [64]. The conduction band is mainly composed of the Ti 3d orbitals. In the cubic phase, the 3d orbitals split into t_{2g} and e_g,

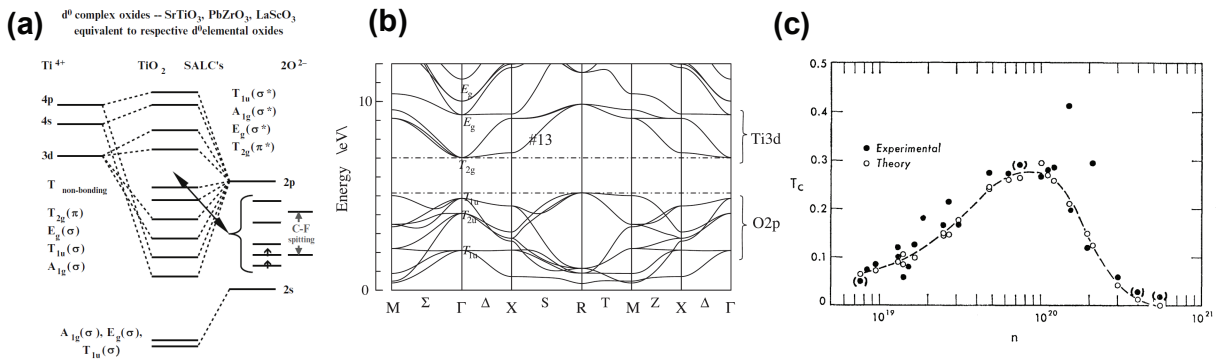

Figure 2: (a) The orbital hybridization of $SrTiO_3$. The conduction band is from the Ti 3d orbitals, and most importantly, the t_{2g} manifold. The primary contribution of the valence band is the 2p orbitals of oxygen atoms. Adapted from [60]. (b) An DFT calculation of the electronic structure for cubic phase $SrTiO_3$. The t_{2g} are the lowest lying conduction bands. The #13 is the d_{xy} band. Adapted from [61]. (c) The superconducting transition temperature T_c of $SrTiO_3$ traces out a dome shape. Adapted from [62].

as shown in Figure 2 (a) [60]. Figure 2 (b) [61] is a typical DFT calculation of the band structure. The d_{xy} (the 13 in Figure 2), d_{yz} and d_{xz} orbitals of t_{2g} bands are degenerate at the conduction band minimum, the Γ point, as shown in Figure 2 (b) [61]. The indirect band gap and the direct band gap observed in VEELS are assigned to R → Γ and Γ → Γ, respectively [63]. In the tetragonal phase, the primitive cell is doubled, and the folding of the first Brillouin zone maps both the R and Γ of the cubic structure into Γ [65]. Stress and strain can also modify the band structure, for example, see the ARPES work by Chang et al. [66], or theoretical calculation by Khaber et al. [67].

The t_{2g} manifold is expected to further split due to the AFD transition and atomic spin-orbit interaction. The expected energy scale is ranges from a few eV to a few tens of eV. However, since the early characterization by Uwe et al. [68, 69] with Raman scattering and Shubnikov-de Haas (SdH) oscillations, ARPES by Chang et al. [70], and theoretical calculations such as Marques et al. [71], no consensus about how large the splitting should be has been reached. The details of the band structure are still difficult to obtain. Tools

such as ARPES, magnetotransport, and DFT all have various difficulties. The critical features of size around a few meV such as the aforementioned spin-orbit splitting or tetragonal splitting are too small for ARPES to resolve. Magnetotransport measurements yield widely varying effective mass [61, 69, 72] and do not agree well with DFT calculations [73, 74, 75]. (See Section I.B.2.d for more detailed Shubnikov-de Haas (SdH) quantum oscillations for $LaAlO_3/SrTiO_3$ and related system). Standard DFT tends to overestimate the c/a ratio, AFD rotation angle, and underestimate the bandgap [65]. These problems have been taken care of in the modern hybrid DFT calculations such as LDA+U, GW, etc, but which method is most reliable for the rest of the band structure remains an open question? For a more extensive discussion see, for example, Evarestov [76].

3. Defect of $SrTiO_3$

Various types of defects can be found in $SrTiO_3$ and they can have a huge impact on the structural, electronic, magnetic, optical, and electronic properties. For example, Sr-vacancies and related defect centers may be responsible for increased tetragonality [59] and emergent ferroelectricity in $SrTiO_3$ films [55, 56, 57]. Oxygen vacancies are the most abundant and important species of point defects in $SrTiO_3$. They are easy to introduce, remove and manipulate, and have wide influence on the properties. For instance, they can provide electron conduction, blue light emission, and dilute magnetism. In this section, we will mostly focus on oxygen vacancies, and will briefly discuss other defect complexes, e.g., terraces. See the recent review by Marshall et al. [77] for nanolines and related ionic transport of oxygen vacancies supported STM studies, Szot et al.[78] for dislocations, and Sanchez et al. [79] for defects related to treated surface such as vacancy puddles and meandering terraces.

Oxygen vacancies (V_O, or $\ddot{V}_O$ using KrögerVink notation [80]) are the most studied defects in $SrTiO_3$ [77]. Oxygen vacancies can be introduced by annealing $SrTiO_3$ under low oxygen partial pressure, which is one of the primary ways of creating $n-$type $SrTiO_3$. The distribution and migration of the isolated oxygen vacancies is typically analyzed using a thermally-activated ionic diffusion model. The diffusion constant is a function of many variables including temperature, oxygen partial pressure, hopping paths (which are found

to be dominated by the edges of the TiO_6 octahedral, see [81, 82]), electric field, and light [83]. The distribution of oxygen vacancies may not always be uniform [84, 85]. Beyond the single vacancy diffusion model, oxygen vacancies may cluster, such as the apical-divacancy configuration predicted by Cuong et al. [81]. They may also cluster around dislocations, and have higher ionic mobility around dislocations [86], twin walls ([87] for $CaTiO_3$). They may also perturb the crystal structure [88] and induce AFD rotation [89].

Each oxygen vacancy nominally dopes the sample with two electrons, $2e^-$. Those electrons may remain localized and may not be necessarily conductive [90]. The carrier freeze-out was observed for the 2DEG at the $LaAlO_3/SrTiO_3$ interface [85] as well as oxygen deficit $SrTiO_3$ [91]. The wavefunction spread for the vacancy-derived electrons are expected to depend on the vacancy configuration [92] and the overall structure (e.g., cubic vs. tetragonal) [88]. There may also be subtler differences between Nb-doped $SrTiO_3$ and oxygen-reduced $SrTiO_3$. Early STM studies reported two superconducting gaps in Nb-$SrTiO_3$ but only one gap is observed for oxygen reduced $SrTiO_3$ [93]. Subsequent low-temperature STM experiments have failed to observe the second superconducting gap in Nb-$SrTiO_3$ [94] (Section I.A.4).

Oxygen vacancies cause dramatic changes in optical properties. Upon introduction of oxygen vacancies, the color of $SrTiO_3$ changes from transparent to blue [59, 95]. Upon the application of electric field at elevated temperature, the oxygen vacancies migrate, resulting in a gradient of color [95]. Photoluminescence peaks at 430 nm are observed for oxygen deficient $SrTiO_3$ samples, regardless how the oxygen vacancies are introduced [96]. Upon cooling down, the blue (430 nm) peak shifts toward green (550 nm). At $T = 160$ K, a new peak shows up at 380 nm. After the introduction of oxygen vacancies, $SrTiO_3$ can be very photoconductive. By exciting with merely sub-bandgap light (2.9 eV), an increase in the conductivity by 2 orders of magnitude is observed. The enhanced conductivity can persists for days [97]. The reversible switching controlled by UV light and water immersion for $LaAlO_3/SrTiO_3$ has been reported [98, 99].

Terraces are unit-cell-sized (3.904 Å) steps that appear due to miscut angles of the $SrTiO_3$ crystal. The larger the miscut angle, the smaller the lateral size of the terraces. Typically, terraces are not visible (under atomic force microscope imaging) for samples of

mixed termination. Clean and flat terraces appear after surface treatment (to obtain single termination, most commonly TiO_2 termination [100]) and are often used as a preliminary step in the growth of epitaxial layers.

Currently, the impact of the terraces on the electronic properties of $SrTiO_3$ is not very clear. However, for 2DEG at the $LaAlO_3/SrTiO_3$ interface, two reports suggested that the terraces may enhance the mobility [101] or impede transport perpendicular to the terrace direction [102]. Fix et al. [101] compared samples with miscut angle $\alpha = 0.2°$ to those with $\alpha = 8°$ (denser terraces). Higher mobility with roughly a third of carrier concentration is observed for the $\alpha = 8°$ samples. Fix et al. suggested that the terraces may act as traps for low-mobility carriers [101]. On the other hand, Brinks et al. [102] reported anisotropic resistance for different transport direction. Brinks et al. suggested that the observed anisotropy is due to difference in transport along or perpendicular to the terrace direction [102]. However, these effects have not been distinguished from other sources of anisotropic flow, e.g., due to ferroelastic domains [103].

4. Superconductivity of $SrTiO_3$

In 1964, Schooley et al. [3] observed superconductivity in oxygen-reduced $SrTiO_3$ at $T_c \sim 250 - 280$ mK. $SrTiO_3$ was the first complex oxide found to be superconducting, and the inspiration for Bednorz and Muller in the search for new superconducting compounds with high critical temperatures [104]. The critical temperature of the superconductivity as a function of carrier concentration traces out a dome peaked at $T_c \sim 450$ mK [62, 105, 62], similar to other unconventional superconductors such as cuprates [106], heavy-fermion superconductors [107], and iron-based superconductors [108]. Again, just as those unconventional superconductors, there is no widely accepted theory which is able to fully describe superconductivity in $SrTiO_3$.

$SrTiO_3$ is superconducting at very low carrier concentration, at 10^{15}cm^{-3} [109, 110, 111]. This low carrier concentration implies a small Fermi energy. Therefore the superconductivity of $SrTiO_3$ is in the nonadiabatic regime ($E_F < \hbar\omega_D$) or the anti−adiabatic limit ($E_F \ll \hbar\omega_D$) where the BCS−Midgal−Eliashberg theory is not applicable [112]. Lin et al. [113] argue

that the insensitivity of T_c and H_{c2} to defect concentration implies s-wave pairing, as a consequence of Andersons theorem [114].

There are many unanswered questions concerning the nature and pairing mechanism governing superconductivity in $SrTiO_3$ (for more details, see recent reviews by Collignon et al. [115] and by Gastiasoro et al. [116]):

I. Is $SrTiO_3$ a multiband superconductor? Early tunneling spectroscopy measurement by Binnig et al. [93] revealed two distinct superconducting gaps in the Nb-doped $SrTiO_3$, suggesting that the superconductivity is supported by at least two bands. The double gaps are not observed in the oxygen-deficient samples of the same work [93]. However, no follow-up experiments reported a second superconducting gap in either $SrTiO_3$ [117] or $SrTiO_3$-based 2DES [118], nor did a recent scanning tunneling microscopy experiment on Nb-doped $SrTiO_3$ by Ha et al.[94]. Note that these experiments accessed wide range of carrier concentration including the region above the lowest Lifshtiz point mapped out by Lin et al. [75] for bulk $SrTiO_3$ or Joshua et al. [119, 120] for 2DEG.

II. The nature of the electron pairing in $SrTiO_3$ has been pondered since the discovery of superconductivity in $SrTiO_3$ in 1964 and has remained enigmatic for half a century [112]. A paired, non-superconducting phase was first proposed by Eagles in 1969 [121] and subsequently used to explain [122] the two-step resistance drop of the superconducting transition reported by Tainsh et al. [123] in Zn-doped SrTiO3. With the development of $SrTiO_3$-based heterostructures, questions about the nature of the superconducting gap and pairing have been revisited. A pseudogap signature was reported by Richter et al. by planar tunneling measurements on top-gated $LaAlO_3/SrTiO_3$ [118]. Cheng et al. used a single-electron transistor fabricated within the $LaAlO_3/SrTiO_3$ interface, to show that electrons are paired far outside the superconducting regime [124].

III. Conventional BCS pairing is built on attractive electron-electron interactions that are usually mediated by electron-phonon coupling. Experimentally, strong electron-phonon coupling (described as polarons) has been observed in ARPES [125, 126] and tunneling spectroscopy [127, 117]. Those polarons are assigned to the LO4, LO3, and LO2 modes [127, 117], with the largest energy scale being $\hbar\omega_{LO4} \sim 90 - 100$meV, depending on the techniques employed [125, 117, 126, 127] and no difference between bulk or 2DES is found.

The coupling strength decreases with increased carrier concentration [126, 117]. The possibility of those LO modes giving rise to pairing has been considered [128, 112], despite the questionable applicability of Eliashberg theory. (See [112] for the treatment and [129] for the follow up discussions.) Besides the aforementioned LO modes, other alternatives have been considered. Candidates range from the soft phonons of the AFD modes [130], soft phonons of the FE modes [131], FE modes with biphonons [132], plasmons with polar optical phonons [133], plasmons [129], TO phonons [134] (followup [135] and [136]), and cooperative Jahn−Teller distortions [137].

IV. A relatively new picture links superconductivity to the ferroelectric quantum critical point [138], analogous to the description of superconductivity in cuprates driven by magnetic quantum critical point for the cuprates. However, the link between superconductivity and ferroelectricity is not clear. It was reported by Itoh et al. [139] that the isotope ^{16}O to ^{18}O substitution can induce ferroelectricity in $SrTiO_3$. Stucky et al. [54] reported that the same isotope substitution raised T_c by 50% as well as the upper critical field H_c2 by a factor of two. However, Ca-substitution is also known to be able to induce ferroelectricity [48, 49], Behnia et al. reported both weakened [12] and enhanced superconductivity[140] upon Ca-substitution.

B. $LaAlO_3/SrTiO_3$ and its 2-Dimensional Electron System (2DES)

The 2-dimensional electron system (2DES) formed at the $LaAlO_3/SrTiO_3$ interface, first reported by Ohtomo et al. [141], is the most extensively studied conductive $SrTiO_3$-based heterointerface. $LaAlO_3/SrTiO_3$ has a critical thickness of 4 u.c. of crystalline $LaAlO_3$ [142] and the $SrTiO_3$ substrate must be TiO2-terminated [141, 143]. This interface also has been found to exhibit emergent behavior such as an electric gate-tunable metal-insulator-transition for critical thickness ($\sim$ 3 u.c.) [142, 144]. The interface is superconducting [145] and controllable with an electric field [146] (Section I.B.4). Magnetism has also been reported at this interface [147, 148, 149] (Section I.B.3).

The $LaAlO_3$ layer need not be (100) oriented or even crystalline. Chen et al. [151]

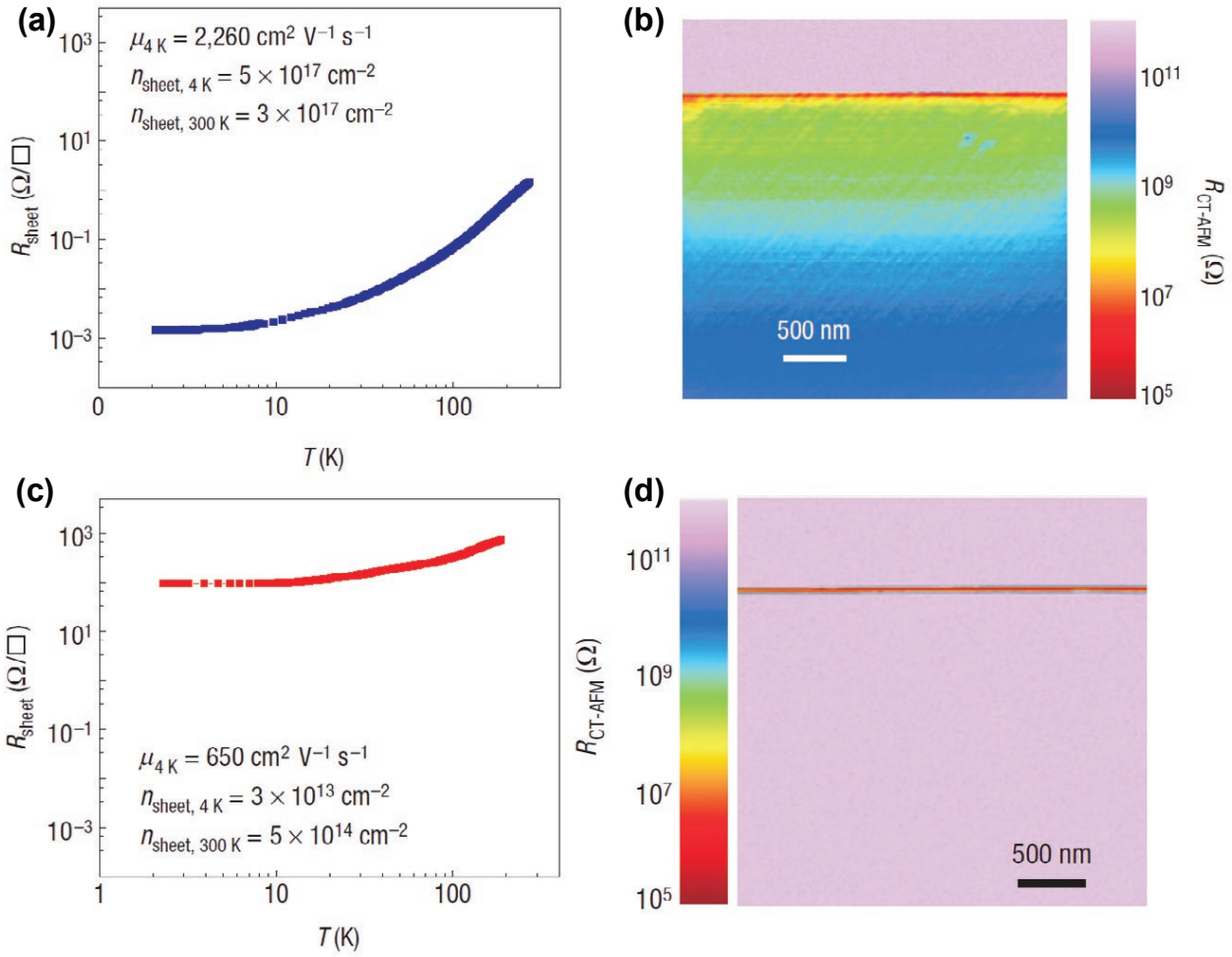

Figure 3: Electron profile probed by conductive-tip AFM (CT-AFM), for the unannealed and annealed samples. (a) The sheet resistance as a function of the temperature for the unannealed sample. The 2D carrier concentration 5×10^{17} cm^{-2} is unphysically high. (b) The electron profile for the unannealed sample seen under CT-AFM. The electrons are not well confined and spread into the $SrTiO_3$ bulk. (c) The sheet resistance for the sample annealed at high oxygen partial pressure (P_{O_2} = 400 mbar) after the growth. (d) The CT-AFM image for the annealed sample. The electrons are confined at the interface with width $\sim$ 7nm. (a)-(d) Adapted from [150].

found that amorphous-$LaAlO_3/SrTiO_3$ can produce a conducting interface. The conducting interface was attributed to oxygen vacancies [151]. A conductive interface on (110) and (111) $SrTiO_3$ was observed [152, 153]; both interfaces are non-polar. Even *conventional* $LaAlO_3/SrTiO_3$ interfaces can be enhanced with a $SrCuO_3$ overlayer to promote oxygen exchange with the surface, leading to a reduced number of oxygen vacancies, which is correlated with higher-mobility transport [154].

In addition to bare $SrTiO_3$ and $LaAlO_3/SrTiO_3$, a variety of other heterostructures have conductive interfaces [155, 156, 157, 158, 159, 160, 161, 162, 163, 164, 165], although some are insulating [156, 160, 166, 167, 168, 169, 170]. Trilayer $SrTiO_3/LaTiO_3/SrTiO_3$ heterostructures were found to be conductive even to one unit cell of LaTiO3 [171] and believed to support a 2DES and 2-dimensional hole gas (2DHG) on the $LaAlO_3/SrTiO_3$ and $SrTiO_3/LaAlO_3$ interface, respectively [172]. The $GdTiO_3/SrTiO_3$ quantum wells have been explored as candidate Mott insulators [173, 174, 175, 176, 177, 178]. Others result in ultrahigh carrier density like $NdTiO_3/SrTiO_3$ [179]. A spinel/perovskite interface $\gamma-Al_2O_3/SrTiO_3$ [180, 181] with extreme mobility enhancement (as high as 140,000 cm^2/Vs) has also been reported.

1. 2D but Not Really 2D: $SrTiO_3$ Ferroelastic Domains and Walls

The physics is drastically different in lower dimensions. In some heterostructures, electrons (or holes) can be confined at the interface. Because the confinement can be very narrow, subbands can form due to quantum confinement of the electron (hole) wavefunction perpendicular to the heterostructures planar dimension (conventionally referred to as the z-direction). This quantization leads to steps in the 2D density of states and many other notable and interesting effects. A proper 2DES strictly refers to conditions in which only the lowest subband is occupied [182]. Electrons in 2D or 3D are usually well described by Fermi liquid (FL) theory (reviewed, e.g. by Schultz [183]). However, there are notable departures from FL behavior that are often ascribed to strong electron correlations. There have been many recent reviews on strongly correlated electron systems, see, for examples [184, 185, 186, 187]. In the oxide literature, 2D electrons are often referred to as 2D electron liquids (2DELs) [188]. As we will see below, the degree to which electron correlations

manifest themselves can depend on many parameters, e.g. magnetic field, carrier density, and temperature. Therefore, in this review we will use the more agnostic term *2D electron system* (2DES) to encompass all behavior that is 2D, regardless of the degree of electron correlation. Systems that are not clearly 2D but confined will be described as quasi-2D or quasi-2DES.

The 2D transport may be highly inhomogeneous, percolative, and phase separated [148, 189]. The inhomogeneity may be a possible explanation for the sub-quantum conductance (e^2/h) knee of at the metal-to-insulator transition [190, 191]. $SrTiO_3$ forms ferroelastic domains at $T_{AFD} = 105$ K (Section I.A.1). These domains not only modulates the current density [192], but also introduce strong anisotropy [103], and offset superconducting transition temperature [193].

The domain can be controlled by gating [194, 195, 196]. The ferroelastic domain configuration is coupled to the ferroelectric phase: it is necessary to warm the sample above T_{AFD} to remove the polarization of strain induced ferroelectricity [44]. The domain walls may be polarized, as seen under scanning single electron transistor [195]. The domain wall may attract defects such as oxygen vacancies. The ferroelastic domain configuration may also be coupled to the magnetic degree of freedom, as suggested by Ngo et al. [197] in hysteretic tunneling magnetoresistance between $Co/Ti/LaAlO_3/SrTiO_3$. The tunneling magnetoresistance has 2-fold symmetry while the coercivity has 4-fold symmetry and would change configuration only when the sample is warmed through T_{AFD}. A form of magnetism that is coupled to the ferroelastic domains has been reported by Christensen et al. [198] seen under scanning SQUID.

2. Transport of $LaAlO_3/SrTiO_3$ 2DES

a. Anisotropic Magnetoresistance Anisotropic magnetoresistance is very commonly reported for $LaAlO_3/SrTiO_3$ [148, 199, 200, 201, 202, 203, 204, 205, 206, 207] and other $SrTiO_3$-based heterostructures [208, 209]. In short, the magnetoresistance for different magnetic field directions can be summarized as follows:

I. Out-of-plane magnetic field: most commonly positive ($\Delta R > 0$) [210, 208, 148, 199, 202,

209]. In the small to intermediate field regime the magnetoresistance is dominated by weak localization (at lower carrier concentration) or (antilocalization at higher concentration). At larger field, quantum oscillation is observed. Both the weak localization and quantum oscillations will be discussed in the next several sections.

II. In-plane magnetic field and perpendicular to the direction of transport: the magnetoresistance, though sometimes positive ($\Delta R > 0$) at smaller field, would eventually turn negative ($\Delta R < 0$) at large magnetic field [208, 148, 211, 212, 202, 203]. A negative magnetoresistance as large as $\Delta R/R = -70\%$ was reported [211]. The negative magnetoresistance persists up to $T = 20$K [211].

III. in plane, parallel to transport: usually negative ($\Delta R < 0$) [148].

The in-plane anisotropy of the magnetoresistance is a combination of II, and III. However, there is a marked dichotomy of the in plane anisotropy for carrier concentration $n_e < n_L$ and $n_e > n_L$, where $n_L$is the Lifshitz point. [119, 120, 213]. As the magnetic field is swept in plane, a sinusoidal magnetoresistance is observed when the carrier concentration $n_e < n_L$, as shown in Figure 4 (b). The anisotropy becomes irregular or of higher harmonics when $n_e > n_L$(Figure 4 (c) and (e)) [119, 213, 120]. The anisotropy vanishes at T$\sim$35 K [200]. A similar temperature is reported for the anisotropy of [110] and [111] $SrTiO_3$ as well [205, 206].

b. Spin-Orbit Coupling (SOC) Gate tunable spin-orbit coupling of $SrTiO_3$-based 2DES has been reported [212, 214, 215, 216, 217, 218, 219, 220]. The Rashba spin-orbit coupling is expected due to the surface inversion symmetry breaking of the interface. Both k-linear and k-cubic Rashba spin-orbit interaction may be possible. The k-linear Rashba interaction has a Hamiltonian of the form $H_{R1} = \alpha_{R1} i(k_-\sigma_+ - k_+\sigma_-)$, where $\sigma_\pm = (\sigma_x \pm i\sigma_y)/2$ and $k_\pm = k_x \pm ik_y$ while the k-cubic Rashba interaction is $H_{R3} = \alpha_{R3} i(k_-^3\sigma_+ - k_+^3\sigma_-)$. Theoretical calculations suggested that the Rashba spin-orbit coupling would be dominantly k-cubic in d_{yz}/d_{xz} [221, 222, 223] with an energy scale of fews meV to $\sim$ 20 meV. On the other hand, the Rashba interaction may be k-linear [222], k-cubic or negligible in d_{xy} [223].

The reports on spin-orbit coupling are primarily using the following measurement: (1) the Weak localization (WL) and anti-localization (WAL) in the magnetoconductance. (2) The superconductivity upper critical field and its violation of the Pauli paramagnetic depairing

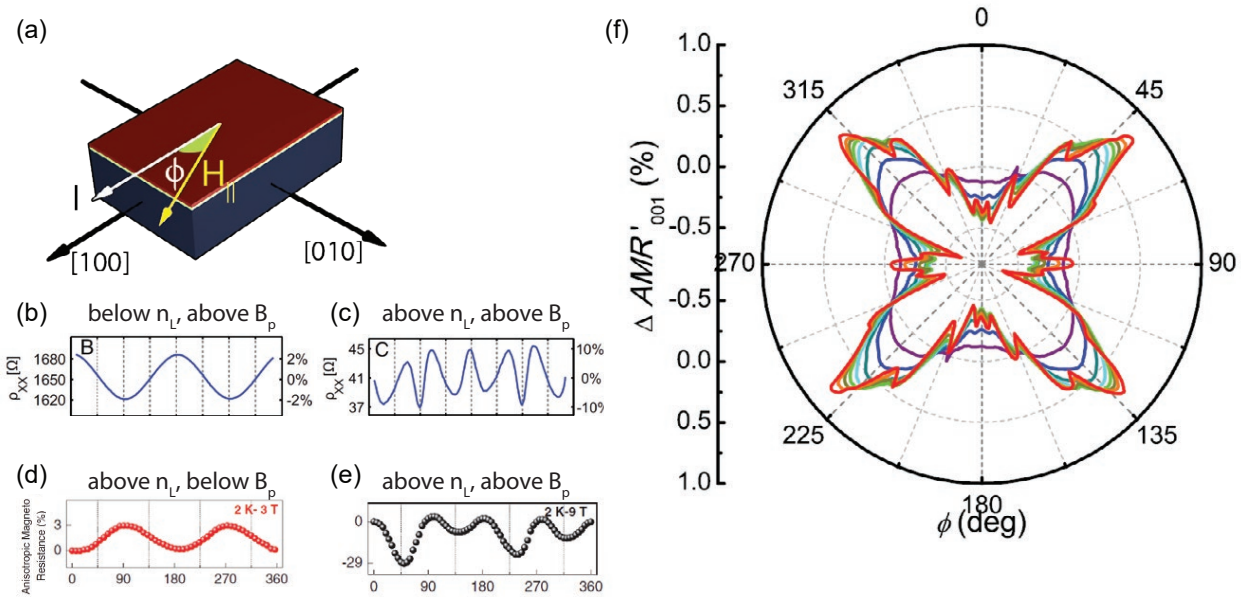

Figure 4: Anisotropic magnetoresistance. (a) The setup for the in-plane anisotropic magnetoresistance measurement. The anisotropy (excluding the 2-fold Lorentz contribution) only appears when the both the carrier concentration $n_e > n_L$ and $B > B_p$. The transition from regular sinusoidal to irregular or higher harmonics is revealed when the carrier concentration is increased from $n_e < n_L$ (b) to $n_e > n_L$ (c), or when from $B < B_p$ (d) to and $B > B_p$ (e). (f) The complex anisotropy with rich structure reported by Miao et al. [205]. Adapted from [205]. (b) and (c) Adapted from [120]. (d) and (e) Adapted from [213].

limit (also Chandrasekhar−Clogston limit). (3) Spin injection and spincharge conversion such as the inverse Edelstein effect. (4) Spin- and angle-resolved photoemission spectroscopy (SARPES). The strength of the spin-orbit interaction is tunable (by applying gate voltage) in all cases (except (4), in which the tunability is not explored [224]), this is expected for Rashba-type spin-orbit interaction. However, there are some inconsistencies among reports. For example, the trends of the tunable spin-orbit coupling observed with WAL and those deduced from the violation of the Chandrasekhar−Clogston limit are opposite to each other. Furthermore, a change of sign of the Rashba coefficient is reported for the case of spin-

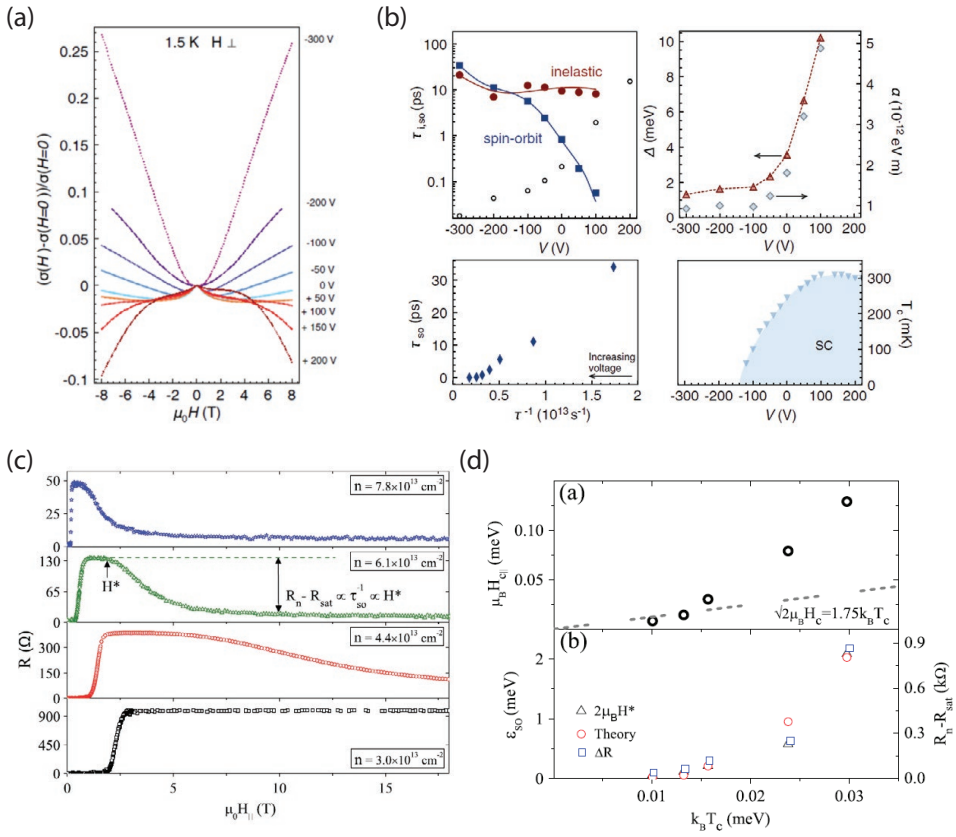

Figure 5: Gate-tunable spin-orbit interaction. (a) The evolution of the magnetoconductance as a function of gate voltage. The crossover from WL to WAL is observed. Adapted from [214]. (b) Caviglia et al. [214] then fitted the data to the MF theory, obtaining the spin-orbit strength $\Delta \sim 1 - 10$ meV. Left Panels: various dephasing time from the fit. Right panels: The Δ increases sharply near the gate voltage corresponding to the superconducting transition at lower temperature. Adapted from [214]. (c) The evolution of the resistance as a function of in-plane magnetic field at different gate voltage. (d) Upper: the evolution of in-plane the upper critical field as the gate voltage is varied. (Plotted against $k_B T_c$). Lower, the spin-orbit strength obtained from the violation of the Pauli limit, using $g\mu_B H^* = \epsilon_{SO}$. (c) and (d) Adapted from [212].

injection [225]. The reports with SARPES are more controversial. Santander-Syro et al. [224] reported an extremely large spin-splitting of 100 meV. But the spin splitting was not observed in the follow up work by McKeown Walker et al. [226]. Here we briefly discuss the results from the first two methods (using magnetotransport). The spintronic-related works will be discussed in Section I.B.2.f.

WL and WAL in the magnetoconductance. In order to get a good quantitative match between experimental and theoretical results for the magnetoresistance, spinorbit effects must be included. These effects fall into two major categories with competing mechanisms of action. The more simplistic mechanism is known as the Elliot−Yafet (EY) mechanism of spin relaxation [227, 228]. In this case, the electron spins relax as the spin-orbit interaction causes them to not be in a pure spin state and thus their spin may change with each scattering event, leading to a case where the spin-orbit relaxation time is proportional to the elastic scattering lifetime, $\tau_{SO} \propto \tau_{el}$. The other mechanism, the Dyakonov−Perel (DP) mechanism, is the result of spin precession in an inhomogeneous magnetic field between scattering events and thus the spin-orbit relaxation time scales inversely with the elastic scattering lifetime, $\tau_{SO} \propto 1/\tau_{el}$ [229]. Utilizing these relaxation mechanisms to understand the magnetoresistance of two-dimensional systems has led to two classes of models. The Maekawa−Fukuyama (MF) equation (k-independent corrections) [230] and the Hikami−Larkin−Nagaoka (HLN) equation (k-cubic corrections) [231] use the EY mechanism to describe the magnetoresistance, while the results of Iordanskii, Lyanda-Geller, and Pikus (ILP) assume the DP relaxation mechanism through a spin-dependent vector potential (has both k-linear and k-cubic corrections) [232]. Below we describe the experimental results for $LaAlO_3/SrTiO_3$ and the applications of these models to understand the dominant relaxation method.

In the first report of Rashba SOC in $LaAlO_3/SrTiO_3$ using WAL, Caviglia et al [214] used MF and obtained gate tunable τ_{SO} that decreases with gate voltage. τ_{SO} decreases sharply by 3 orders of magnitude. τ_i has a power-law dependence and decreases with increased temperature ($\tau_i \propto T^{-p}$ for some power p). A WL to WAL crossover can be seen in Figure 5 (a). The onset of sharp increase of Δ (decrease in τ_{SO}) roughly matches the gate voltage value for insulator-superconductor transition at lower temperatures (Figure 5 (b)). $\tau_{SO} \propto 1/\tau_{el}$ is

observed therefore DP is suggested. On the other hand, Nakamura et al [215] used ILP and found the WAL can be fitted only when the k-linear dependence is rejected (leaving only k-cubic term).

No $\tau_{SO} \propto 1/\tau_{el}$ is observed therefore EY is excluded. Later, Liang et al [218] reported a non-monotonic evolution of the coupling strength as a function of gate voltage. Also with ILP, k-cubic Rashba interaction is identified. The Rashba interaction is attributed to the d_{xz}/d_{yz} band, which has a spin splitting peaked at the avoided crossing. This assignment also explains the non-monotonic gate dependence of the coupling strength. The opposite dependence on gate reported by Caviglia et al [214] and Ben Shalom et al [212] may also be explained if the range covered by them are on two different sides of the maximum.

Violation of the Chandrasekhar−Clogston limit in the upper critical field. Spin-orbit coupling is one of the possible causes for violation of the Chandrasekhar−Clogston limit. As the in-plane magnetic field is applied, Ben Shalom et al. [212] observed a three-stage evolution of the magnetoresistance as a function of the field, as shown in Figure 5 c: (i) superconducting state for $0 < B < \mu_0 H_{c2}^{||}$, (ii) resistive state with nearly constant resistance for $\mu_0 H_{c2}^{||} < B < \mu_0 H^*$, and (iii) a sudden drop of resistance when $\mu_0 H^* < B$. Both $\mu_0 H_{c2}^{||}$ and $\mu_0 H^*$ increase with decreasing carrier concentration.

The Clogston−Chandrasekhar limit $H_{c2,BCS}^{||} < 1.76 k_B T_c/\sqrt{2}\mu_B$ (k_B: the Boltzmann constant; μ_B: the Bohr magneton) is violated at lower carrier concentration. Ben Shalom et al. assigned H^* to spin-orbit interaction, and obtain the energy scale from $g\mu_B H^* = \epsilon_{SO}$, and spin-orbit scattering time from $\epsilon_{SO} = h/\tau_{SO}$ increases with decreasing carrier concentration. H^* becomes large and inaccessible ($H^* > 18$ T) for the experimental setup at carrier concentration $n_{Hall} = 3.0 \times 10^{13}$ cm^{-2}. The effect of H^* is observed till $T = 100$ K [212]. Later, in δ-doped $SrTiO_3$, Kim et al. [233] fitted the observed angular dependence of Werthamer-Helfand-Hohenberg (WHH) theory (which extends the result of Gor'kov on H_{c2} of Type-II superconductors by including the Pauli spin paramagnetism and spin-orbit scattering off impurities) and obtained an energy scale ~ 2 meV for SOC. In the thickness dependence of τ_{SO} and τ_{el}, no traits of DP or EY are observed. Furthermore, since there is no apparent surface inversion symmetry breaking of the δ-doped $SrTiO_3$ in [233] because both sides of the δ layer is covered with undoped $SrTiO_3$ buffer layer, Kim et al suggest that

the observed violation of the Pauli limit is intrinsic to $SrTiO_3$.

c. Anomalous Hall Effect For $SrTiO_3$-based heterostructures, a change of the Hall coefficient (slope of the Hall resistance) with applied magnetic field (Figure 6 a) is commonly observed [210, 234, 119, 120, 235, 212, 201, 204, 209, 236, 237, 238, 239, 240]. The origin of this nonlinearity is still unclear. It was thought to be due to multiband transport [210, 234, 204, 218]. However, recently Gunkel et al. [235] pointed out that the multiband conduction model was able to capture the field dependence of the Hall coefficient R_H except the small upturn near the zero field, as shown in Figure 6 (b). Gunkel et al. introduced an additional term R_0^{AHE}, with Langevin-type polarizable spin-1/2. The R_0^{AHE} fits the upturn well, but the observed (1) temperature independent saturation field (2) temperature dependent R_0^{AHE} are not expected for the Langevin-type model. Joshua et al. probed this nonlinearity of the Hall resistance R_xy with a large in plane plus a small out of plane magnetic field [120] (Figure 6 (c)). The critical field B_p for the onset of the change of R_H increases with decreasing carrier concentration when $n_e > n_L$ and diverges as n_e approaches n_L.

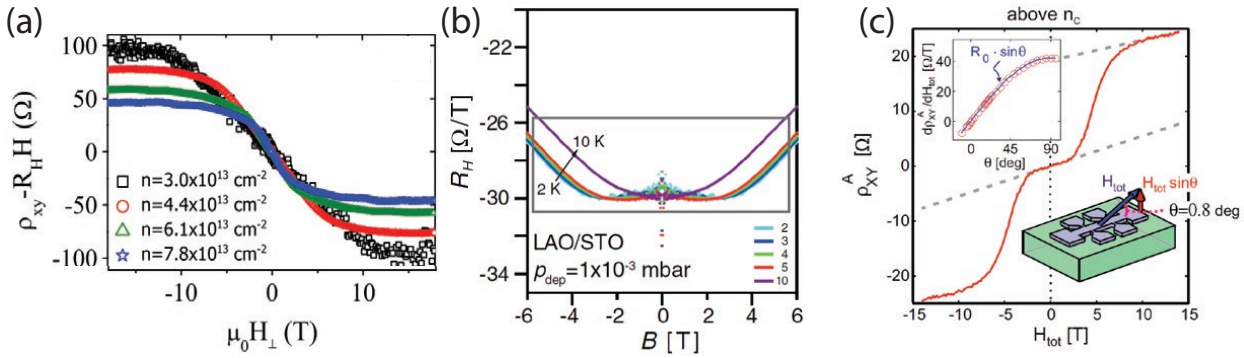

Figure 6: Nonlinear and anomalous Hall effect. (a) Nonlinearity in the Hall measurement. R_H (the slope of the Hall resistance R_{xy}). Adapted from [212]. (b) Hall coefficient R_H as a function of the magnetic field. The small upturn for $B \sim -3$ T to $B \sim +3$ T deviates from the parabolic-like dependence expected for 2-band model. Additional R_0^{AHE} was introduced to fit this deviation. Adapted from [235]. (c) The evolution of ρ_{xy} as a function of magnetic field H_{tot}, 0.8° to the direction of transport. Adapted from [120].

d. Shubnikov−de Haas (SdH) Oscillation Shubnikov−de Haas (SdH) oscillation is very commonly reported (Figure 7 (a)). So far, there have been many reports of SdH for $SrTiO_3$-based 2DESs. From the archetypical $LaAlO_3/SrTiO_3$ [210, 241, 242, 243, 244, 245], ionic liquid gated $LaAlO_3/SrTiO_3$ [246], $SrCuO_2$ capped $LaAlO_3/SrTiO_3$ [247], with insertion of 1 u.c. LSMO [181, 248], δ-doped $SrTiO_3$ [249, 250, 251, 252], Mott Insulator interface $GdTiO_3/SrTiO_3$[174].

SdH is a powerful tool to probe the Fermi surface, as the frequency of the SdH is related to the Fermi surface area via the Onsager relation $F = (\Phi_0/2\pi^2)A$. Dimensionality and the confinement of the 2DES can also be learned from the angular dependence of the SdH, as no SdH should be observed with in-plane magnetic field. The 2D-3D crossover at about thickness $d = 64$ nm for δ-doped $SrTiO_3$ was observed by Kim et al. [251]. The 3D conduction nature is indeed observed in two earlier reports [141, 253] whose samples were grown at low oxygen partial pressure $P(O_2) = 10^{-4} - 10^{-6}$ mbar without post annealing and carrier concentration far beyond typical range $10^{12} - 10^{14}\text{cm}^{-2}$.

Although the SdH is commonly observed for this system, a comprehensive picture built upon all of the aforementioned reports is proven difficult to obtain. Experimentally determined parameters such as the effective masses vary from 0.62 m_e to 2.7 m_e. Maximally 5 SdH frequencies have been reported [247]. Properly assigning the subbands convoluted by Zeeman energy, Landau levels, tetragonal energy, atomic and Rashba spin-orbit coupling is challenging. Below are the major issues:

I. Missing carriers. In all of the aforementioned reports for SdH at $SrTiO_3$-based 2DEGs, the carrier concentration determined from SdH (n_{SdH}) is consistently smaller than the carrier concentration n_{Hall} determined from the Hall effect. The ratio n_{SdH}/n_{Hall} range from 4% in [250], to recently 90% in [252]. There are two primary (non-mutually exclusive) explanations. The first explanation is that nontrivial degeneracies may present, from the 3-fold valley degeneracy [210], 2-fold spin degeneracy, to 4-fold magnetic breakdown orbits [242] have been considered. The second explanation is that there may exist unknown carriers who suffer from extensive scattering and have a mobility too low to show SdH. This scenario seems to be supported by increased n_{SdH}/n_{Hall} and coincides with higher mobility of the samples, larger $\Delta R/R$ of SdH. Also, in the dimensionality

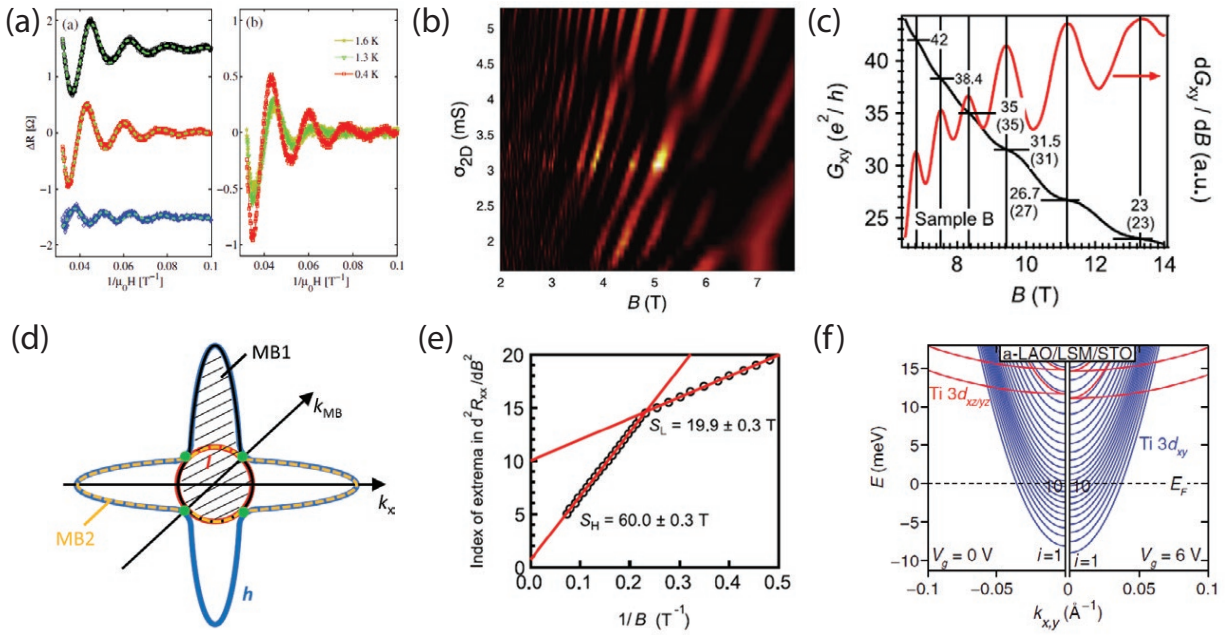

Figure 7: Shubnikov-de Haas (SdH) oscillations. (a) SdH reported by Ben Shalom et al. [210]. Adapted from [210]. (b) The evolution of the SdH as a function of gate voltage. Both peak-splitting and phase jumps are visible. Adapted from [243]. (c) The QHE-like plateaus with associated SdH oscillations reported by Xie et al. [242]. The plateaus have $\Delta\nu \sim 4$. (d) To explain the $\Delta\nu \sim 4$, Xie el al. suggested a 4-fold magnetic broken (MB) down orbits, shown as the shaded area. The inner Fermi surface dominates the transport at lower magnetic field ($B < 3.3$ T) while the MB orbits dominate at higher magnetic field. ($B > 3.3$ T). (e) The SdH frequence changes from $F = 20$ T to $F = 60$ T at about $B = 3.3$ T. Thus, the area for the MB orbits have to be 3 times of that of the inner Fermi surface. (c), (d) and (e) Adapted from [242]. (f) The 10-band model proposed by Trier et al. [248] to explain the observed $\Delta\nu \sim 10, 20$. Adapted from [248].

crossover comparison by Kim et al. [251], the inconsistency is smaller for the $d = 124$ nm sample, compared to $d = 37$ nm sample. This inconsistency also disappears in the 3D sample ($d = 800$ nm, $d = 1280$ nm) in Allen et al. [74]. These low mobility carriers may also be the reason for imperfect QHE reported so far [242, 252, 248].

II. Subband assignment. What are the subbands responsible for the observed SdH frequencies? The observed frequencies were often assigned by their effective mass, d_{xy} if m^*_{SdH} is lighter (typically $0.7-1m_e$) [174], and d_{xz}/d_{yz} if m^*_{SdH} is heavier ($m^*_{SdH} > 2m_e$) [245]. Detailed assignment is especially difficult when five frequencies with corresponding energy levels only few tenths of an meV apart [247].

As the gate voltage increases, the oscillations shift toward larger Fermi surface (due to the population of the carriers [241, 243] (Figure 7 (b)). However, at higher carrier concentration, Maniv et al. [244], reported a non-monotonous behavior of the SdH frequency as a function of the gate voltage V_G. The SdH frequency decreases after $V_G = 3$ V. Maniv et al. suggested that the SdH is from d_{xz}/d_{yz}, and they are repelled by d_{xy} at higher carrier concentration. For follow up, see Smink et al. [254] and Maniv et al. [255]. Notably, the carrier concentration supported in $GdTiO_3/SrTiO_3$[174] is an order of magnitude larger than all the other reports.

As the field increases, various types of change in F have been reported. For example, Jalan et al. reported a shift of the frequency [250]. The two Rashba branches F^+ and F^- shift in opposite directions with the increased field in Fte et al. [243]. For harmonically related frequencies, the lower harmonic disappears or changes into a higher harmonic after some field strength, most commonly $F \to 2F$ [174, 248, 252], except $F \to 3F$ in [242]. The $F \to 2F$ is usually explained with spin-splitting, except [252]. We discuss [242] and [252] in the next section.

e. Quantum Hall Effect Quantum Hall effect (QHE) with fully resovled series of filling factors ν is still elusive for $SrTiO_3$-based 2DES. Instead of perfectly quantized at $G_{xy} = \nu e^2/h$ at integer filling factor ν, the observed plateaus of the Hall conductance G_{xy} is often not perfect, limited to higher filling factors, and with nontrivial degeneracies, such as $\Delta\nu = 2$ in [252], $\Delta\nu = 4$ in [242], and $\Delta\nu = 10$ or 20 in Ref. [248].

To explain the observed $\Delta\nu \sim 10$ or 20, (raw value $\nu = 30.6$, 41.0, 53.5, 68.5, 88.5, etc), Trier et al. [248] proposed a picture consisting of 10 simultaneously populated bands with $s = \pm 1/2$ degeneracy. At $B < 6$ T, and SdH frequency $\Delta\nu \sim 20$ is observed. At $B > 6$, on the other hand, the plateaus become $\Delta\nu \sim 10$, and SdH frequency becomes twice as large, at $F = 25$ T. This is attributed to the splitting of the spin degeneracy. The 10-band picture

is also used to explain $n_{Hall} \sim 10 n_{SdH}$. As the gate voltage increases, the second band (of the 10 bands) has largest response.

Xie et al. [242] reported $\Delta\nu \sim 4$ with raw values $\nu = 23$, 26.7, 31.5, 35, 38.4, 42 (one of the four sets of presented data)(Figure 7 (c)). A change of SdH frequency from $F = 20$ T at $B < 4.3$ T to $F = 60$ T (three times as large) at $B > 4.3$ T is observed (Figure 7 (e)). Xie et al. proposed a magnetic breakdown orbit between the two lowest lying band (the assignment/nomenclature of d_{xy} or d_{yz}/d_{xz} was avoided), as shown in Figure 7 (d). The orbit has 4-fold degeneracy, to account for the $\Delta\nu \sim 4$. The orbit also has to have Fermi surface area $A_{MB} = 3A$, where A is the area of before the magnetic breakdown for $B < 4.3$ T, to explain the three fold change of the SdH frequency.

Matsubara et al. [252] observed $\nu = 4$ and 6, which are currently the lowest filling factor observed in $SrTiO_3$-based system so far. The $\Delta\nu = 2$ is attributed to the spin degeneracy. There are two relevant subbands in the picture (called EB1 and EB2, EB1 has lower energy). Compared to EB1 = d_{xy} and EB2 = = d_{yz}/d_{xz} assignment for interface 2DES, Matsubara et al. pictured that the lowest lying EB1 would have more d_{yz}/d_{xz} character. Both of the bands are dominated by d_{yz}/d_{xz} at the Fermi level. A change of the SdH frequency from $F = 6.4$ T at $B < 3.3$ T to $F = 12.9$ T at $B > 3.3$ T is observed. Instead of explaining this by the lifting of the spin-degeneracy, Matsubara et al. argued that the SdH is dominated by EB2 for $B < 3.3$ T. As the Landau index would be relatively high for EB1 therefore the amplitude would be smaller. On the other hand, EB1 dominates $B > 3.3$ T, as the quantum limit for EB2 may have been reached. This interpretation requires the Fermi surface to satisfy $2A_{EB1} = A_{EB2}$.

f. Spintronic Effects Oxide heterostructures have shown great (and increasing) promise for spintronic [256, 257] applications. The concept of semiconductor spintronics emerged from the successful application of the electron spin degree of freedom for data storage and sensing applications. However, as a full-blown replacement for electron charge, many effects are still missing. In this section we review efforts to measure effects related to spin injection, polarization, diffusion and detection. Many of the experiments performed so far are inspired by work in the semiconductor spintronics community.

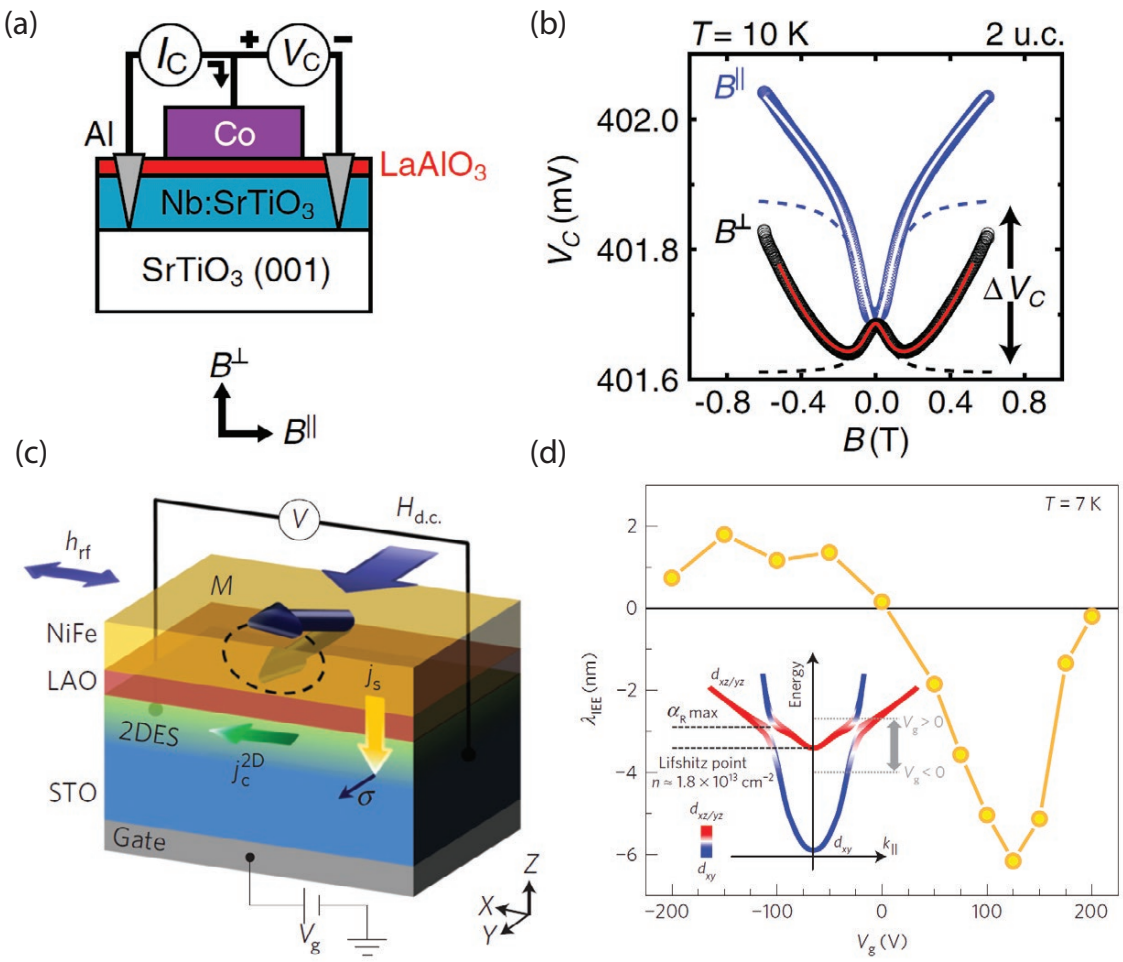

Figure 8: Spintronics effects. (a) The device schematics for 3-terminal tunneling magnetoresistance measurement. (b) The Lorentzian lineshape of the tunneling magnetoresistance measurement. (a) and (b) Adapted from [258]. (c) The device schematics of Lesne et al. [225]. The spin imbalance at the 2DES is created by spin-pumping technique. This spin imbalance is then converted to charge by the Rashba effect at the interface (the inverse Edelstein effect (IEE)). (d) The evolution of the spin to charge conversion efficiency λ_{IEE} as a function of gate voltage V_g. λ_{IEE} changes sign at about $V_g = 0$. Lesne et al. [225] suggested that the sign and the magnitude of α_R may be different for d_{xy} and d_{xz}/d_{yz}. (c) and (d) Adapted from [225].

Large, gate controllable Rashba spin-orbit interaction (Section I.B.2.b) makes the $SrTiO_3$ -based 2DEGs attractive for possible spintronic applications such as spin field effect transistors and electroresistive switches. Devices may also be enriched by taming the complex gate controllable phases. Recent reports includes characterization of spin injection via the Hanle effect [259, 260, 261, 262, 258, 263, 264], and spin-charge conversion by spin pumping followed inverse Edelstein effect (IEE) [225, 265].

The Hanle effect measurement is carried out with a three-terminal geometry between ferromagnetic-insulator-2DEG junction. Current is sourced from the ferromagnetic electrode and the voltage is measured nonlocally (Figure 8 (a)). Then the tunneling magnetoresistance is measured as a function of out-of-plane magnetic field. A Lorentzian lineshape is expected from the Hanle effect: when magnetic field $B^{\perp}$ is applied, spins of the carriers undergo Larmor precession at $\omega_L = g\mu_B B^{\perp}/\hbar$, and creates spin-imbalance voltage drop. The spin lifetime can be calculated from the width of the Lorentzian lineshape. The lineshape is inverted if field parallel to the magnetization of the ferromagnetic electrode is applied. The obtained spin lifetime tau_{sf} is around few ps to few tens of ps. For example, $tau_{sf} = 50$ ps at $T = 2$ K and length scale $l_{sf} = \sqrt{D\tau_{sf}} \sim 1\mu$m in Reyren et al. [260]. Gate dependence of tau_{sf} is observed in Kamerbeek et al. [263] and Han et al. [261] but not Inoue et al. [258]. Both the thickness of the insulating layer and the tunneling resistance are crucial [258]. While the Hanle signal is observed, it may not necessarily come from spin accumulation. Whether spin accumulation with a lifetime long enough to account for the Lorentzian lineshape exist is a question, see [258] for discussions.

On the other hand, efficient spin-charge conversion is reported by Lesne et al. [225] (Figure 8 (c) and (d)) and later by Song et al. [265] and Chauleau et al. [266]. Spin imbalance at the interface is created by spin-pumping. The spin imbalance is then converted back to charge by Rashba SOC (the IEE effect). The spin-to-charge conversion efficiency, described by λ_{IEE} for 2D materials, has a maximum $\lambda_{IEE} = 6.4$ nm ($NiFe/LaAlO_3$(2 u.c.)$/SrTiO_3$ at $T = 7$ K).

This efficiency is not only gate-controllable, but also unprecedentedly high, both as a 2DES and as a 3D equivalent. To compare with 3D materials, λ_{IEE} can be calculated from the spin Hall angle (θ_{SHE}) for 3D materials via $\lambda_{IEE} = \theta_{SHE} l_{sf}$, where l_{sf} is the spin diffusion

length.

$\lambda_{IEE} = 6.4$ nm for $LaAlO_3/SrTiO_3$ is more than ten times larger than the $\lambda_{IEE} = 0.43$ nm for W, which is known for large spin Hall angle. Furthermore, λ_{IEE} and α_R (Rashba coupling strength) are tunable by gate voltage. The evolution of α_R is non-monotonic and changes sign after a critical gate voltage (Figure 8 (d)). Lesne et al suggested that the sign and the magnitude of α_R may be different for d_{xy} and d_{yz}/d_{xz}. Then if the critical voltage corresponds to the Lifshitz point n_L, the α_R may be dominated by d_{xy} at lower gate voltages and by d_{yz}/d_{xz} at higher gate voltage. The non-monotonic evolution is also reported by Song et al [265] at T = 300 K, but the change of sign was not observed [265]. The IEE signal vanishes as the 2DES is depleted [265]. Chauleau et al [266] reported anisotropic IEE signal, which indicates either the spin relaxation depends on the direction of the spin-polarization, or the Rashba field is anisotropic.

3. Magnetism

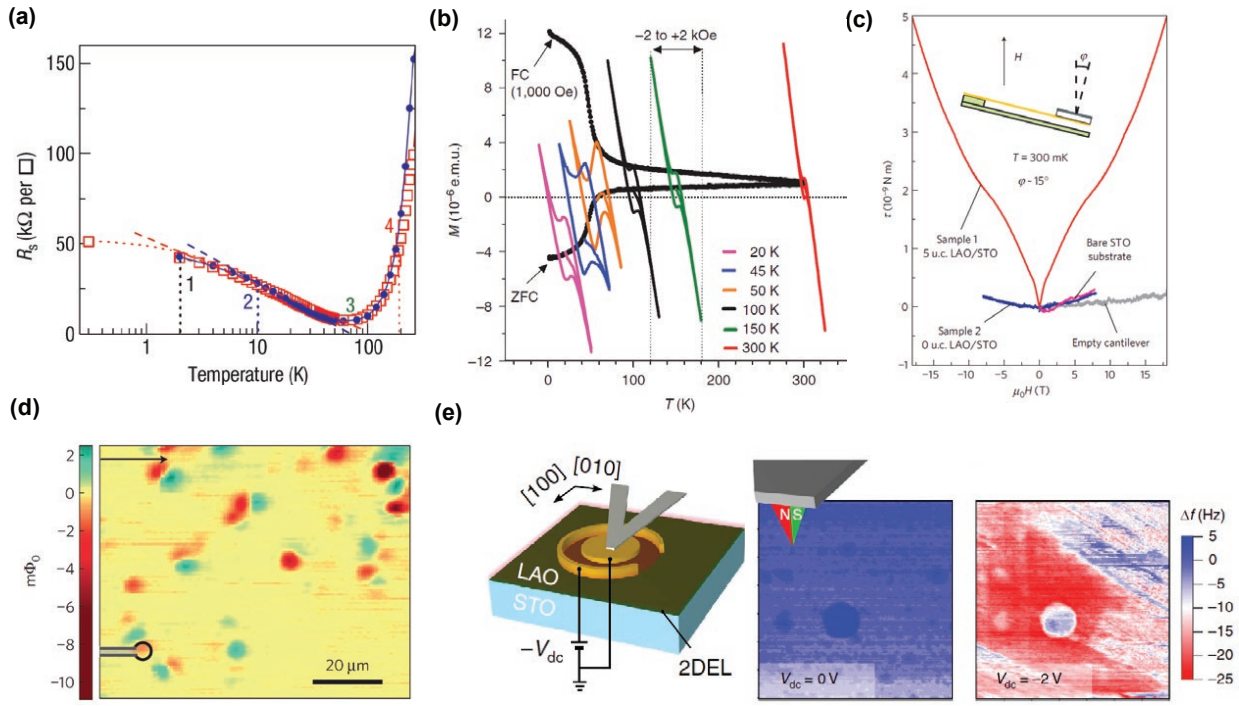

Figure 9: Experimental evidence for ferromagnetism at the $LaAlO_3/SrTiO_3$ interface. (a) Kondo minimum in the temperature dependence of the resistance. Adapted from [147]. (b) SQUID magnetometry: hysteresis loops taken at different temperature superimposed on top of the temperature dependence of magnetic moments. Adapted from [148]. (c) Cantilever-based magnetometry: the magnetic moment induced a torque under external magnetic field, the magnetization of the sample is inferred accordingly. Adapted from [267]. (d) Magnetic patches under scanning SQUID. With a micrometer-sized SQUID on a probe tip, microscopic magnetization can be imaged. Dipole-shaped patches are observed. Adapted from [268]. (e) Room temperature electrically-controlled ferromagnetism observed with magnetic force microscope (MFM). The magnetism signal is observed only when the interface is insulating. Adapted from [149].

$LaAlO_3$ and $SrTiO_3$ are both non-magnetic materials, so the first report of magnetism at the $LaAlO_3/SrTiO_3$ interface in 2007 [147] was quite surprising. There are several prominent reported features: (i) In the temperature dependence of the resistance there is a characteristic

Kondo-like minimum (Figure 9 (a)), followed by a saturation at lower temperature. (ii) The magnetoresistance shows a distinct hysteresis. Although the hysteresis was later ascribed to a magnetocaloric effect [269] there were many follow-up reports of magnetism. To date, the consistency of the results is still lacking, as is a comprehensive picture for the origin and mechanism of the magnetism. In this section, we first discuss some of the most notable experimental studies. We then argue that it is necessary to classify the observed evidence into two categories (i) a proper ferromagnetic phase and (ii) a metamagnetic phase that is a result of the multiband nature of $LaAlO_3/SrTiO_3$ and many body effects. This topic has also been reviewed recently by Pai et al. [2] and interested readers are encouraged to look there for more details.

a. Experimental Evidence The evidence for magnetism at the $LaAlO_3/SrTiO_3$ interface arise from a number of different measurements, including SQUID magnetometry [148], cantilever-based torque magnetometry [267], scanning SQUID magnetometry [268, 270, 271], magnetic force microscopy (MFM) [149], X-ray magnetic circular dichroism (XMCD) [272, 273, 170], and β-NMR [274]. Indirect signatures of magnetism arise in transport studies, and include magnetoresistance anisotropy (Section I.B.2.a), giant (negative) magnetoresistance (Section I.B.2.a) and anomalous Hall effect (Section I.B.2.c).

Kondo effect. The interaction between a dilute magnetic moment and itinerant carriers is known as the Kondo effect [275]. A key characteristic is a resistance minimum at finite temperature followed by an upturn and a saturation at lower temperatures. The resistance vs. temperature curve ($R(T)$) follows a universal scaling function $R_K(T/T_K)$ with a single parameter: the Kondo temperature T_K. The Kondo effect was one of the main signatures of magnetism in $LaAlO_3/SrTiO_3$ first reported by Brinkman et al. [147]. Subsequently, the Kondo effect was widely reported, for $LaAlO_3/SrTiO_3$ [276, 191, 199], electrolytically-gated $SrTiO_3$ [208, 277], $LaAlO_3/EuTiO_3/SrTiO_3$ trilayer structures [278], and in $\delta-$doped $LaTiO_3/SrTiO_3$ [279].

The Kondo temperature is found to increase with carrier concentration [208, 191]. The observed negative magnetoresistance, measured with a magnetic field that is in-plane and perpendicular to the transport direction, has been explained within the context of Kondo

scattering [208], but this negative magnetoresistance may have a different origin, as argued by Diez et al. [211]. Han et al. [280] reported weaker Kondo signatures in samples that were expected to have a higher concentration of oxygen vacancies (growth at lower oxygen partial pressure without post annealing). The explanation was that in the samples with more oxygen vacancies, the conduction networks extended into the bulk and were able to evade the dilute local moments, resulting in the weaker coupling between the iterant carriers and localized moments [280].

The Kondo upturn can be suppressed by light [281, 282], even with sub-bandgap excitation of 650 nm [282]. The suppression of the Kondo effect has been attributed to light-induced charge redistribution [281] and destruction of Kondo coherence [283, 282].

SQUID. Using a SQUID magnetometer, Ariando et al. [148] reported magnetic hysteresis loops of $LaAlO_3/SrTiO_3$ (Figure 9 (b)). The hysteresis loop persisted up to room temperature. There was also a monotonic increase of the measured magnetization as the oxygen partial pressure $P(O_2)$ increases from $P(O_2) = 10^{-6}$ mbar until it peaks at $P(O_2) = 10^{-2}$ mbar.

Scanning SQUID. Bert el al. [268] imaged dipole-like ferromagnetic patches (Figure 9 (d)) by using a scanning SQUID microscope to measure $LaAlO_3/SrTiO_3$. The spatial distribution was found to be highly non-uniform. The magnitude of the magnetization and size also varies from patch to patch. Kalisky et al reported a 3 u.c. critical thickness for the magnetic patches [270], which is the same as the insulator-to-metal transition in $LaAlO_3/SrTiO_3$ [142]. The patches can also be manipulated by using the scanning SQUID probe to push on the sample surface, and they found the orientation of the patches to align preferentially along the crystallographic axes of the sample [271].

The same scanning SQUID magnetometer is capable of measuring diamagnetic susceptibility as well, which can provide a measure of superfluid density [268, 284]. The reported superfluid density was found to be tunable via gating from the back of the sample, while the ferromagnetic patches do not shift within the same range of back gate voltages (-70V to 390V). There was also no correlation found between the ferromagnetic patches and the superfluid density [268, 284, 285]. Curiously, follow-up scanning SQUID experiments by Wijnands et al. [286] found no magnetic patches on samples grown under nominally identical

conditions. Later Christensen et al. reported a second form of the magnetism that is coupled to the ferroelastic domain walls [198].

Magnetic torque magnetometry. Li et al [267] reported in-plane, superparamagnetic-like order of $LaAlO_3/SrTiO_3$ using cantilever-based magnetometry (Figure 9 (c)). The reported magnetization was $\sim$0.3 μ_B per interfacial unit cell. The magnetization was independent of temperature up to 40K, and found to persist beyond 200 K.

β-detected nuclear magnetic resonance and neutron scattering. Salman et al. [274] used β-NMR to study the magnetism of $LaAlO_3/SrTiO_3$. The magnetization of the samples was derived from the relaxation rate of the spin-polarized radioactive ^{8}Li atoms. The spins of ^{8}Li are inferred from the spins of the electron as a product of the β-decay. They reported a magnetization corresponding to $\sim 1.8 \times 10^{-3}\mu_B$/u.c., if uniform magnetization is assumed, which is significantly smaller than that reported by Li et al. [267]. However, if spatial variation is taken into consideration, a local density of $\sim \times 10^{-12}\mu_B$ cm^{-}2, which is on the same order of magnitude reported by Bert et al. [268].

Polarized neutron reflectometry. Fitzsimmons et al. [287] reported a null result for the magnetic order of $LaAlO_3/SrTiO_3$ using polarized neutron reflectometry. In this method the magnetization is obtained from the asymmetry in specular reflectivity, it being a function of wave vector transfer and neutron beam polarization. The observed magnetization was found to be close to the signal-to-noise limit of the measurement, in fields as large as 11T and temperatures as low as 1.7K.

Magnetic force microscopy (MFM). Using magnetic force microscopy (MFM), Bi et al. [149] reported electronically controlled ferromagnetism up to room temperature at the $LaAlO_3/SrTiO_3$ interface (Figure 9 (e)). The interaction between the magnetized tip and the sample surface alters the amplitude, phase, and frequency of the tip oscillation. A gold top gate enables the interface to be depleted of electrons. Magnetization was found only when the sample was gated into the insulating state, and when the MFM probe is magnetized in-plane. The thickness window for magnetic response was found to be 8-25 u.c [288]. Followup efforts with MFM and PFM [289] and Kerr on the similar samples [290].

X-ray magnetic circular dichroism (XMCD). The magnetic moment at the interface can be probed locally using X-ray magnetic circular dichroism (XMCD). The XMCD

signal comes from the asymmetry in the polarization dependent X-ray absorption spectra caused by the magnetic moment. XMCD signal of the Ti L_2, L_3 edges was reported by Lee et al. [272] and Salluzzo et al. [170, 273]. The corresponding magnetic moment is very weak, from $\sim 0.01 - 0.1\mu_B$ per Ti atom in [272], or $< 0.1\mu_B$ in [170]. The above numbers were obtained at $T = 3 - 10$ K. The XMCD signal is not observed at room temperature [272]. While Lee et al. [272] assigned the moment to the orbital of the Ti^{3+} site, the magnetic moment may also be related to the oxygen vacancies, as stronger XMCD signal is observed for the sample with higher concentration of oxygen vacancies [273].

b. Two Types of Magnetism The observed magnetic signatures appear to have two distinct origins: (i) proper ferromagnetism due to localized moments antiferromagnetically coupled to the iterant electrons (similar to the picture proposed by Salluzzo et al. [170, 273] and (ii) metamagnetism resulting from a combination of the multiband effect, SOC, and many body effects. There are several reasons for treating the metamagnetism separately from the aforementioned ferromagnetism. For example, the proper ferromagnetic long-range order can extend up to room temperature, but the metamagnetism has a reported critical temperature of approximately 35K. Additionally, the reported characteristic field B_p of the metamagnetism is inversely dependent on the carrier concentration. B_p can be as large as 14 T (which would be unphysically large as a coercive field for ferromagnetism), for carrier concentrations n_e approaching the Lifshitz transition n_L.

I. Ferromagnetism. Depending on the concentration of iterant carriers n_e and the concentration of the localized moments n_m, the phase of the system can be in several states: (1) a non-magnetic insulator, if $n_m \gg n_e$, i.e., n_m is too high, (2) a ferromagnetic insulator, if $n_m \sim n_e$ (roughly of the same order of magnitude) where the concentration of the itinerant carriers is enough to support long range ferromagnetic order, which survives to room temperature [170, 273], but not enough to form a conducting state, or (3) a Kondo-like conductor without ferromagnetic long range order if $n_m \ll n_e$. In the later state the long-range ferromagnetic order will be destroyed by the flood of iterant carriers. There can also be an accompanying decrease of the concentration of the localized moment n_m due to the global offsets of the chemical potential if the localized moments

are intrinsic, as is the case with Ti^{3+}. The remaining magnetic moments will still be present, as manifested in the characteristic temperature dependent resistance minimum.

The previously discussed ferromagnetism is responsible for most of the direct measurement of magnetization such as scanning SQUID [268, 270, 271], SQUID [148, 199], cantilever magnetometry [267], MFM and MeFM [149, 288], and MCD [291]. This picture does not provide any constraint on local variations of the order parameter, and it does not preclude a non-uniform carrier concentration leading to a phase separation as reported by Ariando et al. [148] or a non-uniform distribution of magnetic patches in the scanning SQUID measurements reported by Bert et al. [268] or the magnetism decorating ferroelastic domains reported by Christensen et al. [198]. However, it does account for the null result reported by Fitzsimmons et al. [287], as in that case the carrier concentration was not actively controlled.

This still does not answer what exactly the local moments are. The local moments responsible for the ferromagnetism could be magnetic impurities, or they may have a more intrinsic origin such state localized by oxygen vacancies. The impurity level of substrates varies across vendors but are mostly in the ppm level [292]. Indeed, as in the case of dilute magnetism in semiconductors, a ppm level of magnetic impurities is enough to induce the magnetization that has been reported [293, 294, 292]. However, a strong connection between the magnetism and oxygen vacancies was reported by Rice et al. [291]. The magnetic circular dichroism signal was observed only for the samples annealed under low oxygen partial pressures (to introduce oxygen vacancies), and disappears once the samples were re-oxygenated [291]. The oxygen vacancies also strongly affect the magnetism of Fe-substitute $SrTiO_3$ ($Sr(Ti_{1-x}Fe_x)O_{3-\delta}$) [295]. Several theoretical studies have linked oxygen vacancies (or vacancy clusters) with magnetism. Vacancies produce in-gap states [296] with various charge states, vacancy clustering configurations [81], and associated magnetic moments of Ti atoms as a function of their relative position with respect to the oxygen vacancies or vacancy clusters [92]. In addition to the Ti-3d orbital possessing a moment, the F-center (single electrons at the vacancy sites) may also possess a magnetic moment [297, 298]. Other defects such as Sr-vacancies have also been considered to be responsible for the observed magnetism [235].

II. Metamagnetism. The second type of magnetism, or *metamagnetism* is due to a combination of the multiband effect, SOC, and electron pairing. The observed signatures are the anisotropy of the magnetoresistance (Section I.B.2.a), giant negative magnetoresistance (Section I.B.2.a), and the anomalous Hall effect (Section I.B.2.c). The local moments can nonetheless influence this metamagnetism and all of the relevant transport properties, but only via the proximity effect. The reports on magnetotransport are discussed in more detail in Section I.B.2.a and Section I.B.2.c, and electronic pairing without superconductivity is discussed in Section I.C.2.

4. Superconductivity in $LaAlO_3/SrTiO_3$

Superconductivity in $LaAlO_3/SrTiO_3$ heterostructures was first reported by Reyren et al. [145]. The superconducting transition temperature $T_c \sim 200$ mK is close to that of bulk $SrTiO_3$. The in-plane upper critical field $H_{c2}^{||}$ is expected to be greater than out-of-plane upper critical field H_{c2}. This result is due to the absence of the flux penetration effect when the field is in-plane [299]. The characteristic thickness, $d_{Tinkham} \sim 10$ nm [300, 233] is an order of magnitude smaller than the Ginzburg−Landau correlation length [301] $\xi_{GL} \sim 100$ nm [145, 233, 212].

From here, Caviglia et al. [146] used back-gated samples to map out a phase diagram (Figure 10 (a)) of the system as a function of temperature and carrier density. The results show an insulating phase at low carrier densities which transitions into a superconducting state at intermediary carrier densities. This phase diagram has been confirmed by other groups [302, 234]. As all of these transitions appeared to be Berezinskii-Kosterlitz-Thouless (BKT) transitions, Schneider et al. [303] performed a series of experiments to find the order parameters at the critical point of the transition, fitting the superconductor-insulator transition into the three-dimensional universality class. This transition is of particular experimental interest as it is one of few experimentally accessible quantum phase transitions. For more details please consult the recent review article by Lin et al. [304]. The dome shape of the T_c as a function of the superfluid density (from scanning SQUID) was also reported by Bert et al. [284] (Figure 10 (b)).

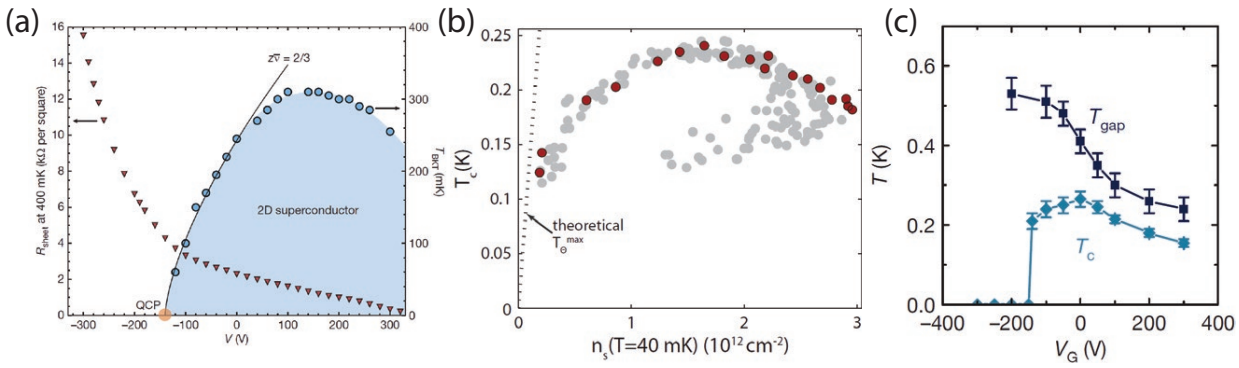

Figure 10: Superconducting dome and pseudogap of $LaAlO_3/SrTiO_3$. (a) The superconducting transition temperature T_c as a function of the gate voltage, mapped out by Caviglia et al. Adapted from [146]. (b) T_c as a function of carrier density inferred from scanning SQUID, by Bert et al. Adapted from [284]. (c) The critical temperature for the pseudogap observed in tunneling spectroscopy as a function of gate voltage, by Richter et al. Adapted from [118].

The peak of this superconducting dome is in the vicinity of the Lifshitz transition [119, 120]. Using a three-band model with repulsive interactions included through Hartree and Fock corrections, Maniv et al. [244, 305] have shown that for some chemical potential range after the Lifshitz transition, two bands are simultaneously occupied. They then argue that this may indicate that instead of the dome being centered on the Lifshitz transition, superconductivity appears only after the transition and persists until the second band is depopulated by interactions and the system enters a conducting state.

In addition to this superconducting dome, Richter et al. [118] showed that the interface also has a pseudo-gap in the insulating region (Figure 10 (c)). As a result, the temperature-carrier density phase diagram of $LaAlO_3/SrTiO_3$ interfaces looks very similar to that of high-T_c superconductors, but at much lower temperatures. By measuring the critical magnetic field of this pseudo-gap, Fillis-Tsirakis et al. [306] argue that a phase coherent paired state persists into the insulating region.

Herranz et al [219] showed that the behavior of the superconducting region is sensitive

to the crystal structure by comparing superconducting (001) and (110) $LaAlO_3/SrTiO_3$ samples. Due to the anisotropic band masses of the t_{2g} bands, these two orientation have different band structures, with (001) interface having the d_{xy} band as the lowest band, while, for the (110) interface, the d_{yz}/d_{xz} bands are the lowest. In the critical magnetic field measurements performed, this difference in confinement led to substantial changes in the anisotropy of the critical magnetic field, both in-plane and perpendicular to the interface. As a result, the superconducting thickness for the (110) interfaces was found to be $d \sim 24-40$ nm, 2-3 times as thick as for the (001) interface.

The electron pairing may be derived from that of $SrTiO_3$ (Section I.A.4 for superconductivity for the bulk $SrTiO_3$), such as the proposed BCS-pairing owning to the LO phonons [307, 308] of $SrTiO_3$. However, this picture needs to treat the non-adiabatic pairing properly if the Midgal-Eliashberg theory is to be applied (Section I.A.4). On the other hand, the confinement and reduced dimensionality may give rise to more exotic pairing, such as d-wave pairing from the electron-electron interactions between itinerant and localized electrons across the interface [309], topological superconductivity in the band from particle-hole fluctuation [310], and surface resonance (oscillatory T_c as a function of the confinement thickness d)[311]. With reports on the coexistence emergent magnetism and superconductivity, other scenarios were also proposed. We describe both the experimental reports and proposed theories in the next section.

a. Coexistence of Superconductivity and Magnetism The coexistence of superconductivity and ferromagnetism at the sample level has been reported using three different techniques. (1) Dikin et al. [312] reported a hysteretic magnetoresistance at, and outside of the superconducting transition. (2) Li et al. [267] reported in plane magnetization of the sample using cantilever-based torque magnetometry. Superconducting transition of the same sample was observed separately via transport measurement. (3) Bert et al. [268], using scanning SQUID magnetometry, mapped the diamagnetic susceptibility (due to superconductivity) as well as the magnetization. The ferromagnetic patches were not correlated with the superconducting regions.

The question is whether the superconductivity and ferromagnetism truly coexist or phase

separated? The latter is suggested by, for example, Mohanta et al. [313]. Locally ferromagnetic puddles could form at the cluster of oxygen vacancies [313]. On the other hand, since the s-wave pairing is not compatible with ferromagnetic order, more exotic scenarios that support true coexistence have also been proposed [314, 315, 316]. They are mostly a version of either p-wave pairing, or FuldeFerrellLarkinOvchinnikov (FFLO) (finite-momentum pairing) [317, 318], and with the help of the Rashba SOC at the interface.

Michaeli et al. [314] suggest helical FFLO pairing at the $LaAlO_3/SrTiO_3$ interface, with the direction of magnetization perpendicular to the transport direction. The Rashba interaction helps the pairing strength to surpass the Pauli depairing limit. The pairing strength is strongest in the low-disorder limit, with an additional local maximum at intermediate impurity concentration. Band specialization occurs and pairing is assigned to the d_{yz}/d_{xz} band. Maximally superconducting transition temperature is expected to occur at nonzero magnetic field. With Rashba SOC, Banerjee et al. [316] proposed a real-space spiral ordering of spins with pitches of tens of nanometers. This model explains the non-hysteric superparamagnetism reported by Li et al in the torque magnetometry. The patches reported by Bert et al. were assigned to broken spirals due to defects. The ferromagnetic order is thought to be mediated by the d_{yz}/d_{xz} band, while superconductivity is assigned to the d_{xy} band and assumed to be conventional. Notably, polar distortion of (Ti-O-Ti) bond may help stabilizing ferromagnetic domains over spirals. Fidkowski et al. [315] considered a spin-orbit mixed s/p-wave pairing of d_{yz}/d_{xz} at the interface, with d_{xy} mostly localized. The s/p-wave pairing is hence compatible with finite magnetic field, and further mediate superconducting grain in the bulk of $SrTiO_3$ close to interface. The SC order is topological, and a 1D wire with p-wave nature would be expected to have Majorana zero modes [319].

5. Optical Properties

a. Photoluminesce The photoluminesence properties of $LaAlO_3/SrTiO_3$ heterostructures appear to be dominated by the $SrTiO_3$ bulk [320, 321]. Thus, at high temperature (> 170 K) a broad blue peak is observed in the photoluminesence spectrum. At lower temperatures, other suppressed effects become apparent, such as single-particle trapping. This

leads to a two-peaked structure in the photoluminesence spectrum in addition to a change in the photoluminescence lifetime, as observed by Yamada et al. [320].

b. Second Harmonic Generation Second-harmonic generation (SHG) is a nonlinear optical process by which the frequency of reflected light is double that of the incident light [322]. In centrosymmetric materials with broken inversion symmetry, the SHG signal a weighted average of the polar asymmetry felt by the electrons. Thus providing a measure of the nonlinear susceptibility of the electron gas. Savoia et al. [323] used SHG to probe $LaAlO_3/SrTiO_3$ interfaces of differing thicknesses. An abrupt transition in the SHG signal was found at 3u.c. thick $LaAlO_3$ and another transition over 4-6 u.c. which result from a precursor effect of the polar catastrophe transferring electrons to localized states at 3u.c. followed by the formation of the conducting layer over 4-6 u.c.. Using selection rules [324] to pick out specific features of the nonlinear susceptibility in the SHG response by manipulating the polarization of the incident light, Rubano et al. [325] were able to show that the SHG response can also contain information about structural properties, showing that $LaAlO_3$ induces a rotation of the oxygen octahedra as well as a relationship between the SHG signal and the lattice mismatch between $SrTiO_3$, and the $LaAlO_3$, $LaGaO_3$, and $NdGaO_3$ overlayers.

C. $LaAlO_3/SrTiO_3$ Devices

Having discussed the 2D-dominated quantum transport in the previous chapter, here we survey the recent observations that have been made possible by devices with reduced dimensions or dimensionality. That the boundary can have fundamental effects in semiconductors (or metals) is first recognized by David J. Thouless [326]. Goswami et al. [327] reported the first superconducting quantum interference devices (SQUID) in this system. Those SQUIDs have dimension about few micrometers, much greater than the superconducting coherence length obtained in earlier reports. The Superconducting single electron transistors (SSET) made out of 2DEG at $LaAlO_3/SrTiO_3$ have proven to be an incredibly powerful probe for

mesoscopic physics in this platform. A paired, non-superconducting phase is observed in the SSETs, with critical pairing field consistently at least an order of magnitude greater than the superconducting upper critical field (Section I.C.2). As the chemical potential of the SSETs are tuned, a crossover of conductance diamonds to loops is observed (Section I.C.3). This crossover is qualitatively captured by a change of interaction sign of the electron-electron interaction, suggesting a BEC-BCS crossover inside of the superconducting dome. One dimensional wires have also had a marked progress in their quality over the past few years. The wires, from those dominated by scattering such as universal conductance fluctuations, wide superconducting transitions, to quantum wires with fully quantized conductance plateaus in steps of e^2/h or with incredibly rich and well resolved subbands interaction (Section I.C.1).

The quasi 1-D superconductivity of c-AFM defined nanowires is reported by Veazey et al. [328]. The width of the nanowires is $w \sim 10$ nm at room temperature, an order of magnitude smaller than the superconductivity coherent length $\xi \sim 100$ nm. The reported transition temperature is slightly lower than that of the 2D counterpart, at $T_c \sim 200$ mK. The transition is wider and with finite residual resistance ($\sim 1.2 - 5.0\text{k}\omega$). Disorder, local hotspot, and thermally-activated phase slips may contribute to the residual resistance. It is worthy to note that, even though the samples are all atomically-flat under AFM, the superconducting nanowires created with c-AFM lithography found to be dependent on the sample location [328]. This may be related to the ferroelastic domains or other sources of inhomogeneity (e.g., oxygen vacancies). Wider structures created by e-beam with width are reported by Stornaiuolo [329], for which UCF is observed when the superconductivity is suppressed by gating.

With c-AFM defined H-bar structure, nonlocal transport is reported by Veazey et al. [330] and Cheng et al. [331]. A change of sign of the nonlocal resistance is observed, but the mechanism is not understood. Recently, nonlocal response attributed to Rashba induced charge-to-spin conversion is reported [264].

Universal conductance fluctuations (UCF) is observed in $SrTiO_3$-based devices with reduced lateral dimensions (typically with width on the order of a μm) [332, 333, 329, 334]. UCF is the reproducible, seemly random, device specific oscillations in the conductance [335]. UCF is a manifestation of coherent scattering of electrons. It is related to weak localization

(WL). The major distinction is that only the averaged interference between the electrons of time-reversed paths is concerned in WL. UCF, on the other hand, is a result of interference between all possible electron paths, which depends magnetic field, carrier concentration, impurity configuration, etc. UCF is therefore device specific *magnetofingerprint*. UCF is characterized by dephasing length L_{phi} and thermal length L_T.

The reported dephasing lengths are $L_{phi} \sim 100 - 300$ nm at low temperature [332, 333]. Stanwyck et al. suggested Kondo scattering may occur, though Kondo resistance minimum is not observed. UCF is also observed in the superconducting critical current Josephson Junction created at $LaAlO_3/SrTiO_3$ [334].

1. Dissipationless Electronic Waveguides

Over the past few years, quasi 1D channel with increased coherence length from few microns have been reported [337, 338]. Dissipationless electron waveguide of 1 micron has recently been achieved [336]. This is by far the cleanest transport observed in any $SrTiO_3$-based system, and is the only quantum wire with attractive electron-electron interaction that has ever been realized. The clean limit of 1D quantum wire is particularly important for investigating the electron-electron interaction, as any disturbance of electronic wavefunction can result in full backscattering. Furthermore, the 1D itself is a quantum critical point.

Electron waveguides with fully quantized lateral and spin modes were reported by Annadi et al [336] recently. Figure 11 (a) is the typical design of an electron waveguide, created with c-AFM lithography. Figure 11 (b) shows quantized conductance plateaus in e^2/h, as a function of a sidegate voltage or chemical potential, at $T = 50$ mK. The subband structure is revealed from the transconductance dG/dV_{sg} spectra (Figure 11 (d)). The subband structure can be described by lateral and vertical spatial quantum numbers as well as the spin degree of freedom. Figure 11 (c) shows the calculated wave functions for the lowest six subbands. Below a pairing field $B_p \sim 1$ T, the lowest two subbands are paired (but not superconducting), as reported by Cheng et al [124] (Section I.C.2). Reentrant pairing of different subbands at finite magnetic field is also observed, such as the $|0, 1, \downarrow>$ and $|1, 0, \uparrow>$ shown in Figure 11 (d). States with the same spin exhibit avoided crossing, e.g. between

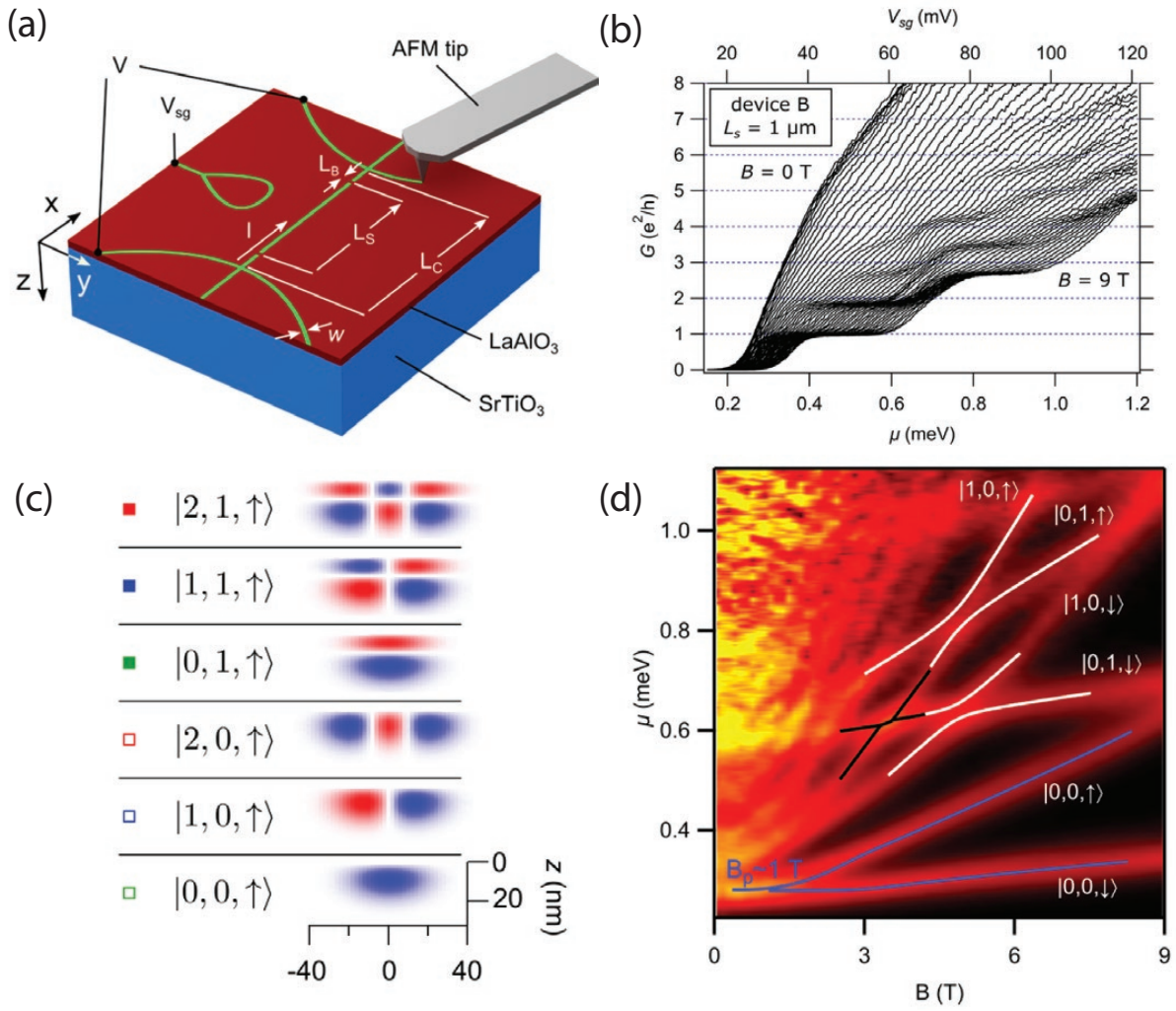

Figure 11: Dissipationless quantum wire. (a) The device design of the quantum wire. (b) The quantized conductance as a function of the chemical potential μ. (c) The spatial modes and spin state of the quantum wire. (d) The evolution of the modes as a function of the spatial mode and spin state. Adapted from [336].

$|0, 1, \downarrow>$ and $|1, 0, \downarrow>$.

2. Electron Pairing without Superconductivity

For the 2DES in $LaAlO_3/SrTiO_3$, strong electron pairing outside of the superconducting phase has been observed [124]. This phase was proposed by Eagles et al [121] for $SrTiO_3$. To probe electron pairing, Cheng et al. [124] used the single electron transistor (SET) geometry, as shown in Figure 12 (a). Figure 12 (b) is the resulting differential conductance (dI/dV) as a function of side-gate voltage (V_{sg}) and out-of-plane magnetic field B. The features in the dI/dV are due to paired or single electron tunneling, as described below.

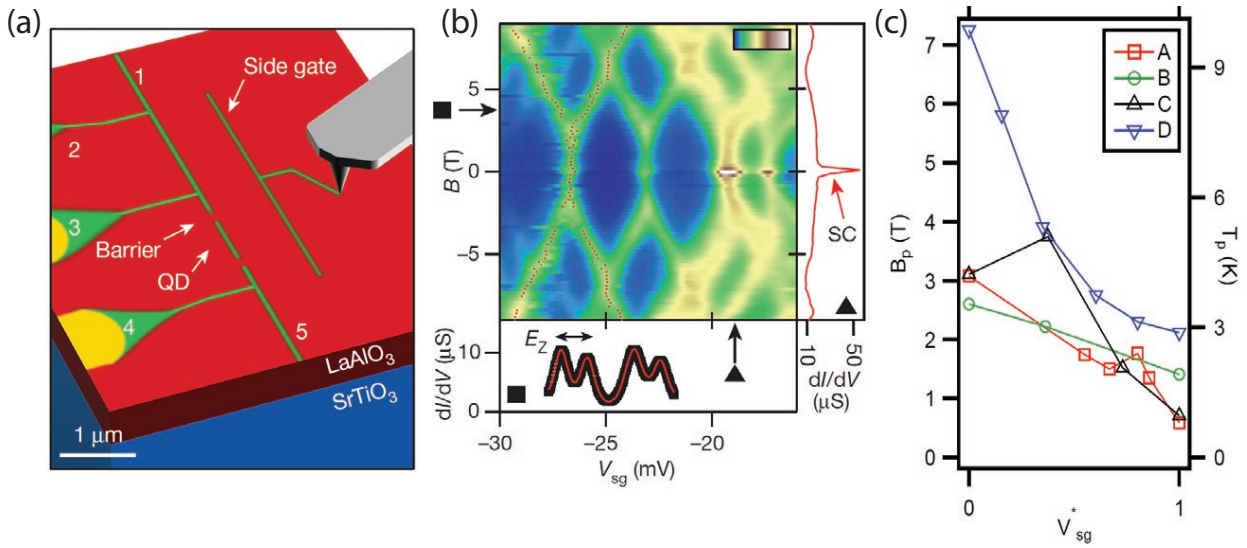

Figure 12: Electronic pairing without superconductivity. (a) The device design of the SET device. (b) The differential conductance (dI/dV) as a function of the sidegate voltage V_{sg}. The features correspond to the resonant tunneling of the single ($B > 2$ T) or paired electrons ($B < 2$ T) through the QD. (c) The dependence of the pairing strength B_p as a function of the normalized sidegate voltage V^*_{sg}. B_p decreases monotonically with increasing V^*_{sg} for all the devices (Four of the devices, A, B, C, and D, are shown). Adapted and annotated from [124].

As the field is increased from $B = 0$ T, several phases are observed for this representative device: (i) $B = 00.2$ T: superconductivity. The SET is in superconducting state, and a peak due to Josephson current marked by black triangles. (ii) $B = 0.2 - 2.0$ T: electron pairing without superconductivity. The transport is still dominated by paired tunneling, even though

the superconductivity is destroyed by the out-of-plane magnetic field $B > \mu_0 H_{c2}$. Electrons remained paired until $B > B_p$. (iii) $B = 2.0 - 5.0$ T: single electron tunneling. The electron pairs are destroyed by $B > B_p$, and the single electrons states are Zeeman-split by the applied magnetic field. (iv) $B = 5.0 - 6.0$ T: reentrant pairing. The range for the reentrant pairing varies from subbands to subbands and device to device. The single-electron tunneling peaks, split from two different neighboring conductance diamonds, lock together and remain paired for about $\Delta B \sim 1.0$ T. The reentrant pairing is also observed in electron waveguides [336], see Section I.C.1. Notably, the pairing field Bp is very strong, compared to the upper critical field $\mu_0 H_{c2}$, and increases with decreasing carrier concentration. B_p as large as ~ 11 T has been observed in an electron waveguide device [336] (Section I.C.1).

The pair splitting is also observed by Prawiroatmodjo et al [339], while Maniv et al [255] reported otherwise. One possible explanation for the null result of Maniv et al [255] is that the pairing field may exceed the maximum magnetic field applied (6 T) in the report.

3. Tunable Electron-Electron Interaction

In Section I.C.2, the magnitude of the electron-electron interaction that gives rise to pairing was shown to be tunable as the pairing field changed with backgate voltage. But the sign of this interaction can also change. Cheng et al [340] observed a distinct crossover from conductance diamonds to Andreev bound states in the differential conductance map of SSETs. Figure 13 (b) is an example of the crossover from conductance diamonds to loop-like features. At lower chemical potential, the electron-electron interaction is attractive, characterized by Hubbard $U > 0$. The pairing is local and BEC-like. As the chemical potential is raised by the increasing sidegate voltage, the interaction becomes repulsive with $U < 0$. The pairing becomes nonlocal, BCS-like, and the Andreev bound states therefore show up.

To explain this crossover, Cheng et al [340] proposed that the effective interaction may have different signs in the t_{2g} manifold: attractive in d_{xy}, and repulsive in d_{yz}/d_{xz}. Thus, at lower chemical potential when only d_{xy} is populated, the effective interaction is attractive. As the chemical potential increased by sidegate, the d_{yz}/d_{xz} start to be populated after the

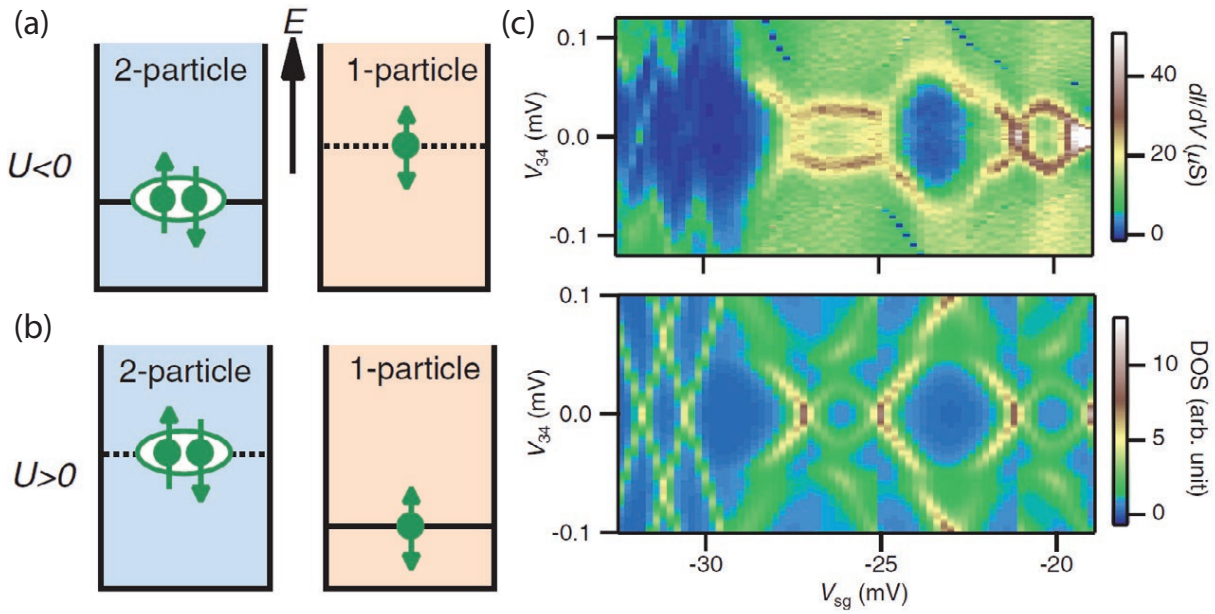

Figure 13: Tunable electron-electron interaction. (a) and (b), the two-electron ground state and one-electron ground state. (a) When $U < 0$, the energy level for the two-electron ground state is lower than that of one-electron ground state. (b) When $U > 0$, the energy level for the two electron ground state is higher than that of single electron ground state. The transport is governed by Andreev reflections. (c) The differential conductance (dI/dV) as a function of the sidegate voltage V_{sg} and the 4-terminal voltage V_{34}. In the lower sidegate regime ($V_{sg} < -29$ mV), the "×" features from pair-tunneling dominate the transport. For higher sidegate voltage ($V_{sg} > -29$ mV), the loop-like features, attributed to Andreev bound states, dominate the transport. Adapted from [340].

Lifshitz point, the effective interaction becomes repulsive. A tunable electron-electron is a useful feature that could potentially be used for quantum simulation.

II. Experimental Techniques

A. Termination, Growth and Related

There are several techniques essential to the discovery of the 2DES at $LaAlO_3/SrTiO_3$ and the c-AFM lithography to work, from the TiO_2 termination due to Kawasaki [100], high-pressure RHEED, and the layer by layer growth with pulsed later deposition.

1. Termination

Under suitable conditions, techniques such as pulsed laser deposition (Section II.A.3) allow materials to grow layer-by-layer with atomic precision, resulting in atomically smooth surfaces. However, in order to achieve this layer-by-layer growth, an atomically flat substrate with controlled surface termination (either TiO_2 or SrO) is essential. The specific surface termination also plays a critical role in the functionality of the 2DES [143]. For a topical review of perovskite surface treatments please see Sanchez et al. [79] and Biswas et al. [341].

A TiO_2 termination can be achieved by selective surface etching treatments such as buffered HF solution developed by Kawasaki et al. [100] and Koster et al. [342]. First, the $SrTiO_3$ substrate is immersed in an HF solution for 20-30 seconds under ultrasonication, followed by rinsing with distilled water. The substrates are then subjected to a high temperature annealing at 950°C in an oxygen atmosphere for 1-2 hours. This single termination is desirable for the heteroepitaxy of abrupt interfaces, preventing the intermixing of ion species at the interface during the deposition. Later in 2008 Kareev et al. [343] developed the *Arkansas etch*, consisting of initially soaking the substrate in DI water followed by soaking in (3:1) mixture of HCl:HNO_3, which claim to achieve TiO_2-termination with lower surface roughness compared with HF etching.

2. High Pressure RHEED

Reflection high-energy electron diffraction (RHEED) is a commonly used technique for monitoring the growth of the thin film [344]. The techniques relies on diffraction pattern of the electron beam of high energy at low glancing angle to the sample surface. While one can learn the crystal structure, stress, texture of the film from the diffraction pattern, the layer-by-layer growth is monitored by the oscillations of the intensity of the specular spot of RHEED. The maximal (minimal) intensity happens when the roughness of the surface is at its minimum (maximum), corresponding to a pristine or fully-covered (half-covered) surface. The growth mode can also be told from the shape of the oscillation (See, for example, [344]).

High-pressure RHEED was developed by Guus J. H. M. Rijnders [345] to operate at higher base pressure (from oxygen partial pressure), which extends the explorable parameter space of the growth of oxide heterostructures, and is a major advance led to high quality $LaAlO_3/SrTiO_3$. In high-pressure RHEED, the electron beam is enclosed in a differentially pumped tube, which extends almost to the sample, to reduce scattering of the electron beam to the molecules in the chamber and ensures the visibility of the RHEED pattern.

3. PLD

Pulsed laser deposition (PLD) is a thin film fabrication technique to prepare various combinations of oxide thin films, interfaces, and heterostructures [346]. Though vapor deposition of thin films using various types of lasers had been known for years, its utility as a method to fabricate high-quality thin films began in the early 1980s. Since its first application in the growth of YBCO thin films [347], PLD has played an instrumental role in the early development of thin film high- superconductor compounds [347, 348].

Figure 14 is a simplified drawing for a typical PLD setup, consisting of a laser source and optics, a target material holder, a sample holder with a heater attachment, and a high-pressure RHEED system to monitor the oxide thin film growth process. Generally, the chamber is connected to high-vacuum pumps that control the vacuum level in the chamber in the pressure range of ultra-high vacuum (UHV) to atmospheric pressure. The chamber is also fitted with various gas lines with fine control (inert, oxygen, and nitrogen) to create the

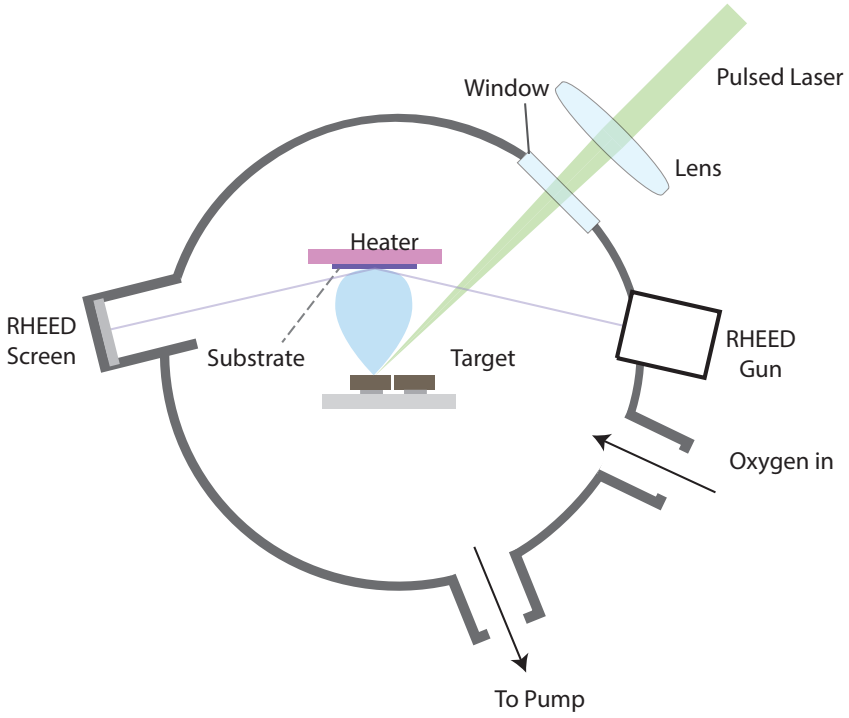

Figure 14: PLD

desired gas environment inside the chamber during the deposition.

In the PLD process, a laser pulse is directed at a target; the target material is ablated due to the localized thermal heating and a resultant plasma forms. The plasma expands into the surrounding vacuum in the form of a *plume* of energetic species containing atoms and ions of the target material. This plume reaches the substrate surface with an average energy per particle of 0.1 to > 10 eV, depending on the pressure of the background gas environment. As a result of the short, high-energy laser pulses, the evaporated material is not in thermodynamic equilibrium. Crucially, the relative amount of different compounds in the plume corresponds to the target composition, even for constituents of very different melting points. In contrast to most other deposition techniques, a desired thin-film stoichiometry can be easily achieved with PLD by using an appropriate target. Adjusting the laser power can trigger cation off-stoichiometry [349, 350]. The ablated species are collected on a substrate that is mounted on a heater. The separation between the target and the sample is an important parameter to be controlled, along with background pressure that can thermalize the ablated species. The substrate material serves as a template that acts like an epitaxial or seed layer for the incoming species to grow.

The laser typically used is a pulsed high-energy excimer laser (KrF 248 nm) with variable repetition rate (usually $1 - 5$ Hz). The laser beam is focused to a spot size of a few mm and energy on the order of 100 mJ. The laser power is a very crucial parameter and should be large enough to create local heating that is larger than the vaporization of the target material in order to get ablation of the target material. It is also important to position the target material that is to be ablated. Usually, the laser beam is incident at an angle of 45°, which allows a vertical ablation of the target. The target position is defined in such a way that the laser hits the target near the focal point of the focusing lens, where basically the beam has a more uniform energy within the spot size. The target specimen is rotated and rastered to get a uniform ablation and to avoid formation of ablated rings or lines at the same area during the ablation.

The next important parameter in PLD is the separation between the target source and substrate. Usually this spacing is about $6 - 10$ cm. Since the ablated plasma contains a high-energy species, to avoid the bombardment of these high energy species (when very near

to target) at the substrate surface and also to avoid a possible non equilibrium deposition (very far from target), it is important to locate the substrate at the desired position from target. The substrate should also be located at the center area of the incoming plasma, where the most uniform deposition takes place.

In order to achieve crystalline cubic phase for $SrTiO_3$ in thin film form, a high temperature deposition is required. Generally, $SrTiO_3$ grows epitaxially and in single cubic phase at elevated temperatures ranging from 550°C and above. Below this temperature $SrTiO_3$ thin films often forms polycrystalline or amorphous phase. $SrTiO_3$ grows epitaxially above 450°C in the (001) direction of substrate; below this temperature, there is no diffraction peak from $SrTiO_3$ film indicating an amorphous phase for $SrTiO_3$. Oxygen partial pressure during growth controls the concentration of oxygen vacancies [351], which, in turn, have extensive effects on various properties.

4. MBE

Molecular beam epitaxy (MBE) [352, 353, 354] is an epitaxial growth technique allowing for the highest quality films, in particular in GaAs/AlGaAs heterostructures [355] but also for the growth of oxides. For a recent review of oxide MBE see Schlom [356]. Figure 15 is a simplified drawing. An effusion cell is used to sublimate a solid source material in order to create a *molecular beam* that travels in a line of sight toward the substrate. The sublimation takes place in a high or ultra-high vacuum (as low as 10-12 mbar), resulting in very small levels of impurities. Generally, epitaxial growth is achieved using very low growth rates. The growth of oxides by MBE is challenging because the presence of oxygen has the potential to disrupt the molecular beams. This problem is dealt with by pumping to deal with the oxygen. In some instances, atomic oxygen or ozone may be used to increase reactivity.

Several variations of MBE are used for the growth of oxides. For $SrTiO_3$-based 2DES, the quantum Hall effect with lowest filling factors were observed in δ-doped $SrTiO_3$ grown in oxide MBE by Matsubara et al. [252], with mobility as high as 18,000 cm^2/Vs. The first reported growth of $LaAlO_3/SrTiO_3$ grown by MBE was by Segal et al. [357]. They use elemental cells with Sr, La, and Al reacted with molecular oxygen at to grow films on

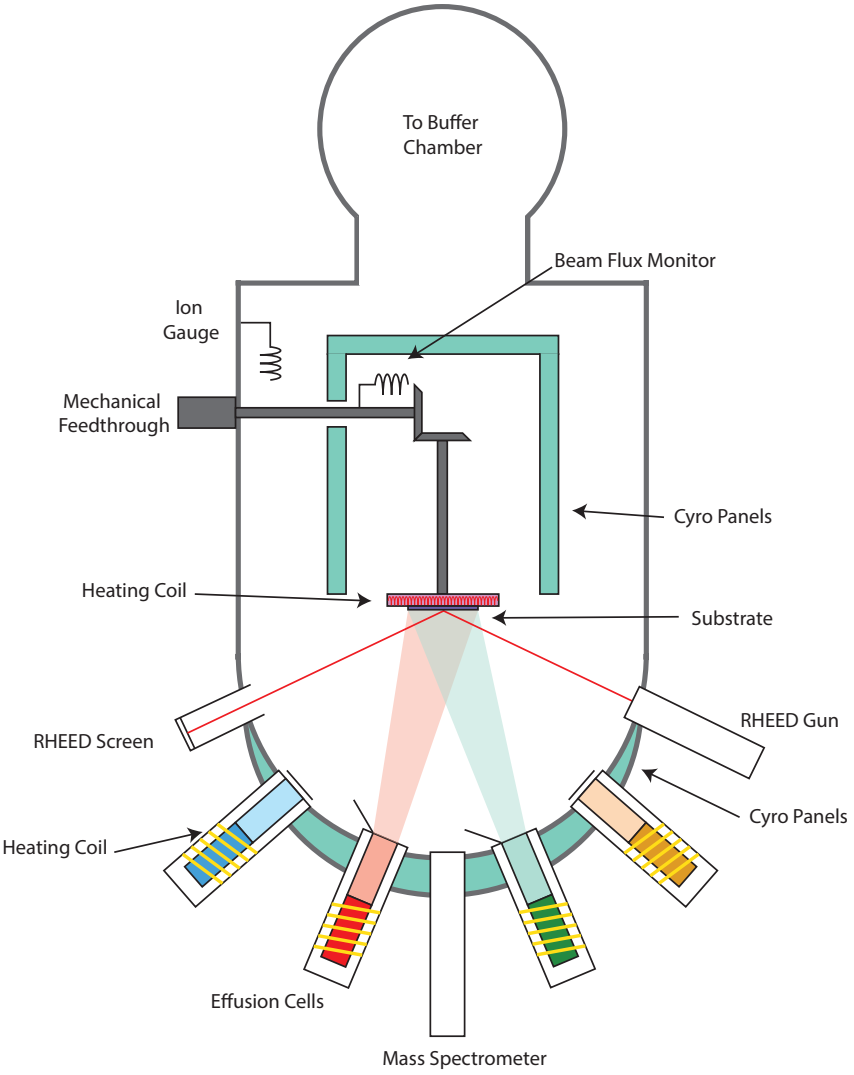

Figure 15: MBE

commercially available TiO_2-terminated $SrTiO_3$. SrO termination was also produced by growing a monolayer of Sr and reacted with O_2.

With Laser MBE [358, 359], a pulsed UV laser ablates a target in order to create the molecular beam. Kanai et al. first used laser MBE to grow the oxide thin film (Ca,Sr)CuO_2 [358]. Laser MBE is very similar to PLD in that all elements are ablated simultaneously. Each also provides unit cell by unit cell growth. The main distinguishing feature of laser MBE is that the pressure is much lower (typically $< 10^{-9}$ Torr) and therefore the mean free path is such that the elements travel in molecular beams. A technique used by Herklotz et al. [360], which has been alternatively called sequential PLD and laser MBE, involves sequentially ablating binary-oxide targets (SrO and TiO_2) to grow $SrTiO_3$ and the Ruddelson-Popper series $Sr_{n-1}Ti_nO_{3n+1}$. Lei et al. use a method they term ALL-Laser MBE to grow high quality $LaAlO_3/SrTiO_3$ [361] They saw no evidence of oxygen vacancies because the growth occurred at high O_2 pressure, a regime not accessible by other growth techniques.

B. c-AFM Lithography

Nanoscale devices can be created using conducting atomic force microscopy (c-AFM) [144, 362, 363, 364]. This approach was based upon a report by Thiel et al. [142] showing that $LaAlO_3/SrTiO_3$ heterostructures with a thickness of 3 unit cells can be metastably switched between insulating and conducting phases using +/- 100 V applied to the back of the $SrTiO_3$ substrate. Cen et al. [362] demonstrated that nanoscale control of the metal-insulator transition can be achieved using a voltage-biased c-AFM tip that is scanned over the top $LaAlO_3$ surface. Devices with characteristic features as small as 2 nm (at room temperature) have been created. The source of the metastability was revealed by Bi et al [98] to be related to a water cycle that exchanges protons between the c-AFM tip and the $LaAlO_3$ surface via a water meniscus. Subsequent experiments showed that the hysteretic conduction reported by Thiel et al. [142] is mediated by atmospheric ions [365], therefore can be viewed as the global version of the c-AFM lithography. The role of surface protonation in regulating conductivity at the $LaAlO_3/SrTiO_3$ interface was investigated more systematically

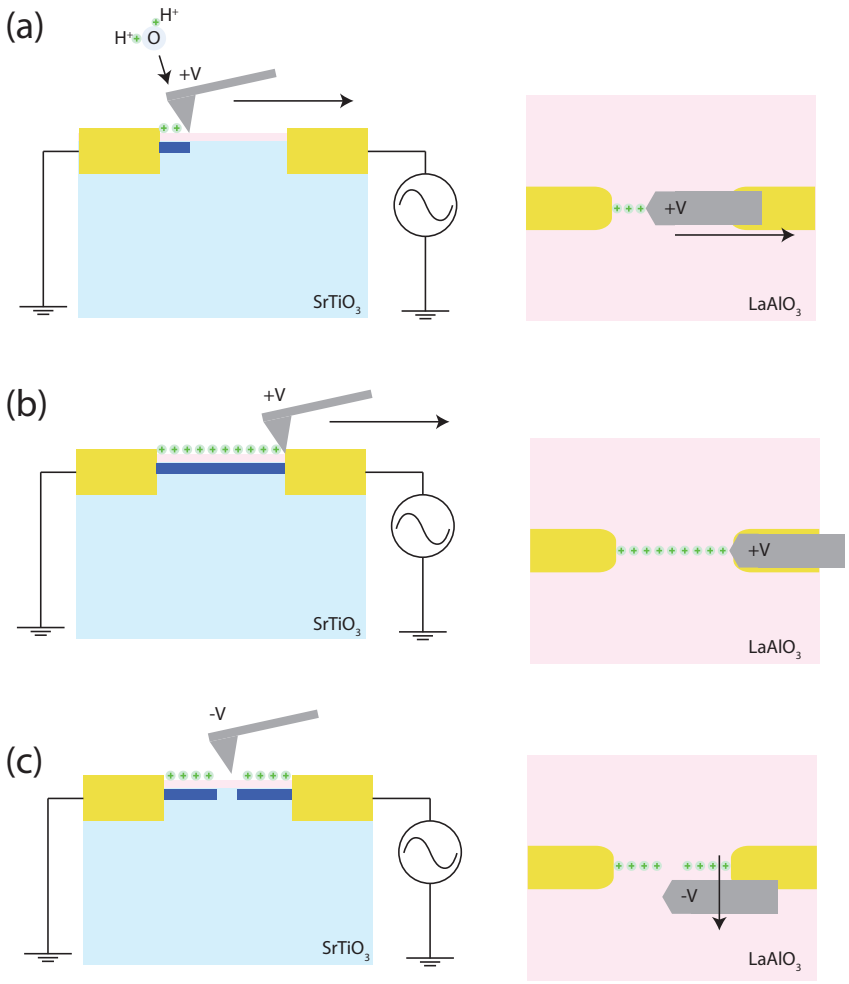

Figure 16: c-AFM-process. Left column: cross sectional view; right column: top view. (a) A positive bias voltage is applied onto the probe of AFM. The voltage dissociates the water molecules in the atmosphere and deposite the protons onto the surface of $LaAlO_3$. (b) A conducting path between the two metallic interface electrodes is complete and a jump of the conductance is observed at this time. (c) To cut the written path, a negative bias voltage is applied onto the probe and the probe is moved across the written path. Courtesy of Jianan Li.

by Brown et al. [99].

Using conductive AFM lithography, a variety of device concepts have been demonstrated, including photodetectors [366], diodes [367], transistors [362, 368], quasi-1D or 1D superconducting channels [331, 328, 369], (superconducting) single electron transistors [370, 124], and electron waveguides [336] (See Section I.C.1), Aharonov-Bohm interference [371] in Hall bar, c-AFM created superconducting nanowire on $LaAlO_3/SrTiO_3$ membrane for strain cell manipulation [372], variants of single electron transistor [373], helical wire [374, 375], sinusoidal wire [376], frictional drag effect between two wires [377], zigzag [378], cross [379, 380], 2D lattice [381], broadband THz generation [382], extended beyond $LaAlO_3/SrTiO_3$ to $CaZrO_3/SrTiO_3$ [383], integration with graphene and edge state engineering [384], and THz response of graphene/$LaAlO_3/SrTiO_3$ [385], frictional drag effect between graphene and $LaAlO_3/SrTiO_3$ [386], with in-situ gold topgate [387, 388], aluminum [389]. There has also been efforts on shot-noise characterization in electron waveguides [390], surface acoustic wave generation and detection [391], single electron on demand source [392], low temperature lithography [393].

Those mesoscopic devices have proven to be incredible tools to reveal the properties of the electronic system. For example, the single electron transistor showed that the electrons in $SrTiO_3$ can still travel in pairs even before the superconducting phase occurs [124]. This observation challenges that whether the BCS theory applies to $SrTiO_3$ in this regime. The electron waveguides [336], on the other hand, not only are an electronic analog to the optical fibers for light, but also are a cleanest, scatter-free manifestation of the confined electronic wavefunction. Their energy spectra have revealed not only the aforementioned electron pairs but also trions (3-body electron bound states), quarternions (4-body bound states), and so on [394].

C. Quantum Transport at MilliKelvin Temperature

Quantum transport is quantum mechanical behaviors in electronic transport. For example, the discretized energy levels in quantum dots results in conductance peaks when the

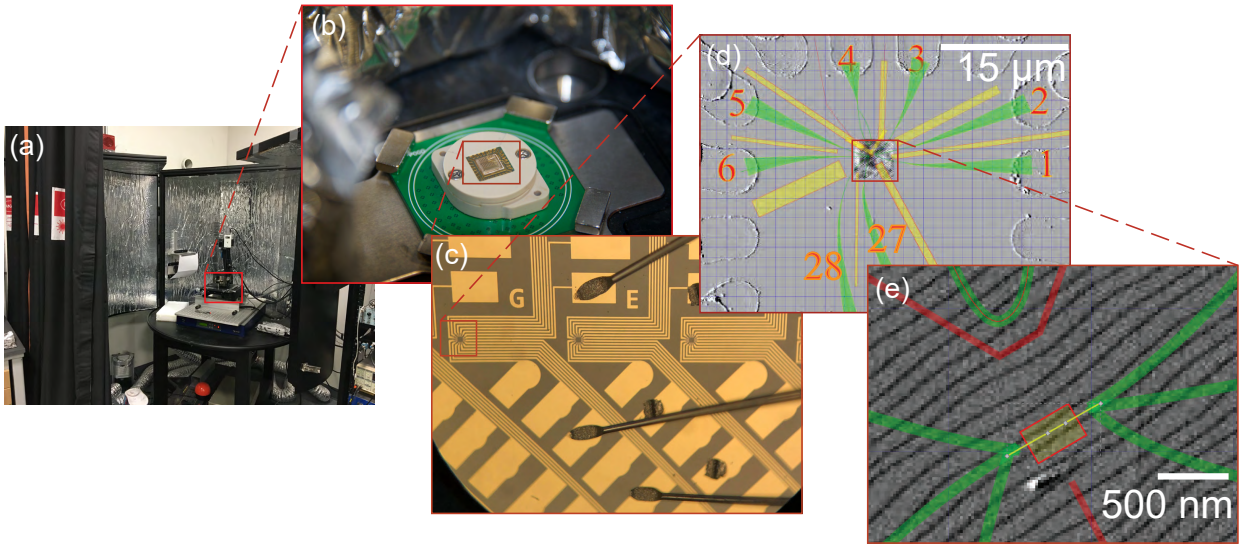

Figure 17: Setup for conductive AFM lithography. (a) Atomic Force Microscope (Asylum MFP−3D). (b) Processed $LaAlO_3/SrTiO_3$ mounted onto a chip carrier and held by a PEEK ZIF socket on PCB. (c) The photolithography defined metallic pattern running from wirebond bonding pads to the central area *canvass*. (d) The desing of a waveguide device in **Inkscape**. (e) Zoomed in design overlayed on the fine AFM scan showing the terrace of the $LaAlO_3/SrTiO_3$ sample.

voltages in the source lead and the drain lead match that of the quantum dot. Conductance quantization due to the discretely populated modes in an electron waveguide (sometimes quantum point contacts are viewed as a short electron wavdguides.) Aharonov-Bohm effect is the effect due to the interference of the electron wavefunction going through two different paths. Superconductivity in mesoscopic devices such as Josephson junction, superconducting quantum interference. Quantum Hall effect, the quantized Hall resistance due to the skipping orbits. There are also Shubnikov-de Haas oscillation, weak anti localization and weak localization, universal conductance fluctuation. Ballisticity and hydrodynamics of electron-electron interaction.

Some of the aforementioned phenomena washed out by thermal broadening when the T is more than a few Kelvins, and some phenonma such as fractional quantum Hall effect has only been reported for T in the milliKelvins regime. For $SrTiO_3$ with superconductivity $T_c = 200 - 300$mK, milliKelvin temperatures is necessary, and a dilution refrigerator is the instrument that is widely used for $T \sim 5$ mK to about 1K.

1. Dilution Cooling

A dilution refrigerator [396] uses ^{3}He and ^{4}He isotopes. The ^{3}He and ^{4}He start separation at $T \sim 870$mK, as shown in Figure 18. The ^{3}He and ^{4}He separated into a ^{3}He concentrated phase and ^{3}He dilute phase. Pure ^{4}He has nulcear spin $I = 0$, and ^{3}He has nulcear spin $I = 1/2$. ^{4}He obeys Bose−Einstein statistics, superfluids at $T = 2.17$K. The ^{3}He does not superfluid on its own until a few mK [397].

The ^{3}He concentration in ^{4}He affects the superfluid transition temperature. ^{3}He is lighter, hence larger zero point motion than ^{4}He, and therefore ^{3}He is more strongly bonded in ^{4}He than in ^{3}He.

The cooling power is $\dot{Q}$ is approximately given by:

$$\dot{Q}[\mathrm{W}] = (\dot{n}_3[\mathrm{mol/s}])(95(T_{MC}[\mathrm{K}]^2) - 11(T_i[\mathrm{K}])^2) \tag{II.1}$$

where n_3 is the flow rate of ^{3}He, T_{MC} is the temperature of the mixing chamber and T_i is the temperature of incoming ^{3}He.

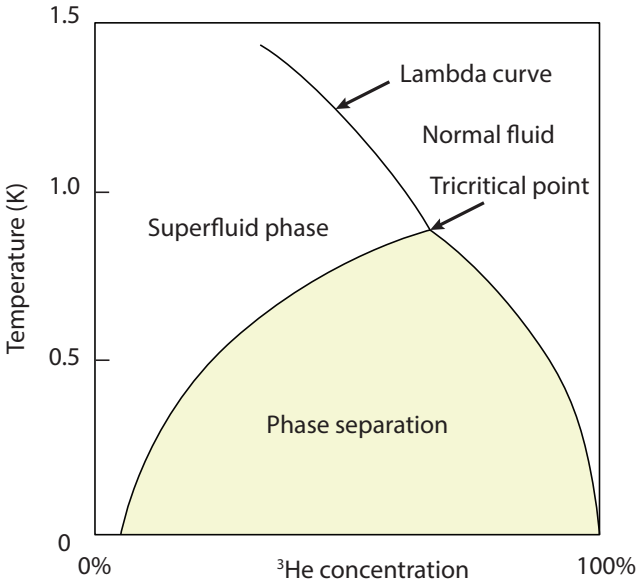

Figure 18: ^{3}He−^{4}He phase diagram, redrawn from [395]

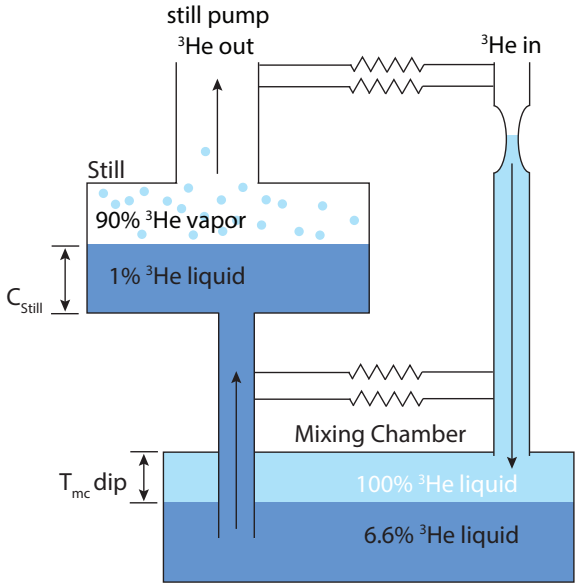

Figure 19: Simplified schematics of a dilution unit

The circulation of the ^{3}He starts (Figure 19) with ^{3}He concentrated gas enters the dilution unit, precooled to about $T = 4$K by the pulsed tube helium compressor in a dry system or the helium bath at $T = 4.2$K followed by a 1K pot in a wet system. The ^{3}He concentrated gas then enters main impedance, cooled by still, secondary impedance, cooled by outgoing ^{3}He via heat exchanger, and enters the mixing chamber. The ^{3}He then dilutes into ^{4}He in the mixing chamber, becomes ^{3}He dilute phase, heading to still and cooling the incoming ^{3}He via heat exchangers. At still, the vapor is dominantly ^{3}He, and turbo pumps are used to remove the ^{3}He, then pumped back into the dilution unit by a mixture pump (plus a compressor in a dry system).

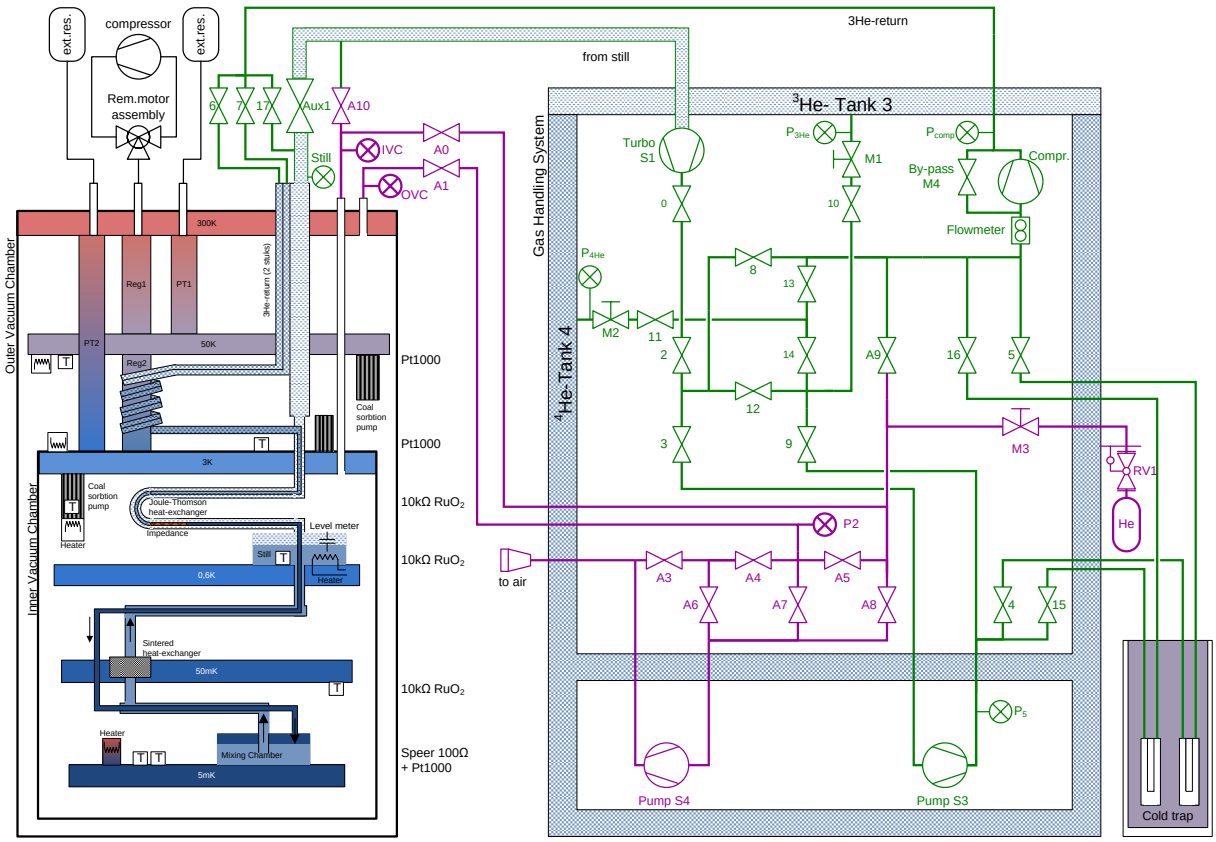

Figure 20: Schematics of the actual gas handling system (GHS) of a Leiden cryofree system. Note that the ^{3}He and ^{4}He dumps are actually the frame of the GHS. Credit: Leiden Cryogenics.

Normally, a dry system does not require much maintenance except servicing the pumps

replacing the compressor. However, leak checking [395] various part of the fridge turns out to be necessary most of the times.

2. Electronics Setup and Related

To remove the unwanted vibration caused by the pumps of the gas handling system (GHS) of the dilution refrigerator, the GHS is placed in a separate **pump room**, while the fridge is located in a dedicated **Scanning Probe Microscopy Room (SPM)** (Figure 21).

The fridge was installed on a concrete block supported by pneumatic vibration isolators. The remote motor of the pulsed tube is mounted onto an aluminum struct that is mechanically decoupled from the fridge body. The linear regulator of the pulsed tube is also used.

The grounding of the system is important. The thermometry as well as the measurement of the device under test can be affected by the grounding configuration. We realized the turbo pump caused noise when during the circulation of the mixture and therefore later moved it out of the power rail that powers the data acquisition electronics.

Figure 22 is the schematics for the electronics for transport characterization. The device under test is mounted on the cold finger of the cold insertable probe of the dilution refrigerator and is termalized to the mixing chamber stage for the dilution refrigerator. The DC connections from the sample, after going through meander filters at low temperature, twist pairs, to a 24-pin Fischer connector connected to a breakout box with $\pi-$fiters. The connections then go to amplfiers such as Kron-Hite 7008 or Femto for voltage or current amplification, and finally to National Instrument NI-4461 cards. The NI-4461 cards are installed into a NI PXIe-1082Q chassis with external power supply to reduce the 60 Hz electric noise in the measurement. The Kron-Hite amplifers were also modified with external power supply.

The computers controlling the GHS and data aquisition hardware are in a third room. All the vacuum lines are running between the pump room and the SPM room. The cables for communication between the computers and the GHS, GHS and their thermometer bridges are running across these rooms. The USB repeaters are necessary for running USB of this

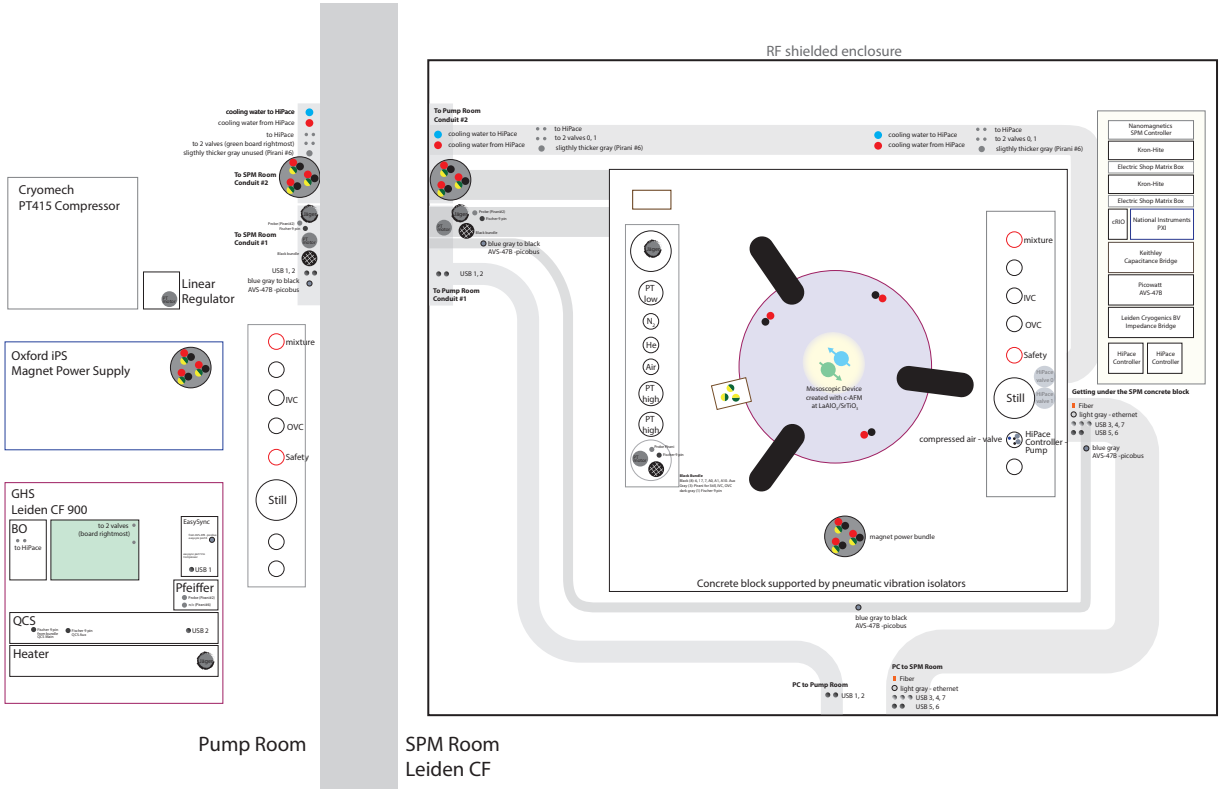

Figure 21: The layout of the major components of the fridge in the SPM Room and the pump room. All the pumps except the two turbo pumps for the still line and the remote motor of the pulsed tube are in the pump room. The electronics for data acquisition are located in the mezzanine of the SPM room to avoid interference due to the stray magnetic field to the electronics.

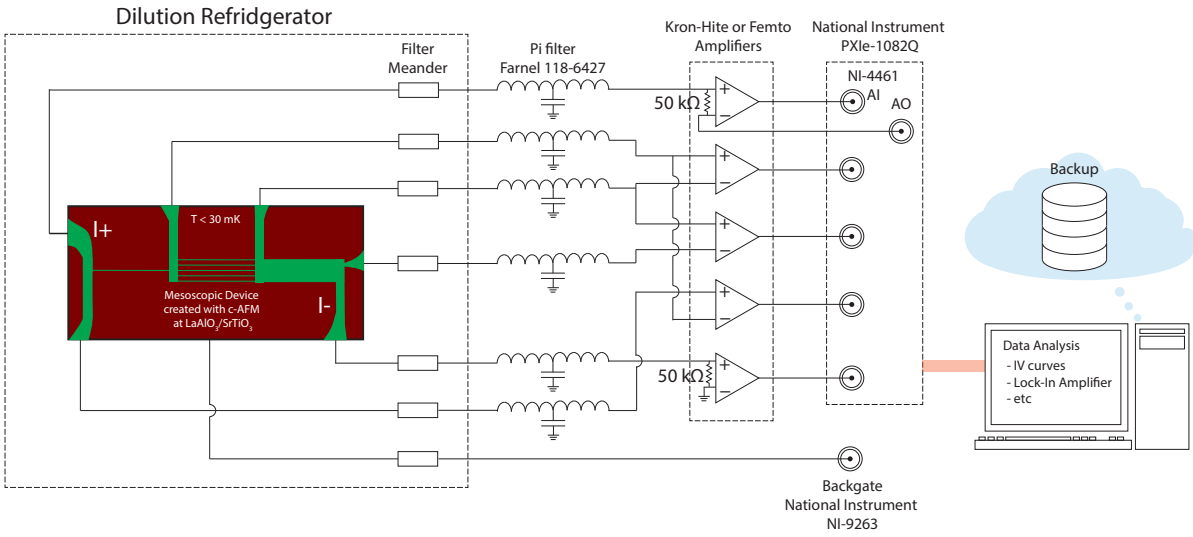

Figure 22: The schematics of the data acquisition setup

length. For the NI PXIe-1082Q chassis, fiber MXI interface was used.

After the device is created with c-AFM lithography and transferred from MFP−3D to this fridge, it takes about 4 hours to reach $T = 4.5$K and about 1 hour to condense the mixture, about 1 more hour to reach $T < 30$mK with based temperature about $T = 24$mK with the cold insertable probe (about $T = 5$mK without).

Figure 24 is the behavior of a typical clean electron waveguide created at $LaAlO_3/SrTiO_3$. The conductance is quantized into multiples of e^2/h and is highly tunable by the sidegate voltage V_{sg}. The different traces were taken at different ouf-of-plane magnetic field.

Figure 25 (a) is the color map of the same data in Figure 24, and Figure 25 (b) is the **transconductance**, dG/dV_{sg}. Complex subband interactions are shown. More details in Section I.C.1.

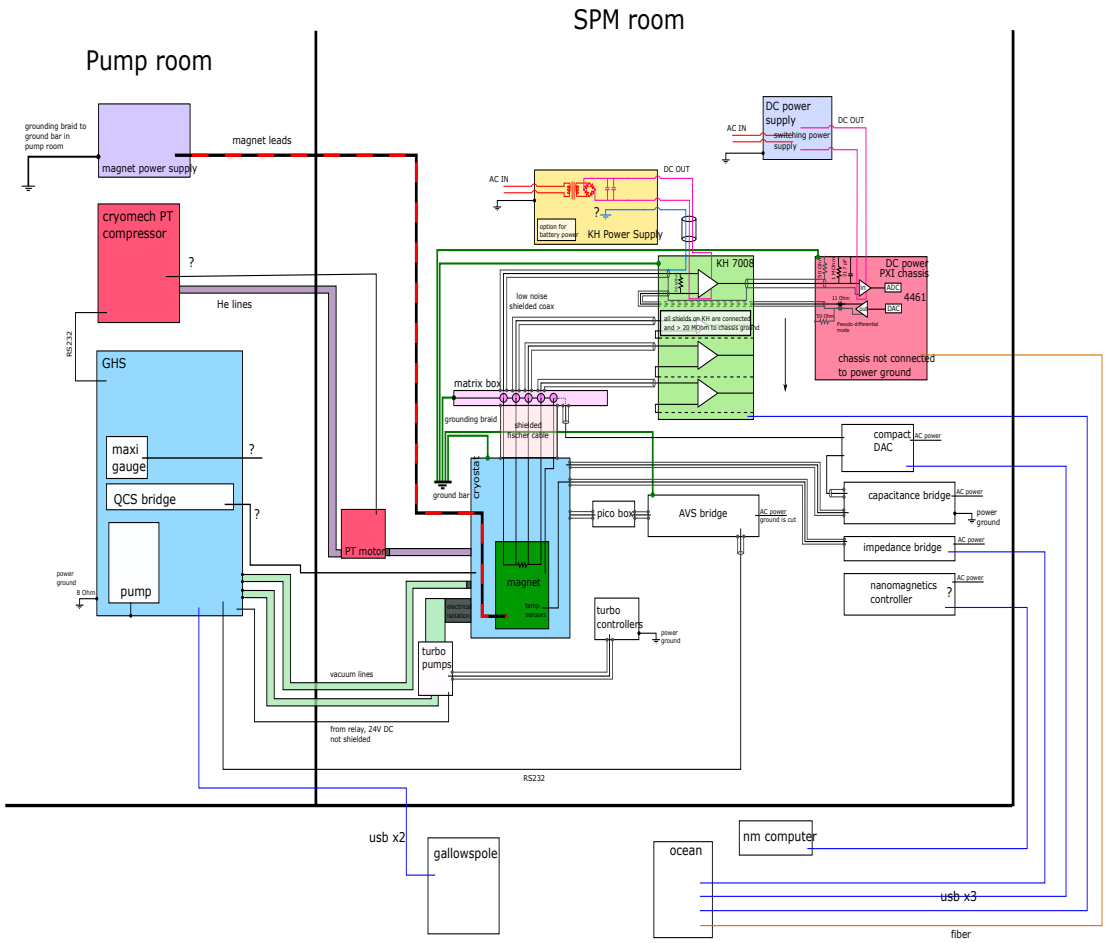

Figure 23: The schematics the grounding setup. Courtesy of Megan Briggeman.

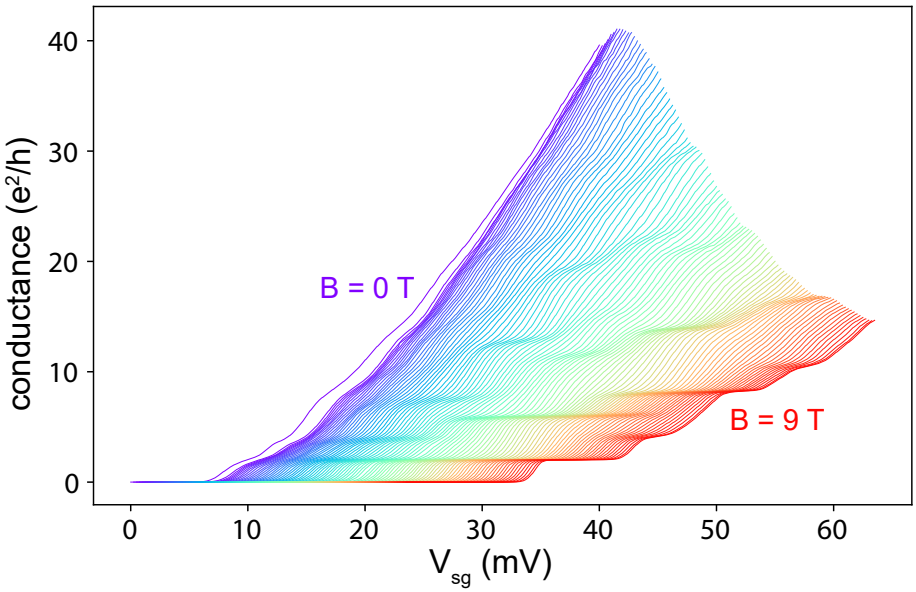

Figure 24: Conductance quantization from device SA02903F.20160627 from $B = 0$T to $B = 9$T. Linecuts are horizontally offset.

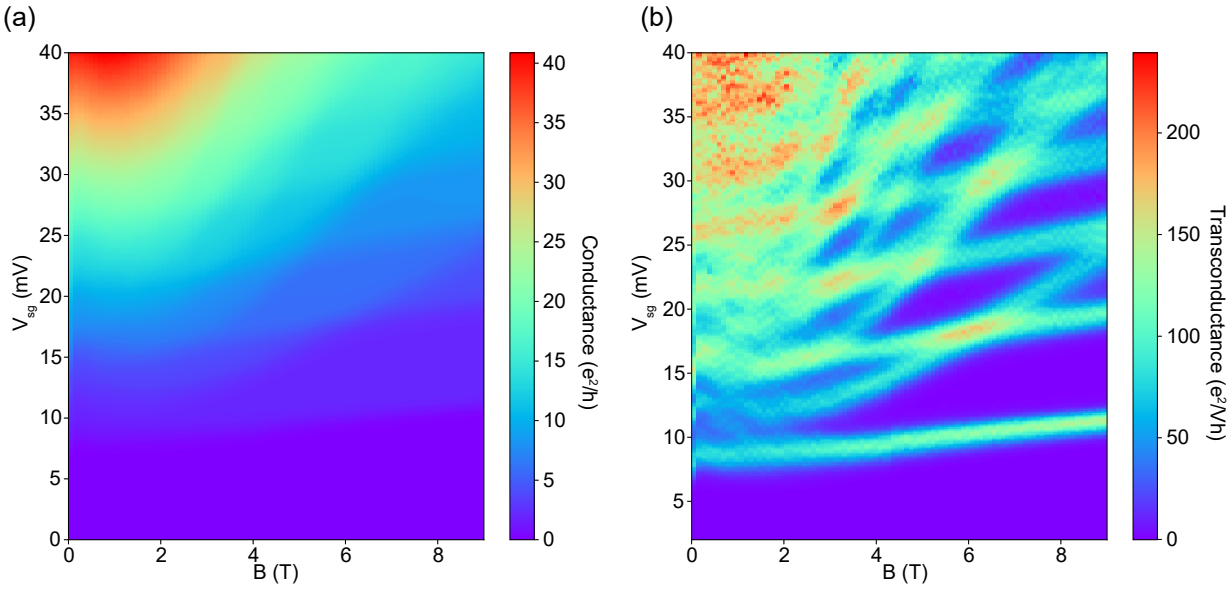

Figure 25: (a) Conductance and (b) Transconductance of the data in Figure 24

D. Scanning Probe Microscopy at MilliKelvins

Local probes at low temperatures are indispensable in understanding the quantum mechanical properties of a mesoscale device beyond electronic transport [398]. Scanning tunneling microscopes and scanning probe microscope are two most common classes of low temperature local probes which often has Å resolution. The first scanning tunneling microscope was implemented in 1981 by Binnig, Rohrer, Weibel and Gerber [399], and the first atomic force microscope in 1985 by Binnig, Quate and Gerbe [400].

Nowadays there has been several state of the art variants such as scanning nanoscale SQUID pioneered by Zeldov [401] and scanning single electron transistor [402]. The techniques have been successfully imaging nanoscale heat dissipassion of quantum Hall states, Poiseuille flow, etc.

1. Scanners for a Low Temperature Scanning Probe Microscope

To scan at low temperature, the most commonly used material is ceramic lead zirconate titanate (PZT, $Pb[Zr_xT_{1-x}]O_3$). PZT is a piezoelectric material. When an electric field is applied, the PZT unit cell is elongated along the direction of the electric field, and shrinks along the orthogonal axes via Poisson effect. PZT-5A, PZT-5H, PZT-8 are the commonly used versions of the PZT. They are poly crystalline after being sintered. Then an electric field is applied to *pool* the PZT to make the prefered orientation of the poly crystalline PZT roughly alinged. At low temperature, the piezoelectric coefficient for PZT is smaller. The piezoelectric coefficient is approximately 0.2 at $T = 4$K to that at $T = 300$K.

PZT can be made into many different shapes. With PZT, the most common form factors of piezo scanners are tube scanners and stack scanners. **Tube scanner**: a tube scanner is a tube-shaped PZT. With just a PZT, it is able to perform motion in all three orthogonal axes, by coating both the outer surface and the inner surface by metal into four quadrants. To move in the z direction, one can apply a differential voltage between all the inner electrodes and all the outer electrodes, as showned in Figure 26. To move in the x, or y direction, one can apply a voltage $+\delta x$ across the inner electrode and the outer electrode at the $+x$

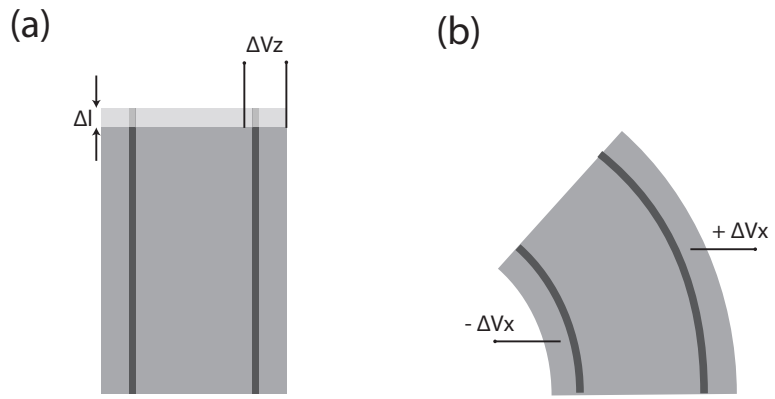

Figure 26: Piezo tube scanner. A tube scanner can motion in a 3 axes. (a) To move in Z direction, apply the same differential voltage across the inner electrodes and the outer electrodes for all the four quadrants. (b) To move in x or y direction, apply a positive differential voltage across the inner and outer electrode on one side and negative differential voltage across the inner and outer electrod on the other side.

quadrant and $-\delta x$ at the $-x$ quadrant. The piezo tube thus distorted along the x direction, as shown in Figure 26. The other advantage of piezo tube scanners is that the resonant frequencies are typically higher than piezo stacks. The disadvantage of piezo tube scanners is that the x, y, z motions are coupled to each other. There are several designs circumvent this problem, such as stacking two piezo tubes with opposite curvatures, or flexture-guided piezo stages. The disavantage for the former is that the scanning range is sacrified, while for the later the stages are usually larger in size.

In addition to the temperature dependence of the piezo coefficients, when operating a piezo scanner, one has also be aware of hysteresis and creep of the piezo stage.

2. Slider for a Low Temperature Scanning Probe Microscope

The scanning range for a typical PZT tube is on the order of 20μm at low temperature. Inertial sliders are useful in moving the sample with respect to the scanner and centering the

region of the interest of the sample with respect to the scanning range of the scanner. The working principal of a slider relies on the **riding sliding** motion, as showed in Figure 27.

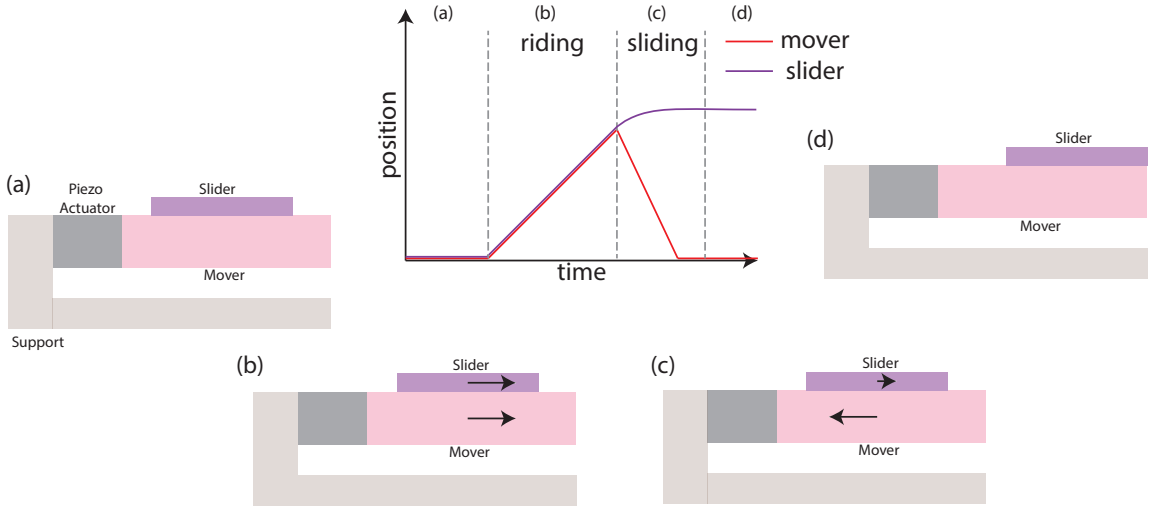

Figure 27: Inertial sliders. Video demonstration.

The slider and the mover are stationery initially, as in Figure 27 (a). Then a sawtooth voltage is applied to the piezo actuator, causing the mover to move accordingly. (b) During the positive motion phase, both the slider and the mover are moving in the $+x$ direction and there is no relative motion between the two. (c) However, as the mover suddenly changes the direction of the motion, the frictional force is not large enough to reverse the motion of the slider, causing the slider to slide with respect to the mover in the $+x$ direction. The frictional force decelerate the slider with respect to the mover and the slider stops, ending with (d) finite relative displacement between the slider and the mover.

The sliders are very common in the nanopositioners at low temperatures. The sliders are also used in low temperature rotators. There are several famous designs such as Pan slider [403, 404].

The AFM probe is mounted onto self-align alignment groove and held by leaf spring. It is crucial that the space between the groove and the AFM probe is free of debris or dust. Any micron size dust can cause a small tilt of the probe. Because the distance between the tip of the AFM probe and the fiber cone is about 20 μm, a small tilt can easily make the

tip run into the fiber cone.

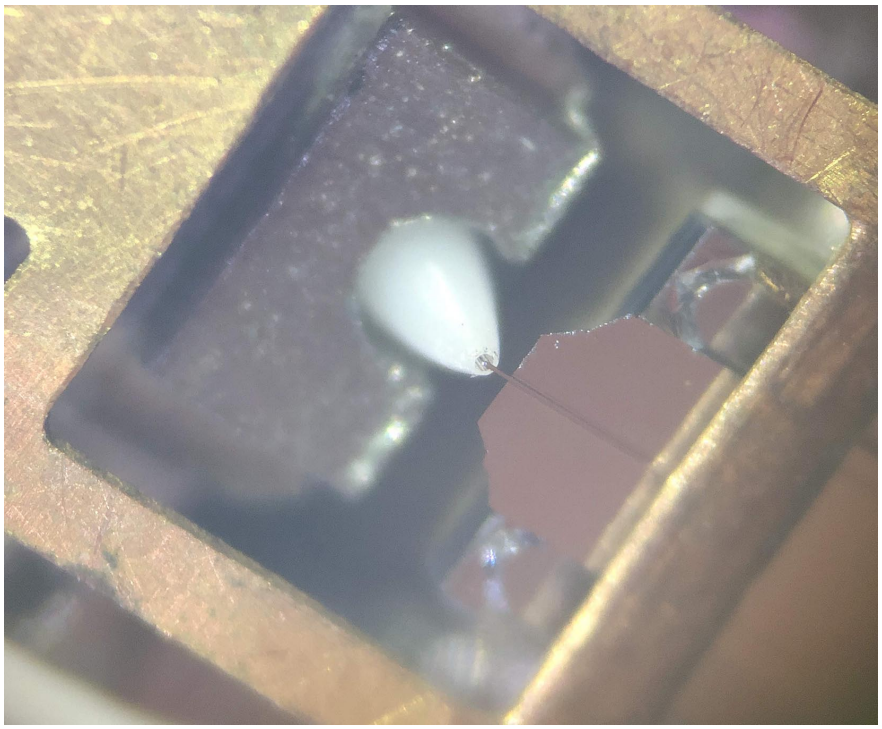

Figure 28: mK-SPM

At milliKelvin temperature, any operation of the scanning probe microscope can easily heat up the system a significantly. Furthermore, even though the cooling power for this system was 900 μW at 100 mK, the cooling power on the cold insertable probe is significantly smaller.

E. Confocal Microscopy at MilliKelvins

A confocal microscope is first patented in 1957 by Marvin Minsky. A confocal microscope is an eponym for an optical setup that uses a set of pinholes to block the light that is out of focus. The details of the microscope are highly flexible and customizable: the light source (laser, halogen lamp), detector (camera, photodiode, avalanche photodiodes (APD), superconducting nanowire single photon detector (SNSPD), spectrometer). Many elements

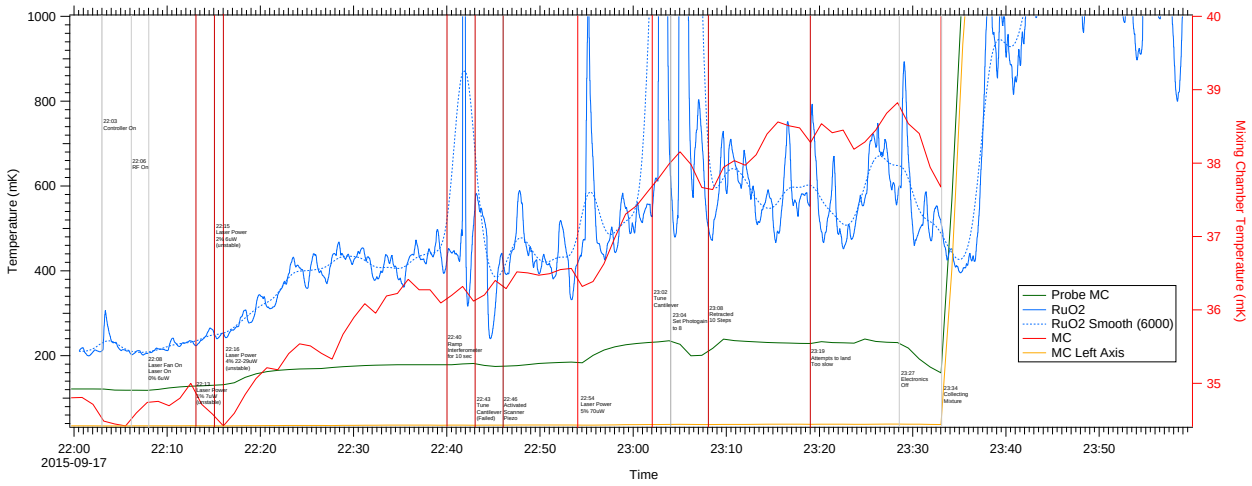

Figure 29: Temperature of mK-SPM

can be added into the optics train, polarization optics, Hanbury-Brown and Twiss, to name but a few. The sample can also be inside of a continuous flow cryostat with an optically accessible window for excitation and collection beam. The beam can also be sent into a dilution refrigerator with relay optics.

Figure 30 is a simplified schematics of the milliKelvin confocal optical setup at the Quantum Sensing Group at Oak Ridge National Lab:

I. Excitation: LED (Thorlabs Solis 505 nm), tungsten lamp (Thorlabs), 532 nm laser (Millennial Edge) or 532 nm laser pumping optical parametric oscillator (OPO) followed by second harmonic generation (Hübner C-WAVE) which covers most of the visible light spectrum.

II. Optics train: Linear polarizers with wave plates on both the excitation arm and the collection arm. The beam is steered by 2-axis galvometer scanner (Thorlabs).

III. Detection: Camera (Thorlabs), avalanche photodiode (APD), superconducting nanowire single photon detector (Quantum Opus) with time tagger (Swabian), spectrometer (Oxford Instrument Kymera with Andor, Light Machinery Hyperfine Spectrometer.)

The $8f$ relay optics and the objective are installed onto the cold insertable probe of Leiden

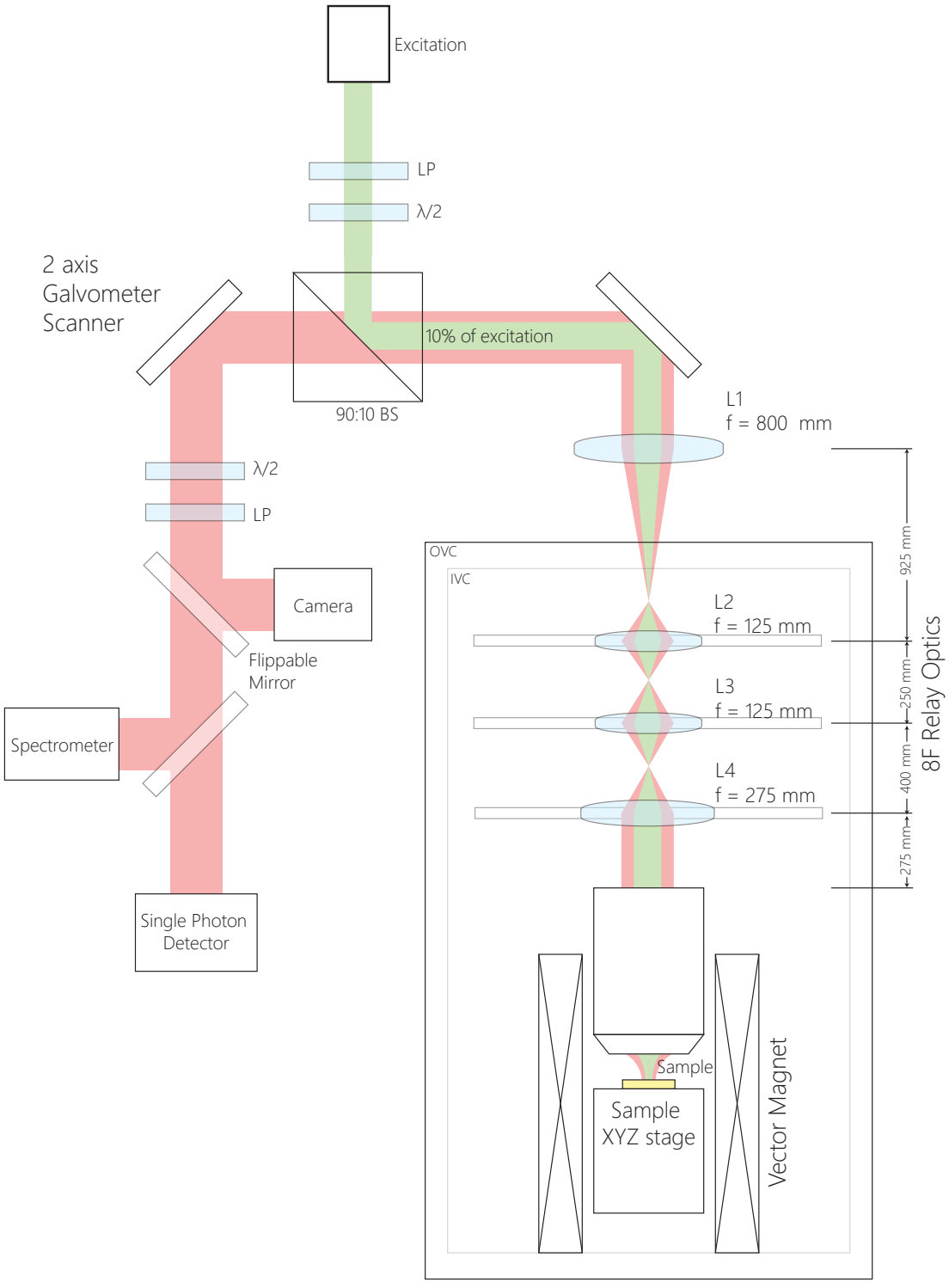

Figure 30: Simplified schematics of the milliKelvin confocal setup. Courtesy Mattew Feldman.

CF1000 CS−81. The relative distance between the sample and the objective is adjusted by x, y, z inertial slider for sample and z for the objective. The collection/excitation power is about 1% at the probe mirror before entering the window. With the power on the order of the a few μW, the temperature change of the mixing chamber stage was not noticeable. The alignment of the system is difficult.

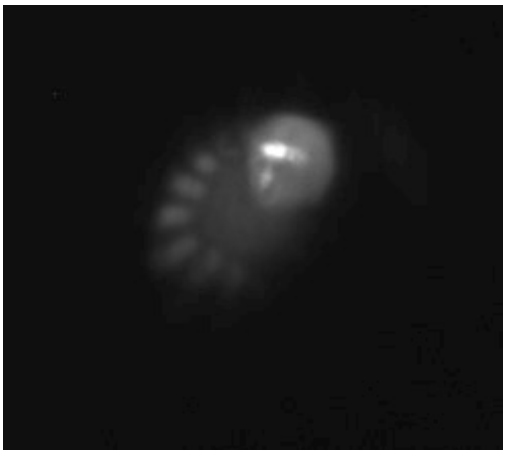

Figure 31: Optical image of a $LaAlO_3/SrTiO_3$ canvass at 29 mK

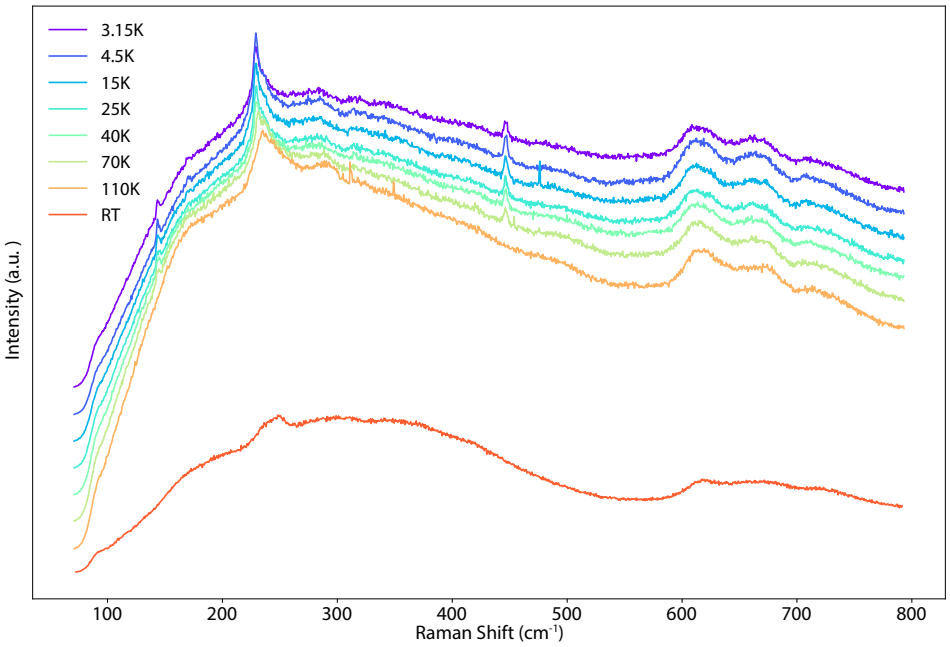

Figure 32: Raman 1.5 K to 300 K. Courtesy of Ben Lawrie.

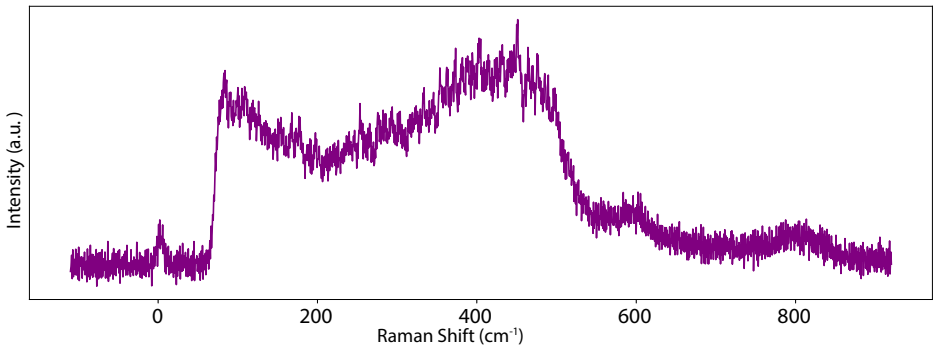

Figure 33: Raman of $SrTiO_3$ taken at mK. The temperature of the mixing chamber stage is 60 mK.

III. One-Dimensional Nature of Superconductivity at the $LaAlO_3/SrTiO_3$ Interface

The contents of this chapter represent a collaborative work published in Yun-Yi Pai, Hyungwoo Lee, Jung-Woo Lee, Anil Annadi, Guanglei Cheng, Shicheng Lu, Michelle Tomczyk, Mengchen Huang, Chang-Beom Eom, Patrick Irvin, Jeremy Levy, *Physical Review Letters* **120** (14), 147001 (2018) [369].

We examine superconductivity in $LaAlO_3/SrTiO_3$ channels with widths that transition from the 1D to 2D regime. The superconducting critical current is independent of the channel width and increases approximately linearly with the number of parallel channels. Signatures of electron pairing outside of the superconducting regime are also found to be independent of channel width. Collectively, these results indicate that superconductivity exists at the boundary of these channels and is absent within the interior region of the channels. The intrinsic 1D nature of superconductivity at the $LaAlO_3/SrTiO_3$ interface imposes strong physical constraints on possible electron pairing mechanisms.

Strontium titanate ($SrTiO_3$ or STO) is a superconducting semiconductor [3] whose pairing mechanism has remained unresolved for more than half of a century. Its behavior is similar to that of high-temperature superconductors in many superficial aspects: both exhibit a dome-shaped superconducting transition temperature versus doping concentration [62], a low-density pseudogap phase [118], a small Fermi energy compared to the Debye frequency [90], and proximity to additional phase transitions [138, 140]. A wide range of pairing mechanisms responsible for superconductivity have been considered, including longitudinal optical phonons [405, 128, 112], antiferrodistortive modes [130], ferroelectric modes [131], plasmons [129], plasmons with optical phonons [133], and Jahn-Teller bipolarons [137].

Recently, interest in the superconducting properties of STO was revived by the development of STO-based heterostructures and nanostructures, and with the $LaAlO_3/SrTiO_3$ (LAO/STO) system [141] in particular. The two-dimensional interface supports superconductivity [145], and it can be electrostatically gated to trace out a superconducting dome [146], similar to the dome originally obtained through chemical doping [62]. The heterostruc-

ture geometry has enabled new probes of the superconducting state that were not feasible previously. For example, planar tunneling experiments have revealed evidence for a pseudogap phase [118] with unexpected in-gap states [406]. Scanning SQUID images [192] show signatures of strong inhomogeneities in superfluid density linked to naturally forming ferroelastic domain structures. Mesoscopic devices created within the LAO/STO interface reveal multiple gap features that have been interpreted as signatures of spin-triplet pairing [407].

Further reduction in dimensionality of LAO/STO devices has become possible through the use of various lithographic techniques [337, 408, 409, 410, 334]. Here we use conductive-atomic force microscope (c-AFM) lithography [144, 362], which relies on AFM tip-controlled protonation/deprotonation [98, 99] of the LAO surface. A variety of quasi-1D and confined (quasi-0D) structures have been created, including superconducting nanowires [328], ballistic 1D channels [338], and single-electron transistors [370], that revealed the existence of electron pairing outside the superconducting state [124]. Despite all of the new information about the superconducting phase, the microscopic origin of the pairing glue remains a mystery.

A. Device Design: Type 1

Here, we systematically investigate low-temperature transport behavior in conducting channels, formed at the LAO/STO interface using c-AFM lithography, with widths ranging between 10 nm and 1 μm. LAO/STO heterostructures are grown by pulsed laser deposition with growth parameters reported in Ref. [99]. The thickness of LAO is fixed to 3.4 u.c. (defined by the number of Reflection High-Energy Electron Diffraction oscillations), resulting in an interface that is close to the critical thickness for the metal-insulator transition [142]. Electrical contact to the LAO/STO interface is made by Ar+ etching (25 nm) followed by sputter depositing Ti/Au (4 nm/25 nm). Conductive nanostructures at the LAO/STO interface are subsequently created using c-AFM lithography [144].

The first family of devices considered here (Figure 34) consists of three sections in series with characteristic widths $w_1 \sim 10$ nm, $w_2 = 100$ nm, and $w_3 = 1$ μm. All three sections (which are subsequently referred to as w_1, w_2, and w_3 sections) have the same length L = 3

μm. The w_1 section is created by writing a single line, while sections w_2 and w_3 are created by raster-scanning a rectangular area along the two principal axes. Conductive rectangular shapes separate the individual wire segments, enabling each to be monitored simultaneously and independently.

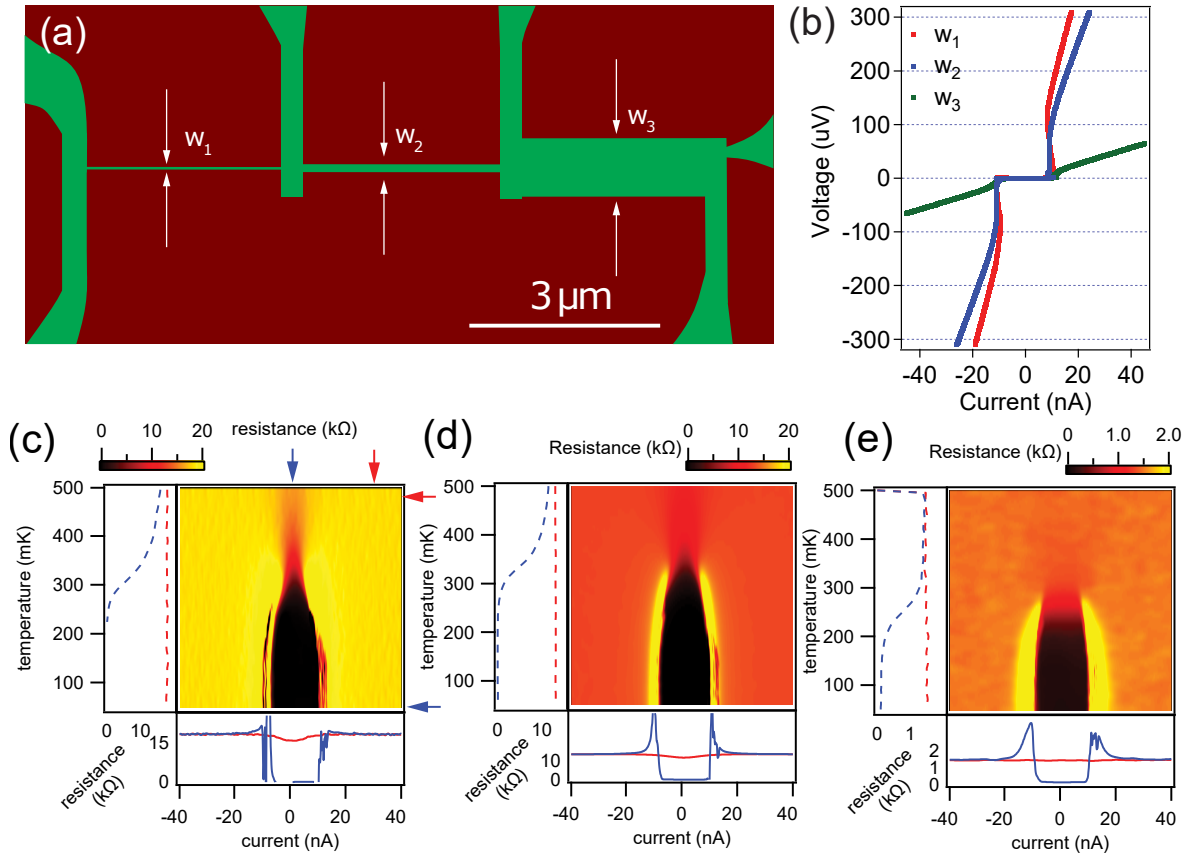

Figure 34: (a) LAO/STO device (top view) consisting of three sections with widths w_1 = 10 nm, w_2 = 100 nm, and w_3 = 1000 nm. All three sections have the same length L = 3 μm. Green (red) areas depict conducting (insulating) regions (b) $I-V$ curves for different channels measured at 50 mK and V_{bg} = -6.5 V. (c-e) Differential resistance (dV/dI) as a function of current and temperature. (c) w_1 section, (d) w_2 section, and (e) w_3 section. Data taken at V_{bg} = -6.5 V and B = 0 T.

After c-AFM lithography, the devices are transferred into a dilution refrigerator and cooled to T = 50 mK. Four-terminal current-voltage ($I-V$) measurements for each of the three sections are recorded as a function of out-of-plane magnetic field (B), temperature,

and back-gate voltage (V_{bg}) which tunes the carrier density [146]. We identify the sharp increase in differential resistance above a critical value I_c with the superconducting switching current, which provides a lower bound for the actual critical current due to various phase-slip mechanisms [411]. The results reported here are representative of three nominally identical sets of devices that show qualitatively similar behavior. Figure 34 (b) shows the 4-terminal $I-V$ curves for the three sections at a back-gate voltage of V_g = -6.5 V and T = 50 mK. While all three sections are superconducting, the critical current $I_{c,i}$ (where i = 1, 2, 3 is the channel index) within each section is remarkably similar ($\sim$ 10 nA), i.e., independent of the channel width. By contrast, the normal-state resistance (i.e., resistance under DC bias that exceeds $I_{c,i}$) decreases monotonically with increasing width: R_1 = 17 kΩ for w_1, R_2 = 11.5 kΩ for w_2, and R_3 =1.4 kΩ for w_3. In particular, the ratio of the normal state resistance of section w_2 and section w_3 is nearly equal to the ratio of the widths w_2/w_3, indicating that the 1D-2D crossover takes place near 100 nm, and that electric flux-focusing effects are not strongly affecting the transverse carrier density profiles in the 2D regime.

Further insight into the superconducting nature of these channels comes from examining the differential resistance (dV/dI), obtained from numerical differentiation of the $I-V$ curves. Figure 34 (c-e) shows the differential resistance of the three different sections as a function of current and temperature. Linecuts at fixed temperatures (T_1 = 50 mK, T_2 = 475 mK) and bias currents (I_1 = 0 nA, I_2 = 30 nA), indicated by arrows, are shown for each device. The superconducting transition temperature is about $T_c \sim$ 300 mK for sections w_1 and w_2, and slightly lower ($T_c \sim$ 250 mK) for section w_3. Notably, when $T > T_c$ a zero bias conductance peak (dip in the differential resistance dV/dI) is observed, for both w_1 and w_2 sections (Figure 34 (c,d)). This feature is much less pronounced for the widest section, w_3 (Figure 34 (e)).

Figure 35 tracks the differential resistance of the three sections as a function of bias current, magnetic field and gate voltage. Intensity plots of $dV/dI(B, I)$ are shown for selected values of V_{bg}. A number of observations can be made:

I. The superconducting upper critical field $\mu_0 H_{c2}$ initially increases with increasing backgate and then decreases. This non-monotonic dependence is reminiscent of the superconducting dome commonly observed for this interface [146].

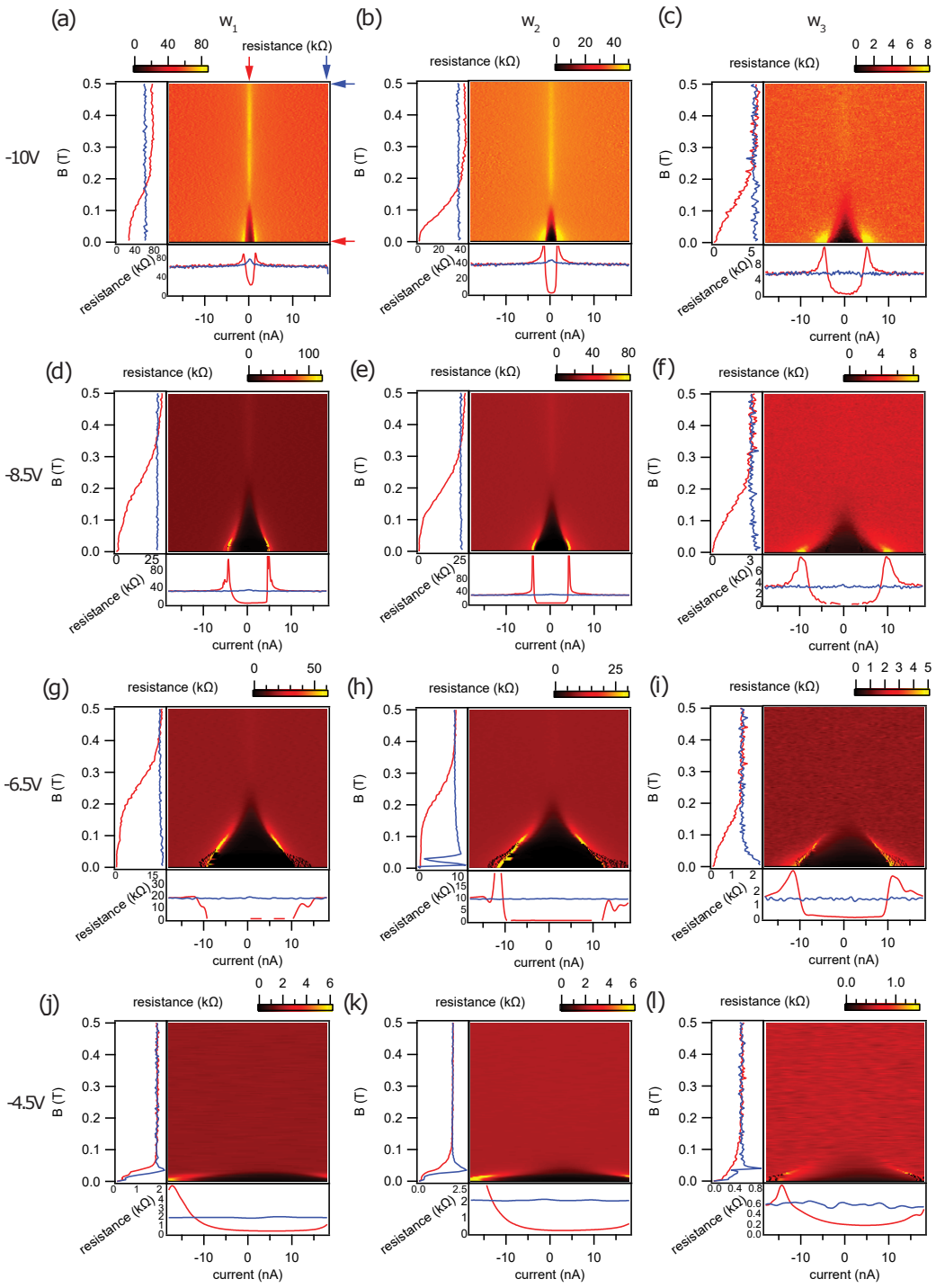

Figure 35: Differential resistance (dV/dI), plotted as a function of current and magnetic field, for each of the three sections at different backgate voltages. The lower panel for each graph shows the horizontal linecuts at $B = 0$ T (red) and $B = 0.5$ T (blue). The left panel shows the vertical linecuts at bias current $I_1 = 0$ nA (red) and $I_2 = 14.5$ nA (blue).

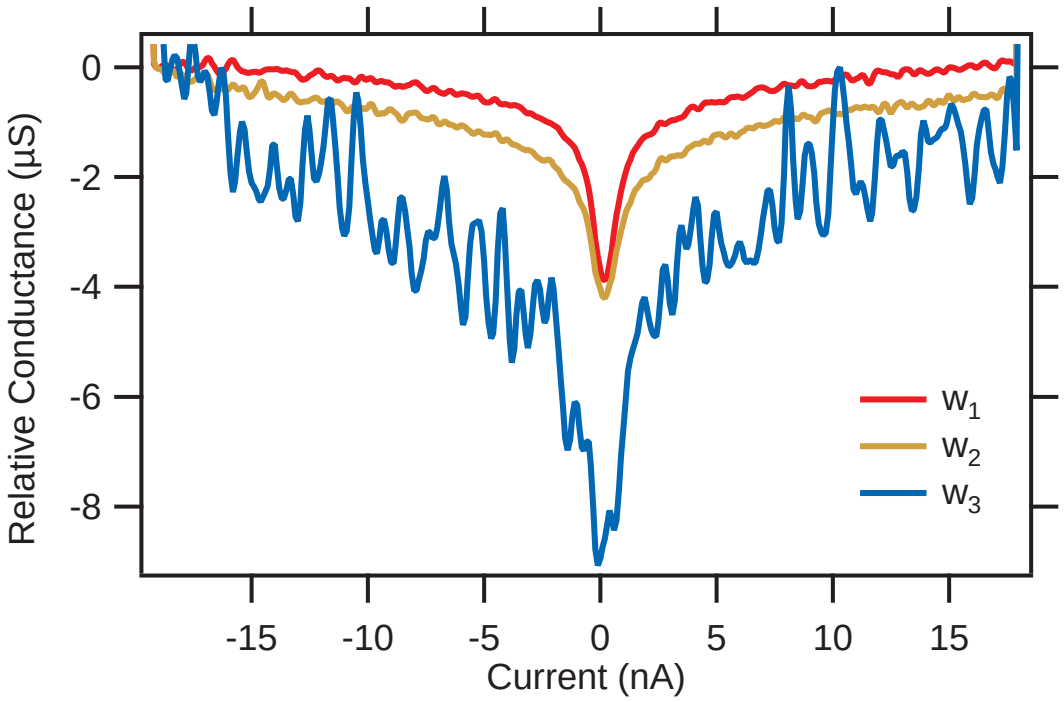

Figure 36: The zero-bias conductance dip for the three sections. The curves are a result of averaging over the range of magnetic field values $B = 0.23$ T 0.73 T, at backgate $V_{bg} = -10$ V. Note that the size of the zero-bias conductance dip is similar for sections w_1 and w_2, and approximately twice as large for section w_3.

II. The critical current increases monotonically when increasing the backgate voltages for all three sections. The critical currents for the three sections are strikingly similar to one another, except at the most negative backgate value.

III. A zero-bias conductance dip (peak in the differential resistance dV/dI) is observed above H_{c2} (e.g., Figure 35 (a)) and is most pronounced at the most negative backgate voltages. We associate this feature, as well as the zero-bias conductance peak in Figure 34 (c-e), with a previously identified phase in which electrons are paired but not superconducting [124]. Figure 36 shows the cross sections of the zero-bias conductance dip for the three sections. The conductance dip for the three section widths (Figure 36) is nearly the same for the w_1 and w_2 sections, and it is approximately twice as large for the w_3 channel. The conductance dip therefore appears to behave similarly to the superconducting critical current, in that it does not increase linearly with the channel width.

IV. The pronounced differences between the widest section, w_3, and the two narrower sections cannot be ascribed to the writing process, since section w_2 is created by raster-scanning and w_1 is created by moving the AFM tip along a single line. In other words, the fact that sections w_1 and w_2 behave similarly, and significantly different from section w_3, illustrates that the pairing is influenced by the physical geometry rather than the method in which the conducting regions are produced.

The results presented thus far are consistent with a scenario in which superconductivity and pairing exist within a quasi-1D ($w \sim 50$ -100 nm) portion of the channel, and in which superconductivity and pairing coexist with a parallel, non-superconducting (2D) bulk phase. The superconducting critical current density for section w_3 ($j_c \sim 10$ nA/μm) is comparable to what has been reported for the bulk LAO/STO interface [145, 217], while the critical current density of section w_2 is an order of magnitude higher.

B. Device Design: Type II

A possible explanation is that superconductivity exists only within a 1D region of the 2D channel, i.e., the outer edge(s). To test the hypothesis, we investigate a second type of device,

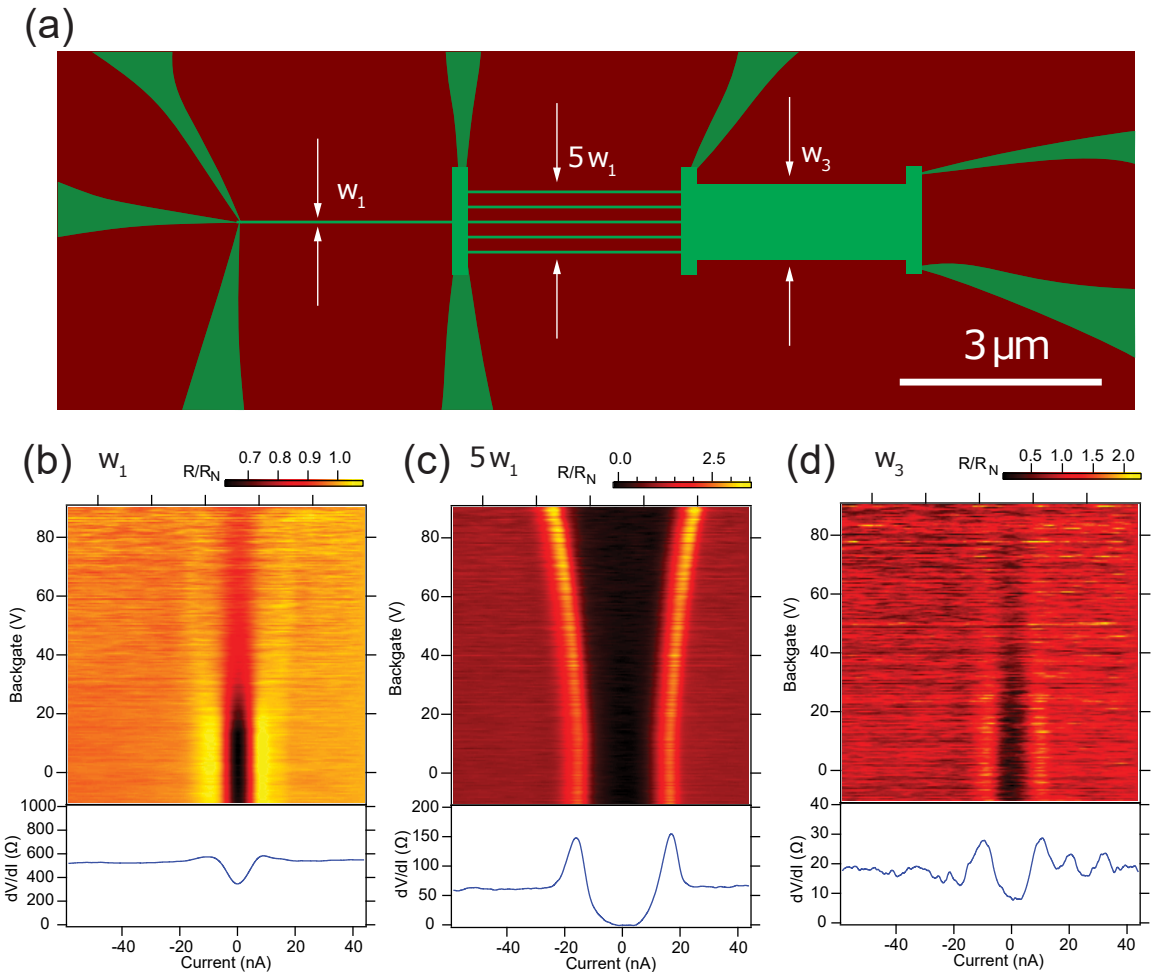

Figure 37: (a) Multi-channel device consist of three sections. Left: single nanowire (w_1). Middle: five nanowires in parallel, 200 nm apart ($5w_1$). Right: 1 μm-wide channel (w_3). All three sections have the same length L = 3 μm. (b) The normalized differential resistance as a function of current and the backgate voltage, for the single nanowire section. The differential resistance in the color scale is normalized with respect to the normal state value. Lower panel: linecut of the raw differential resistance for the w_1 section, (c) $5w_1$ section, and (d) w_3 section, at backgate $V = 0$ V. All data shown here is acquired at T= 30 mK.

as shown in Figure 37 (a). The device consists of three sections in series: from left, a single w_1 $\sim$ 10 nm nanowire ("w_1"), a section of five parallel nanowires of width 10 nm ("$5w_1$") spaced 200 nm apart, and a $w_3 = 1$ μm section ("w_3"). The differential resistance $dV/dI(I, V_{sg})$ is measured for each of the three sections (Figure 37 (b-d)). Overall, the conductance of this device is higher, reflecting the available range over which this device could be gated. At gate voltages $V_{bg} < -20$ V, the voltage leads become insulating, preventing reliable measurements from being made. The critical current for the $5w_1$ channel is 4-5 times larger than the other two sections, and it exhibits a different dependence on back-gate voltage. Meanwhile, channels w_1 and w_3 have similar superconducting critical currents; however, w_3 possesses a non-superconducting, parallel conductance that is an order-of-magnitude larger than channel w_1. This second class of experiments support the idea that superconductivity is associated with the channel boundaries, and that the interior bulk of the channels do not form a superconducting phase.

C. 1D Superconductivity and Ferroelastic Domains

What might cause only the conducting boundaries of these channels to be superconducting? One possibility is that the center of the conductive channels is overdoped, i.e., on the high-density side of the superconducting dome, while the surrounding area is insulating, i.e., underdoped. In this scenario, a quasi-1D strip for which the doping is optimal should exist along each boundary (Figure 38 (a)). This simple picture satisfactorily predicts a width-independent critical current, and gives the correct scaling of parallel background conductance. However, this scenario does not explain why there should be a superconducting dome in the first place.

STO undergoes a cubic-to-tetragonal antiferrodistortive transition at $T_{AFD} = 105$ K. The transition combines antiphase rotations of TiO_6 cages with elongation of the unit cell along the axis of the rotation. Below this transition, ferroelastic domains form with different orientations (X, Y, Z), separated by nanometer-scale domain walls. These domain walls can be driven by electrostatic gating [195] and are observed to be highly conductive [192]. Previ-

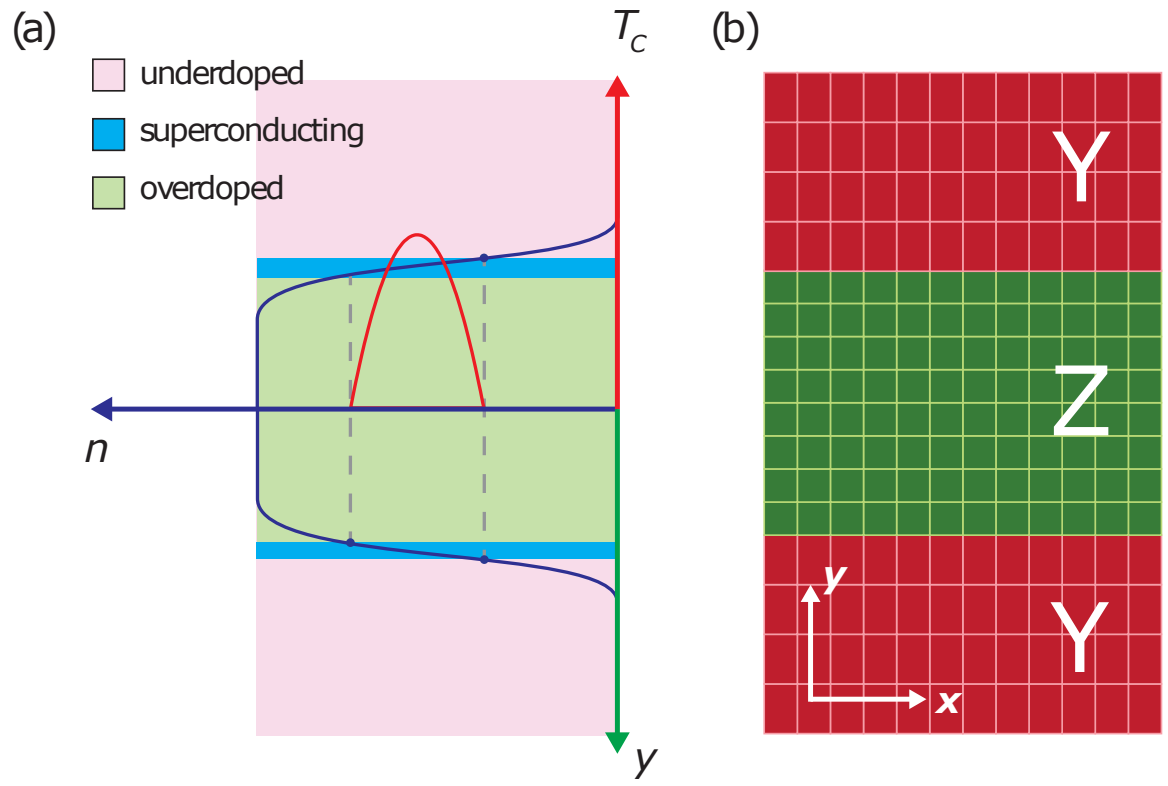

Figure 38: (a) Schematic illustrating how quasi-1D regions of optimal doping can be found near the insulating boundaries of a 2D conducting channel that is overdoped in the 2D bulk region. Dashed lines indicate lower and upper boundaries of the superconducting dome (red curve). The electron density profile (dark blue curve) is overdoped in the center, underdoped in the insulation regions, and optimally doped along a narrow region on both edges, where the density falls within the superconducting dome. (b) Illustration of expected ferroelastic domain structure associated with a conductive region (Z domain) surrounded by insulating boundaries (Y domains).

ously, piezoelectric force microscopy imaging experiments on conductive LAO/STO nanostructures show that conductive regions formed by c-AFM lithography form regions elongated in z-direction (surrounded by cubic insulating regions) at room temperature [412]. This elongation configuration is expected to persist to low temperatures and seed the formation of the Z-oriented ferroelastic domains surrounded by regions that have strain-compensating X or Y domains (Figure 38 (b)). Ferroelastic domain boundaries created at room temperature by c-AFM lithography thus naturally coincide with the edges that separate conducting and insulating regions. If ferroelastic domain walls indeed bracket the edges of conducting nanostructures, one may naturally wonder whether they can mediate electron pairing. Ferroelastic domain walls, with widths that are believed to be comparable to the unit cell [413], possess structural, electronic, and point-defect properties that differ significantly from the uniform domains, which can vary from ∼10 nanometers to many micrometers in extent. Typical superconducting critical current densities reported for 2D LAO/STO are consistent with an average density of one domain wall per micron, where each domain wall is associated with ∼10 nA of supercurrent. The domain walls position may fluctuate dynamically and couple to electronic states, yielding an attractive interaction. Alternatively, ferroelastic domain walls may trap high densities of oxygen vacancies [87] or other point defects that act as negative-U centers [414, 415]. Far outside of the superconducting regime (either $T > T_c$ or $|B| > \mu_0 H_{c2}$), signatures of pairing without superconductivity [124] are observed that scale independently of the width of the channel. In Figure 34 (c,d), a zero-bias conductance dip appears for temperatures as high as $T = 500$ mK, while are zero-bias resistive features persist at high magnetic fields that are similar in nature to pseudogap signatures reported by Richter et al. [118] and multigap features measured by Stornaiuolo et al. [407].The presence and relevance of quasi-1D channels is not restricted to the artificially constructed channels created by c-AFM lithography. A variety of spatially-resolved imaging techniques have revealed strongly inhomogeneous electron transport at the 2D LAO/STO interface, and have demonstrated that current flows preferentially along ferroelastic domain boundaries, affecting properties in both the normal state [192, 103, 416] and superconducting [193] regime.

Regardless of the pairing mechanism, superconductivity in the strict 1D limit is of fundamental interest of its own right [411, 417]. Low-dimensional superconductivity has been

considered in several proposals to support Majorana fermions [319, 418]. While there are theoretical predictions for topologically protected edge modes at STO surfaces [419], there is no evidence so far that topology plays an important role in stabilizing the superconducting state in the LAO/STO structures described here.In conclusion, we have presented evidence that superconductivity at the LAO/STO interface naturally exists within quasi-1D channels at the edge of conducting 2D regions. The conclusion is supported by transport measurements for two families of devices in which the size and number of nanoscale channels is systematically varied. While the microscopic mechanism for electron pairing and superconductivity in STO is still unresolved, the experimental results presented here provide new stringent geometric constraints and suggest a possible role played by ferroelastic domain boundaries.

IV. Superconductivity in 1D Zigzag Nanowires at $LaAlO_3/SrTiO_3$

$LaAlO_3/SrTiO_3$ exhibits electron pairing far outside of the superconducting state [124]. The superconducting state of $LaAlO_3/SrTiO_3$ also exhibits an intrinsic 1D nature [369] which has been linked to ferroelastic domain structure in the $SrTiO_3$. We further explore the role of ferroelastic domain patterns on superconductivity by creating a series of zig-zag nanowire structures. We find that straight nanowires are comparatively more resistive, both in their normal and superconducting state, than channels that have a zig-zag structure. We discuss possible interplay between the charge degree of freedom and the structural domains and employ state-of-the-art phase-field modeling to simulate the relevant domain morphologies. [420]

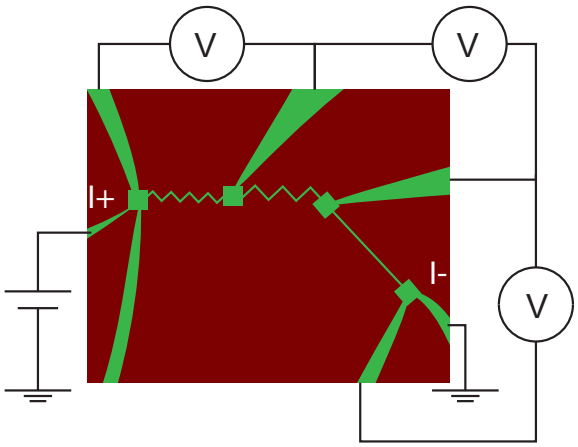

Figure 39: Zigzag device. The device is consisting of 3 sections: each has 0, 5, and 8 right angle turns. The overall length of each section is kept at 3 μm. The current is sourced across the entire device and the voltage drops across section are measured simultaneously.

We studied devices that are consisting of 3 different sections. Figure 39 is a representative device. The devices are consisting of (from left to right) (i) a section of 8 right angle turns, length 3 μm, (ii) a section of 5 right angle turns, length 3 μm, and (iii) a section of straight nanowire, length 3 μm. A total of 6 sets devices were fabricated. The detailed information

of the 6 sets of devices is summarized in Table 1.

Table 1: All the SA02703K devices were created at the same few μm location of the same sample, the same is true for SA03092E and SA03094E except that these devices are consisting of 3 sections next to each other with the 3 sections within each devices characterized simultaneously.

Device	type	R_S	R_N	hysteretic IV?
SA02703K.20130915	0 turns	36 kΩ	48 kΩ	
SA02703K.20130925	23 turns	$<$ 1kΩ	17 kΩ	
SA02703K.20131002	23 turns	$<$ 1kΩ	19 kΩ	∘
SA02703K.20131021	23 turns	$<$ 1kΩ	16 kΩ	∘
SA02703K.20131030	0 turns	2.3kΩ	75 kΩ	∘
SA03092E.20180417	0, 1, 2 turns	$<1, <1, <1$ kΩ	10, 8, 8 kΩ	
SA03094E.20180601	2, 1, 0 turns	$<1, <1, <1$ kΩ	10, 10, 25 kΩ	∘
SA03094E.20180620	2, 1, 0 turns	$<1, <1, 18$ kΩ	25, 15, 38 kΩ	
SA03094E.20180629	8, 5, 0 turns	$<1, <1, 7$ kΩ	1, 2, 18 kΩ	
SA03092E.20190206	8, 5, 0 turns	$<1, <1, <1$ kΩ	10, 10, 20 kΩ	∘
SA03092E.20190517	19, 5, 0 turns	$<1, <1, <1$ kΩ	4, 5, 10 kΩ	∘

A. IV Characteristics and Distribution of the Switching Currents

Figure 40 is a set of current-voltage (IV) curves for the device in Figure 39. The straight section and the 5-turn section are hysteretic. When the current is increased from below the critical current I_c of the nanowire, it stochastically switched from superconducting to normal state at switching current $I_{sw} < I_r$ and a nonzero voltage drop across the nanowire appears. As the current decreases from above the critical current I_c, the nanowire returns at the retrapping current I_r, with $I_r \leq I_{sw} \leq I_c$. In resistively and capacitively shunted

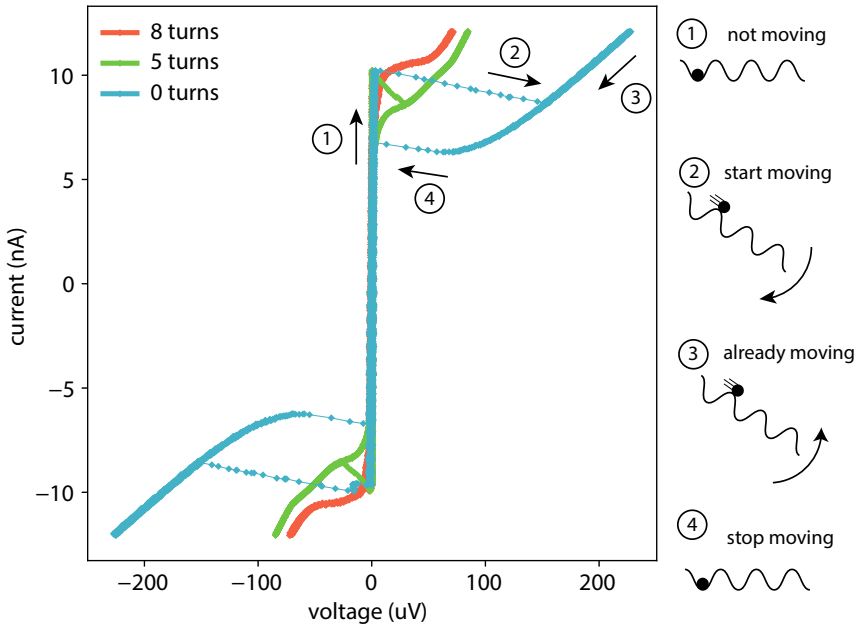

Figure 40: IV curves for a zigzag device

Josephson (RCSJ) model (Figure 40), the system is said to be underdamped when $I_r < I_{sw}$, resulting a hysteretic IV characteristics. The underdamped regime is corresponding to Stewart-McCumber parameter $\beta_c = 2\pi R^2 C/\Phi_0 > 1$ and quality factor $Q > 1$.

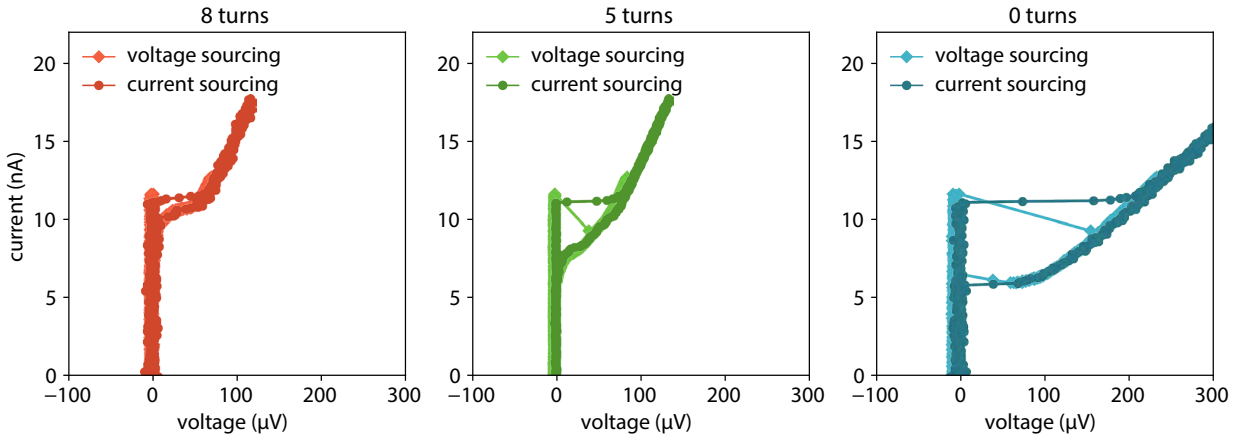

Figure 41: Comparison between voltage sourcing and current sourcing

Additionally, it has been reported that the IV characteristics also depends on the measurement scheme, whether it is current sourcing or voltage sourcing [421]. Figure 41 is a comparison between a set of IV curves taken with voltage sourcing and that with current sourcing. The most ostentatious difference between the two is that there are sections of IV curves that are characterized by negative differential resistance, that is, a negative dV/dI slope. The negative differential resistance are immediately after the I_{sw} when sweeping the voltage such that the current is increased from below the I_c, or immediately after the I_r then the voltage is swept such that the current decreases from above I_c. The negative differential resistance section, for the section right after the I_{sw}, is interpreted as the applied voltage is increased such that the current is large enough for the phase slips start to occur, the current decreases. However, the phase slip center shares the voltage and therefore the voltage across the superconducting region is less, hence the current recovers.

While current sourcing is more common in majority of the reports in the literature, voltage sourcing is the typical setup we use out of the convenience and the configuration of our electronics. All the data presented are from voltage sourcing unless mentioned otherwise.

3 out of the 6 sets of devices exhibited at least one section with underdamped IV characteristics. For all the underdamped devices, the quality factor Q is a monotonic function of the number within the set, i.e., $Q_8 < Q_5 < Q_0$ for the device in Figure 39 and $Q_{19} < Q_5 < Q_0$ for the device SA03092G.20190517. Non-linear, hysteretic IV curves for $LaAlO_3/SrTiO_3$ have been reported in detial by Hurand et al. [422] (see also [423]). The major difference here is that the widths of the nanowires here are on the order of 10 nm.

Figure 42 is a statistics of the I_{sw} for 3 sections of the device in Figure 39 at two temperatures. The width of the distribution of the switching currents σ_{sw} increases with decreasing temperature.

B. Temperature, Field and Gate Dependence

Figure 43 are sets of differential resistance (dV/dI) as a function of current and temperature for the three sections taken under three different backgate voltages: $V_{BG} = 0$ V,

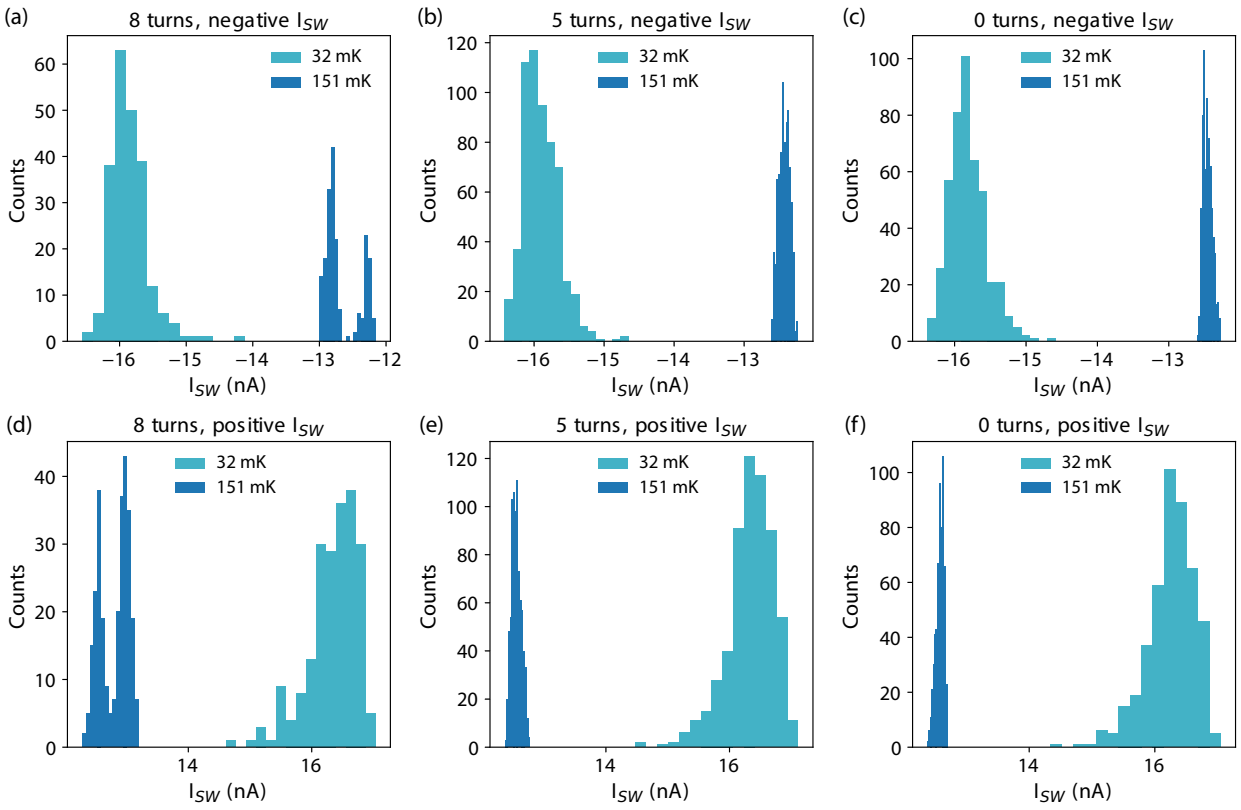

Figure 42: Switching current distribution

$V_{BG} = -1.5$V and $V_{BG} = +1.5$V. Note that the double branches in the differential resistance (for example, in zero turn section, $V_{BG} = 0$ V Figure 43) is from the numerical differentiation applied onto the IV curves that has a negative differential resistance region. This features is gone in current sourcing IV curves.

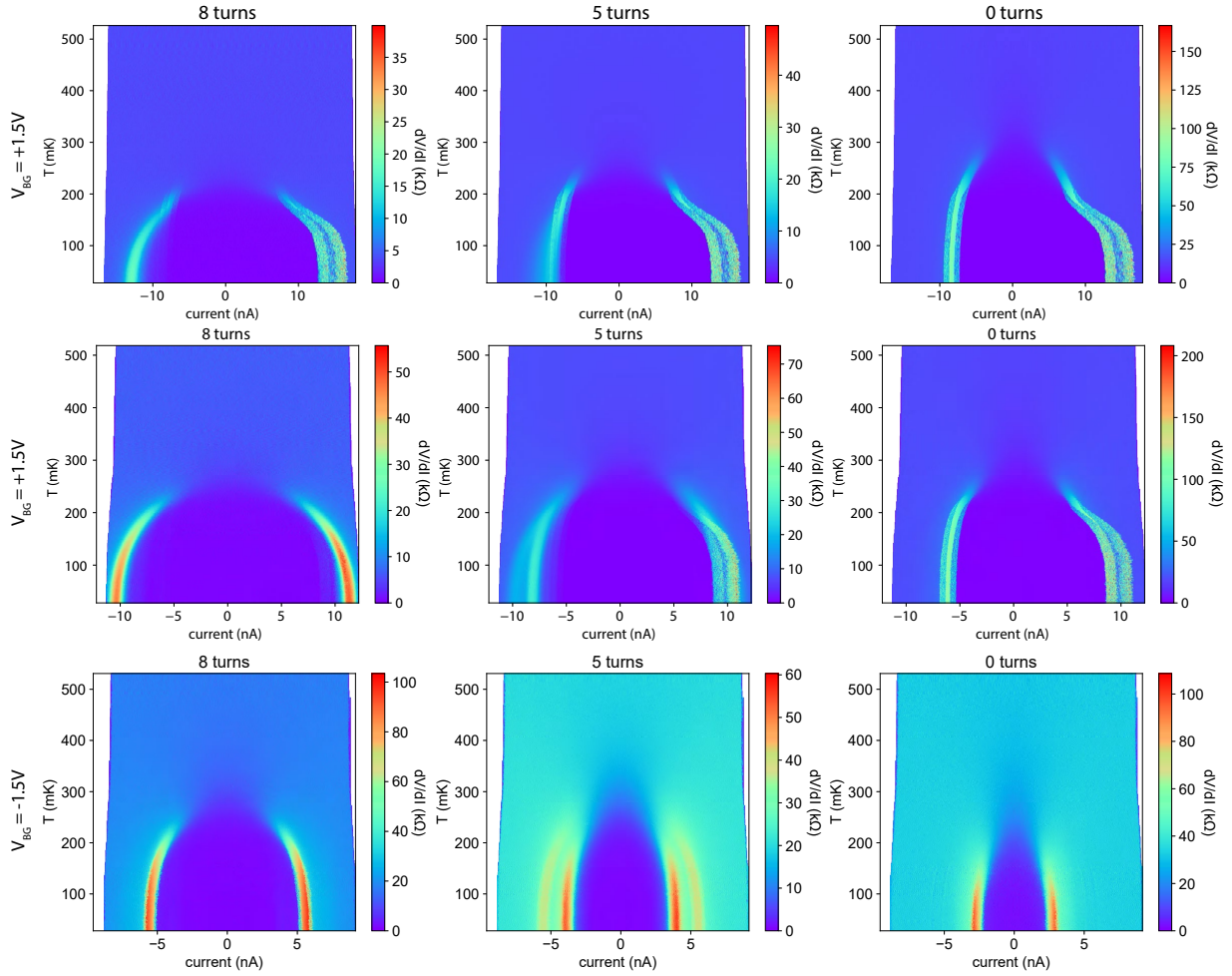

Figure 43: Differential resistance as a function of temperature at $V_{BG} = 0$V

Figure 44 are linecuts at zero bias of 43. While all of the three sections respond to the applied backgate voltage V_{BG}, the straight nanowire section is the most sensitve in the sense that $T_{c,0} < T_{c,5} < T_{c,8}$ at $V_{BG} = -1.5$ V to $T_{c,0} \sim T_{c,5} \sim T_{c,8}$ at $V_{BG} = 0$ V then $T_{c,0} > T_{c,5} > T_{c,8}$ at $V_{BG} = +1.5$ V.

Figure 45 are differential resistances (dV/dI) as a function of current and out-of-plane

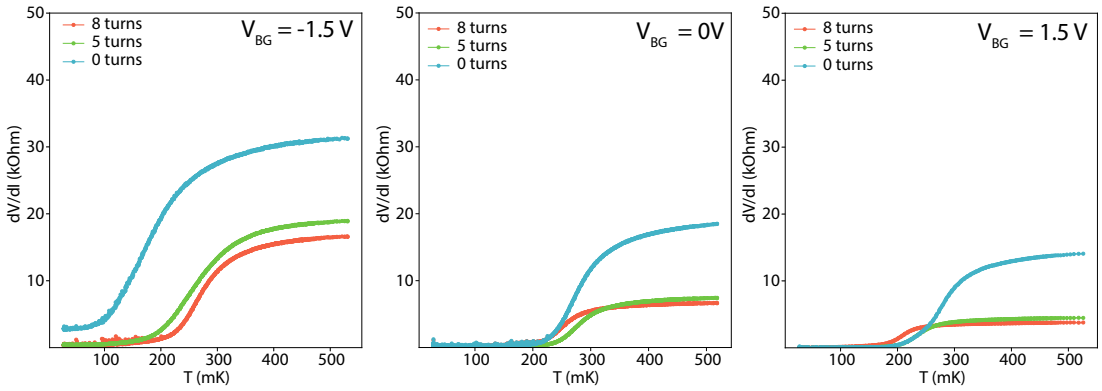

Figure 44: Temperature dependence at three different gate voltages

magnetic field for the three sections. Note that this device was unstable, resulting in the stripes in the dV/dI. Figure 46 are the time-series of the differential resistance at zero bias for the three sections at $B = 0$ T. The device resistances oscillate violently after several days of measurement. This is the only devices within all the 6 sets of devices that showed this instability.

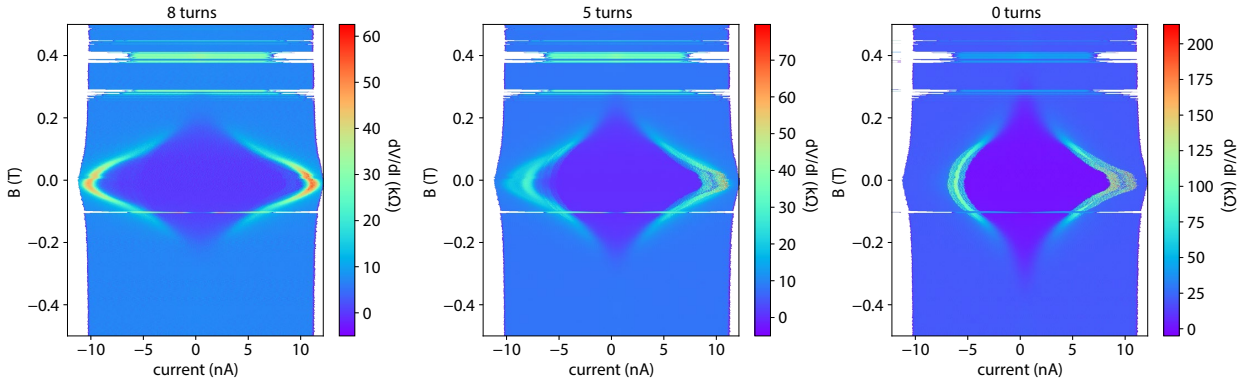

Figure 45: Differential resistance as a function of field at $V_{BG} = 0$V

Figure 47 are differential resistances (dV/dI) as a function of current and out-of-plane magnetic field for the three sections.

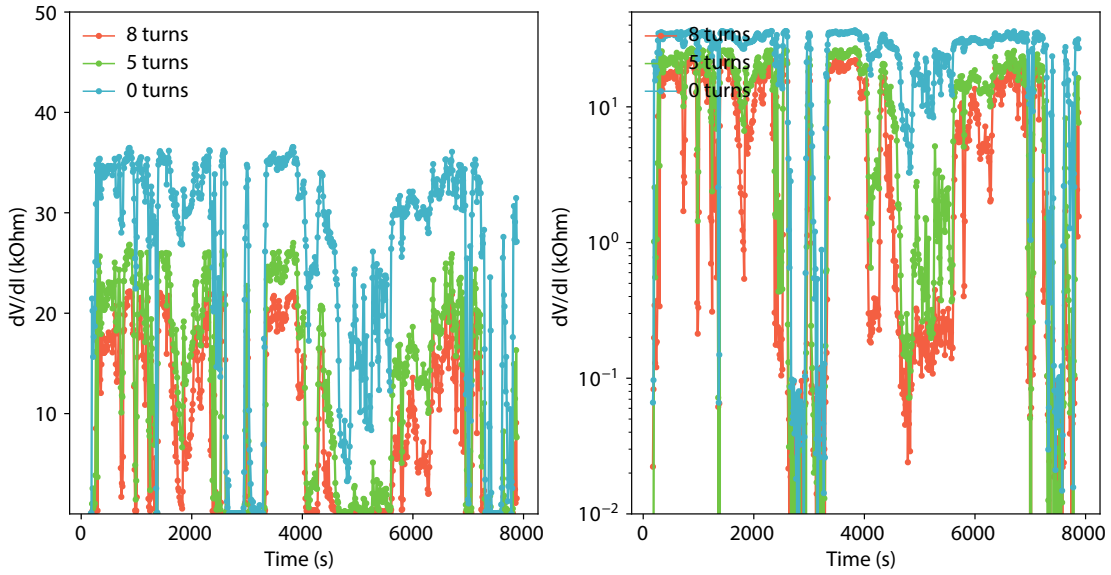

Figure 46: Stability of the three sections

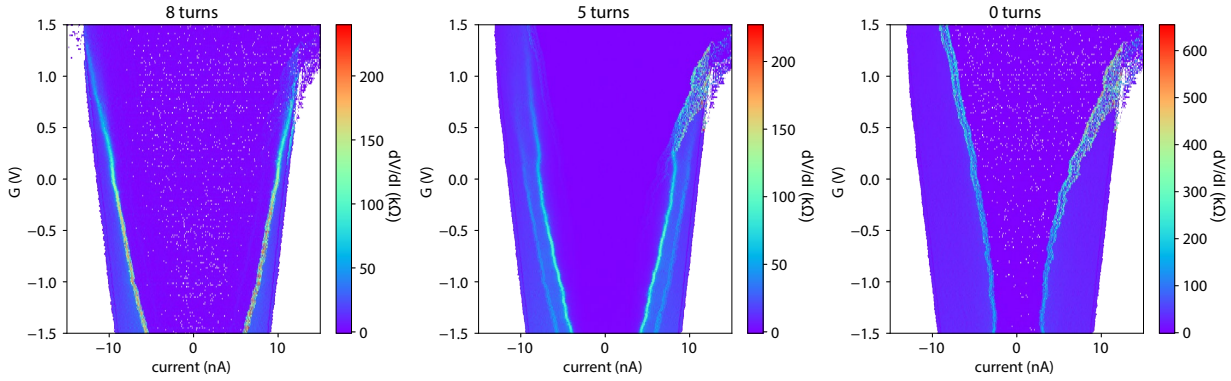

Figure 47: Differential resistance as a function of gate at $B = 0$T

C. Second Sets of Devices and Discussion

Table 1 summarizes the total of $5+6\times3$ of sections of nanowires and their zero bias residual resistance for the superconducting states R_S and normal state resistance R_N. Note that majority of the $R_N > h/4e^2 = 6470.7\Omega$ but all superconducting, unlike the superconducting-insulator transition bifircation at $h/4e^2$ commonly reported. Figure 48 is the distribution of the R_S and R_N. Both the R_S and R_N distributed toward more resistive as the number of sharp turns decreases. This trend is not perfect especially when the number of the turns is only 0, 1, 2.

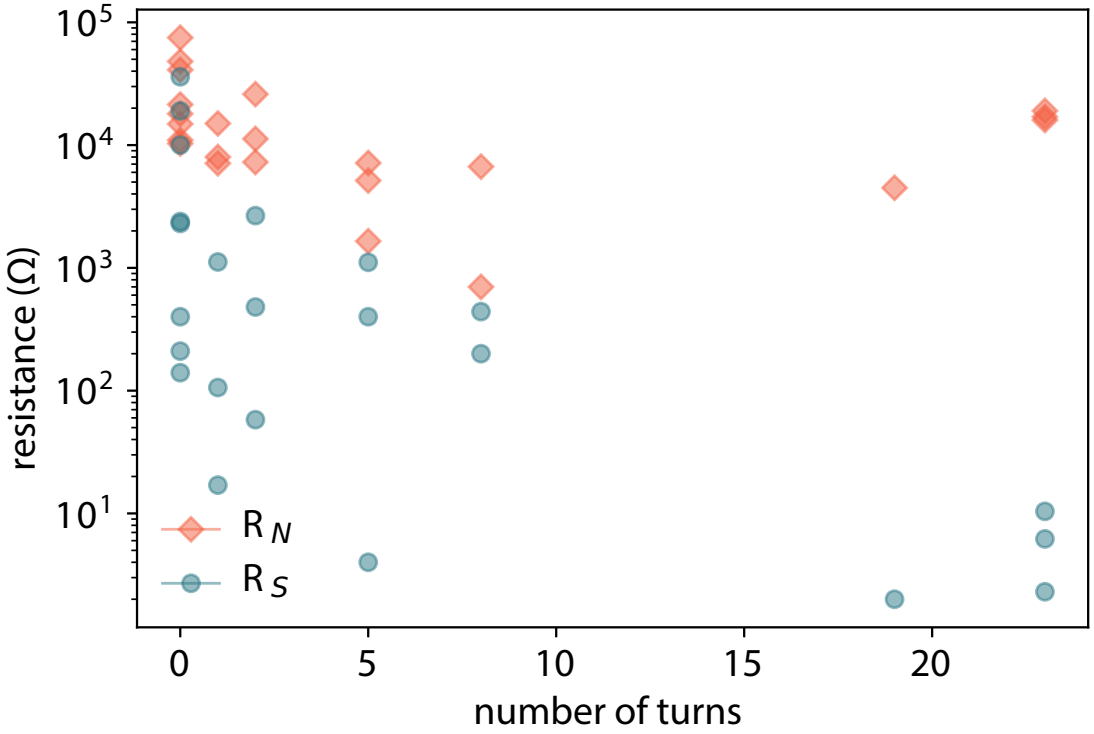

Figure 48: Distribution of R_S and R_N for zigzag devices

Now the first question is why the channels become less resistive when the number of the sharp turns increases. One simple explanation is from the intrinsic ferroelastic domains of $SrTiO_3$. As $SrTiO_3$ is cooled below $T < T_{AFD}$, ferroelastic domains of different orientation forms. The domains modulates the conductivity, current density, superconductivity, and was considered one of many possible pairing glues of $SrTiO_3$. If charge distribution elongates the

lattice in the out of plane direction [412] and seeds the Z oriented domains at $T < T_{AFD}$ (phase field modeling in Section V.C). However, the ferroelastic domain has a $c/a = 1.00056$ ratio. Not only the sample will become strained locally, the domain morphology promoted by charge distribution will have to compete with the domain morphology pinned by the boundary conditions such as electrodes from photolithography. Furthermore, larger scale single domain will also be heavily punished unless there is only one domain orientation.

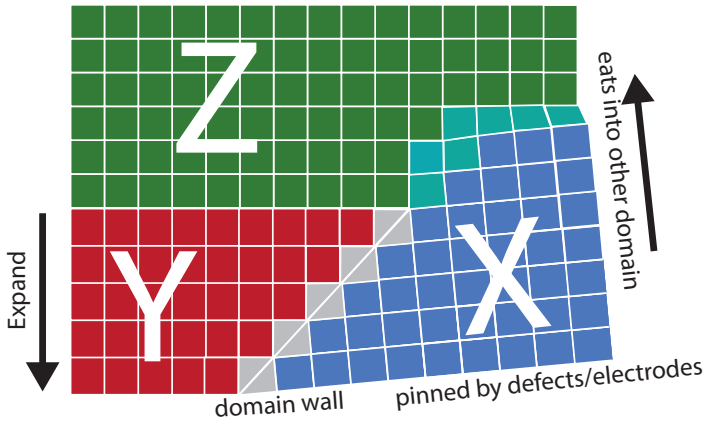

Figure 49: Domain seeding and frustration

If a straight wire along the X−axis promotes an Y−Z−Y domain morphology (Figure 38 (b)), an zigzag with right angle turns such that each subsection is either along the (100) or (010) of the crystallographic axis, the zigzag is expected to promote a zigzag of Z−oriented domain sandwiched by twinning X− and Y− domains. The major difference is that the twining morphology distributed the overall distortion in the X, Y direction evenly, instead of only Y as in the case for a straight nanowire along the X − axis. This configuration is less energetically costly and more stable whereas the straigh wire gets frustrated more easily (Figure 49). This also explains that the sections with more sharp turns are less tunable by gate voltages in 44.

How about the nonidealities and the violators of this trends? Experimentally, there are many more parameters needed to be kept track of: the angle of the sharp turns, the relative angle between the nanowires and the crystallographic axis, the pitch of the sharp turns,

etc. Additionally, as straight nanowires and zigzag nanowires seed their preferred domain morphologies, so do the leads. These domain morphologies, in turn, become boundary conditions for each other and have to compete.

V. Phase Field Modeling of $SrTiO_3$

Phase field modeling is one of the numerical methods that has been applied to modeling multiferroic materials [424]. There are several branches of computational methods on studying complex oxides, from first principles, effective Hamiltonian, molecular dynamics, Ginzburg-Landau theory-based phenomenological models. The atomitistic methods such as first principles, density functional theory are used for calculation properties such as band structure of smaller scale of lattice, while finite element and phase field modeling more toward mesoscaled domain morphology. Recently it has been successfully employed to explain the observed room temperature polar skyrmion [425], domain morphology of piezo material $Pb(Mg_{1/3}Nb2/3)O_3$-$PbTiO_3$ (PMN-PT) which becomes transparent after ac-polling [426]. In addition to the domain morphology of complex oxides, phase field modeling has also been applied to grain growth in metals, alloys, needle crystal growth of lithium in lithium ion batteries, for example.

Phase field modeling is a continuum theory originated from Landau's mean field theory. Contrary to the finite element method, phase field is a frequency (semi-implicit Fourier-spectral) method [427]. It employs only the lower frequency components, which, equivalently assuming certain smoothness of the field in the real space; therefore, the computational cost is significantly reduced. The calculation is also therefore basis-dependent; the underlying simulation procedures has to be modified if the space of interest is to be changed from Cartesian coordinate system to curvilinear coordinate systems.

The fields in phase field modeling are the order parameters such as ferroelectric polar distortion or oxygen octahedra tilt. But the order parameters here in phase field modeling do not necessarily proportional to the real physical amplitude of the property of interest, but just some convenient quantity that can uniquely specify the phase transition. The size of the system depends on the computation power and the size of the domain wall. Typically, one needs more than 1.5 lattice sites across the domain wall. Phase field does not have the need of artificially create boundary condition exactly at the domain wall. However, it is also important to note that, as a continuum method, phase-field is agnostic to the atomistic

details, such as whether the domain walls are at Sr-O plane or at the Ti-O plane for $SrTiO_3$. The resulting order parameters as a function of the sites are discretized numerical solution of this continuum method.

Phase field modeling is consisting of two steps: (1) getting/fitting experimental parameters such as susceptibilities in order to obtain a set of thermodynamic potential parameters (Section V.A.1) for Landau functional (Section V.A). (2) let the order parameters such as polarization $\mathbf{P} = (P_1, P_2, P_3)$, octahedra tilt $\mathbf{Q} = (Q_1, Q_2, Q_3)$ evolve (Section V.B).

A. Landau-Ginzburg-Devonshire Expansion

To consider the thermodynamic description of the system, the order parameters can be chosen to be the order parameter of the polarization $\mathbf{P} = (P_1, P_2, P_3)$ (unit C/m^2), and the order parameter for the linear dispacement of the oxygen atoms due to the antiphase rotation of the oxygen octahedra $\mathbf{Q} = (Q_1, Q_2, Q_3)$ (unit m). The Landau free energy can then be expanded (to the fourth order) [428]:

$$F = \int [f_{bulk}(\mathbf{P}, \mathbf{Q}) + f_{elastic}(\mathbf{P}, \mathbf{Q}, \epsilon) + f_{grad}(\nabla \mathbf{P}, \nabla \mathbf{Q}) + f_{electric}(\mathbf{P}, \mathbf{E})] dV \tag{V.1}$$

f_{bulk} is given by:

$$\begin{aligned} f_{bulk}(\mathbf{P}, \mathbf{Q}) = {} & \alpha_1(P_1^2 + P_2^2 + P_3^2) + \alpha_{11}(P_1^4 + P_2^4 + P_3^4) + \alpha_{12}(P_1^2P_2^2 + P_2^2P_3^2 + P_1^2P_3^2) \\ & + \beta_1(Q_1^2 + Q_2^2 + Q_3^2) + \beta_{11}(Q_1^4 + Q_2^4 + Q_3^4) + \beta_{12}(Q_1^2Q_2^2 + Q_1^2Q_3^2 + Q_2^2Q_3^2) \\ & - t_{11}(P_1^2Q_1^2 + P_2^2Q_2^2 + P_3^2Q_3^2) \\ & - t_{12}(P_1^2Q_2^2 + P_2^2Q_1^2 + P_3^2Q_2^2 + P_2^2Q_3^2 + P_3^2Q_1^2 + P_1^2Q_3^2) \\ & - t_{44}(P_1P_2Q_1Q_2 + P_1P_3Q_1Q_3 + P_2P_3Q_2Q_3) \end{aligned} \tag{V.2}$$

where α_{ij} are the Landau-Ginzburg-Devonshire coefficients for $\mathbf{P} = (P_1, P_2, P_3)$ and are responsible for the dielectric susceptibility of the material. βij are the corresponding parameters for the $\mathbf{Q} = (Q_1, Q_2, Q_3)$. The t_{ij} are the rotopolar coupling coefficients.

$f_{elastic}$ is given by:

$$f_{elastic}(\mathbf{P}, \mathbf{Q}, \epsilon) = \frac{1}{2} c_{ijkl}(\epsilon_{ij} - \epsilon^0_{ij})(\epsilon_{ij} - \epsilon^0_{ij}) \tag{V.3}$$

with

$$\epsilon^0_{ij} = Q_{ijkl} P_k P_l + \Lambda_{ijkl} Q_k Q_l \tag{V.4}$$

The c_{ijkl} are the stiffness tensor. The ϵ_{ij} are the strain state with respect to the parent pseudo-cubic lattice. The ϵ^0_{ij} is the stress-free strain (*eigenstrain*) due to the polar, structural distortion, defect, charge, or temperature, etc.

The gradient energy $f_{grad}(\nabla \mathbf{P}, \nabla \mathbf{Q})$, i.e., the energy for the domain walls of the order parameters, is given by:

$$f_{grad}(\nabla \mathbf{P}, \nabla \mathbf{Q}) = \frac{1}{2} G_p \frac{\partial P_i}{\partial x_j} \frac{\partial P_i}{\partial x_j} + \frac{1}{2} G_q \frac{\partial Q_i}{\partial x_j} \frac{\partial Q_i}{\partial x_j} \tag{V.5}$$

The electrostatic energy $f_{electric}(\mathbf{P}, \mathbf{E})$ is given by:

$$f_{electric}(\mathbf{P}, \mathbf{E}) = -\frac{1}{2} \mathbf{P} \cdot \mathbf{E} \tag{V.6}$$

1. Thermodynamic Potential Parameters

The thermodynamic potential parameters for Landau functional are the α_{ij}, β_{ij}, t_{ij}, etc in Equation V.2. They describe how the order parameters interact with each other at a given strain, electric field, defect, temperature conditions. The values of those parameters are fitted, inferred, or calculated from various experimental characterization or first principle calculations. The resulting parameters can vary significantly and hence the resulting domain morphologies. For a material such as strontium titanate, the set of the parameter is never perfect. Finding a set of parameter that captures majority of the behavior of strontium titnate is challenging.

One immediate example, as discussed in Li et al [428], is that the reported α_{12} values in the literature ranged from 1.7×10^{-12} cm^6 dyne/ esu^4 to 5.5×10^{-12} cm^6 dyne/ esu^4. As one can see, larger α_{12} increases the free energy of the domains with simultaneous polarization along two directions, i.e., the orthorhombic domains (Table 4). In Li et al [428], increasing α_{12} from 1.7×10^{-12} cm^6 dyne/ esu^4 to 5.5×10^{-12} cm^6 dyne/ esu^4, under tensile strain (0.94%, 0.94%, 0) will change the resulting domain morphology completely. The former will yield majority of orthorhombic domains while the latter overwhelmingly tetragonal domains.

The normalization factor p_0 (unit C/m^2) and q_0 (unit m) are used to rescale the order parameter $\mathbf{P}$, $\mathbf{Q}$, respectively. Since the typically values of the $||\mathbf{P}|| \sim 0.1$ and $||\mathbf{Q}|| \sim 10^{-12} - 10^{-11}$ are orders of magnitude different from each other, $\mathbf{P}$, $\mathbf{Q}$ are rescaled in order to make sure both of them are making use of the dynamic range of the real double precision float (`real(kind=rdp)` in FORTRAN). Ideally, the choice of the p_0 and q_0 should not change the resulting domain morphology, provided that the precision is infinite. In reality, the domains are sensitive to p_0 and q_0, since they effectively dictate the upper bounds of the order parameter, the lower bounds, and how fine the values of the order parameters can change. Further more, as the simulation proceeds, these small steps build up (See Figure 62).

The results $\mathbf{P}$, $\mathbf{Q}$ from previous simulation can be used as the initial state for new simulations, instead of Gaussian noise. Care must be taken as the initial condition may trap the order parameter to local minima of the configuration space, and as a result, appear to

Table 2: Range for thermodynamic potential parameters used for $SrTiO_3$ in this thesis. The starting range is from Li et al. [428] and [429]. Only α_1 and β_1 are temperature dependent, following Barrett's relation [430].

Parameter	Value	Unit (SI)
α_1	$4.06 \times 10^7(1/tanh(54/T) - 1/tanh(54/30))$	$C^{-2}m^2N$
α_{11}	1.701×10^9	$C^{-4}m^6N$
α_{12}	3.65×10^9 to 4.44×10^9	$C^{-4}m^6N$
Q_{11}	0.04581	$C^{-2}m^4$
Q_{12}	-0.0135	$C^{-2}m^4$
Q_{44}	0.0096	$C^{-2}m^4$
C_{11}	3.36×10^{11}	$m^{-2}N$
C_{12}	1.07×10^{11}	$m^{-2}N$
C_{44}	1.27×10^{11}	$m^{-2}N$
β_1	$1.32 \times 10^{29}(1/tanh(145/T) - 1/tanh(145/105))$	$m^{-2}m^{-2}N$
β_{11}	0.96×10^{50} to 1.69×10^{50}	$m^{-4}m^{-2}N$
β_{12}	3.96×10^{50} to 6.00×10^{50}	$m^{-4}m^{-2}N$
L_{11}	8.7×10^{18} to 11.3×10^{18}	m^{-2}
L_{12}	-7.8×10^{18}	m^{-2}
L_{44}	-9.88×10^{18} to -9.2×10^{18}	m^{-2}
t_{11}	-5.94×10^{29} to -1.74×10^{29}	$C^{-2}N$
t_{12}	-7.55×10^{28}	$C^{-2}N$
t_{44}	5.86×10^{29}	$C^{-2}N$
p_0	0.01 to 0.1	C/m^2
q_0	1.0×10^{-12}	m

be non-thermalized.

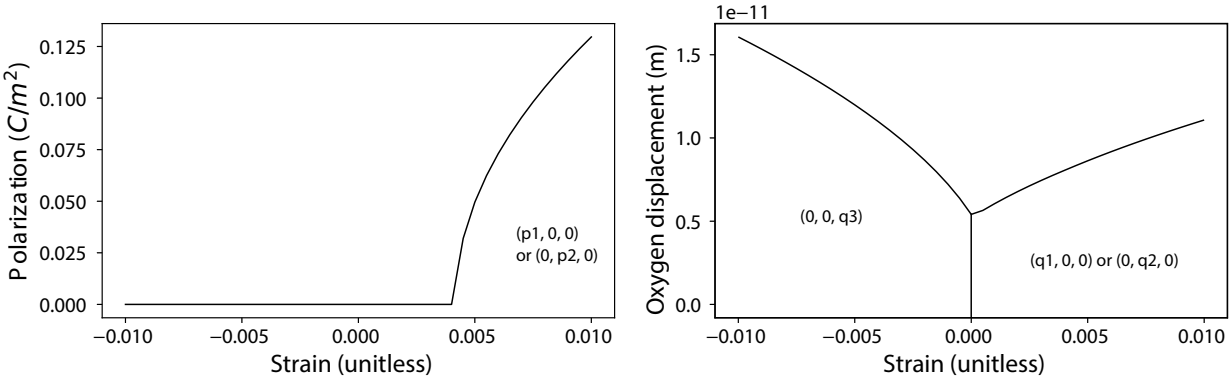

Figure 50: Phase diagram under biaxial strain. Courtest Jacob Zorn.

I started with the thermodynamic potential parameters used in Li et al. [428] and Sheng et al. [429]. The range of the thermodynamic potential parameters I explored is listed in Table 2. Before running the simulation, one can also minimize the functional (Equation V.2) with the thermodynamic potential parameters to get a set of order parameters $\mathbf{P}$, $\mathbf{Q}$ and the most probable phase under the given strain, temperature conditions (Figure 50).

B. Domain Evolution

The spatial and temporal evolution of the order parameters are described by time dependent Ginzburg-Landau equations:

$$\frac{\partial p_i(\mathbf{x},t)}{\partial t} = -L_p \frac{\delta F}{\delta p_i(\mathbf{x},t)}, i = 1,2,3 \tag{V.7}$$

$$\frac{\partial q_i(\mathbf{x},t)}{\partial t} = -L_q \frac{\delta F}{\delta q_i(\mathbf{x},t)}, i = 1,2,3 \tag{V.8}$$

where L_p and L_q are the kinetic coefficients. They are related to the mobilities of the domains.

C. Domain Morphologies for $SrTiO_3$ with a Given Charge Distribution

To see the how the domains evolve given charge distribution, a series of simulation were performed. The system size is $128\Delta x \times 128\Delta x \times 36\Delta x$[1]. From bottom, the first 12 layers being substrate (unused), 20 layers being the $SrTiO_3$, and the top 4 layer being vacuum or air. The charge distribution is fixed (set as `defectE.in` in MuPro), with $Q = 1$ for y site $42 < y < 85$ and z site $21 < z < 33$, and $Q = 0$ for the rest. The $Q = 1$ is normalized as $Q = 10^9$ C/ m^3 in the calculation.

Figure 51 (a) is the specified charge distribution. The temperature is set to $T = 40$ K. The gradient components were set to 0.4, -0.4 and 0.4. The strain $\mathbf{e} = (e_{s1}, e_{s2})$ is set to zero (0, 0). The initial noise magnitude for the polarization and the octahedral tilt are 0.05 and 1×10^{-12}, respectively. The thermodynamic potential parameters are listed in Table 6 and is within the range of Table 2. The simulation reaches 60,000 steps in just under 48 hours with 4 cores allocated.

Figure 51 (b) is the resulting polarization vector. The sites occupied by the specified charge are polarized along $+z$ preferentially. Figure 51 (d) is the polarization domain of (b). Figure 51 (c) is the resulting octahedra tilt domains. The sites occupied by charges are dominantly z-oriented ($c + (0, 0, 1)$ and $c - (0, 0, -1)$ domains), sandwitched by mostly y oriented domains ($a2 + (0, 1, 0)$ and $a2 - (0, -1, 0)$ domains). Figure 51 (e) is the domain morphology of the top surface of (c), and (f) for (d). Note that in order to assign domain for each site, a threshold value has to be set (to eliminate false domains). Threshold used for (c) is 5×10^{-13}, (d) is 0.15, (e) is 1×10^{-12}, and (f) is 0.05.

[1]The size of the system is also an important set of parameters. While a system size of $128\Delta x \times 128\Delta x \times 36\Delta x$ is not much of a computational burden. However, reading in initial states and charge distribution adds resource time. Plus, the size of the files are about 68 MB (for vector fields) for this system size and grows rapidly, so is the time it takes to transfer files off the cluster or visualization.

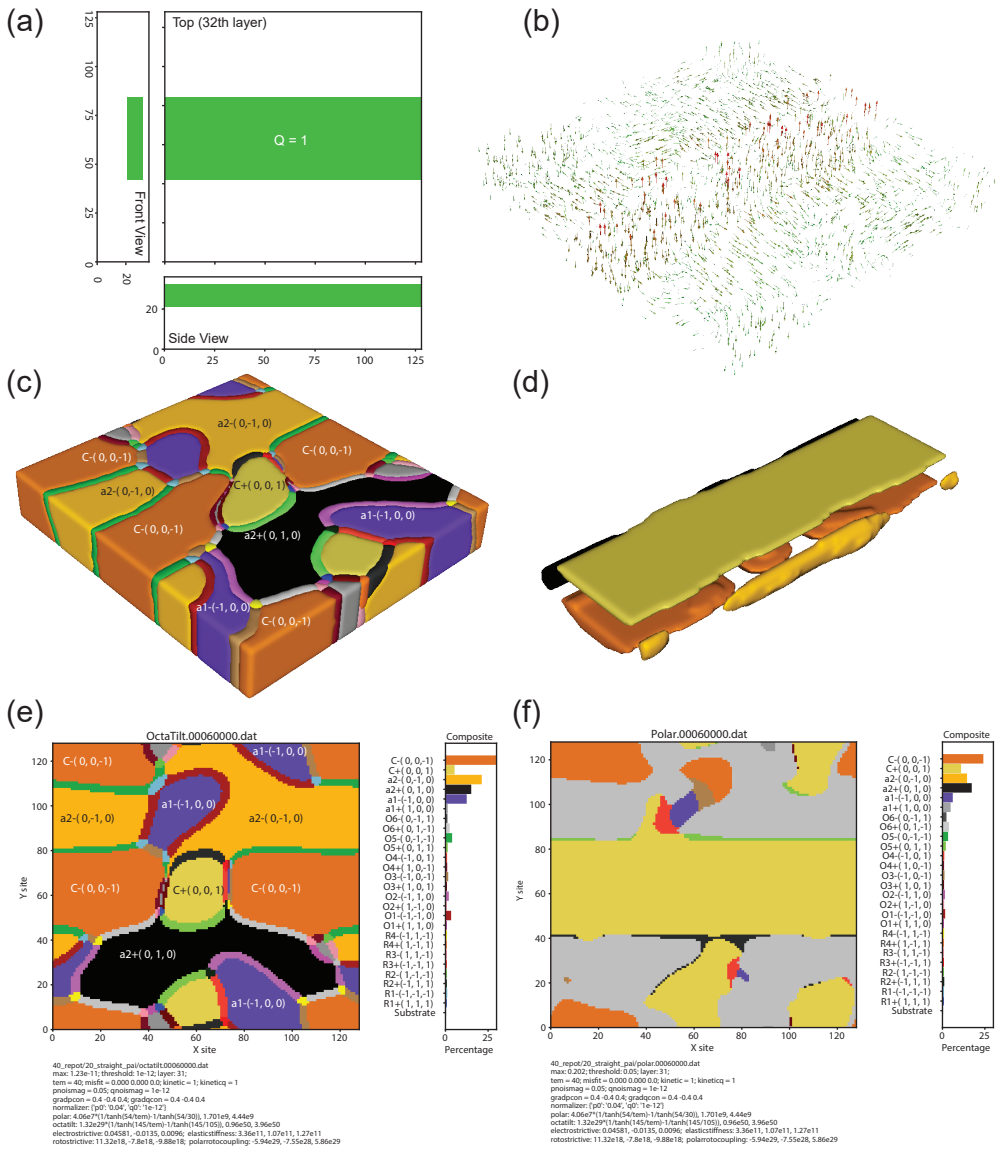

Figure 51: Simulation with initial rectangular charge distribution. (a) Charge distribution. (b) Polarization vector, visualized with MuVis SimpleView (Courtesy Xiaoxing Cheng). (c) Octahedra tilt domains, visualized with MuVis SimpleView. (d) Polar distortion domains, visualized with MuVis SimpleView. (e) Left: Top surface (layer 32 in MuPro; 31 in Python) for (c) with the same color scheme for the domains. Right: Histogram for the domain population. (f) Left: Top surface for (d) with smaller threshold (0.05) for domain assignment. Right: Histogram for the domain population.

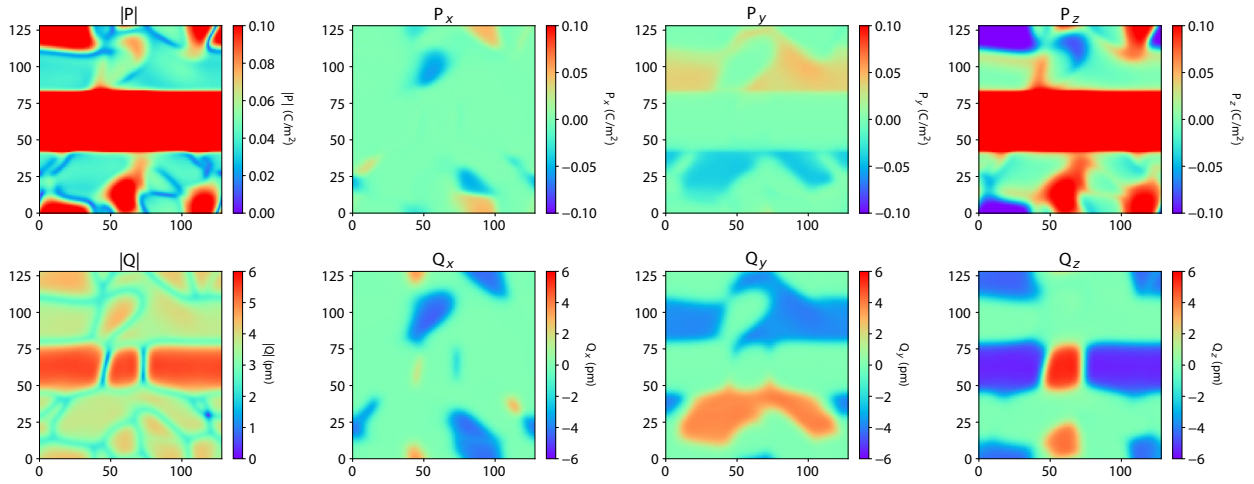

Figure 52: Comparison between with and without initial charge. (a) Octahedra tilt domain morphology with the charge distribution. (b) Octahedra tilt domain morphology without charge distribution. Thermodynamic potential parameters are in Table 6.

Figure 52 is the raw order parameters **P**, **Q**. The maximal magnitude for **P** is about 0.1 C/m^2 and **Q** about 6 pm. Note that the even though there are experimental evidences about the polar nature of the octahedra tilt domain walls (both experimental [195] and computational [431, 432, 433]), the domain walls in the simulations here are not. Gu et al. [434] reported that, with addtional flexoelectric coupling terms or improper antiferroelectric−antiferroelastic coupling terms, phase-field simulation can reproduce the polar nature of the octahedra tilt domain walls for $CaTiO_3$. For $SrTiO_3$, regardless of with or without the flexoelectric coupling, the hard walls remain polar while the easy walls are not [433].

Figure 53 is comparison between the octahedra tilt domains with charge distribution (a) and without charge distribution (b). Figure 53 (a) is from the same simulation run as that in Figure 51. For (b), all parameters such as the thermodynamic potential parameters and all the settings are kept the same except that there is no charge distribution for (b). The region that is occupied by charges in (a) is marked by white dashed-line rectangle in both (a) and (b). While in (a) that the sites occupied by charges are z−oriented (c+ and c− domains) and sandwitched by y−oriented domains, the sites in (b) for comparison do have

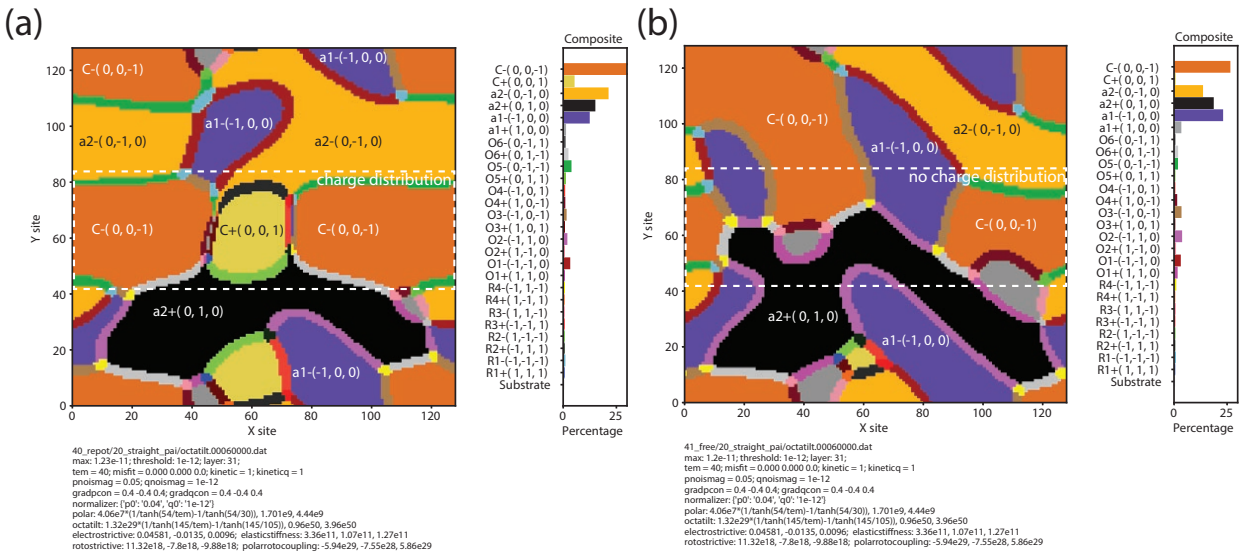

Figure 53: Comparison between with and without initial charge. (a) Octahedra tilt domain morphology with the charge distribution. (b) Octahedra tilt domain morphology without charge distribution. Thermodynamic potential parameters are in Table 6.

more equally populated z− and y− domains.

D. Domain Morphologies for $SrTiO_3$ with a Uniaxial Strain

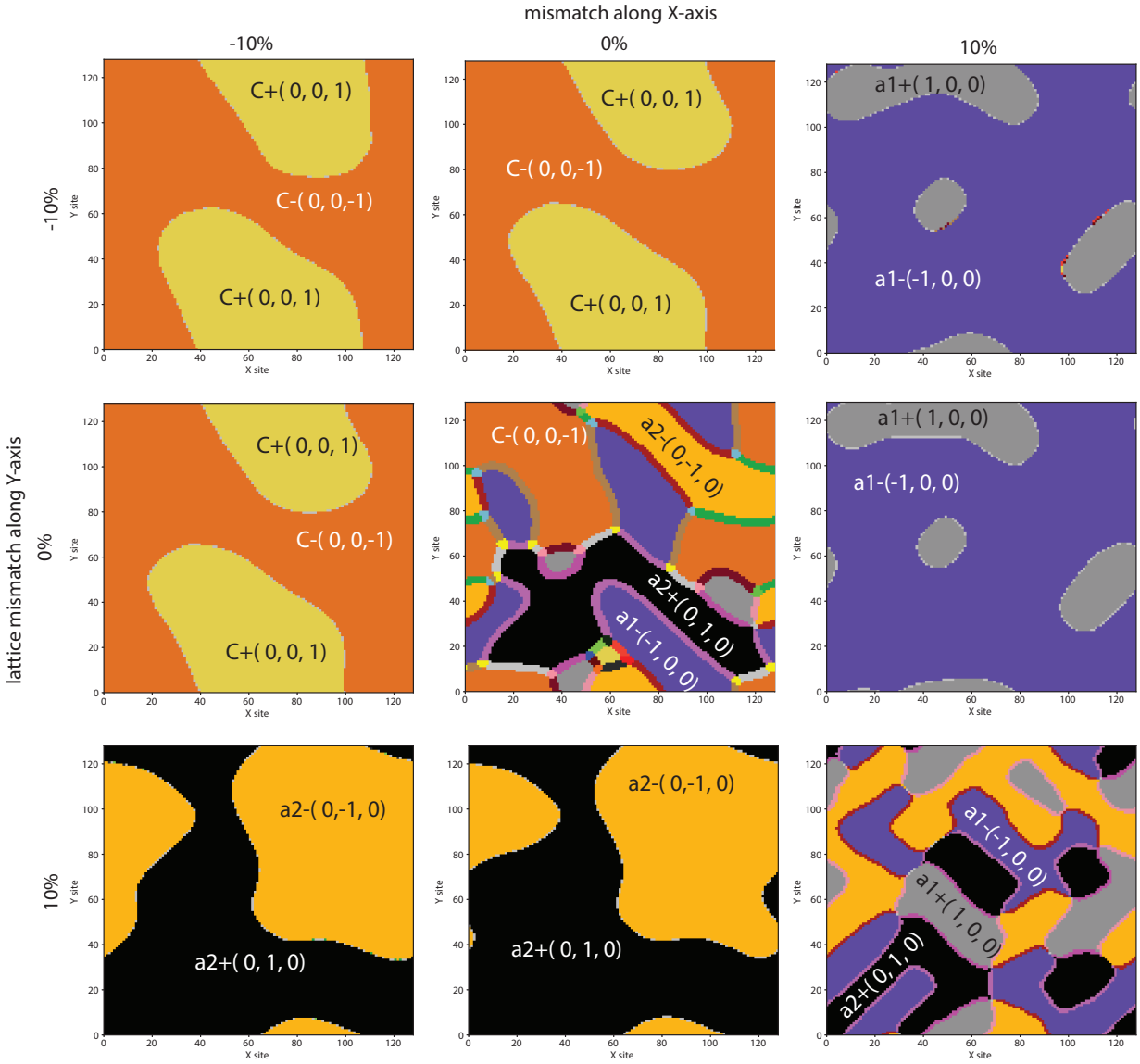

Figure 54: Strain dependence. Thermodynamic potential parameters are in Table 6.

Figure 54 is a set of simulations with different uniaxial strain condition from $\mathbf{e} = (e_{s1}, e_{s2}) = (-0.1,\ -0.1)$ to $(+0.1,\ +0.1)$. The system size is $128\Delta x \times\ 128\Delta x \times 36\Delta x$, with the first 12 layers being substrate (unused), 20 layers being the $SrTiO_3$, and the top 4 layer being vacuum or air. The temperature is set to $T = 40$K. The gradient components

were set to 0.4, −0.4 and 0.4. The thermodynamic potential parameters are the same Table 6. Note that a strain of 0.1 = 10% in any of the axis is larger than the fracture point of stoichiometric $SrTiO_3$ at room temperature [435].

E. Domain Morphologies for $SrTiO_3$ with Electric Field

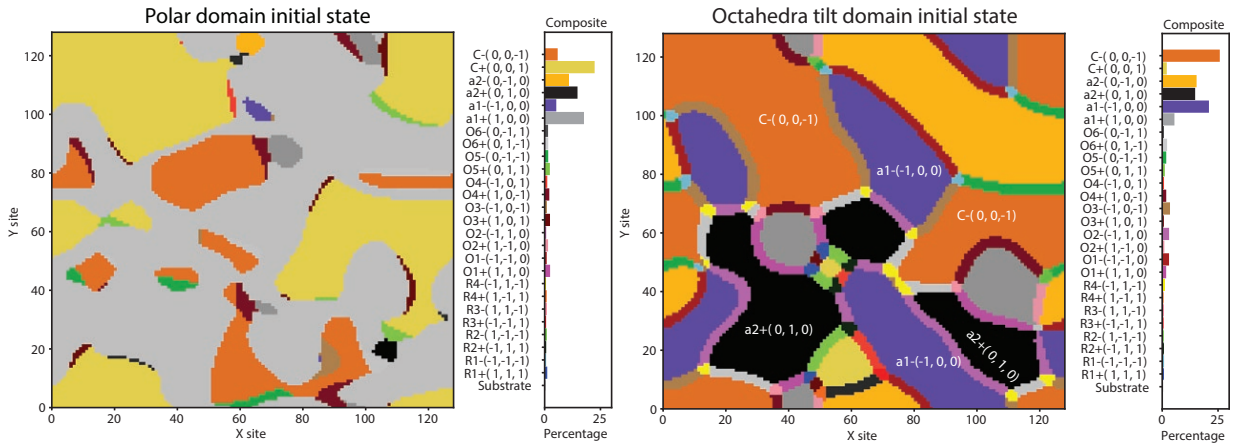

Figure 55: Initial octahedra tilt domain morphology for electric field dependence

The evolution of the domain morphology for $SrTiO_3$ as a function of applied electric field is not well understood [195, 436, 437]. For the 2DES at $SrTiO_3$, it is commonly thought that the applied electric field tunes the carrier concentration: positive gate voltage increases the carrier concentration of the 2DES and conversely negative gate voltages decreases the carrier concentration. However, the gate voltages **also** triggers the motion of domains. Honig et al. [195] reported that both positive and negative voltages push the domain walls out of the sample. Casals et al. [436] found the need of introducing additional trilinear term to capture the interaction between electric polar mode, octahedra tilt, and an antiferroelectric mode in order to describe the system. The domain dynamics fits power low well [438], mimicing self-organized criticality in an avalanche [439].

Figure 56 is a set of simulations with different voltages applied across $SrTiO_3$. The system size is $128\Delta x \times 128\Delta x \times 36\Delta x$, with the first 12 layers being substrate (unused), 20

layers being the $SrTiO_3$, and the top 4 layer being vacuum or air. The temperature is set to $T = 40$ K. The gradient components were set to 0.4, -0.4 and 0.4. The thermodynamic potential parameters are the same Table 6.

Different from all of aforementioned simulations, here a set of initial polarization order parameters and octahedra tilt order parameters are used (Figure 55). This set of initial condition **P**, **Q** is the final result from the simulation run in Figure 53 (b). They were generated from free evolution of Table 6.

When $V = +10$ V is applied across $SrTiO_3$, in simulation, the polar domain responds and becomes all $c-(0,0,-1)$ domains quickly. The $V = -10$ V creates $c+(0,0,1)$ domains. The octahedra tilt domains evolve slower in the simulations. For octahedra tilt domains, while majority of the domain morphologies seems to be similar between $V = +10$V and $V = -10$V, which is consistent to Honig et al. [195], there are also some subtle differences. The $V = +10$V has more orange $a2-(0,-1,0)$ domains and $V = -10$V has more $a2+(0,1,0)$ domains.

We also simulated the domain evolution as a function of electric field for the domain morphology obtained from the rectangular charge distribution in Figure 51 (a). The initial state **P**, **Q** for the simulation are Figure 51 (f) and (e), respectively.

Figure 57 is the result of the simulation. We see: (1) the polar domains become all $c+(0,0,1)$ for $V = -10$ V, and all $c-(0,0,-1)$ for $V = 10$ V before 200 steps. (2) Both the octatilt domain $c+(0,0,1)$ and $c-(0,0,-1)$ expand in respond to the applied electric field in the z direction, regardless of the polarity of the electric field. (3) While $V = 10$ V creates more $O5-(0,-1,-1)$ and $O6+(0,1,-1)$ domains, $V = -10$ V creates more $O6-(0,-1,1)$ and $O5+(0,1,1)$ domains.

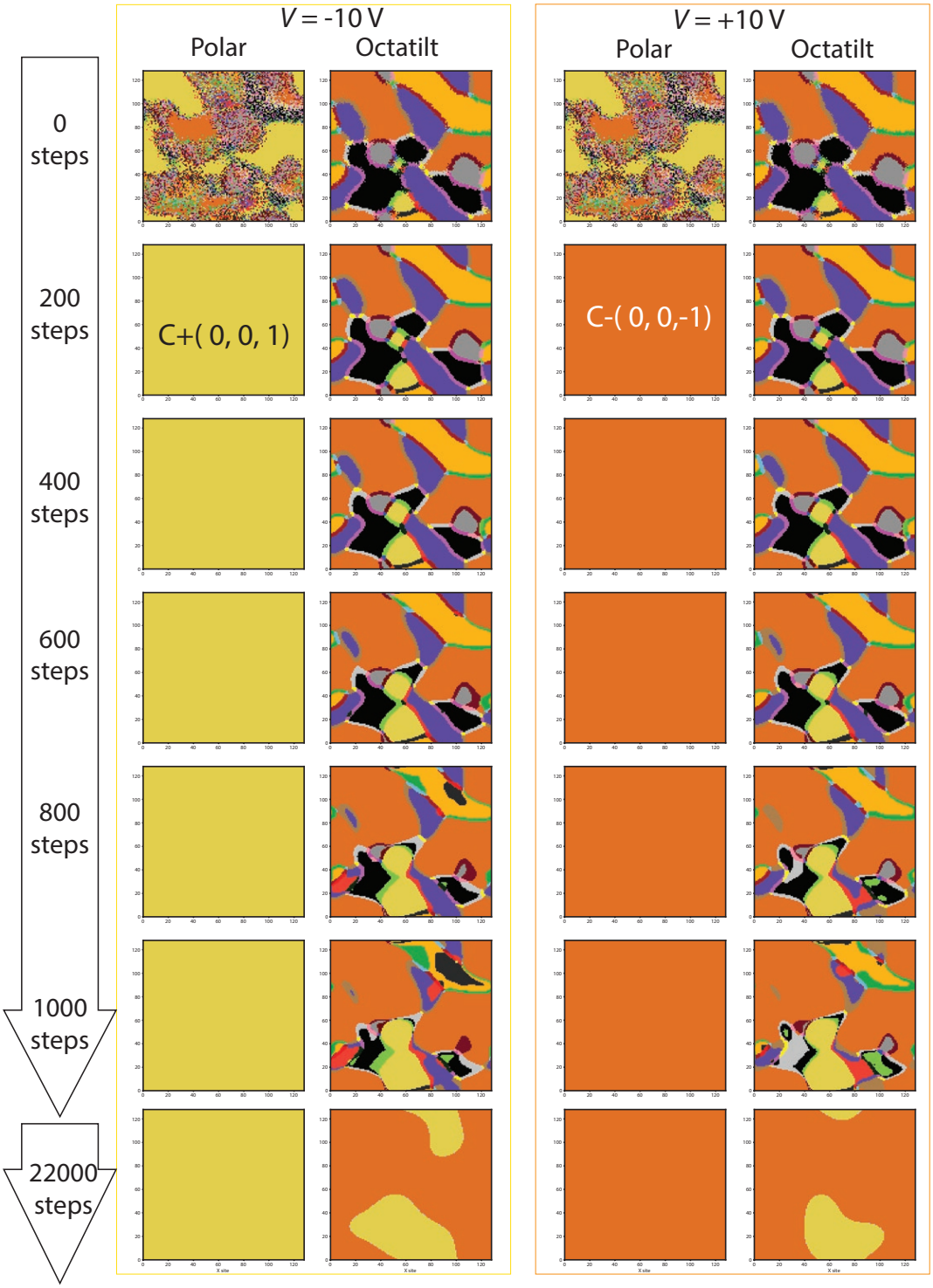

Figure 56: Voltage dependence for initial states from strain free condition

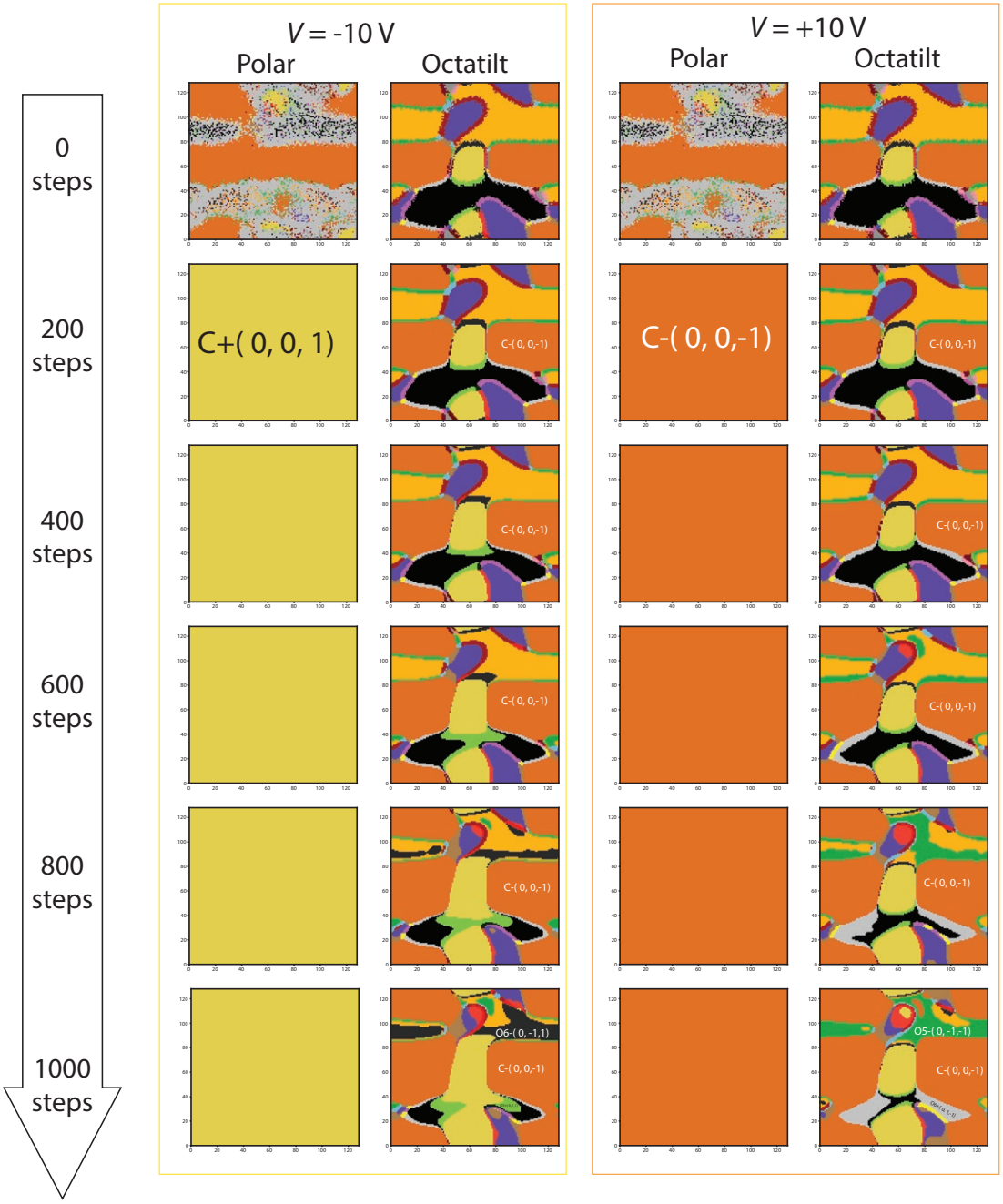

Figure 57: Voltage dependence for domains seeded by a nanowire. The initial **P**, **Q** for the simulation are given by Figure 51 (f) and (e), respectively.

F. Temperature Dependence

Figure 58 is a set of simulations with different temperature from $T = 300$ K to $T = 10$ K. The system size is $128\Delta x \times 128\Delta x \times 36\Delta x$, with the first 12 layers being substrate (unused), 20 layers being the $SrTiO_3$, and the top 4 layer being vacuum or air. The gradient components were set to 0.4, -0.4 and 0.4. The thermodynamic potential parameters are the same Table 6. The charge distribution is Figure 51 (a).

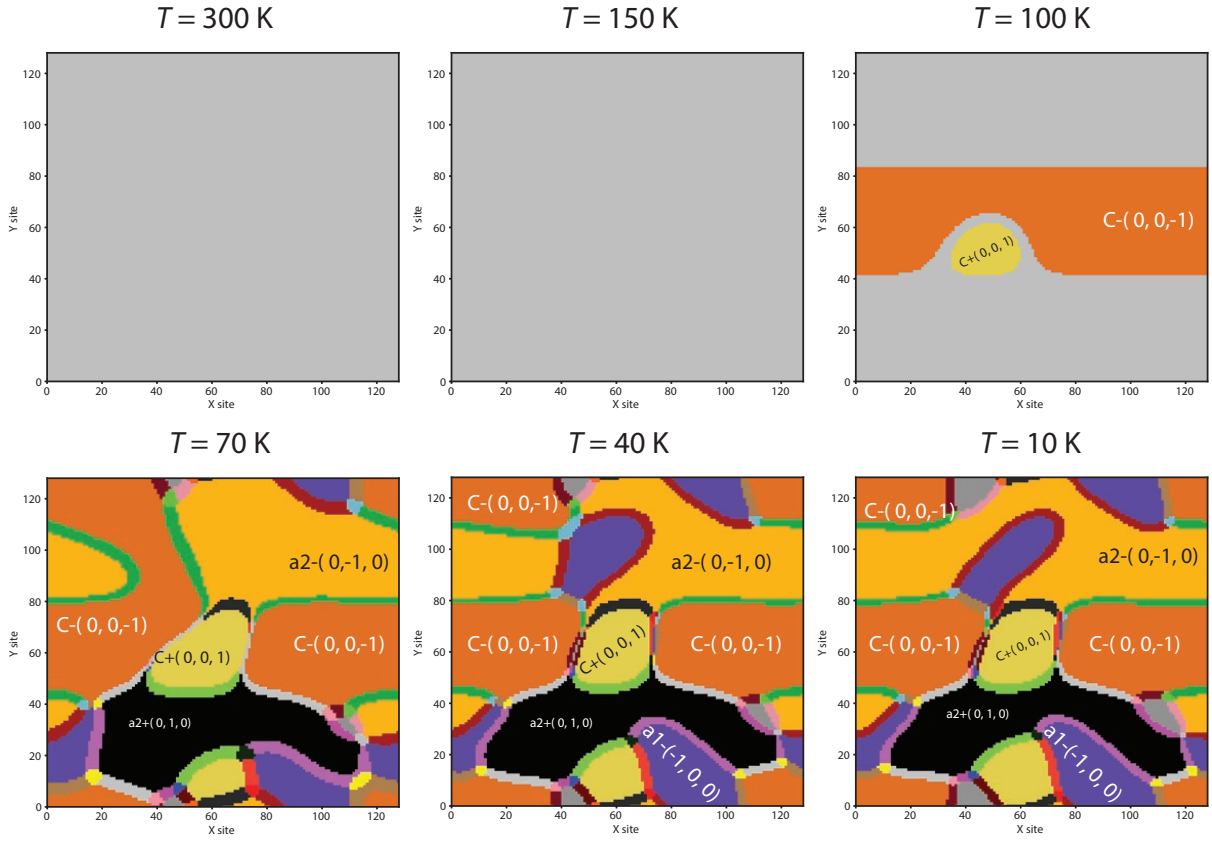

Figure 58: Temperature dependence for domains seeded by a nanowire

We see that the when $T < T_{AFD} = 105$ K, z-oriented octahedra tilt domains $c+(0,0,1)$, $c-(0,0,-1)$ are formed preferentially.

G. Seeding Dependence

Figure 59 is a set of simulations with different charge distribution: (a) $39\Delta x \times 39\Delta x \times 15\Delta x$, (b) $39\Delta x \times 39\Delta x \times 11\Delta x$ (c) $128\Delta x \times 42\Delta x \times 11\Delta x$, (d) zigzag with thickness $15\Delta x$. The system size is $128\Delta x \times 128\Delta x \times 36\Delta x$, with the first 12 layers being substrate (unused), 20 layers being the $SrTiO_3$, and the top 4 layer being vacuum or air. The gradient components were set to 0.4, -0.4 and 0.4. The thermodynamic potential parameters are the same Table 6. The temperature is $T = 40$ K.

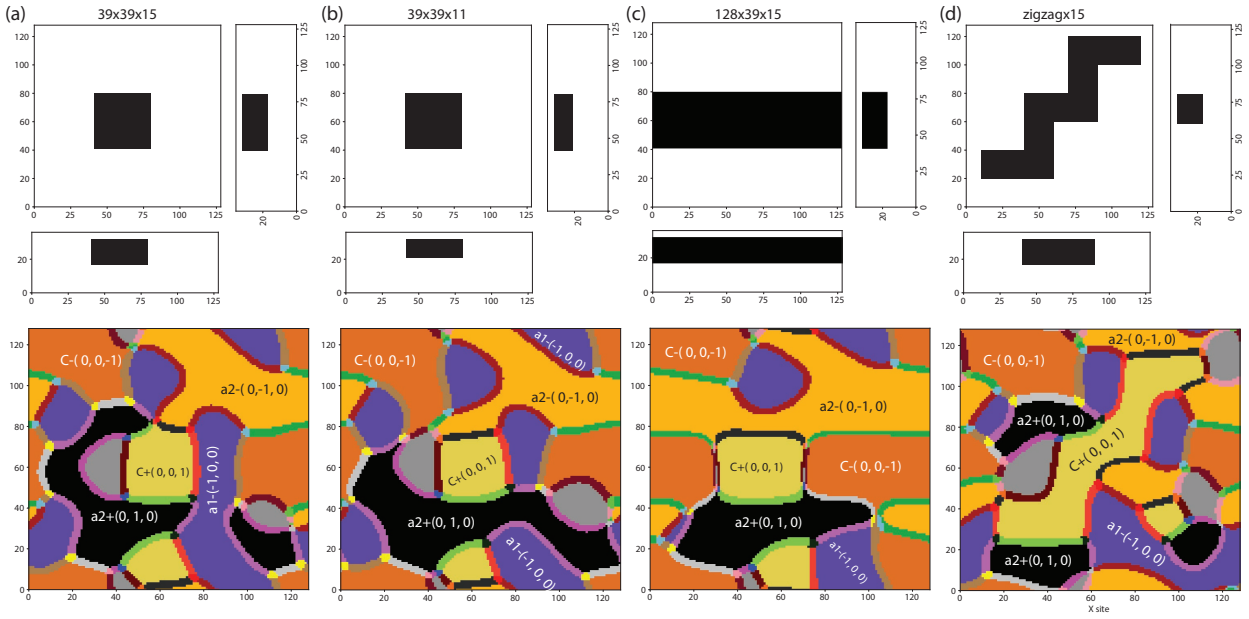

Figure 59: Seeding dependence. (a) Top: A $39\Delta x \times 39\Delta x \times 15\Delta x$ charge distribution. $z = 31$ slice, $x = 64$ slice and $y = 64$ slice. Bottom: resulting octahedra tilt domains. (b) Top: $39\Delta x \times 39\Delta x \times 11\Delta x$ charge distribution. Bottom: resulting octahedra tilt domains. (c) Top: $128\Delta x \times 42\Delta x \times 11\Delta x$ charge distribution. Bottom: resulting octahedra tilt domains. (d) Top: zigzag with thickness $15\Delta x$ charge distribution. Bottom: resulting octahedra tilt domains.

We see that for the seeded region, z-oriented octahedra tilt domains $c + (0, 0, 1)$, $c - (0, 0, -1)$ are formed preferentially. The seeding is not as effective as the thickness of the charge distribution is reduced or the lateral size of the charge distribution decreases (not

shown), and a rectangular charge distribution seeds the z-oriented octahedra tilt domains successfully more easily. One possible explanation is that with the periodic boundary conditions (in x and y) are used, the domain wall energy for domain morphology seeded by the rectangular charge distribution maybe less than those seeded by square or a zigzag charge distribution.

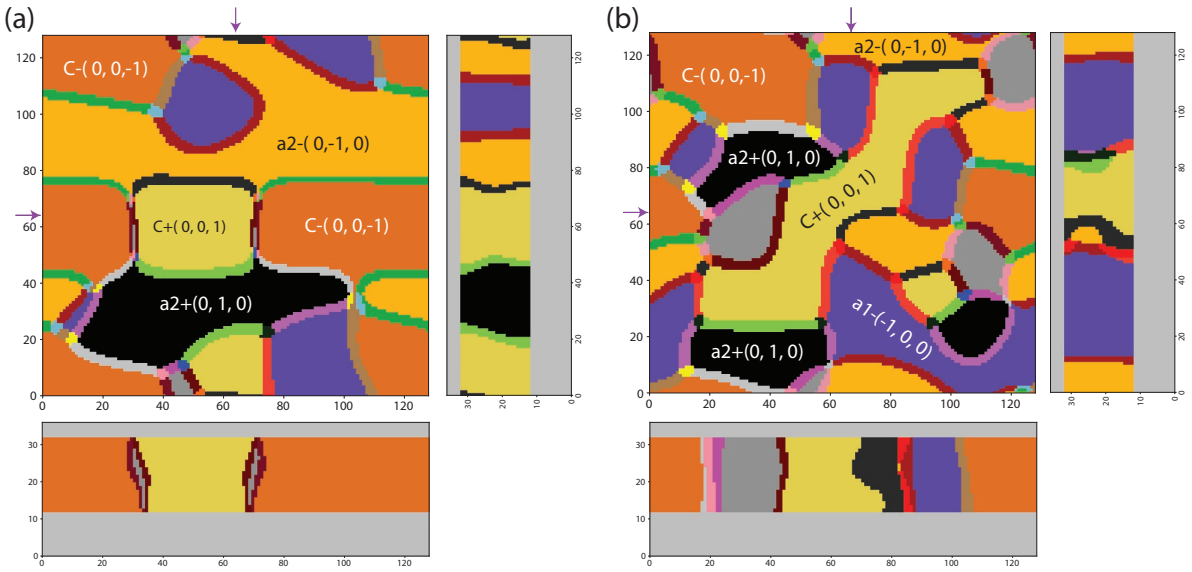

Figure 60: Cross section for charge seeded domains of Figure 59. The right and bottom inset are $x = 64$ slice and $y = 64$ slice.

It is worth noting that for a zigzag distribution, a continuous $c+(0, 0, 1)$ domain occupies the zigzag, whereas $c + (0, 0, 1)$ and $c - (0, 0, -1)$ and domain walls are inside of a straight nanowire. For a domain wall such that the axes of rotation across the wall lie in the wall, the oxygen octahedra on the two sides of the wall are in phase with each other. This configuration is the type-II domain wall discussed in Xue et al. [440]. Because the displacements of an oxygen atom that is shared by the two octahedra on the both side are opposite to each other, the domain walls of this kind are expected to be higher energy.

While this may be too early to draw any conclusion at this stage, but having no addtional domain wall inside of a zigzag channel may be a possible reason for lower resistance in a zigzag nanowire as well as lower residual resistance in the superconducting state for a zigzag

nanowire compared to those in a straight nanowire, as reported in Chapter IV.

VI. Conclusions and Outlook

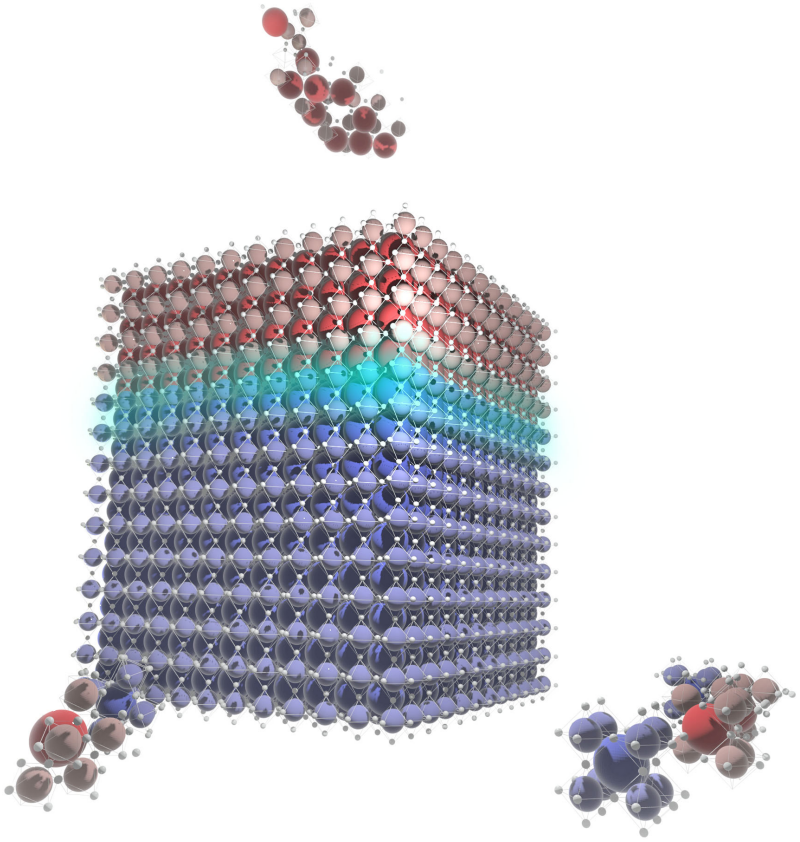

Figure 61: $LaAlO_3/SrTiO_3$

In this thesis, I have summarized our work on mesoscaled superconducting devices created at $LaAlO_3/SrTiO_3$, more specifically, 1D superconducting nanowires and 1D zigzag nanowires. Our work on phase-field modeling $SrTiO_3$ is also included. The relevant experimental techniques as well as the current status of the field are also summarized.

There are many future follow up works to be done: (1) continuation on local probe characterization of mesoscale devices created at $LaAlO_3/SrTiO_3$, with scanning probe and/or scanning optical probe. (2) Phase-field modeling can continue to be employed for describing the interaction between charge, polar, octahedra tilt, defect.

More broadly speaking, there are many direction for the research on $SrTiO_3$ to go.

Just as we listed in [1], fields outside of $SrTiO_3$ such as spintronics, 1D physics, Majorana zero modes, etc, to name but a few, may be benefited from understanding $SrTiO_3$. On the underhand, for $SrTiO_3$ itself, $SrTiO_3$ has been studied for a long time. Because of its intrinsic complexity with multitude of coupled degree of freedoms, fully understand this material is proven to be difficult. Thanks to the renewed interests and advances in experimental and computational techniques. Many new findings have been reported from Long-sought phases such as preformed pairs were reported. Not only many *established* of the understandings on this material deserves to be revisited with refined tools in our hands, more sophisticated devices that now we are able to create with this material system could also be used to reveal the physics we are trying to understand or the physics yet to be found.

Appendix A. Maintenance Done for Leiden CF900

- changed the leads of the magnet
- wrote magnet software verion 1 and Euler sweeper
- precooled circuit leak
- sorption pumps regeneration
- compressor membrane replacement
- replaced tip-seal pump with IGX claw pump
- replaced scrolled module cables of helium compressor
- broke scroll module
- replaced flexlines of compressor twice
- added 3rd cold trap
- replaced EPROM twice
- removed the chatter valve in helium compressor
- recharged ^{3}He.
- replaced plunger in the valve block
- replaced fiber glass rods of the probe
- clamp reinforcement
- replaces fans in the magnet power supply
- cooling power tests
- single shot tests
- valve before aux trap leaks
- database integration

Appendix B. Some Details for Phase Field Simulation of $SrTiO_3$

Figure 62 is the distribution of final **P**, **Q** of a set of simulations plotted against p_0. p_0 ranged from 0.01 to 0.1, with q_0 at 1×10^{-12}). (Note: some of the other thermodynamic parameters are not kept the same but they are not the major source of the difference showed in this set of distribution.)

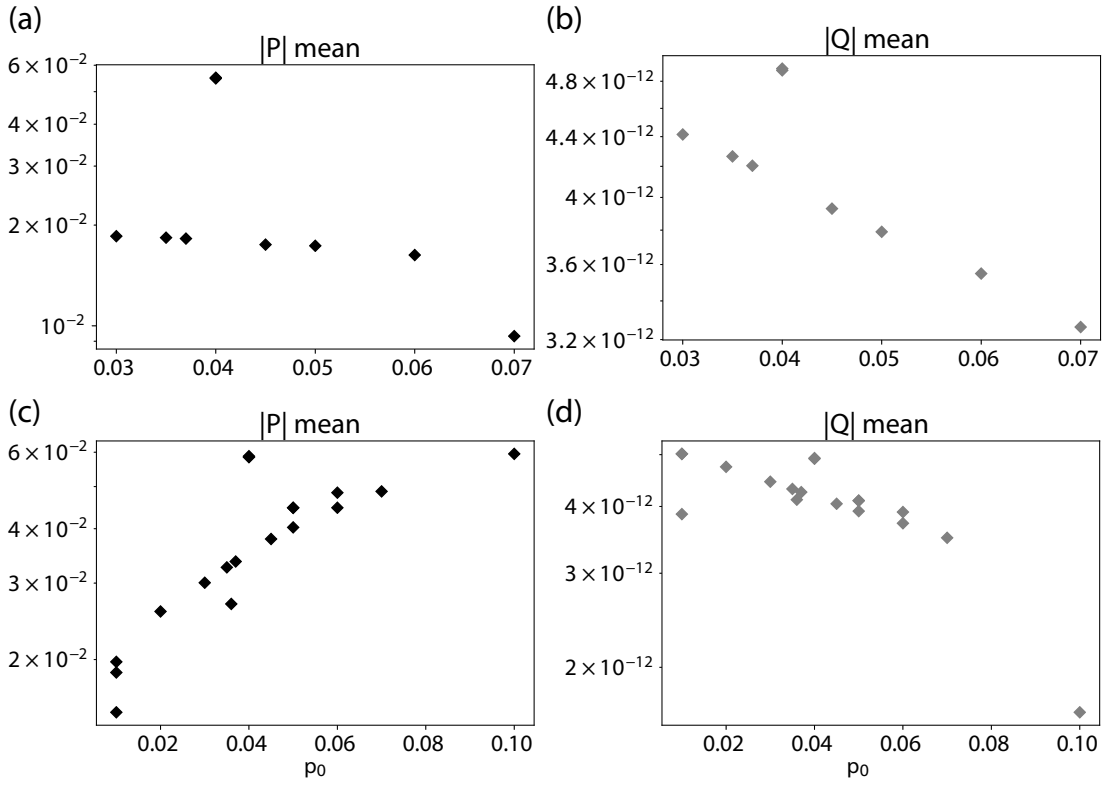

Figure 62: Distribution of resulting **P**, **Q** as a function of the p_0. q_0 is kept at 1×10^{-12}. (a) and (b) from simulations without charge distribution, while (c) and (d) are from those with charge distribution in Figure 51 (a).

Table 3: Rhombohedral distortions

Distortion type	Name	Distortion Vector
Rhombohedral	R1+	(1, 1, 1)
Rhombohedral	R1-	(-1, -1, -1)
Rhombohedral	R2+	(-1, 1, 1)
Rhombohedral	R2-	(1, -1, -1)
Rhombohedral	R3+	(-1, -1, 1)
Rhombohedral	R3-	(1, 1, -1)
Rhombohedral	R4+	(1, -1, 1)
Rhombohedral	R4-	(-1, 1, -1)

Table 4: Orthorhombic distortions

Distortion type	Name	Distortion Vector
Orthorhombic	O1+	(1, 1, 0)
Orthorhombic	O1-	(-1, -1, 0)
Orthorhombic	O2+	(1, -1, 0)
Orthorhombic	O2-	(-1, 1, 0)
Orthorhombic	O3+	(1, 0, 1)
Orthorhombic	O3-	(-1, 0, -1)
Orthorhombic	O4+	(1, 0, -1)
Orthorhombic	O4-	(-1, 0, 1)
Orthorhombic	O5+	(0, 1, 1)
Orthorhombic	O5-	(0, -1, -1)
Orthorhombic	O6+	(0, 1, -1)
Orthorhombic	O6-	(0, -1, 1)

Table 5: Tetragonal distortions

Distortion type	Name	Distortion Vector
Tetragonal, X	a1+	(1, 0, 0)
Tetragonal, X	a1-	(-1, 0, 0)
Tetragonal, Y	a2+	(0, 1, 0)
Tetragonal, Y	a2-	(0, -1, 0)
Tetragonal, Z	c+	(0, 0, 1)
Tetragonal, Z	c-	(0, 0, -1)

Table 6: Thermodynamic potential parameters pot.in no. 20

Parameter	Value	Unit (SI)
α_1	$4.06 \times 10^7(1/tanh(54/T) - 1/tanh(54/30))$	$C^{-2}m^2N$
α_{11}	1.701×10^9	$C^{-4}m^6N$
α_{12}	4.44×10^9	$C^{-4}m^6N$
Q_{11}	0.04581	$C^{-2}m^4$
Q_{12}	-0.0135	$C^{-2}m^4$
Q_{44}	0.0096	$C^{-2}m^4$
C_{11}	3.36×10^{11}	$m^{-2}N$
C_{12}	1.07×10^{11}	$m^{-2}N$
C_{44}	1.27×10^{11}	$m^{-2}N$
β_1	$1.32 \times 10^{29}(1/tanh(145/T) - 1/tanh(145/105))$	$m^{-2}m^{-2}N$
β_{11}	0.96×10^{50}	$m^{-4}m^{-2}N$
β_{12}	3.96×10^{50}	$m^{-4}m^{-2}N$
L_{11}	11.3×10^{18}	m^{-2}
L_{12}	-7.8×10^{18}	m^{-2}
L_{44}	-9.88×10^{18}	m^{-2}
t_{11}	-5.94×10^{29}	$C^{-2}N$
t_{12}	-7.55×10^{28}	$C^{-2}N$
t_{44}	5.86×10^{29}	$C^{-2}N$
p_0	0.04	$\mathrm{C/m^2}$
q_0	1.0×10^{-12}	m

Appendix C. Scripts in Python

I include one of the example utility scripts that I used for 3D visualizing the domain morphology here. For other repositories and utilities, I stored at my GitHub: https://github.com/yypai.

```
from yyp_helper import *
from cxx import *
import plotly.express as px
import plotly.graph_objects as go
from plotly.subplots import make_subplots
from tkinter import Tk
from tkinter.filedialog import askopenfilename

'''
Utility 1: plot the 3d scaler value
pfDat_to_df (path_of_tsv_file) -> dataframe
with columns x, y, z, n for scalar data or
x, y, z, gx, gy, gz, lx, ly, lz for vector field
max display number set to some 20000 prevent crash.
'''

# max number of data points to be plotted;
# 20000 seems work okay on my 2012 old mac.
max_display_number = 20000

dfQ = pfDat_to_df(filename)
fig = go.Figure(data=[go.Scatter3d(
    x=dfQ.x[::dfQ.shape[0]//max_display_number],
    y=dfQ.y[::dfQ.shape[0]//max_display_number],
    z=dfQ.z[::dfQ.shape[0]//max_display_number],
    mode='markers',
    marker=dict(
        size=1,
        color=dfQ.n[::dfQ.shape[0]//max_display_number],
        opacity=0.6,
    )
)])

fig.update_layout(scene_aspectmode='manual',
                  scene_aspectratio=dict(x=1, y=1, z=0.1))
fig.update_layout(margin=dict(l=0, r=0, b=0, t=0))
fig.update_layout(template="none")
fig.show()
```

```
39
40
41  '''
42  Utility 2: plot the 3d domain
43  readDatFerroDomain (path_of_tsv_file, threshold, 180 deg) ->
44  3D numpy array of domain index
45  dfo_pd = dat_to_df(df[:, :, 11:25], list('xyz')) makes the 3D
46  numpy into dataframe with column name A
47  dfo_pd['A'].apply(lambda x: toDomain(x)) maps the domain index
48  to string such as a1+ (1, 0, 0) etc
49  '''
50
51
52  max_display_number = 20000
53
54  df = readDatFerroDomain(filename, 1e-12, 180)
55  dfo_pd = dat_to_df(df[:, :, 11:25], list('xyz'))
56  domain3D = dfo_pd['A'].apply(lambda x: toDomain(x))
57
58
59  fig = go.Figure(data=[go.Scatter3d(
60      x=dfo_pd.x[::dfo_pd.shape[0]//max_display_number],
61      y=dfo_pd.y[::dfo_pd.shape[0]//max_display_number],
62      z=dfo_pd.z[::dfo_pd.shape[0]//max_display_number],
63      mode='markers',
64      hovertext=domain3D[::domain3D.shape[0]//max_display_number],
65      marker=dict(
66          size=2,
67          color=dfo_pd.A[::dfo_pd.shape[0]//max_display_number],
68          colorscale=paiColor,   # choose a colorscale
69          opacity=0.6,
70      )
71  )])
72
73  fig.update_layout(scene_aspectmode='manual',
74                    scene_aspectratio=dict(x=1, y=1, z=0.1))
75
76  fig.update_layout(margin=dict(l=0, r=0, b=0, t=0))
77  fig.update_layout(template="none")
78  fig.show()
79
80  '''
81  Utility 3: plot the 3d vector field
82  pfDat_to_df (path_of_tsv_file) -> dataframe
83  with columns x, y, z, n for scalar data
84  or x, y, z, gx, gy, gz, lx, ly, lz for vector field
85  max display number set to some 20000 prevent crash.
```

```
'''

df = pfDat_to_df(filename)

max_value = df.iloc[:, 3:].max().max()
max_display_number = 10000
scale = 1/max_value

fig = go.Figure(data = go.Cone(
    x=df.x[::dfo_pd.shape[0]//max_display_number],
    y=df.y[::dfo_pd.shape[0]//max_display_number],
    z=df.z[::dfo_pd.shape[0]//max_display_number],
    u=df.gx[::dfo_pd.shape[0]//max_display_number]*scale,
    v=df.gy[::dfo_pd.shape[0]//max_display_number]*scale,
    w=df.gz[::dfo_pd.shape[0]//max_display_number]*scale,
    colorscale='icefire',
    sizemode="absolute",
    sizeref=0.5))

fig.update_layout(scene=dict(aspectratio=dict(x=1, y=1, z=0.8),
                  camera_eye=dict(x=1.2, y=1.2, z=0.6)))
fig.update_layout(template="none")
fig.show()
```

Bibliography

[1] Yun-Yi Pai, Anthony Tylan-Tyler, Patrick Irvin, and Jeremy Levy. Physics of $SrTiO_3$-based heterostructures and nanostructures: a review. *Reports on Progress in Physics*, 81:036503, 2018.

[2] Yun-Yi Pai, Anthony Tylan-Tyler, Patrick Irvin, and Jeremy Levy. *$LaAlO_3/SrTiO_3$: a tale of two magnetisms*, volume 2, book section 12. CRC Press, 2019.

[3] J. F. Schooley, W. R. Hosler, and Marvin L. Cohen. Superconductivity in semiconducting $SrTiO_3$. *Physical Review Letters*, 12(17):474–475, 1964.

[4] Bao Lee Phoon, Chin Wei Lai, Joon Ching Juan, Pau-Loke Show, and Wei-Hsin Chen. A review of synthesis and morphology of $SrTiO_3$ for energy and other applications. *International Journal of Energy Research*, 0(0), 2019.

[5] Richard J. D. Tilley. *Perovskites : Structure-Property Relationships (1)*. Wiley, Chicester, GB, 2016.

[6] V. M. Goldschmidt. Die gesetze der krystallochemie. *Naturwissenschaften*, 14(21):477–485, 1926.

[7] Myung-Hwan Whangbo, Elijah E. Gordon, Jerry L. Bettis, Annette Bussmann-Holder, and Jrgen Khler. Tolerance factor and cationanion orbital interactions differentiating the polar and antiferrodistortive structures of perovskite oxides abo3. *Zeitschrift fr anorganische und allgemeine Chemie*, 641(6):1043–1052, 2015.

[8] J. Hutton and R. J. Nelmes. High-resolution studies of cubic perovskites by elastic neutron diffraction. ii. $SrTiO_3$, $KMnF_3$, $RbCaF_3$ and $CsPbCl_3$. *Journal of Physics C: Solid State Physics*, 14(12):1713, 1981.

[9] R. D. Shannon and C. T. Prewitt. Effective ionic radii in oxides and fluorides. *Acta Crystallographica Section B*, 25(5):925–946, 1969.

[10] A.P. Jones, F. Wall, and C.T. Williams. *Rare Earth Minerals: Chemistry, Origin and Ore Deposits*. Springer Netherlands, 1995.

[11] Ulrich Aschauer and Nicola A. Spaldin. Competition and cooperation between antiferrodistortive and ferroelectric instabilities in the model perovskite $SrTiO_3$. *Journal of Physics: Condensed Matter*, 26(12):122203, 2014.

[12] B. S. de Lima, M. S. da Luz, F. S. Oliveira, L. M. S. Alves, C. A. M. dos Santos, F. Jomard, Y. Sidis, P. Bourges, S. Harms, C. P. Grams, J. Hemberger, X. Lin,

B. Fauqu, and K. Behnia. Interplay between antiferrodistortive, ferroelectric, and superconducting instabilities in $Sr_{1-x}Ca_xTiO_{3-\delta}$. *Physical Review B*, 91(4):045108, 2015.

[13] L. Rimai and G. A. deMars. Electron paramagnetic resonance of trivalent gadolinium ions in strontium and barium titanates. *Physical Review*, 127(3):702–710, 1962.

[14] Farrel W. Lytle. X–ray diffractometry of lowtemperature phase transformations in strontium titanate. *Journal of Applied Physics*, 35(7):2212–2215, 1964.

[15] P. A. Fleury, J. F. Scott, and J. M. Worlock. Soft phonon modes and the 110°k phase transition in srtio$_3$. *Phys. Rev. Lett.*, 21:16–19, Jul 1968.

[16] K. A. Mller, W. Berlinger, and F. Waldner. Characteristic structural phase transition in perovskite-type compounds. *Physical Review Letters*, 21(12):814–817, 1968.

[17] G. Shirane and Y. Yamada. Lattice-dynamical study of the 110°k phase transition in srtio$_3$. *Phys. Rev.*, 177:858–863, Jan 1969.

[18] A. Buckley, J. P. Rivera, and E. K. H. Salje. Twin structures in tetragonal $SrTiO_3$: The ferroelastic phase transition and the formation of needle domains. *Journal of Applied Physics*, 86(3):1653–1656, 1999.

[19] A. Glazer. The classification of tilted octahedra in perovskites. *Acta Crystallographica Section B*, 28(11):3384–3392, 1972.

[20] Bin Okai and Jiichiro Yoshimoto. Pressure dependence of the structural phase transition temperature in $SrTiO_3$ and kmnf3. *Journal of the Physical Society of Japan*, 39(1):162–165, 1975.

[21] B. Bonello, M. Fischer, and A. Zarembowitch. Acoustical measurements in solids under very high pressure. *Ultrasonics*, 27(6):343–348, 1989.

[22] A. Hachemi, H. Hachemi, A. Ferhat-Hamida, and L. Louail. Elasticity of $SrTiO_3$ perovskite under high pressure in cubic, tetragonal and orthorhombic phases. *Physica Scripta*, 82(2):025602, 2010.

[23] Andrzej Grzechnik, George H. Wolf, and Paul F. McMillan. Raman scattering study of $SrTiO_3$ at high pressure. *Journal of Raman Spectroscopy*, 28(11):885–889, 1997.

[24] D. Cabaret, B. Couzinet, A.M. Flank, J.P. Iti, P. Lagarde, and A. Polian. Ti k preedge in $SrTiO_3$ under pressure: Experiments and fullpotential firstprinciples calculations. *AIP Conference Proceedings*, 882(1):120–122, 2007.

[25] Mael Guennou, Pierre Bouvier, Jens Kreisel, and Denis Machon. Pressure-temperature phase diagram of $SrTiO_3$ up to 53 gpa. *Physical Review B*, 81(5):054115, 2010.

[26] H. Hnnefeld, T. Niemller, J. R. Schneider, U. Rtt, S. Rodewald, J. Fleig, and G. Shirane. Influence of defects on the critical behavior at the 105 k structural phase transition of $SrTiO_3$: On the origin of the two length scale critical fluctuations. *Physical Review B*, 66(1):014113, 2002.

[27] R. A. Cowley. Lattice dynamics and phase transitions of strontium titanate. *Physical Review*, 134(4A):A981–A997, 1964.

[28] K. A. Muller and H. Burkard. $SrTiO_3$ - intrinsic quantum paraelectric below 4 k. *Physical Review B*, 19(7):3593–3602, 1979.

[29] W. Cochran. Crystal stability and the theory of ferroelectricity. *Physical Review Letters*, 3(9):412–414, 1959.

[30] D. Buerle, D. Wagner, M. Whlecke, B. Dorner, and H. Kraxenberger. Soft modes in semiconducting $SrTiO_3$: Ii. the ferroelectric mode. *Zeitschrift fr Physik B Condensed Matter*, 38(4):335–339, 1980.

[31] N. Bickel, G. Schmidt, K. Heinz, and K. Mller. Ferroelectric relaxation of the $SrTiO_3$ (100) surface. *Physical Review Letters*, 62(17):2009–2011, 1989.

[32] V. Ravikumar, D. Wolf, and V. P. Dravid. Ferroelectric-monolayer reconstruction of the $SrTiO_3$ (100) surface. *Physical Review Letters*, 74(6):960–963, 1995.

[33] Anspoks Andris, Timoshenko Janis, Purans Juris, Rocca Francesco, Trepakov Vladimir, Dejneka Alexander, and Itoh Mitsuru. Local dynamics and phase transition in quantum paraelectric $SrTiO_3$ studied by Ti K-edge X-ray absorption spectroscopy. *Journal of Physics: Conference Series*, 712(1):012101, 2016.

[34] A. Bussmann-Holder and A. R. Bishop. Incomplete ferroelectricity in $SrTi_{18}O_3$. *The European Physical Journal B - Condensed Matter and Complex Systems*, 53(3):279–282, 2006.

[35] O. Tikhomirov, H. Jiang, and J. Levy. Local ferroelectricity in $SrTiO_3$ thin films. *Physical Review Letters*, 89(14):147601, 2002.

[36] J. H. Haeni, P. Irvin, W. Chang, R. Uecker, P. Reiche, Y. L. Li, S. Choudhury, W. Tian, M. E. Hawley, B. Craigo, A. K. Tagantsev, X. Q. Pan, S. K. Streiffer, L. Q. Chen, S. W. Kirchoefer, J. Levy, and D. G. Schlom. Room-temperature ferroelectricity in strained $SrTiO_3$. *Nature*, 430(7001):758–761, 2004.

[37] H. W. Jang, A. Kumar, S. Denev, M. D. Biegalski, P. Maksymovych, C. W. Bark, C. T. Nelson, C. M. Folkman, S. H. Baek, N. Balke, C. M. Brooks, D. A. Tenne, D. G. Schlom, L. Q. Chen, X. Q. Pan, S. V. Kalinin, V. Gopalan, and C. B. Eom. Ferroelectricity in strain-free $SrTiO_3$ thin films. *Physical Review Letters*, 104(19):197601, 2010.

[38] M. D. Biegalski, Y. Jia, D. G. Schlom, S. Trolier-McKinstry, S. K. Streiffer, V. Sherman, R. Uecker, and P. Reiche. Relaxor ferroelectricity in strained epitaxial $SrTiO_3$ thin films on $DyScO_3$ substrates. *Applied Physics Letters*, 88(19):192907, 2006.

[39] P. Zubko, G. Catalan, A. Buckley, P. R. L. Welche, and J. F. Scott. Strain-gradient-induced polarization in $SrTiO_3$ single crystals. *Physical Review Letters*, 99(16):167601, 2007.

[40] J. Hemberger, P. Lunkenheimer, R. Viana, R. Bohmer, and A. Loidl. Electric-field-dependent dielectric-constant and nonlinear susceptibility in $SrTiO_3$. *Physical Review B*, 52(18):13159–13162, 1995.

[41] R. C. Neville, B. Hoeneisen, and C. A. Mead. Permittivity of strontium titanate. *Journal of Applied Physics*, 43(5):2124–2131, 1972.

[42] P. A. Fleury and J. M. Worlock. Electric-field-induced raman scattering in $SrTiO_3$ and ktao3. *Physical Review*, 174(2):613–623, 1968.

[43] P. A. Fleury and J. M. Worlock. Electric-field-induced raman effect in paraelectric crystals. *Physical Review Letters*, 18(16):665–667, 1967.

[44] Hiromoto Uwe and Tunetaro Sakudo. Stress-induced ferroelectricity and soft phonon modes in $SrTiO_3$. *Physical Review B*, 13(1):271–271, 1976.

[45] W. J. Burke and R. J. Pressley. Stress induced ferroelectricity in $SrTiO_3$. *Solid State Communications*, 9(3):191–195, 1971.

[46] Darrell G. Schlom, Long-Qing Chen, Chang-Beom Eom, Karin M. Rabe, Stephen K. Streiffer, and Jean-Marc Triscone. Strain tuning of ferroelectric thin films. *Annual Review of Materials Research*, 37(1):589–626, 2007.

[47] M. P. Warusawithana, C. Cen, C. R. Sleasman, J. C. Woicik, Y. L. Li, L. F. Kourkoutis, J. A. Klug, H. Li, P. Ryan, L. P. Wang, M. Bedzyk, D. A. Muller, L. Q. Chen, J. Levy, and D. G. Schlom. A ferroelectric oxide made directly on silicon. *Science*, 324(5925):367–370, 2009.

[48] T. Mitsui and W. B. Westphal. Dielectric and X–ray studies of $Ca_xBa_{1-x}TiO_3$ and $Ca_xSr_{1-x}TiO_3$. *Physical Review*, 124(5):1354–1359, 1961.

[49] J. G. Bednorz and K. A. Mller. $Sr_{1-x}Ca_xTiO_3$: An XY quantum ferroelectric with transition to randomness. *Physical Review Letters*, 52(25):2289–2292, 1984.

[50] V. V. Lemanov, E. P. Smirnova, and E. A. Tarakanov. Ferroelectric properties of $srtio_3$-$pbtio_3$ solid solutions. *Physics of the Solid State*, 39(4):628–631, Apr 1997.

[51] V. V. Lemanov, E. P. Smirnova, P. P. Syrnikov, and E. A. Tarakanov. Phase transitions and glasslike behavior in $sr_{1-x}ba_xtio_3$. *Phys. Rev. B*, 54:3151–3157, Aug 1996.

[52] M. Itoh, R. Wang, Y. Inaguma, T. Yamaguchi, Y. J. Shan, and T. Nakamura. Ferroelectricity induced by oxygen isotope exchange in strontium titanate perovskite. *Physical Review Letters*, 82(17):3540–3543, 1999.

[53] Ruiping Wang and Mitsuru Itoh. Suppression of the quantum fluctuation in ^{18}O-enriched strontium titanate. *Physical Review B*, 64(17):174104, 2001.

[54] A. Stucky, G. W. Scheerer, Z. Ren, D. Jaccard, J. M. Poumirol, C. Barreteau, E. Giannini, and D. van der Marel. Isotope effect in superconducting n-doped $SrTiO_3$. *Scientific Reports*, 6:37582, 2016.

[55] Y. S. Kim, J. Kim, S. J. Moon, W. S. Choi, Y. J. Chang, J. G. Yoon, J. Yu, J. S. Chung, and T. W. Noh. Localized electronic states induced by defects and possible origin of ferroelectricity in strontium titanate thin films. *Applied Physics Letters*, 94(20):202906, 2009.

[56] Fang Yang, Qinghua Zhang, Zhenzhong Yang, Junxing Gu, Yan Liang, Wentao Li, Weihua Wang, Kuijuan Jin, Lin Gu, and Jiandong Guo. Room-temperature ferroelectricity of $SrTiO_3$ films modulated by cation concentration. *Applied Physics Letters*, 107(8):082904, 2015.

[57] Konstantin Klyukin and Vitaly Alexandrov. Effect of intrinsic point defects on ferroelectric polarization behavior of $SrTiO_3$. *Physical Review B*, 95(3):035301, 2017.

[58] Y. S. Kim, D. J. Kim, T. H. Kim, T. W. Noh, J. S. Choi, B. H. Park, and J.-G. Yoon. Observation of room-temperature ferroelectricity in tetragonal strontium titanate thin films on $SrTiO_3$ (001) substrates. *Applied Physics Letters*, 91(4):042908, 2007.

[59] Sang A. Lee, Hoidong Jeong, Sungmin Woo, Jae-Yeol Hwang, Si-Young Choi, Sung-Dae Kim, Minseok Choi, Seulki Roh, Hosung Yu, Jungseek Hwang, Sung Wng Kim, and Woo Seok Choi. Phase transitions via selective elemental vacancy engineering in complex oxide thin films. *Scientific Reports*, 6:23649, 2016.

[60] Gerald Lucovsky. *Long Range Cooperative and Local Jahn-Teller Effects in Nanocrystalline Transition Metal Thin Films*, pages 767–808. Springer Berlin Heidelberg, Berlin, Heidelberg, 2009.

[61] Koun Shirai and Kazunori Yamanaka. Mechanism behind the high thermoelectric power factor of $SrTiO_3$ by calculating the transport coefficients. *Journal of Applied Physics*, 113(5):053705, 2013.

[62] C. S. Koonce, Marvin L. Cohen, J. F. Schooley, W. R. Hosler, and E. R. Pfeiffer. Superconducting transition temperatures of semiconducting $SrTiO_3$. *Physical Review*, 163(2):380–390, 1967.

[63] K. van Benthem, C. Elssser, and R. H. French. Bulk electronic structure of $SrTiO_3$: Experiment and theory. *Journal of Applied Physics*, 90(12):6156–6164, 2001.

[64] S. Piskunov, E. Heifets, R. I. Eglitis, and G. Borstel. Bulk properties and electronic structure of $SrTiO_3$, $BaTiO_3$, $PbTiO_3$ perovskites: an ab initio HF/DFT study. *Computational Materials Science*, 29(2):165–178, 2004.

[65] E. Heifets, E. Kotomin, and V. A. Trepakov. Calculations for antiferrodistortive phase of $SrTiO_3$ perovskite: hybrid density functional study. *Journal of Physics: Condensed Matter*, 18(20):4845, 2006.

[66] Young Jun Chang, Guru Khalsa, Luca Moreschini, Andrew L. Walter, Aaron Bostwick, Karsten Horn, A. H. MacDonald, and Eli Rotenberg. Uniaxial strain induced band splitting in semiconducting $SrTiO_3$. *Physical Review B*, 87(11):115212, 2013.

[67] L. Khaber, A. Beniaiche, and A. Hachemi. Electronic and optical properties of $SrTiO_3$ under pressure effect: Ab initio study. *Solid State Communications*, 189:32–37, 2014.

[68] Hiromoto Uwe, Tunetaro Sakudo, and Hirotaka Yamaguchi. Interband electronic raman scattering in $SrTiO_3$. *Japanese Journal of Applied Physics*, 24(S2):519, 1985.

[69] Hiromoto Uwe, Ryozo Yoshizaki, Tunetaro Sakudo, Akio Izumi, and Takuya Uzumaki. Conduction band structure of $SrTiO_3$. *Japanese Journal of Applied Physics*, 24(S2):335, 1985.

[70] Young Jun Chang, Aaron Bostwick, Yong Su Kim, Karsten Horn, and Eli Rotenberg. Structure and correlation effects in semiconducting $SrTiO_3$. *Physical Review B*, 81(23), 2010.

[71] M. Marques, L. K. Teles, V. Anjos, L. M. R. Scolfaro, J. R. Leite, V. N. Freire, G. A. Farias, and E. F. da Silva. Full-relativistic calculations of the $SrTiO_3$ carrier effective masses and complex dielectric function. *Applied Physics Letters*, 82(18):3074–3076, 2003.

[72] H. P. R. Frederikse, W. R. Hosler, W. R. Thurber, J. Babiskin, and Siebenma.Pg. Shubnikov-de haas effect in $SrTiO_3$. *Physical Review*, 158(3):775, 1967.

[73] L. F. Mattheiss. Energy bands for $KNiF_3$, $SrTiO_3$, $KMoO_3$, and $KTaO_3$. *Physical Review B*, 6(12):4718–4740, 1972.

[74] S. J. Allen, B. Jalan, S. Lee, D. G. Ouellette, G. Khalsa, J. Jaroszynski, S. Stemmer, and A. H. MacDonald. Conduction-band edge and Shubnikov-de Haas effect in low-electron-density $SrTiO_3$. *Physical Review B*, 88(4), 2013.

[75] Xiao Lin, German Bridoux, Adrien Gourgout, Gabriel Seyfarth, Steffen Krmer, Marc Nardone, Benot Fauqu, and Kamran Behnia. Critical doping for the onset of a two-band superconducting ground state in $SrTiO_{3-\delta}$. *Physical Review Letters*, 112(20):207002, 2014.

[76] R. A. Evarestov. *Ternary Oxides*, pages 545–610. Springer Berlin Heidelberg, Berlin,

Heidelberg, 2015.

[77] Matthew S. J. Marshall, Andres E. Becerra-Toledo, Laurence D. Marks, and Martin R. Castell. *Defects on Strontium Titanate*, pages 327–349. Springer International Publishing, Cham, 2015.

[78] Krzysztof Szot, Wolfgang Speier, Gustav Bihlmayer, and Rainer Waser. Switching the electrical resistance of individual dislocations in single-crystalline $SrTiO_3$. *Nature Materials*, 5(4):312–320, 2006.

[79] Florencio Sanchez, Carmen Ocal, and Josep Fontcuberta. Tailored surfaces of perovskite oxide substrates for conducted growth of thin films. *Chemical Society Reviews*, 43(7):2272–2285, 2014.

[80] F. A. Krger and H. J. Vink. *Relations between the Concentrations of Imperfections in Crystalline Solids*, volume Volume 3, pages 307–435. Academic Press, 1956.

[81] Do Duc Cuong, Bora Lee, Kyeong Mi Choi, Hyo-Shin Ahn, Seungwu Han, and Jaichan Lee. Oxygen vacancy clustering and electron localization in oxygen-deficient $SrTiO_3$: LDA+U study. *Physical Review Letters*, 98(11):115503, 2007.

[82] Hanzig Juliane, Zschornak Matthias, Mehner Erik, Hanzig Florian, Mnchgesang Wolfram, Leisegang Tilmann, Stcker Hartmut, and C. Meyer Dirk. The anisotropy of oxygen vacancy migration in $SrTiO_3$. *Journal of Physics: Condensed Matter*, 28(22):225001, 2016.

[83] Y. Li, Y. Lei, B. G. Shen, and J. R. Sun. Visible-light-accelerated oxygen vacancy migration in strontium titanate. *Scientific Reports*, 5:14576, 2015.

[84] K. Szot, W. Speier, R. Carius, U. Zastrow, and W. Beyer. Localized metallic conductivity and self-healing during thermal reduction of $SrTiO_3$. *Physical Review Letters*, 88(7):075508, 2002.

[85] Z. Q. Liu, D. P. Leusink, X. Wang, W. M. Lu, K. Gopinadhan, A. Annadi, Y. L. Zhao, X. H. Huang, S. W. Zeng, Z. Huang, A. Srivastava, S. Dhar, T. Venkatesan, and Ariando. Metal-insulator transition in $SrTiO_{3-x}$ thin films induced by frozen-out carriers. *Physical Review Letters*, 107(14), 2011.

[86] Dario Marrocchelli, Lixin Sun, and Bilge Yildiz. Dislocations in $SrTiO_3$: Easy to reduce but not so fast for oxygen transport. *Journal of the American Chemical Society*, 137(14):4735–4748, 2015.

[87] Liliana Goncalves-Ferreira, Simon A. T. Redfern, Emilio Artacho, Ekhard Salje, and William T. Lee. Trapping of oxygen vacancies in the twin walls of perovskite. *Physical Review B*, 81(2):024109, 2010.

[88] Arvids Stashans and Fernando Vargas. Periodic LUC study of F centers in cubic and

tetragonal $SrTiO_3$. *Materials Letters*, 50(23):145–148, 2001.

[89] Minseok Choi, Fumiyasu Oba, Yu Kumagai, and Isao Tanaka. Anti-ferrodistortive-like oxygen-octahedron rotation induced by the oxygen vacancy in cubic $SrTiO_3$. *Advanced Materials*, 25(1):86–90, 2013.

[90] Chungwei Lin and Alexander A. Demkov. Electron correlation in oxygen vacancy in $SrTiO_3$. *Physical Review Letters*, 111(21):217601, 2013.

[91] Z. Q. Liu, W. M. Lu, X. Wang, Z. Huang, A. Annadi, S. W. Zeng, T. Venkatesan, and Ariando. Magnetic-field induced resistivity minimum with in-plane linear magnetoresistance of the fermi liquid in $SrTiO_3$-x single crystals. *Physical Review B*, 85(15), 2012.

[92] Michaela Altmeyer, Harald O. Jeschke, Oliver Hijano-Cubelos, Cyril Martins, Frank Lechermann, Klaus Koepernik, Andrs F. Santander-Syro, Marcelo J. Rozenberg, Roser Valent, and Marc Gabay. Magnetism, spin texture, and in-gap states: Atomic specialization at the surface of oxygen-deficient $SrTiO_3$. *Physical Review Letters*, 116(15):157203, 2016.

[93] G. Binnig, A. Baratoff, H. E. Hoenig, and J. G. Bednorz. Two-band superconductivity in Nb-doped $SrTiO_3$. *Physical Review Letters*, 45(16):1352–1355, 1980.

[94] Fabian Natterer Hongwoo Baek William G. Cullen Young Kuk Jeonghoon Ha, Guru Khalsa and Joseph A. Stroscio. Direct local measurement of the superconducting energy gap of nb doped $SrTiO_3$. In *APS Meeting Abstracts*, 2016.

[95] Joseph Blanc and David L. Staebler. Electrocoloration in $SrTiO_3$: Vacancy drift and oxidation-reduction of transition metals. *Physical Review B*, 4(10):3548–3557, 1971.

[96] Daisuke Kan, Takahito Terashima, Ryoko Kanda, Atsunobu Masuno, Kazunori Tanaka, Shucheng Chu, Hirofumi Kan, Atsushi Ishizumi, Yoshihiko Kanemitsu, Yuichi Shimakawa, and Mikio Takano. Blue-light emission at room temperature from Ar^+-irradiated $SrTiO_3$. *Nat Mater*, 4(11):816–819, 2005.

[97] Marianne C. Tarun, Farida A. Selim, and Matthew D. McCluskey. Persistent photoconductivity in strontium titanate. *Physical Review Letters*, 111(18):187403, 2013.

[98] F. Bi, D. F. Bogorin, C. Cen, C. W. Bark, J. W. Park, C. B. Eom, and J. Levy. "water-cycle" mechanism for writing and erasing nanostructures at the $LaAlO_3/SrTiO_3$ interface. *Applied Physics Letters*, 97(17):173110, 2010.

[99] Keith A. Brown, Shu He, Daniel J. Eichelsdoerfer, Mengchen Huang, Ishan Levy, Hyungwoo Lee, Sangwoo Ryu, Patrick Irvin, Jose Mendez-Arroyo, Chang-Beom Eom, Chad A. Mirkin, and Jeremy Levy. Giant conductivity switching of $LaAlO_3/SrTiO_3$ heterointerfaces governed by surface protonation. *Nature Communications*, 7:10681, 2016.

[100] Masashi Kawasaki, Kazuhiro Takahashi, Tatsuro Maeda, Ryuta Tsuchiya, Makoto Shinohara, Osamu Ishiyama, Takuzo Yonezawa, Mamoru Yoshimoto, and Hideomi Koinuma. Atomic control of the $SrTiO_3$ crystal surface. *Science*, 266(5190):1540–1542, 1994.

[101] T. Fix, F. Schoofs, Z. Bi, A. Chen, H. Wang, J. L. MacManus-Driscoll, and M. G. Blamire. Influence of $SrTiO_3$ substrate miscut angle on the transport properties of $LaAlO_3/SrTiO_3$ interfaces. *Applied Physics Letters*, 99(2), 2011.

[102] P. Brinks, W. Siemons, J. E. Kleibeuker, G. Koster, G. Rijnders, and M. Huijben. Anisotropic electrical transport properties of a two-dimensional electron gas at $SrTiO_3$-$LaAlO_3$ interfaces. *Applied Physics Letters*, 98(24):242904, 2011.

[103] Yiftach Frenkel, Noam Haham, Yishai Shperber, Christopher Bell, Yanwu Xie, Zhuoyu Chen, Yasuyuki Hikita, Harold Y. Hwang, and Beena Kalisky. Anisotropic transport at the $LaAlO_3/SrTiO_3$ interface explained by microscopic imaging of channel-flow over $SrTiO_3$ domains. *ACS Applied Materials & Interfaces*, 8(19):12514–12519, 2016.

[104] J. Georg Bednorz and K. Alex Muller. Perovskite-type oxides - the new approach to High-T_c superconductivity. *Nobel Lecture*, 1987.

[105] J. F. Schooley, W. R. Hosler, E. Ambler, J. H. Becker, Marvin L. Cohen, and C. S. Koonce. Dependence of the superconducting transition temperature on carrier concentration in semiconducting $SrTiO_3$. *Physical Review Letters*, 14(9):305–307, 1965.

[106] Elbio Dagotto. Correlated electrons in high-temperature superconductors. *Reviews of Modern Physics*, 66(3):763–840, 1994.

[107] Christian Pfleiderer. Superconducting phases of f-electron compounds. *Reviews of Modern Physics*, 81(4):1551–1624, 2009.

[108] G. R. Stewart. Superconductivity in iron compounds. *Reviews of Modern Physics*, 83(4):1589–1652, 2011.

[109] Xiao Lin, Zengwei Zhu, Benot Fauqu, and Kamran Behnia. Fermi surface of the most dilute superconductor. *Physical Review X*, 3(2):021002, 2013.

[110] D. M. Eagles. Comment on two papers claiming records for the lowest carrier concentration at which superconductivity has been observed. *arXiv:1604.05660*, 2016.

[111] D. M. Eagles. Superconductivity at very low carrier concentrations and indications of a charged bose gas in $SrTi_{0.97}Zr_{0.03}O_3$. *Solid State Communications*, 60(6):521–524, 1986.

[112] Lev P. Gor'kov. Phonon mechanism in the most dilute superconductor n-type $SrTiO_3$. *Proceedings of the National Academy of Sciences*, 113(17):4646–4651, 2016.

[113] Xiao Lin, Carl Willem Rischau, Cornelis J. van der Beek, Benoît Fauqué, and Kamran Behnia. s-wave superconductivity in optimally doped $SrTi_{1-x}Nb_xO_3$ unveiled by electron irradiation. *Phys. Rev. B*, 92:174504, Nov 2015.

[114] P. W. Anderson. Theory of dirty superconductors. *Journal of Physics and Chemistry of Solids*, 11(1):26–30, 1959.

[115] Clment Collignon, Xiao Lin, Carl Willem Rischau, Benot Fauqu, and Kamran Behnia. Metallicity and superconductivity in doped strontium titanate. *Annual Review of Condensed Matter Physics*, 10(1):25–44, 2019.

[116] Maria N. Gastiasoro, Jonathan Ruhman, and Rafael M. Fernandes. Superconductivity in dilute $SrTiO_3$: a review, 2019.

[117] Adrian G. Swartz, Hisashi Inoue, Tyler A. Merz, Yasuyuki Hikita, Srinivas Raghu, Thomas P. Devereaux, Steven Johnston, and Harold Y. Hwang. Polaronic behavior in a weak-coupling superconductor. *Proceedings of the National Academy of Sciences*, 115(7):1475–1480, 2018.

[118] C. Richter, H. Boschker, W. Dietsche, E. Fillis-Tsirakis, R. Jany, F. Loder, L. F. Kourkoutis, D. A. Muller, J. R. Kirtley, C. W. Schneider, and J. Mannhart. Interface superconductor with gap behaviour like a high-temperature superconductor. *Nature*, 502(7472):528–531, 2013.

[119] A. Joshua, S. Pecker, J. Ruhman, E. Altman, and S. Ilani. A universal critical density underlying the physics of electrons at the $LaAlO_3/SrTiO_3$ interface. *Nature Communications*, 3:1129, 2012.

[120] Arjun Joshua, Jonathan Ruhman, Sharon Pecker, Ehud Altman, and Shahal Ilani. Gate-tunable polarized phase of two-dimensional electrons at the $LaAlO_3/SrTiO_3$ interface. *Proceedings of the National Academy of Sciences*, 110(24):9633, 2013.

[121] D. M. Eagles. Possible pairing without superconductivity at low carrier concentrations in bulk and thin-film superconducting semiconductors. *Physical Review*, 186(2):456, 1969.

[122] D. M. Eagles, R. J. Tainsh, and C. Andrikidis. Evidence for pairing without superconductivity from resistance between 130 mK and 70 mK in a specimen of ceramic Zr-doped $SrTiO_3$. *Physica C: Superconductivity*, 157(1):48–52, 1989.

[123] R. J. Tainsh and C. Andrikidis. Superconducting transitions from states with low normal conductivity in ceramic $SrTi_{0.97}Zr_{0.03}O_3$. *Solid State Communications*, 60(6):517–519, 1986.

[124] G. Cheng, M. Tomczyk, S. Lu, J. P. Veazey, M. Huang, P. Irvin, S. Ryu, H. Lee, C. B. Eom, C. S. Hellberg, and J. Levy. Electron pairing without superconductivity. *Nature*, 521(7551):196, 2015.

[125] Chaoyu Chen, Jos Avila, Emmanouil Frantzeskakis, Anna Levy, and Maria C. Asensio. Observation of a two-dimensional liquid of Fröhlich polarons at the bare $SrTiO_3$ surface. *Nature Communications*, 6:8585, 2015.

[126] Z. Wang, S. McKeown Walker, A. Tamai, Y. Wang, Z. Ristic, F. Y. Bruno, A. de la Torre, S. Ricco, N. C. Plumb, M. Shi, P. Hlawenka, J. Sanchez-Barriga, A. Varykhalov, T. K. Kim, M. Hoesch, P. D. C. King, W. Meevasana, U. Diebold, J. Mesot, B. Moritz, T. P. Devereaux, M. Radovic, and F. Baumberger. Tailoring the nature and strength of electron-phonon interactions in the $SrTiO_3$ (001) 2d electron liquid. *Nat Mater*, 15(8):835–839, 2016.

[127] Hans Boschker, Christoph Richter, Evangelos Fillis-Tsirakis, Christof W. Schneider, and Jochen Mannhart. Electronphonon coupling and the superconducting phase diagram of the $LaAlO_3SrTiO_3$ interface. *Scientific Reports*, 5:12309, 2015.

[128] Alexis Baratoff and Gerd Binnig. Mechanism of superconductivity in $SrTiO_3$. *Physica B+C*, 108(1):1335–1336, 1981.

[129] Jonathan Ruhman and Patrick A. Lee. Superconductivity at very low density: The case of strontium titanate. *Physical Review B*, 94(22):224515, 2016.

[130] J. Appel. Soft-mode superconductivity in $SrTiO_3$. *Physical Review*, 180(2):508–516, 1969.

[131] Jonathan M. Edge, Yaron Kedem, Ulrich Aschauer, Nicola A. Spaldin, and Alexander V. Balatsky. Quantum critical origin of the superconducting dome in $SrTiO_3$. *Physical Review Letters*, 115(24):247002, 2015.

[132] D. van der Marel, F. Barantani, and C. W. Rischau. Possible mechanism for superconductivity in doped $srtio_3$. *Phys. Rev. Research*, 1:013003, Aug 2019.

[133] Yasutami Takada. Theory of superconductivity in polar semiconductors and its application to n-type semiconducting $SrTiO_3$. *Journal of the Physical Society of Japan*, 49(4):1267–1275, 1980.

[134] Peter Wölfle and Alexander V. Balatsky. Superconductivity at low density near a ferroelectric quantum critical point: Doped $SrTiO_3$. *Phys. Rev. B*, 98:104505, Sep 2018.

[135] Jonathan Ruhman and Patrick A. Lee. Comment on "superconductivity at low density near a ferroelectric quantum critical point: Doped $SrTiO_3$", 2019.

[136] Peter Wölfle and Alexander V. Balatsky. Reply to comment on "superconductivity at low density near a ferroelectric quantum critical point: doped $SrTiO_3$", 2019.

[137] A. Stashans, H. Pinto, and P. Sanchez. Superconductivity and Jahn-Teller polarons in titanates. *Journal of Low Temperature Physics*, 130(3-4):415–423, 2003.

[138] S. E. Rowley, L. J. Spalek, R. P. Smith, M. P. M. Dean, M. Itoh, J. F. Scott, G. G. Lonzarich, and S. S. Saxena. Ferroelectric quantum criticality. *Nat Phys*, 10(5):367–372, 2014.

[139] Mitsuru Itoh and Ruiping Wang. Quantum ferroelectricity in $SrTiO_3$ induced by oxygen isotope exchange. *Applied Physics Letters*, 76(2):221–223, 2000.

[140] Carl Willem Rischau, Xiao Lin, Christoph P. Grams, Dennis Finck, Steffen Harms, Johannes Engelmayer, Thomas Lorenz, Yann Gallais, Benoit Fauque, Joachim Hemberger, and Kamran Behnia. A ferroelectric quantum phase transition inside the superconducting dome of $Sr_{1-x}Ca_xTiO_{3-\delta}$. *Nat Phys*, 13:643, 2017.

[141] A. Ohtomo and H. Y. Hwang. A high-mobility electron gas at the $LaAlO_3/SrTiO_3$ heterointerface. *Nature*, 427(6973):423–426, 2004.

[142] S. Thiel, G. Hammerl, A. Schmehl, C. W. Schneider, and J. Mannhart. Tunable quasi-two-dimensional electron gases in oxide heterostructures. *Science*, 313(5795):1942–1945, 2006.

[143] Naoyuki Nakagawa, Harold Y. Hwang, and David A. Muller. Why some interfaces cannot be sharp. *Nat Mater*, 5(3):204–209, 2006.

[144] C. Cen, S. Thiel, G. Hammerl, C. W. Schneider, K. E. Andersen, C. S. Hellberg, J. Mannhart, and J. Levy. Nanoscale control of an interfacial metal-insulator transition at room temperature. *Nature Materials*, 7(4):298–302, 2008.

[145] N. Reyren, S. Thiel, A. D. Caviglia, L. Fitting Kourkoutis, G. Hammerl, C. Richter, C. W. Schneider, T. Kopp, A. S. Ruetschi, D. Jaccard, M. Gabay, D. A. Muller, J. M. Triscone, and J. Mannhart. Superconducting interfaces between insulating oxides. *Science*, 317(5842):1196–1199, 2007.

[146] A. D. Caviglia, S. Gariglio, N. Reyren, D. Jaccard, T. Schneider, M. Gabay, S. Thiel, G. Hammerl, J. Mannhart, and J. M. Triscone. Electric field control of the $LaAlO_3/SrTiO_3$ interface ground state. *Nature*, 456(7222):624–627, 2008.

[147] A. Brinkman, M. Huijben, M. Van Zalk, J. Huijben, U. Zeitler, J. C. Maan, W. G. Van der Wiel, G. Rijnders, D. H. A. Blank, and H. Hilgenkamp. Magnetic effects at the interface between non-magnetic oxides. *Nature Materials*, 6(7):493–496, 2007.

[148] Ariando, X. Wang, G. Baskaran, Z. Q. Liu, J. Huijben, J. B. Yi, A. Annadi, A. Roy Barman, A. Rusydi, S. Dhar, Y. P. Feng, J. Ding, H. Hilgenkamp, and T. Venkatesan. Electronic phase separation at the $LaAlO_3/SrTiO_3$ interface. *Nature Communications*, 2:188, 2011.

[149] Feng Bi, Mengchen Huang, Sangwoo Ryu, Hyungwoo Lee, Chung-Wung Bark, Chang-Beom Eom, Patrick Irvin, and Jeremy Levy. Room-temperature electronically-

controlled ferromagnetism at the $LaAlO_3/SrTiO_3$ interface. *Nature Communications*, 5:5019, 2014.

[150] M. Basletic, J. L. Maurice, C. Carretero, G. Herranz, O. Copie, M. Bibes, E. Jacquet, K. Bouzehouane, S. Fusil, and A. Barthelemy. Mapping the spatial distribution of charge carriers in $LaAlO_3/SrTiO_3$ heterostructures. *Nature Materials*, 7(8):621–625, 2008.

[151] Yunzhong Chen, Nini Pryds, Josee E. Kleibeuker, Gertjan Koster, Jirong Sun, Eugen Stamate, Baogen Shen, Guus Rijnders, and Soren Linderoth. Metallic and insulating interfaces of amorphous $SrTiO_3$-based oxide heterostructures. *Nano Letters*, 11(9):3774–3778, 2011.

[152] G. Herranz, F. Snchez, N. Dix, M. Scigaj, and J. Fontcuberta. High mobility conduction at (110) and (111) $LaAlO_3/SrTiO_3$ interfaces. *Scientific Reports*, 2:758, 2012.

[153] S. McKeown Walker, A. de la Torre, F. Y. Bruno, A. Tamai, T. K. Kim, M. Hoesch, M. Shi, M. S. Bahramy, P. D. C. King, and F. Baumberger. Control of a two-dimensional electron gas on $srtio_3(111)$ by atomic oxygen. *Phys. Rev. Lett.*, 113:177601, Oct 2014.

[154] Mark Huijben, Gertjan Koster, Michelle K. Kruize, Sander Wenderich, Jo Verbeeck, Sara Bals, Erik Slooten, Bo Shi, Hajo J. A. Molegraaf, Josee E. Kleibeuker, Sandra van Aert, Jeroen B. Goedkoop, Alexander Brinkman, Dave H. A. Blank, Mark S. Golden, Gustaaf van Tendeloo, Hans Hilgenkamp, and Guus Rijnders. Defect engineering in oxide heterostructures by enhanced oxygen surface exchange. *Advanced Functional Materials*, 23(42):5240–5248, 2013.

[155] C. He, T. D. Sanders, M. T. Gray, F. J. Wong, V. V. Mehta, and Y. Suzuki. Metal-insulator transitions in epitaxial lavo3 and latio3 films. *Physical Review B*, 86(8):081401, 2012.

[156] P. Perna, D. Maccariello, M. Radovic, U. Scotti di Uccio, I. Pallecchi, M. Codda, D. Marre, C. Cantoni, J. Gazquez, M. Varela, S. J. Pennycook, and F. Miletto Granozio. Conducting interfaces between band insulating oxides: The $lagao3/SrTiO_3$ heterostructure. *Applied Physics Letters*, 97(15), 2010.

[157] A. Annadi, A. Putra, Z. Q. Liu, X. Wang, K. Gopinadhan, Z. Huang, S. Dhar, T. Venkatesan, and Ariando. Electronic correlation and strain effects at the interfaces between polar and nonpolar complex oxides. *Physical Review B*, 86(8), 2012.

[158] A. Annadi, A. Putra, A. Srivastava, X. Wang, Z. Huang, Z. Q. Liu, T. Venkatesan, and Ariando. Evolution of variable range hopping in strongly localized two dimensional electron gas at $ndalo3/SrTiO_3$ (100) heterointerfaces. *Applied Physics Letters*, 101(23), 2012.

[159] C. P. Chang, J. G. Lin, H. T. Jeng, S. L. Cheng, W. F. Pong, Y. C. Shao, Y. Y.

Chin, H. J. Lin, C. W. Chen, J. R. Yang, C. H. Chen, and M. W. Chu. Atomic-scale observation of a graded polar discontinuity and a localized two-dimensional electron density at an insulating oxide interface. *Physical Review B*, 87(7), 2013.

[160] Sang Woon Lee, Yiqun Liu, Jaeyeong Heo, and Roy G. Gordon. Creation and control of two-dimensional electron gas using al-based amorphous oxides/$SrTiO_3$ heterostructures grown by atomic layer deposition. *Nano Letters*, 12(9):4775–4783, 2012.

[161] M. L. Reinle-Schmitt, C. Cancellieri, D. Li, D. Fontaine, M. Medarde, E. Pomjakushina, C. W. Schneider, S. Gariglio, Ph Ghosez, J. M. Triscone, and P. R. Willmott. Tunable conductivity threshold at polar oxide interfaces. *Nat Commun*, 3:932, 2012.

[162] D. F. Li, Yan Wang, and J. Y. Dai. Tunable electronic transport properties of $DyScO_3$/$SrTiO_3$ polar heterointerface. *Applied Physics Letters*, 98(12), 2011.

[163] A. Kalabukhov, R. Gunnarsson, T. Claeson, and D. Winkler. Electrical transport properties of polar heterointerface between ktao3 and $SrTiO_3$. *arXiv:0704.1050*, 2007.

[164] Yunzhong Chen, Felix Trier, Takeshi Kasama, Dennis V. Christensen, Nicolas Bovet, Zoltan I. Balogh, Han Li, Karl Tor Sune Thydn, Wei Zhang, Sadegh Yazdi, Poul Norby, Nini Pryds, and Sren Linderoth. Creation of high mobility two-dimensional electron gases via strain induced polarization at an otherwise nonpolar complex oxide interface. *Nano Letters*, 15(3):1849–1854, 2015.

[165] Pengfa Xu, Wei Han, Philip M. Rice, Jaewoo Jeong, Mahesh G. Samant, Katayoon Mohseni, Holger L. Meyerheim, Sergey Ostanin, Igor V. Maznichenko, Ingrid Mertig, Eberhard K. U. Gross, Arthur Ernst, and Stuart S. P. Parkin. Reversible formation of 2d electron gas at the $LaFeO_3$/$SrTiO_3$ interface via control of oxygen vacancies. *Advanced Materials*, pages 1604447–n/a, 2017.

[166] S. A. Chambers, L. Qiao, T. C. Droubay, T. C. Kaspar, B. W. Arey, and P. V. Sushko. Band alignment, built-in potential, and the absence of conductivity at the lacro3/$SrTiO_3$ (001) heterojunction. *Physical Review Letters*, 107(20):206802, 2011.

[167] X. Renshaw Wang, C. J. Li, W. M. L, T. R. Paudel, D. P. Leusink, M. Hoek, N. Poccia, A. Vailionis, T. Venkatesan, J. M. D. Coey, E. Y. Tsymbal, Ariando, and H. Hilgenkamp. Imaging and control of ferromagnetism in lamno3/$SrTiO_3$ heterostructures. *Science*, 349(6249):716–719, 2015.

[168] Y. Anahory, L. Embon, C. J. Li, S. Banerjee, A. Meltzer, H. R. Naren, A. Yakovenko, J. Cuppens, Y. Myasoedov, M. L. Rappaport, M. E. Huber, K. Michaeli, T. Venkatesan, Ariando, and E. Zeldov. Emergent nanoscale superparamagnetism at oxide interfaces. *Nat Commun*, 7, 2016.

[169] Mark Charles Monti. *The effect of epitaxial strain and $R3^+$ magnetism on the interfaces between polar perovskites and $SrTiO_3$*. Thesis, The University of Texas at

Austin, 2011.

[170] M. Salluzzo, S. Gariglio, D. Stornaiuolo, V. Sessi, S. Rusponi, C. Piamonteze, G. M. De Luca, M. Minola, D. Marr, A. Gadaleta, H. Brune, F. Nolting, N. B. Brookes, and G. Ghiringhelli. Origin of interface magnetism in bimno3/$SrTiO_3$ and $LaAlO_3$/$SrTiO_3$ heterostructures. *Physical Review Letters*, 111(8):087204, 2013.

[171] R. Ohtsuka, M. Matvejeff, K. Nishio, R. Takahashi, and M. Lippmaa. Transport properties of latio3/$SrTiO_3$ heterostructures. *Applied Physics Letters*, 96(19):192111, 2010.

[172] M. Huijben, D. Kockmann, J. Huijben, J. E. Kleibeuker, A. van Houselt, G. Koster, D. H. A. Blank, H. Hilgenkamp, G. Rijnders, A. Brinkman, and H. J. W. Zandvliet. Local probing of coupled interfaces between two-dimensional electron and hole gases in oxide heterostructures by variable-temperature scanning tunneling spectroscopy. *Physical Review B*, 86(3), 2012.

[173] Pouya Moetakef, Clayton A. Jackson, Jinwoo Hwang, Leon Balents, S. James Allen, and Susanne Stemmer. Toward an artificial mott insulator: Correlations in confined high-density electron liquids in $SrTiO_3$. *Phys. Rev. B.*, 86:201102(R), 2012.

[174] Pouya Moetakef, Daniel G. Ouellette, James R. Williams, S. James Allen, Leon Balents, David Goldhaber-Gordon, and Susanne Stemmer. Quantum oscillations from a two-dimensional electron gas at a mott/band insulator interface. *Appl. Phys. Lett.*, 101:151604, 2012.

[175] Pouya Moetakef, Tyler A. Cain, Daniel G. Ouellette, Jack Y. Zhang, Dmitri O. Klenov, Anderson Janotti, Chris G.VandeWalle, Siddharth Rajan, S. James Allen, and Susanne Stemmer. Electrostatic carrier doping of gdtio3/$SrTiO_3$ interfaces. *Appl. Phys. Lett.*, 99:232116, 2011.

[176] P. Moetakef, D. G. Ouellette, J. Y. Zhang, T. A. Cain, S. J. Allen, and S. Stemmer. Growth and properties of gdtio3 films prepared by hybrid molecular beam epitaxy. *Journal of Crystal Growth*, 355(1):166–170, 2012.

[177] R. F. Need, B. J. Isaac, B. J. Kirby, J. A. Borchers, S. Stemmer, and Stephen D. Wilson. Interface-driven ferromagnetism within the quantum wells of a rare earth titanate superlattice. *Phys. Rev. Lett.*, 117:037205, Jul 2016.

[178] Hrishit Banerjee, Sumilan Banerjee, Mohit Randeria, and Tanusri Saha-Dasgupta. Electronic structure of oxide interfaces: A comparative analysis of gdtio3/$SrTiO_3$ and $LaAlO_3$/$SrTiO_3$ interfaces. *Scientific Reports*, 5:18647, 2015.

[179] Peng Xu, Timothy C. Droubay, Jong Seok Jeong, K. Andre Mkhoyan, Peter V. Sushko, Scott A. Chambers, and Bharat Jalan. Quasi 2d ultrahigh carrier density in a complex oxide broken-gap heterojunction. *Advanced Materials Interfaces*, pages n/a–n/a, 2015.

[180] Y. Z. Chen, N. Bovet, F. Trier, D. V. Christensen, F. M. Qu, N. H. Andersen, T. Kasama, W. Zhang, R. Giraud, J. Dufouleur, T. S. Jespersen, J. R. Sun, A. Smith, J. Nygrd, L. Lu, B. Bchner, B. G. Shen, S. Linderoth, and N. Pryds. A high-mobility two-dimensional electron gas at the spinel/perovskite interface of γ-al$_2$o$_3$/SrTiO$_3$. *Nature Communications*, 4:1371, 2013.

[181] Y. Z. Chen, F. Trier, T. Wijnands, R. J. Green, N. Gauquelin, R. Egoavil, D. V. Christensen, G. Koster, M. Huijben, N. Bovet, S. Macke, F. He, R. Sutarto, N. H. Andersen, J. A. Sulpizio, M. Honig, G. E. D. K. Prawiroatmodjo, T. S. Jespersen, S. Linderoth, S. Ilani, J. Verbeeck, G. Van Tendeloo, G. Rijnders, G. A. Sawatzky, and N. Pryds. Extreme mobility enhancement of two-dimensional electron gases at oxide interfaces by charge-transfer-induced modulation doping. *Nature Materials*, 14(8):801, 2015.

[182] G. Bastard. *Wave mechanics applied to semiconductor heterostructures*. Les ditions de Physique, 1988.

[183] H. J. Schulz, G. Cuniberti, and P. Pieri. Fermi liquids and luttinger liquids, 1998.

[184] G. R. Stewart. Non-fermi-liquid behavior in d- and f-electron metals. *Reviews of Modern Physics*, 73(4):797–855, 2001.

[185] B. Spivak, S. V. Kravchenko, S. A. Kivelson, and X. P. A. Gao. Colloquium: Transport in strongly correlated two dimensional electron fluids. *Reviews of Modern Physics*, 82(2):1743–1766, 2010.

[186] Ali Yazdani, Eduardo H. da Silva Neto, and Pegor Aynajian. Spectroscopic imaging of strongly correlated electronic states. *Annual Review of Condensed Matter Physics*, 7(1):11–33, 2016.

[187] Guest Editors, Laura H. Greene, Joe Thompson, and Jrg Schmalian. Strongly correlated electron systemsreports on the progress of the field. *Reports on Progress in Physics*, 80(3):030401, 2017.

[188] Jochen Mannhart and D. G. Schlom. Oxide interfacesan opportunity for electronics. *Science*, 327(5973):1607–1611, 2010.

[189] S. Caprara, J. Biscaras, N. Bergeal, D. Bucheli, S. Hurand, C. Feuillet-Palma, A. Rastogi, R. C. Budhani, J. Lesueur, and M. Grilli. Multiband superconductivity and nanoscale inhomogeneity at oxide interfaces. *Physical Review B*, 88(2):020504, 2013.

[190] Y. C. Liao, T. Kopp, C. Richter, A. Rosch, and J. Mannhart. Metal-insulator transition of the LaAlO$_3$-SrTiO$_3$ interface electron system. *Physical Review B*, 83(7):075402, 2011.

[191] Wei-Nan Lin, Jun-Feng Ding, Shu-Xiang Wu, Yong-Feng Li, James Lourembam, Santiranjan Shannigrahi, Shi-Jie Wang, and Tom Wu. Electrostatic modulation of

$LaAlO_3/SrTiO_3$ interface transport in an electric double-layer transistor. *Advanced Materials Interfaces*, 1(1):1300001–n/a, 2014.

[192] Beena Kalisky, Eric M. Spanton, Hilary Noad, John R. Kirtley, Katja C. Nowack, Christopher Bell, Hiroki K. Sato, Masayuki Hosoda, Yanwu Xie, Yasuyuki Hikita, Carsten Woltmann, Georg Pfanzelt, Rainer Jany, Christoph Richter, Harold Y. Hwang, Jochen Mannhart, and Kathryn A. Moler. Locally enhanced conductivity due to the tetragonal domain structure in $LaAlO_3/SrTiO_3$ heterointerfaces. *Nature Materials*, 12:1091–1095, 2013.

[193] Hilary Noad, Eric M. Spanton, Katja C. Nowack, Hisashi Inoue, Minu Kim, Tyler A. Merz, Christopher Bell, Yasuyuki Hikita, Ruqing Xu, Wenjun Liu, Arturas Vailionis, Harold Y. Hwang, and Kathryn A. Moler. Variation in superconducting transition temperature due to tetragonal domains in two-dimensionally doped $SrTiO_3$. *Physical Review B*, 94(17):174516, 2016.

[194] Z. Erlich, Y. Frenkel, J. Drori, Y. Shperber, C. Bell, H. K. Sato, M. Hosoda, Y. Xie, Y. Hikita, H. Y. Hwang, and B. Kalisky. Optical study of tetragonal domains in $LaAlO_3/SrTiO_3$. *Journal of Superconductivity and Novel Magnetism*, 28(3):1017–1020, 2015.

[195] M. Honig, J. A. Sulpizio, J. Drori, A. Joshua, E. Zeldov, and S. Ilani. Local electrostatic imaging of striped domain order in $LaAlO_3/SrTiO_3$. *Nature Materials*, 12:1112–1118, 2013.

[196] H. J. Harsan Ma, S. Scharinger, S. W. Zeng, D. Kohlberger, M. Lange, A. Stöhr, X. Renshaw Wang, T. Venkatesan, R. Kleiner, J. F. Scott, J. M. D. Coey, D. Koelle, and Ariando. Local electrical imaging of tetragonal domains and field-induced ferroelectric twin walls in conducting $srtio_3$. *Phys. Rev. Lett.*, 116:257601, Jun 2016.

[197] Thach D. N. Ngo, Jung-Won Chang, Kyujoon Lee, Seungju Han, Joon Sung Lee, Young Heon Kim, Myung-Hwa Jung, Yong-Joo Doh, Mahn-Soo Choi, Jonghyun Song, and Jinhee Kim. Polarity-tunable magnetic tunnel junctions based on ferromagnetism at oxide heterointerfaces. *Nature Communications*, 6:8035, 2015.

[198] D. V. Christensen, Y. Frenkel, Y. Z. Chen, Y. W. Xie, Z. Y. Chen, Y. Hikita, A. Smith, L. Klein, H. Y. Hwang, N. Pryds, and B. Kalisky. Strain-tunable magnetism at oxide domain walls. *Nature Physics*, 2018.

[199] Hai-Long Hu, Rong Zeng, Anh Pham, Thiam Teck Tan, Zhigang Chen, Charlie Kong, Danyang Wang, and Sean Li. Subtle interplay between localized magnetic moments and itinerant electrons in $LaAlO_3/SrTiO_3$ heterostructures. *ACS Applied Materials & Interfaces*, page 1363013636, 2016.

[200] M. Ben Shalom, C. W. Tai, Y. Lereah, M. Sachs, E. Levy, D. Rakhmilevitch, A. Palevski, and Y. Dagan. Anisotropic magnetotransport at the $SrTiO_3/LaAlO_3$

interface. *Physical Review B*, 80(14):140403, 2009.

[201] Snir Seri and Lior Klein. Antisymmetric magnetoresistance of the $SrTiO_3/LaAlO_3$ interface. *Physical Review B*, 80(18):180410, 2009.

[202] X. Wang, W. M. Lu, A. Annadi, Z. Q. Liu, K. Gopinadhan, S. Dhar, T. Venkatesan, and Ariando. Magnetoresistance of two-dimensional and three-dimensional electron gas in $LaAlO_3/SrTiO_3$ heterostructures: Influence of magnetic ordering, interface scattering, and dimensionality. *Physical Review B*, 84(7):075312, 2011.

[203] A. Fte, S. Gariglio, A. D. Caviglia, J. M. Triscone, and M. Gabay. Rashba induced magnetoconductance oscillations in the $LaAlO_3$-$SrTiO_3$ heterostructure. *Physical Review B*, 86(20):201105, 2012.

[204] Snir Seri, Moty Schultz, and Lior Klein. Interplay between sheet resistance increase and magnetotransport properties in $LaAlO_3/SrTiO_3$. *Physical Review B*, 86(8):085118, 2012.

[205] Ludi Miao, Renzhong Du, Yuewei Yin, and Qi Li. Anisotropic magneto-transport properties of electron gases at $SrTiO_3$ (111) and (110) surfaces. *Applied Physics Letters*, 109(26):261604, 2016.

[206] P. K. Rout, I. Agireen, E. Maniv, M. Goldstein, and Y. Dagan. Six-fold crystalline anisotropic magnetoresistance in the (111) $\mathbf{laalo_3/srtio_3}$ oxide interface. *Phys. Rev. B*, 95:241107, Jun 2017.

[207] H. J. Harsan Ma, J. Zhou, M. Yang, Y. Liu, S. W. Zeng, W. X. Zhou, L. C. Zhang, T. Venkatesan, Y. P. Feng, and Ariando. Giant crystalline anisotropic magnetoresistance in nonmagnetic perovskite oxide heterostructures. *Physical Review B*, 95(15):155314, 2017.

[208] Menyoung Lee, J. R. Williams, Sipei Zhang, C. Daniel Frisbie, and D. Goldhaber-Gordon. Electrolyte gate-controlled kondo effect in $SrTiO_3$. *Physical Review Letters*, 107(25):256601, 2011.

[209] H. J. Harsan Ma, Z. Huang, W. M. L, A. Annadi, S. W. Zeng, L. M. Wong, S. J. Wang, T. Venkatesan, and Ariando. Tunable bilayer two-dimensional electron gas in $LaAlO_3/SrTiO_3$ superlattices. *Applied Physics Letters*, 105(1):011603, 2014.

[210] M.; Ben Shalom, A.; Ron, A.; Palevski, and Y.; Dagan. Shubnikov-de haas oscillations in $SrTiO_3/LaAlO_3$ interface. *Physical Review Letters*, 105(20):206401, 2010.

[211] M. Diez, A. M. R. V. L. Monteiro, G. Mattoni, E. Cobanera, T. Hyart, E. Mulazimoglu, N. Bovenzi, C. W. J. Beenakker, and A. D. Caviglia. Giant negative magnetoresistance driven by spin-orbit coupling at the $laalo_3/srtio_3$ interface. *Phys. Rev. Lett.*, 115:016803, Jul 2015.

[212] M. Ben Shalom, M. Sachs, D. Rakhmilevitch, A. Palevski, and Y. Dagan. Tuning spin-orbit coupling and superconductivity at the $SrTiO_3/LaAlO_3$ interface: a magnetotransport study. *Physical Review Letters*, 104(12):126802, 2010.

[213] A. Annadi, Z. Huang, K. Gopinadhan, X. Renshaw Wang, A. Srivastava, Z. Q. Liu, H. Harsan Ma, T. P. Sarkar, T. Venkatesan, and Ariando. Fourfold oscillation in anisotropic magnetoresistance and planar hall effect at the $LaAlO_3/SrTiO_3$ heterointerfaces: Effect of carrier confinement and electric field on magnetic interactions. *Physical Review B*, 87(20):201102, 2013.

[214] A. D. Caviglia, M. Gabay, S. Gariglio, N. Reyren, C. Cancellieri, and J. M. Triscone. Tunable rashba spin-orbit interaction at oxide interfaces. *Physical Review Letters*, 104(12):126803, 2010.

[215] H. Nakamura, T. Koga, and T. Kimura. Experimental evidence of cubic rashba effect in an inversion-symmetric oxide. *Physical Review Letters*, 108(20), 2012.

[216] D. Stornaiuolo, S. Gariglio, A. Fte, M. Gabay, D. Li, D. Massarotti, and J. M. Triscone. Weak localization and spin-orbit interaction in side-gate field effect devices at the $LaAlO_3/SrTiO_3$ interface. *Physical Review B*, 90(23):235426, 2014.

[217] S. Hurand, A. Jouan, C. Feuillet-Palma, G. Singh, J. Biscaras, E. Lesne, N. Reyren, A. Barthlmy, M. Bibes, J. E. Villegas, C. Ulysse, X. Lafosse, M. Pannetier-Lecoeur, S. Caprara, M. Grilli, J. Lesueur, and N. Bergeal. Field-effect control of superconductivity and rashba spin-orbit coupling in top-gated $LaAlO_3/SrTiO_3$ devices. *Scientific Reports*, 5:12751, 2015.

[218] Haixing Liang, Long Cheng, Laiming Wei, Zhenlin Luo, Guolin Yu, Changgan Zeng, and Zhenyu Zhang. Nonmonotonically tunable rashba spin-orbit coupling by multiple-band filling control in$SrTiO_3$-based interfacial d-electron gases. *Physical Review B*, 92(7):075309, 2015.

[219] Gervasi Herranz, Gyanendra Singh, Nicolas Bergeal, Alexis Jouan, Jrme Lesueur, Jaume Gzquez, Mara Varela, Mateusz Scigaj, Nico Dix, Florencio Snchez, and Josep Fontcuberta. Engineering two-dimensional superconductivity and rashba spinorbit coupling in $LaAlO_3/SrTiO_3$ quantum wells by selective orbital occupancy. *Nature Communications*, 6:6028, 2015.

[220] G. Singh, A. Jouan, S. Hurand, C. Palma, P. Kumar, A. Dogra, R. Budhani, J. Lesueur, and N. Bergeal. Effect of disorder on superconductivity and rashba spin-orbit coupling in $LaAlO_3/SrTiO_3$ interfaces. *arXiv:1610.01380*, 2016.

[221] Z. C. Zhong, A. Toth, and K. Held. Theory of spin-orbit coupling at $LaAlO_3/SrTiO_3$ interfaces and $SrTiO_3$ surfaces. *Physical Review B*, 87(16):161102, 2013.

[222] Younghyun Kim, Roman M. Lutchyn, and Chetan Nayak. Origin and transport signatures of spin-orbit interactions in one- and two-dimensional $SrTiO_3$-based het-

erostructures. *Physical Review B*, 87(24):245121, 2013.

[223] K. V. Shanavas. Theoretical study of the cubic rashba effect at the $SrTiO_3$ (001) surfaces. *Physical Review B*, 93(4):045108, 2016.

[224] A. F. Santander-Syro, F. Fortuna, C. Bareille, T. C. Rdel, G. Landolt, N. C. Plumb, J. H. Dil, and M. Radovi. Giant spin splitting of the two-dimensional electron gas at the surface of $SrTiO_3$. *Nature Materials*, 13(12):1085–1090, 2014.

[225] E. Lesne, Yu Fu, S. Oyarzun, J. C. Rojas-Sanchez, D. C. Vaz, H. Naganuma, G. Sicoli, J. P. Attane, M. Jamet, E. Jacquet, J. M. George, A. Barthelemy, H. Jaffres, A. Fert, M. Bibes, and L. Vila. Highly efficient and tunable spin-to-charge conversion through rashba coupling at oxide interfaces. *Nature Materials*, 15(12):12611266, 2016.

[226] S. McKeown Walker, S. Ricc, F. Y. Bruno, A. de la Torre, A. Tamai, E. Golias, A. Varykhalov, D. Marchenko, M. Hoesch, M. S. Bahramy, P. D. C. King, J. Snchez-Barriga, and F. Baumberger. Absence of giant spin splitting in the two-dimensional electron liquid at the surface of $SrTiO_3$ (001). *Physical Review B*, 93(24):245143, 2016.

[227] R. J. Elliott. Theory of the effect of spin-orbit coupling on magnetic resonance in some semiconductors. *Physical Review*, 96(2):266–279, 1954.

[228] Y. Yafet. *g Factors and Spin-Lattice Relaxation of Conduction Electrons*, volume Volume 14, pages 1–98. Academic Press, 1963.

[229] MI Dyakonov and VI Perel. Spin relaxation of conduction electrons in noncentrosymmetric semiconductors. *Soviet Physics Solid State, Ussr*, 13(12):3023–3026, 1972.

[230] Sadamichi Maekawa and Hidetoshi Fukuyama. Magnetoresistance in two-dimensional disordered systems: Effects of zeeman splitting and spin-orbit scattering. *Journal of the Physical Society of Japan*, 50(8):2516–2524, 1981.

[231] Shinobu Hikami, Anatoly I. Larkin, and Yosuke Nagaoka. Spin-orbit interaction and magnetoresistance in the two dimensional random system. *Progress of Theoretical Physics*, 63(2):707–710, 1980.

[232] S. V. Iordanskii, Y. B. Lyanda-Geller, and G. E. Pikus. Weak localization in quantum wells with spin-orbit interaction. *Soviet Journal of Experimental and Theoretical Physics Letters*, 60:206, 1994.

[233] M. Kim, Y. Kozuka, C. Bell, Y. Hikita, and H. Y. Hwang. Intrinsic spin-orbit coupling in superconducting delta-doped $SrTiO_3$ heterostructures. *Physical Review B*, 86(8), 2012.

[234] C. Bell, S. Harashima, Y. Kozuka, M. Kim, B. G. Kim, Y. Hikita, and H. Y. Hwang. Dominant mobility modulation by the electric field effect at the $LaAlO_3/SrTiO_3$ interface. *Physical Review Letters*, 103(22):226802, 2009.

[235] F. Gunkel, Chris Bell, Hisashi Inoue, Bongju Kim, Adrian G. Swartz, Tyler A. Merz, Yasuyuki Hikita, Satoshi Harashima, Hiroki K. Sato, Makoto Minohara, Susanne Hoffmann-Eifert, Regina Dittmann, and Harold Y. Hwang. Defect control of conventional and anomalous electron transport at complex oxide interfaces. *Physical Review X*, 6(3):031035, 2016.

[236] D. Stornaiuolo, C. Cantoni, G. M. De Luca, R. Di Capua, E. Di. Gennaro, G. Ghiringhelli, B. Jouault, D. Marre, D. Massarotti, F. Miletto Granozio, I. Pallecchi, C. Piamonteze, S. Rusponi, F. Tafuri, and M. Salluzzo. Tunable spin polarization and superconductivity in engineered oxide interfaces. *Nature Materials*, 15(3):278–283, 2016.

[237] A. Fte, C. Cancellieri, D. Li, D. Stornaiuolo, A. D. Caviglia, S. Gariglio, and J.-M. Triscone. Growth-induced electron mobility enhancement at the $LaAlO_3/SrTiO_3$ interface. *Applied Physics Letters*, 106(5):051604, 2015.

[238] J. S. Kim, S. S. A. Seo, M. F. Chisholm, R. K. Kremer, H. U. Habermeier, B. Keimer, and H. N. Lee. Nonlinear hall effect and multichannel conduction in latio3/$SrTiO_3$ superlattices. *Physical Review B*, 82(20):201407, 2010.

[239] Patrick Gallagher, Menyoung Lee, Trevor A. Petach, Sam W. Stanwyck, James R. Williams, Kenji Watanabe, Takashi Taniguchi, and David Goldhaber-Gordon. A high-mobility electronic system at an electrolyte-gated oxide surface. *Nature Communications*, 6:6437, 2015.

[240] Yeonbae Lee, Colin Clement, Jack Hellerstedt, Joseph Kinney, Laura Kinnischtzke, Xiang Leng, S. D. Snyder, and A. M. Goldman. Phase diagram of electrostatically doped $SrTiO_3$. *Physical Review Letters*, 106(13):136809, 2011.

[241] A. D. Caviglia, S. Gariglio, C. Cancellieri, B. Sacepe, A. Fete, N. Reyren, M. Gabay, A. F. Morpurgo, and J. M. Triscone. Two-dimensional quantum oscillations of the conductance at $LaAlO_3/SrTiO_3$ interfaces. *Physical Review Letters*, 105(23), 2010.

[242] Y. W. Xie, C. Bell, M. Kim, H. Inoue, Y. Hikita, and H. Y. Hwang. Quantum longitudinal and hall transport at the $LaAlO_3/SrTiO_3$ interface at low electron densities. *Solid State Communications*, 197:25–29, 2014.

[243] A. Fte, S. Gariglio, C. Berthod, D. Li, D. Stornaiuolo, M. Gabay, and J. M. Triscone. Large modulation of the shubnikovde haas oscillations by the rashba interaction at the $LaAlO_3/SrTiO_3$ interface. *New Journal of Physics*, 16(11):112002, 2014.

[244] E. Maniv, M. Ben Shalom, A. Ron, M. Mograbi, A. Palevski, M. Goldstein, and Y. Dagan. Strong correlations elucidate the electronic structure and phase diagram of $LaAlO_3/SrTiO_3$ interface. *Nature Communications*, 6:8239, 2015.

[245] Ming Yang, Kun Han, Olivier Torresin, Mathieu Pierre, Shengwei Zeng, Zhen Huang, T. V. Venkatesan, Michel Goiran, J. M. D. Coey, Ariando, and Walter Escoffier. High

field magneto-transport in two-dimensional electron gas $LaAlO_3/SrTiO_3$. *Applied Physics Letters*, 109(12):122106, 2016.

[246] Shengwei Zeng, Weiming L, Zhen Huang, Zhiqi Liu, Kun Han, Kalon Gopinadhan, Changjian Li, Rui Guo, Wenxiong Zhou, Haijiao Harsan Ma, Linke Jian, Thirumalai Venkatesan, and Ariando. Liquid-gated high mobility and quantum oscillation of the two-dimensional electron gas at an oxide interface. *ACS Nano*, 10(4):4532–4537, 2016.

[247] A. McCollam, S. Wenderich, M. K. Kruize, V. K. Guduru, H. J. A. Molegraaf, M. Huijben, G. Koster, D. H. A. Blank, G. Rijnders, A. Brinkman, H. Hilgenkamp, U. Zeitler, and J. C. Maan. Quantum oscillations and subband properties of the two-dimensional electron gas at the $LaAlO_3/SrTiO_3$ interface. *APL Mater.*, 2(2):022102, 2014.

[248] Felix Trier, Guenevere E. D. K. Prawiroatmodjo, Zhicheng Zhong, Dennis Valbjørn Christensen, Merlin von Soosten, Arghya Bhowmik, Juan Maria García Lastra, Yunzhong Chen, Thomas Sand Jespersen, and Nini Pryds. Quantization of hall resistance at the metallic interface between an oxide insulator and $SrTiO_3$. *Phys. Rev. Lett.*, 117:096804, Aug 2016.

[249] Y. Kozuka, M. Kim, C. Bell, B. G. Kim, Y. Hikita, and H. Y. Hwang. Two-dimensional normal-state quantum oscillations in a superconducting heterostructure. *Nature*, 462(7272):487–490, 2009.

[250] Bharat Jalan, Susanne Stemmer, Shawn Mack, and S. James Allen. Two-dimensional electron gas in δ-doped $SrTiO_3$. *Physical Review B*, 82(8):081103, 2010.

[251] M. Kim, C. Bell, Y. Kozuka, M. Kurita, Y. Hikita, and H. Y. Hwang. Fermi surface and superconductivity in low-density high-mobility δ-doped $SrTiO_3$. *Physical Review Letters*, 107(10):106801, 2011.

[252] Y. Matsubara, K. S. Takahashi, M. S. Bahramy, Y. Kozuka, D. Maryenko, J. Falson, A. Tsukazaki, Y. Tokura, and M. Kawasaki. Observation of the quantum hall effect in δ-doped $SrTiO_3$. *Nature Communications*, 7:11631, 2016.

[253] G. Herranz, M. Basletic, M. Bibes, C. Carretero, E. Tafra, E. Jacquet, K. Bouzehouane, C. Deranlot, A. Hamzic, J. M. Broto, A. Barthelemy, and A. Fert. High mobility in $LaAlO_3/SrTiO_3$ heterostructures: origin, dimensionality, and perspectives. *Phys Rev Lett*, 98(21):216803, 2007.

[254] A. E. M. Smink, J. C. de Boer, M. P. Stehno, A. Brinkman, W. G. van der Wiel, and H. Hilgenkamp. Gate-tunable band structure of the $LaAlO_3$-$SrTiO_3$ interface. *arXiv:1610.02299*, 2016.

[255] E. Maniv, A. Ron, M. Goldstein, A. Palevski, and Y. Dagan. Tunneling into a quantum confinement created by a single-step nanolithography of conducting oxide interfaces. *Physical Review B*, 94(4):045120, 2016.

[256] S. A. Wolf, D. D. Awschalom, R. A. Buhrman, J. M. Daughton, S. von Molnar, M. L. Roukes, A. Y. Chtchelkanova, and D. M. Treger. Spintronics: A spin-based electronics vision for the future. *Science*, 294(5546):1488–1495, 2001.

[257] Igor Žutić, Jaroslav Fabian, and S. Das Sarma. Spintronics: Fundamentals and applications. *Rev. Mod. Phys.*, 76:323–410, Apr 2004.

[258] Hisashi Inoue, Adrian G. Swartz, Nicholas J. Harmon, Takashi Tachikawa, Yasuyuki Hikita, Michael E. Flatt, and Harold Y. Hwang. Origin of the magnetoresistance in oxide tunnel junctions determined through electric polarization control of the interface. *Physical Review X*, 5(4):041023, 2015.

[259] M. Bibes, N. Reyren, E. Lesne, J.-M. George, C. Deranlot, S. Collin, A. Barthlmy, and H. Jaffrs. Towards electrical spin injection into $LaAlO_3$-$SrTiO_3$. *Philosophical Transactions of the Royal Society of London A: Mathematical, Physical and Engineering Sciences*, 370(1977):4958–4971, 2012.

[260] N. Reyren, M. Bibes, E. Lesne, J. M. George, C. Deranlot, S. Collin, A. Barthlmy, and H. Jaffrs. Gate-controlled spin injection at $LaAlO_3/SrTiO_3$ interfaces. *Physical Review Letters*, 108(18):186802, 2012.

[261] Wei Han, Xin Jiang, Adam Kajdos, See-Hun Yang, Susanne Stemmer, and Stuart S. P. Parkin. Spin injection and detection in lanthanum- and niobium-doped $SrTiO_3$ using the hanle technique. *Nature Communications*, 4:2134, 2013.

[262] Adrian G. Swartz, Satoshi Harashima, Yanwu Xie, Di Lu, Bongju Kim, Christopher Bell, Yasuyuki Hikita, and Harold Y. Hwang. Spin-dependent transport across co/$LaAlO_3/SrTiO_3$ heterojunctions. *Applied Physics Letters*, 105(3):032406, 2014.

[263] A. M. Kamerbeek, P. Högl, J. Fabian, and T. Banerjee. Electric field control of spin lifetimes in $Nb\text{-}SrTiO_3$ by spin-orbit fields. *Phys. Rev. Lett.*, 115:136601, Sep 2015.

[264] Mi-Jin Jin, Seon Young Moon, Jungmin Park, Vijayakumar Modepalli, Junhyeon Jo, Shin-Ik Kim, Hyun Cheol Koo, Byoung-Chul Min, Hyun-Woo Lee, Seung-Hyub Baek, and Jung-Woo Yoo. Nonlocal spin diffusion driven by giant spin hall effect at oxide heterointerfaces. *Nano Letters*, 2016.

[265] Qi Song, Hongrui Zhang, Tang Su, Wei Yuan, Yangyang Chen, Wenyu Xing, Jing Shi, Ji Rong Sun, and Wei Han. Observation of inverse edelstein effect in rashba-split 2deg between $SrTiO_3$ and $LaAlO_3$ at room temperature. *arXiv:1609.06207*, 2016.

[266] J. Y. Chauleau, M. Boselli, S. Gariglio, R. Weil, G. de Loubens, J. M. Triscone, and M. Viret. Efficient spin-to-charge conversion in the 2d electron liquid at the lao/sto interface. *EPL (Europhysics Letters)*, 116(1):17006, 2016.

[267] L. Li, C. Richter, J. Mannhart, and R. C. Ashoori. Coexistence of magnetic order and two-dimensional superconductivity at $LaAlO_3/SrTiO_3$ interfaces. *Nature Physics*,

7(10):762–766, 2011.

[268] Julie A.; Bert, Beena; Kalisky, Christopher; Bell, Minu; Kim, Yasuyuki; Hikita, Harold Y.; Hwang, and Kathryn A.; Moler. Direct imaging of the coexistence of ferromagnetism and superconductivity at the $LaAlO_3/SrTiO_3$ interface. *Nature Physics*, 7(10):767–771, 2011.

[269] Veerendra K. Guduru. *Surprising Magnetotransport in Oxide Heterostructures*. Thesis, 2014.

[270] Beena Kalisky, Julie A. Bert, Brannon B. Klopfer, Christopher Bell, Hiroki K. Sato, Masayuki Hosoda, Yasuyuki Hikita, Harold Y. Hwang, and Kathryn A. Moler. Critical thickness for ferromagnetism in $LaAlO_3/SrTiO_3$ heterostructures. *Nature Communications*, 3:922, 2012.

[271] B. Kalisky, J. A. Bert, C. Bell, Y. W. Xie, H. K. Sato, M. Hosoda, Y. Hikita, H. Y. Hwang, and K. A. Moler. Scanning probe manipulation of magnetism at the $LaAlO_3/SrTiO_3$ heterointerface. *Nano Letters*, 12(8):4055–4059, 2012.

[272] J. S. Lee, Y. W. Xie, H. K. Sato, C. Bell, Y. Hikita, H. Y. Hwang, and C. C. Kao. Titanium dxy ferromagnetism at the $LaAlO_3/SrTiO_3$ interface. *Nature Materials*, 12(8):703–706, 2013.

[273] Marco Salluzzo. *Electronic Reconstruction at the Interface Between Band Insulating Oxides: The $LaAlO_3/SrTiO_3$ System*, pages 181–211. Springer International Publishing, Cham, 2015.

[274] Z. Salman, O. Ofer, M. Radovic, H. Hao, M. Ben Shalom, K. H. Chow, Y. Dagan, M. D. Hossain, C. D. P. Levy, W. A. MacFarlane, G. M. Morris, L. Patthey, M. R. Pearson, H. Saadaoui, T. Schmitt, D. Wang, and R. F. Kiefl. Nature of weak magnetism in $SrTiO_3/LaAlO_3$ multilayers. *Physical Review Letters*, 109(25):257207, 2012.

[275] Jun Kondo. Resistance minimum in dilute magnetic alloys. *Progress of Theoretical Physics*, 32(1):37–49, 1964.

[276] N. Banerjee, M. Huijben, G. Koster, and G. Rijnders. Direct patterning of functional interfaces in oxide heterostructures. *Applied Physics Letters*, 100(4), 2012.

[277] Mingyang Li, Tanja Graf, Thomas D. Schladt, Xin Jiang, and Stuart S. P. Parkin. Role of percolation in the conductance of electrolyte-gated $SrTiO_3$. *Physical Review Letters*, 109(19):196803, 2012.

[278] G. M. De Luca, R. Di Capua, E. Di Gennaro, F. Miletto Granozio, D. Stornaiuolo, M. Salluzzo, A. Gadaleta, I. Pallecchi, D. Marr, C. Piamonteze, M. Radovic, Z. Ristic, and S. Rusponi. Transport properties of a quasi-two-dimensional electron system formed in $LaAlO_3$/eutio3/$SrTiO_3$ heterostructures. *Physical Review B*, 89(22):224413, 2014.

[279] Shubhankar Das, A. Rastogi, Lijun Wu, Jin-Cheng Zheng, Z. Hossain, Yimei Zhu, and R. C. Budhani. Kondo scattering in δ-doped latio3/$SrTiO_3$ interfaces: Renormalization by spin-orbit interactions. *Physical Review B*, 90(8):081107, 2014.

[280] K. Han, N. Palina, S. W. Zeng, Z. Huang, C. J. Li, W. X. Zhou, D. Y. Wan, L. C. Zhang, X. Chi, R. Guo, J. S. Chen, T. Venkatesan, A. Rusydi, and A. Ariando. Controlling kondo-like scattering at the $SrTiO_3$-based interfaces. *Scientific Reports*, 6:25455, 2016.

[281] K. X. Jin, W. Lin, B. C. Luo, and T. Wu. Photoinduced modulation and relaxation characteristics in $LaAlO_3/SrTiO_3$ heterointerface. *Scientific Reports*, 5:8778, 2015.

[282] G. Z. Liu, J. Qiu, Y. C. Jiang, R. Zhao, J. L. Yao, M. Zhao, Y. Feng, and J. Gao. Light induced suppression of kondo effect at amorphous $LaAlO_3/SrTiO_3$ interface. *Applied Physics Letters*, 109(3):031110, 2016.

[283] C. Latta, F. Haupt, M. Hanl, A. Weichselbaum, M. Claassen, W. Wuester, P. Fallahi, S. Faelt, L. Glazman, J. von Delft, H. E. Tureci, and A. Imamoglu. Quantum quench of kondo correlations in optical absorption. *Nature*, 474(7353):627–630, 2011.

[284] Julie A. Bert, Katja C. Nowack, Beena Kalisky, Hilary Noad, John R. Kirtley, Chris Bell, Hiroki K. Sato, Masayuki Hosoda, Yasayuki Hikita, Harold Y. Hwang, and Kathryn A. Moler. Gate-tuned superfluid density at the superconducting $LaAlO_3/SrTiO_3$ interface. *Physical Review B*, 86(6):060503, 2012.

[285] Julie A. Bert. *Superconductivity in Reduced Dimensions*. Doctoral thesis, Stanford University, CA, USA., 2012.

[286] Tom Wijnands. *Scanning Superconducting Quantum Interference Device Microscopy*. Masters thesis, University of Twente, Enschede, the Netherlands, 2013.

[287] M. R. Fitzsimmons, N. W. Hengartner, S. Singh, M. Zhernenkov, F. Y. Bruno, J. Santamaria, A. Brinkman, M. Huijben, H. J. A. Molegraaf, J. de la Venta, and Ivan K. Schuller. Upper limit to magnetism in $LaAlO_3/SrTiO_3$ heterostructures. *Physical Review Letters*, 107(21):217201, 2011.

[288] Feng Bi, Mengchen Huang, Hyungwoo Lee, Chang-Beom Eom, Patrick Irvin, and Jeremy Levy. $LaAlO_3$ thickness window for electronically controlled magnetism at $LaAlO_3/SrTiO_3$ heterointerfaces. *Applied Physics Letters*, 107(8):082402, 2015.

[289] Qing Guo, Jianan Li, Mengchen Huang, Hyungwoo Lee, Chang-Beom Eom, Patrick Irvin, and Jeremy Levy. Correlations between magnetic and piezoelectric response at gated $LaAlO_3/SrTiO_3$ interfaces. In *APS Meeting Abstracts*, 2016.

[290] Jianan Li, Qing Guo, Feng Bi, Mengchen Huang, Hyungwoo Lee, Chang-Beom Eom, Patrick Irvin, and Jeremy Levy. Magneto-optical Kerr probing of LAO/STO interface ferromagnetism. In *APS Meeting Abstracts*, 2016.

[291] W. D Rice, P. Ambwani, M. Bombeck, J. D. Thompson, G. Haugstad, C. Leighton, and S. A Crooker. Persistent optically induced magnetism in oxygen-deficient strontium titanate. *Nature Materials*, 13(5):481–487, 2014.

[292] J. M. D. Coey, M. Venkatesan, and P. Stamenov. Surface magnetism of strontium titanate. *Journal of Physics: Condensed Matter*, 28(48):485001, 2016.

[293] J.M.D. Coey and S.A. Chambers. Oxide dilute magnetic semiconductorsfact or fiction? *MRS Bulletin*, 33(11):1053–1058, 2008.

[294] M. A. Garcia, E. Fernandez Pinel, J. de la Venta, A. Quesada, V. Bouzas, J. F. Fernandez, J. J. Romero, M. S. Martin-Gonzalez, and J. L. Costa-Kramer. Sources of experimental errors in the observation of nanoscale magnetism. *Journal of Applied Physics*, 105(1):013925, 2009.

[295] Taichi Goto, Dong Hun Kim, Xueyin Sun, Mehmet C. Onbasli, Juan M. Florez, Shyue Ping Ong, Patricio Vargas, Karl Ackland, Plamen Stamenov, Nicolas M. Aimon, Mitsuteru Inoue, Harry L. Tuller, Gerald F. Dionne, J. Michael D. Coey, and Caroline A. Ross. Magnetism and faraday rotation in oxygen-deficient polycrystalline and single-crystal iron-substituted strontium titanate. *Physical Review Applied*, 7(2):024006, 2017.

[296] N. Pavlenko, T. Kopp, E. Y. Tsymbal, J. Mannhart, and G. A. Sawatzky. Oxygen vacancies at titanate interfaces: Two-dimensional magnetism and orbital reconstruction. *Physical Review B*, 86(6):064431, 2012.

[297] Alejandro Lopez-Bezanilla, P. Ganesh, and Peter B. Littlewood. Magnetism and metal-insulator transition in oxygen-deficient $SrTiO_3$. *Physical Review B*, 92(11):115112, 2015.

[298] Alejandro Lopez-Bezanilla, P. Ganesh, and Peter B. Littlewood. Research update: Plentiful magnetic moments in oxygen deficient $SrTiO_3$. *APL Mater.*, 3(10):100701, 2015.

[299] M. Tinkham. Effect of fluxoid quantization on transitions of superconducting films. *Physical Review*, 129(6):2413–2422, 1963.

[300] N. Reyren, S. Gariglio, A. D. Caviglia, D. Jaccard, T. Schneider, and J. M. Triscone. Anisotropy of the superconducting transport properties of the $LaAlO_3/SrTiO_3$ interface. *Applied Physics Letters*, 94(11), 2009.

[301] V. L. Ginzburg. On surface superconductivity. *Physics Letters*, 13(2):101–102, 1964.

[302] S. Gariglio, N. Reyren, A. D. Caviglia, and J. M. Triscone. Superconductivity at the $LaAlO_3/SrTiO_3$ interface. *Journal of Physics-Condensed Matter*, 21(16), 2009.

[303] T. Schneider, A. D. Caviglia, S. Gariglio, N. Reyren, and J. M. Triscone.

Electrostatically-tuned superconductor-metal-insulator quantum transition at the $LaAlO_3/SrTiO_3$ interface. *Physical Review B*, 79(18), 2009.

[304] Yen-Hsiang Lin, J. Nelson, and A. M. Goldman. Superconductivity of very thin films: The superconductorinsulator transition. *Physica C: Superconductivity and its Applications*, 514:130–141, 2015.

[305] Eran Maniv, Yoram Dagan, and Moshe Goldstein. Correlation-induced band competition in $SrTiO_3/LaAlO_3$. *MRS Advances*, 2:1243–1248, 2017.

[306] E. Fillis-Tsirakis, C. Richter, J. Mannhart, and H. Boschker. Evidence for superconducting phase coherence in the metallic/insulating regime of the $LaAlO_3$ $SrTiO_3$ interface electron system. *New Journal of Physics*, 18(1):013046, 2016.

[307] S. N. Klimin, J. Tempere, J. T. Devreese, and D. van der Marel. Interface superconductivity in $LaAlO_3$-$SrTiO_3$ heterostructures. *Physical Review B*, 89(18):184514, 2014.

[308] S. N. Klimin, J. Tempere, J. T. Devreese, and D. van der Marel. Multiband superconductivity due to the electronlophonon interaction in strontium titanate and on a $SrTiO_3/LaAlO_3$ interface. *Journal of Superconductivity and Novel Magnetism*, pages 1–5, 2016.

[309] C. Stephanos, T. Kopp, J. Mannhart, and P. J. Hirschfeld. Interface-induced d-wave pairing. *Physical Review B*, 84(10):100510, 2011.

[310] Mathias S. Scheurer and Jrg Schmalian. Topological superconductivity and unconventional pairing in oxide interfaces. *Nature Communications*, 6:6005, 2015.

[311] D. Valentinis, S. Gariglio, A. Fte, J.-M. Triscone, C. Berthod, and D. van der Marel. Surfing the shape resonances at the $LaAlO_3/SrTiO_3$ interface. *arXiv:1611.07763*, 2016.

[312] D. A. Dikin, M. Mehta, C. W. Bark, C. M. Folkman, C. B. Eom, and V. Chandrasekhar. Coexistence of superconductivity and ferromagnetism in two dimensions. *Physical Review Letters*, 107(5):056802, 2011.

[313] N. Mohanta and A. Taraphder. Oxygen vacancy clustering and pseudogap behaviour at the laalo 3 /srtio 3 interface. *Journal of Physics: Condensed Matter*, 26(21):215703, 2014.

[314] Karen Michaeli, Andrew C. Potter, and Patrick A. Lee. Superconducting and ferromagnetic phases in $SrTiO_3/LaAlO_3$ oxide interface structures: Possibility of finite momentum pairing. *Physical Review Letters*, 108(11):117003, 2012.

[315] Lukasz Fidkowski, Hong-Chen Jiang, Roman M. Lutchyn, and Chetan Nayak. Magnetic and superconducting ordering in one-dimensional nanostructures at the

$LaAlO_3/SrTiO_3$ interface. *Physical Review B*, 87(1):014436, 2013.

[316] Sumilan Banerjee, Onur Erten, and Mohit Randeria. Ferromagnetic exchange, spin-orbit coupling and spiral magnetism at the $LaAlO_3/SrTiO_3$ interface. *Nature Physics*, 9(10):626–630, 2013.

[317] Peter Fulde and Richard A. Ferrell. Superconductivity in a strong spin-exchange field. *Physical Review*, 135(3A):A550–A563, 1964.

[318] A. I. larkin and Y. N. Ovchinnikov. Nonuniform state of superconductors. *Sov. Phys. JETP*, 20:762, 1965.

[319] Y. Oreg, G. Refael, and F. von Oppen. Helical liquids and majorana bound states in quantum wires. *Physical Review Letters*, 105(17):177002, 2010.

[320] Yasuhiro Yamada, Hideki Yasuda, Takeshi Tayagaki, and Yoshihiko Kanemitsu. Temperature dependence of photoluminescence spectra of nondoped and electron-doped $SrTiO_3$: Crossover from auger recombination to single-carrier trapping. *Physical Review Letters*, 102(24), 2009.

[321] H. J. Harsan Ma, T. Venkatesan, S. J. Wang, and Ariando. Temperature dependence of photoluminescence spectra of bilayer two-dimensional electron gases in $LaAlO_3/SrTiO_3$ superlattices: coexistence of auger recombination and single-carrier trapping. *AIP Advances*, 5(6):067163, 2015.

[322] R.W. Boyd. *Nonlinear Optics*. Elsevier Science, 2003.

[323] A. Savoia, D. Paparo, P. Perna, Z. Ristic, M. Salluzzo, F. Miletto Granozio, U. Scotti di Uccio, C. Richter, S. Thiel, J. Mannhart, and L. Marrucci. Polar catastrophe and electronic reconstructions at the $LaAlO_3/SrTiO_3$ interface: Evidence from optical second harmonic generation. *Physical Review B*, 80(7), 2009.

[324] Domenico Paparo, Andrea Rubano, and Lorenzo Marrucci. Optical second-harmonic generation selection rules and resonances in buried oxide interfaces: the case of $LaAlO_3/SrTiO_3$. *Journal of the Optical Society of America B*, 30(9):2452–2460, 2013.

[325] A. Rubano, C. Aruta, U. Scotti di Uccio, F. Miletto Granozio, L. Marrucci, T. Gnter, T. Fink, M. Fiebig, and D. Paparo. Electronic states at polar/nonpolar interfaces grown on $SrTiO_3$ studied by optical second harmonic generation. *Physical Review B*, 88(24):245434, 2013.

[326] Y. Imry. *Introduction to Mesoscopic Physics*. OUP Oxford, 2008.

[327] Srijit Goswami, Emre Mulazimoglu, Ana M. R. V. L. Monteiro, Roman Wlbing, Dieter Koelle, Reinhold Kleiner, Ya M. Blanter, Lieven M. K. Vandersypen, and Andrea D. Caviglia. Quantum interference in an interfacial superconductor. *Nat Nano*, 11:861–865, 2016.

[328] Joshua P. Veazey, Guanglei Cheng, Patrick Irvin, Cheng Cen, Daniela F. Bogorin, Feng Bi, Mengchen Huang, Chung-Wung Bark, Sangwoo Ryu, Kwang-Hwan Cho, Chang-Beom Eom, and Jeremy Levy. Oxide-based platform for reconfigurable superconducting nanoelectronics. *Nanotechnology*, 24(37):375201, 2013.

[329] D. Stornaiuolo, S. Gariglio, N. J. G. Couto, A. Fte, A. D. Caviglia, G. Seyfarth, D. Jaccard, A. F. Morpurgo, and J.-M. Triscone. In-plane electronic confinement in superconducting $LaAlO_3/SrTiO_3$ nanostructures. *Applied Physics Letters*, 101(22):222601, 2012.

[330] J. P. Veazey, G. Cheng, S. Lu, M. Tomczyk, F. Bi, M. Huang, S. Ryu, C. W. Bark, K. H. Cho, C. B. Eom, P. Irvin, and J. Levy. Nonlocal current-voltage characteristics of gated superconducting sketched oxide nanostructures. *Europhysics Letters*, 103(5):57001, 2013.

[331] Guanglei Cheng, Joshua P. Veazey, Patrick Irvin, Cheng Cen, Daniela F. Bogorin, Feng Bi, Mengchen Huang, Shicheng Lu, Chung-Wung Bark, Sangwoo Ryu, Kwang-Hwan Cho, Chang-Beom Eom, and Jeremy Levy. Anomalous transport in sketched nanostructures at the $LaAlO_3/SrTiO_3$ interface. *Physical Review X*, 3(1):011021, 2013.

[332] D. Rakhmilevitch, M. Ben Shalom, M. Eshkol, A. Tsukernik, A. Palevski, and Y. Dagan. Phase coherent transport in $SrTiO_3/LaAlO_3$ interfaces. *Physical Review B*, 82(23), 2010.

[333] Sam W. Stanwyck, P. Gallagher, J. R. Williams, and David Goldhaber-Gordon. Universal conductance fluctuations in electrolyte-gated $SrTiO_3$ nanostructures. *Applied Physics Letters*, 103(21):213504, 2013.

[334] A. M. R. V. L. Monteiro, D. J. Groenendijk, N. Manca, E. Mulazimoglu, S. Goswami, Ya Blanter, L. M. K. Vandersypen, and A. D. Caviglia. Side gate tunable josephson junctions at the $LaAlO_3/SrTiO_3$ interface. *Nano Letters*, 2017.

[335] Paul McConville and Norman O. Birge. Weak localization, universal conductance fluctuations, and 1/f noise in ag. *Physical Review B*, 47(24):16667–16670, 1993.

[336] Anil Annadi, Guanglei Cheng, Hyungwoo Lee, Jung-Woo Lee, Shicheng Lu, Anthony Tylan-Tyler, Megan Briggeman, Michelle Tomczyk, Mengchen Huang, David Pekker, Chang-Beom Eom, Patrick Irvin, and Jeremy Levy. Quantized ballistic transport of electrons and electron pairs in $LaAlO_3/SrTiO_3$ nanowires. *Nano Letters*, 18(7):4473–4481, 2018.

[337] A. Ron and Y. Dagan. One-dimensional quantum wire formed at the boundary between two insulating $LaAlO_3/SrTiO_3$ interfaces. *Physical Review Letters*, 112(13):136801, 2014.

[338] Michelle Tomczyk, Guanglei Cheng, Hyungwoo Lee, Shicheng Lu, Anil Annadi, Joshua P. Veazey, Mengchen Huang, Patrick Irvin, Sangwoo Ryu, Chang-Beom

Eom, and Jeremy Levy. Micrometer-scale ballistic transport of electron pairs in $LaAlO_3/SrTiO_3$ nanowires. *Physical Review Letters*, 117(9):096801, 2016.

[339] Guenevere E. D. K. Prawiroatmodjo, Martin Leijnse, Felix Trier, Yunzhong Chen, Dennis V. Christensen, Merlin von Soosten, Nini Pryds, and Thomas S. Jespersen. Transport and excitations in a negative-u quantum dot at the $LaAlO_3/SrTiO_3$ interface. *Nature Communications*, 8(1):395, 2017.

[340] Guanglei Cheng, Michelle Tomczyk, Alexandre B. Tacla, Hyungwoo Lee, Shicheng Lu, Josh P. Veazey, Mengchen Huang, Patrick Irvin, Sangwoo Ryu, Chang-Beom Eom, Andrew Daley, David Pekker, and Jeremy Levy. Tunable electron-electron interactions in $LaAlO_3/SrTiO_3$ nanostructures. *Physical Review X*, 6(4):041042, 2016.

[341] Abhijit Biswas, Chan Ho Yang, Ramamoorthy Ramesh, and Yoon H. Jeong. Atomically flat single terminated oxide substrate surfaces. *arXiv:1705.03436*, 2017.

[342] Gertjan Koster, Boike L. Kropman, Guus J. H. M. Rijnders, Dave H. A. Blank, and Horst Rogalla. Quasi-ideal strontium titanate crystal surfaces through formation of strontium hydroxide. *Applied Physics Letters*, 73(20):2920–2922, 1998.

[343] M. Kareev, S. Prosandeev, J. Liu, C. Gan, A. Kareev, J. W. Freeland, Min Xiao, and J. Chakhalian. Atomic control and characterization of surface defect states of tio(2) terminated srtio(3) single crystals. *Applied Physics Letters*, 93(6), 2008.

[344] Buzea Cristina and Robbie Kevin. State of the art in thin film thickness and deposition rate monitoring sensors. *Reports on Progress in Physics*, 68(2):385, 2005.

[345] G. J. H. M. Rijnders, G. Koster, D. H. A. Blank, and H. Rogalla. In situ monitoring during pulsed laser deposition of complex oxides using reflection high energy electron diffraction under high oxygen pressure. *Applied Physics Letters*, 70(14):1888–1890, 1997.

[346] P. R. Willmott and J. R. Huber. Pulsed laser vaporization and deposition. *Reviews of Modern Physics*, 72(1):315–328, 2000.

[347] D. Dijkkamp, T. Venkatesan, X. D. Wu, S. A. Shaheen, N. Jisrawi, Y. H. MinLee, W. L. McLean, and M. Croft. Preparation of ybacu oxide superconductor thin films using pulsed laser evaporation from high tc bulk material. *Applied Physics Letters*, 51(8):619–621, 1987.

[348] X. D. Wu, T. Venkatesan, A. Inam, X. X. Xi, Q. Li, W. L. McLean, C. C. Chang, D. M. Hwang, R. Ramesh, L. Nazar, B. Wilkens, S. A. Schwarz, R. T. Ravi, J. A. Martinez, P. England, J. M. Tarascon, R. E. Muenchausen, S. Foltyn, R. C. Estler, R. C. Dye, A. R. Garcia, and N. S. Nogar. Pulsed laser deposition of high tc superconducting thin films: Present and future. *MRS Proceedings*, 191, 1990.

[349] Tsuyoshi Ohnishi, Keisuke Shibuya, Takahisa Yamamoto, and Mikk Lippmaa. Defects

and transport in complex oxide thin films. *Journal of Applied Physics*, 103(10):103703, 2008.

[350] G. Z. Liu, Q. Y. Lei, and X. X. Xi. Stoichiometry of $SrTiO_3$ films grown by pulsed laser deposition. *Applied Physics Letters*, 100(20):202902, 2012.

[351] D. A. Muller, N. Nakagawa, A. Ohtomo, J. L. Grazul, and H. Y. Hwang. Atomic-scale imaging of nanoengineered oxygen vacancy profiles in $SrTiO_3$. *Nature*, 430(7000):657–661, 2004.

[352] J. R. Arthur A. Y. Cho. Molecular beam epitaxy. *Progress in Solid State Chemistry*, 10:157–191, 1975.

[353] B. A. Joyce. Molecular beam epitaxy. *Reports on Progress in Physics*, 48(12):1637, 1985.

[354] W. Patrick McCray. Mbe deserves a place in the history books. *Nat Nano*, 2(5):259–261, 2007.

[355] Loren Pfeiffer and K. W. West. The role of mbe in recent quantum hall effect physics discoveries. *Physica E: Low-dimensional Systems and Nanostructures*, 20(12):57–64, 2003.

[356] Darrell G. Schlom. Perspective: Oxide molecular-beam epitaxy rocks! *APL Mater.*, 3(6):062403, 2015.

[357] Y. Segal, J. H. Ngai, J. W. Reiner, F. J. Walker, and C. H. Ahn. X-ray photoemission studies of the metal-insulator transition in $LaAlO_3/SrTiO_3$ structures grown by molecular beam epitaxy. *Physical Review B*, 80(24):241107, 2009.

[358] Masaki Kanai, Tomoji Kawai, and Shichio Kawai. Atomic layer and unit cell layer growth of (ca,sr)cuo2 thin film by laser molecular beam epitaxy. *Applied Physics Letters*, 58(7):771–773, 1991.

[359] Opel Matthias. Spintronic oxides grown by laser-mbe. *Journal of Physics D: Applied Physics*, 45(3):033001, 2012.

[360] A. Herklotz, K. Drr, T. Z. Ward, G. Eres, H. M. Christen, and M. D. Biegalski. Stoichiometry control of complex oxides by sequential pulsed-laser deposition from binary-oxide targets. *Applied Physics Letters*, 106(13):131601, 2015.

[361] Qingyu Lei, Maryam Golalikhani, Bruce A. Davidson, Guozhen Liu, D. G. Schlom, Qiao Qiao, Yimei Zhu, Ravini U. Chandrasena, Weibing Yang, Alexander X. Gray, Elke Arenholz, Andrew K. Farrar, Dmitri A. Tenne, Minhui Hu, Jiandong Guo, Rakesh K. Singh, and X. X. Xi. Constructing oxide interfaces and heterostructures by atomic layer-by-layer laser molecular beam epitaxy. *arXiv:1610.06885*, 2016.

[362] C. Cen, S. Thiel, J. Mannhart, and J. Levy. Oxide nanoelectronics on demand. *Science*, 323(5917):1026–1030, 2009.

[363] Y. W. Xie, C. Bell, T. Yajima, Y. Hikita, and H. Y. Hwang. Charge writing at the $LaAlO_3/SrTiO_3$ surface. *Nano Letters*, 10(7):2588–2591, 2010.

[364] M. Boselli, D. Li, W. Liu, A. Fte, S. Gariglio, and J. M. Triscone. Characterization of atomic force microscopy written conducting nanowires at $LaAlO_3/SrTiO_3$ interfaces. *Applied Physics Letters*, 108(6):061604, 2016.

[365] M. C. Huang, F. Bi, C. W. Bark, S. Ryu, K. H. Cho, C. B. Eom, and J. Levy. Non-local piezoresponse of $LaAlO_3/SrTiO_3$ heterostructures. *Applied Physics Letters*, 104(16):161606, 2014.

[366] P. Irvin, Y. J. Ma, D. F. Bogorin, C. Cen, C. W. Bark, C. M. Folkman, C. B. Eom, and J. Levy. Rewritable nanoscale oxide photodetector. *Nature Photonics*, 4(12):849–852, 2010.

[367] Daniela F. Bogorin, Chung Wung Bark, Ho Won Jang, Cheng Cen, Chad M. Folkman, Chang-Beom Eom, and Jeremy Levy. Nanoscale rectification at the $LaAlO_3/SrTiO_3$ interface. *Applied Physics Letters*, 97(1):013102, 2010.

[368] P. Irvin, M. Huang, F. J. Wong, T. D. Sanders, Y. Suzuki, and J. Levy. Gigahertz-frequency operation of a $LaAlO_3/SrTiO_3$-based nanotransistor. *Applied Physics Letters*, 102(10):103113, 2013.

[369] Yun-Yi Pai, Hyungwoo Lee, Jung-Woo Lee, Anil Annadi, Guanglei Cheng, Shicheng Lu, Michelle Tomczyk, Mengchen Huang, Chang-Beom Eom, Patrick Irvin, and Jeremy Levy. One-dimensional nature of superconductivity at the $LaAlO_3/SrTiO_3$ interface. *Physical Review Letters*, 120(14):147001, 2018.

[370] G. Cheng, P. F. Siles, F. Bi, C. Cen, D. F. Bogorin, C. W. Bark, C. M. Folkman, J. W. Park, C. B. Eom, G. Medeiros-Ribeiro, and J. Levy. Sketched oxide single-electron transistor. *Nature Nanotechnology*, 6(6):343–347, 2011.

[371] Patrick Irvin, Hyungwoo Lee, Jung-Woo Lee, Megan Briggeman, Shicheng Lu, Anil Annadi, Guanglei Cheng, Michelle Tomczyk, Jinanan Li, Mengchen Huang, Chang-Beom Eom, and Jeremy Levy. Strong aharonov-bohm quantum interference in simply connected $LaAlO_3/SrTiO_3$ structures. *Phys. Rev. B*, 100:161103, Oct 2019.

[372] Xinyi Wu, Megan Briggeman, Joseph Albro, Jianan Li, Jungwoo Lee, Hyungwoo Lee, Chang-Beom Eom, Patrick Irvin, and Jeremy Levy. Uniaxial Strain Effect on Superconductivity in $LaAlO_3/SrTiO_3$ Nanostructures. In *APS March Meeting Abstracts*, volume 2019 of *APS Meeting Abstracts*, page C05.012, Jan 2019.

[373] Philip Shenk, John Maier, Juliana Sebolt, Jungwoo Lee, Hyungwoo Lee, Chang-Beom Eom, Jianan Li, Patrick Irvin, and Jeremy Levy. Single-Electron Charging Effects

in Sketched $LaAlO_3/SrTiO_3$ Single-Electron Transistors. In *APS March Meeting Abstracts*, volume 2019 of *APS Meeting Abstracts*, page V11.011, Jan 2019.

[374] Megan Briggeman, Jianan Li, Mengchen Huang, Anthony Tylan-Tyler, Hyungwoo Lee, Jungwoo Lee, Chang-Beom Eom, Patrick Irvin, and Jeremy Levy. Engineered Helicity of One-Dimensional $LaAlO_3/SrTiO_3$ Nanowires. In *APS March Meeting Abstracts*, volume 2019 of *APS Meeting Abstracts*, page K46.003, Jan 2019.

[375] Megan Briggeman, Jianan Li, Mengchen Huang, Hyungwoo Lee, Jung-Woo Lee, Kitae Eom, Chang-Beom Eom, Patrick Irvin, and Jeremy Levy. Engineered spin-orbit interactions in $laalo_3/srtio_3$-based 1d serpentine electron waveguides, 2019.

[376] Megan Briggeman, Hyungwoo Lee, Jung-Woo Lee, Kitae Eom, Franois Damanet, Elliott Mansfield, Jianan Li, Mengchen Huang, Andrew J. Daley, Chang-Beom Eom, Patrick Irvin, and Jeremy Levy. One-dimensional kronig-penney superlattices at the $laalo_3/srtio_3$ interface, 2019.

[377] Yuhe Tang, Anthony Tylan-Tyler, Hyungwoo Lee, Jung-Woo Lee, Michelle Tomczyk, Mengchen Huang, Chang-Beom Eom, Patrick Irvin, and Jeremy Levy. Long-range non-coulombic electronelectron interactions between $LaAlO_3/SrTiO_3$ nanowires. *Advanced Materials Interfaces*, 6(15):1900301, 2019.

[378] Yun-Yi Pai, Megan Briggeman, Hyungwoo Lee, Jung-Woo Lee, Mengchen Huang, Jianan Li, Chang-Beom Eom, Patrick Irvin, and Jeremy Levy. Superconductivity in 1D Zigzag Nanowires. In *APS March Meeting Abstracts*, volume 2019 of *APS Meeting Abstracts*, page P09.014, Jan 2019.

[379] Aditi Nethwewala, Anthony Tylan-Tyler, Yuhe Tang, Jianan Li, Hyungwoo Lee, Jungwoo Lee, Chang-Beom Eom, Patrick Irvin, and Jeremy Levy. Quantum transport of nanoscale Hall crosses. In *APS Meeting Abstracts*, 2018.

[380] Aditi Nethwewala, Hyungwoo Lee, Megan Briggeman, Yuhe Tang, Jianan Li, Jung-Woo Lee, Chang-Beom Eom, Patrick Irvin, and Jeremy Levy. Inhomogeneous energy landscape in $LaAlO_3/SrTiO_3$ nanostructures. *Nanoscale Horiz.*, 4:1194–1201, 2019.

[381] Shan Hao, Jianan Li, Yuhe Tang, Aditi Nethwewala, Yang Hu, Hyungwoo Lee, Jungwoo Lee, Chang-Beom Eom, Patrick Irvin, and Jeremy Levy. Toward 2D Fermi-Hubbard Quantum Simulation with and Oxide Nanoelectronic Platform. In *APS March Meeting Abstracts*, volume 2019 of *APS Meeting Abstracts*, page P05.007, Jan 2019.

[382] Lu Chen, Erin Sutton, Hyungwoo Lee, Jung-Woo Lee, Jianan Li, Chang-Beom Eom, Patrick Irvin, and Jeremy Levy. Over 100-thz bandwidth selective difference frequency generation at $LaAlO_3/SrTiO_3$ nanojunctions. *Light: Science & Applications*, 8(1), 2019.

[383] Lu Chen, Jianan Li, Yuhe Tang, Yun-Yi Pai, Yunzhong Chen, Nini Pryds, Patrick

Irvin, and Jeremy Levy. Extreme reconfigurable nanoelectronics at the cazro3/$SrTiO_3$ interface. *Advanced Materials*, 30(33):1801794, 2018.

[384] Jianan Li, Qing Guo, Lu Chen, Shan Hao, Yang Hu, Jen-Feng Hsu, Hyungwoo Lee, Jung-Woo Lee, Chang-Beom Eom, Brian D'Urso, Patrick Irvin, and Jeremy Levy. Reconfigurable edge-state engineering in graphene using $LaAlO_3/SrTiO_3$ nanostructures. *Applied Physics Letters*, 114(12):123103, 2019.

[385] Erin Sutton, Lu Chen, Jianan Li, Qing Guo, Hyungwoo Lee, Jungwoo Lee, Chang-Beom Eom, Patrick Irvin, and Jeremy Levy. THz spectroscopy of graphene coupled to $LaAlO_3/SrTiO_3$ nanoscale junctions. In *APS March Meeting Abstracts*, volume 2019 of *APS Meeting Abstracts*, page R11.015, Jan 2019.

[386] Qing Guo, Jianan Li, Jen-Feng Hsu, Hyungwoo Lee, Chang-Beom Eom, Patrick Irvin, Brian D'Urso, and Jeremy Levy. Coulomb drag between graphene and $LaAlO_3/SrTiO_3$ heterostructures. In *APS March Meeting Abstracts*, volume 2019 of *APS Meeting Abstracts*, page V14.001, Jan 2019.

[387] Yun-Yi Pai, Dong-Wook Park, Mengchen Huang, Anil Annadi, Hyungwoo Lee, Zhenqiang Ma, Chang-Beom Eom, Patrick Irvin, and Jeremy Levy. Vertical gating of sketched nanodevices. In *APS March Meeting Abstracts*, volume 2016 of *APS Meeting Abstracts*, page S24.003, Jan 2016.

[388] Yun-Yi Pai, Mengchen Huang, Hyungwoo Lee, Chang-Beom Eom, Patrick Irvin, and Jeremy Levy. $LaAlO_3/SrTiO_3$ field-effect nanodevices using in-situ-grown Au top gates. In *APS March Meeting Abstracts*, volume 2015 of *APS Meeting Abstracts*, page G13.004, Mar 2015.

[389] Shan Hao, Jianan Li, Hyungwoo Lee, Jung-Woo Lee, Chang-Beom Eom, Patrick Irvin, and Jeremy Levy. Transport Characteristics of Al/LAO/STO-LAO/STO Nanostructures. In *APS March Meeting Abstracts*, volume 2018 of *APS Meeting Abstracts*, page K18.004, Jan 2018.

[390] Muqing Yu, Yun-Yi Pai, Leena Aggarwal, Hyungwoo Lee, Jungwoo Lee, Chang-Beom Eom, Patrick Irvin, and Jeremy Levy. Shot-Noise Measurements of Waveguides with Attractive Electron-Electron Interactions. In *APS March Meeting Abstracts*, volume 2019 of *APS Meeting Abstracts*, page E16.002, Jan 2019.

[391] Dengyu Yang, Yun-Yi Pai, Yuhe Tang, Yang Hu, Hyungwoo Lee, Jungwoo Lee, Chang-Beom Eom, Patrick Irvin, and Jeremy Levy. Surface Acoustic Wave Generation and Detection on $LaAlO_3/SrTiO_3$. In *APS March Meeting Abstracts*, volume 2019 of *APS Meeting Abstracts*, page R16.008, Jan 2019.

[392] Yang Hu, Yuhe Tang, Dengyu Yang, Yun-Yi Pai, Jianan Li, Hyungwoo Lee, Jung-Woo Lee, Chang-Beom Eom, Patrick Irvin, and Jeremy Levy. Development of single-electron sources in $LaAlO_3/SrTiO_3$ nanostructures. In *APS March Meeting Abstracts*,

volume 2019 of *APS Meeting Abstracts*, page A16.002, Jan 2019.

[393] Joseph Albro, Yun-Yi Pai, Xinyi Wu, Jianan Li, Jessica Montone, Patrick Irvin, and Jeremy Levy. Development of a Portable Conductive AFM Lithography Workstation. In *APS March Meeting Abstracts*, volume 2018 of *APS Meeting Abstracts*, page X09.011, Jan 2018.

[394] Megan Briggeman, Michelle Tomczyk, Binbin Tian, Hyungwoo Lee Jung-Woo Lee, Yuchi He, Anthony Tylan-Tyler, Mengchen Huang, Chang-Beom Eom, David Pekker, Roger S. K. Mong, Patrick Irvin, and Jeremy Levy. Pascal-liquid phases in ballistic one-dimensional $LaAlO_3/SrTiO_3$ channels. *submitted for publication*, 2018.

[395] N.H. Balshaw and Oxford Instruments Group. Scientific Research Division. *Practical Cryogenics: An Introduction to Laboratory Cryogenics*. Oxford Instruments, Scientific Research Division, 1996.

[396] F. Pobell. *Matter and Methods at Low Temperatures*. Springer Berlin Heidelberg, 2007.

[397] David M. Lee. The extraordinary phases of liquid ^{3}he. *Rev. Mod. Phys.*, 69:645–666, Jul 1997.

[398] B. Voigtländer. *Scanning Probe Microscopy: Atomic Force Microscopy and Scanning Tunneling Microscopy*. NanoScience and Technology. Springer Berlin Heidelberg, 2015.

[399] G. Binnig, H. Rohrer, Ch. Gerber, and E. Weibel. Surface studies by scanning tunneling microscopy. *Phys. Rev. Lett.*, 49:57–61, Jul 1982.

[400] G. Binnig, C. F. Quate, and Ch. Gerber. Atomic force microscope. *Phys. Rev. Lett.*, 56:930–933, Mar 1986.

[401] Aviram Uri, Alexander Y. Meltzer, Yonathan Anahory, Lior Embon, Ella O. Lachman, Dorri Halbertal, Naren HR, Yuri Myasoedov, Martin E. Huber, Andrea F. Young, and Eli Zeldov. Electrically tunable multiterminal squid-on-tip. *Nano Letters*, 16(11):6910–6915, 2016. PMID: 27672705.

[402] J. Waissman, M. Honig, S. Pecker, A. Benyamini, A. Hamo, and S. Ilani. Realization of pristine and locally tunable one-dimensional electron systems in carbon nanotubes. *Nature Nanotechnology*, 8(8):569–574, 2013.

[403] S. H. Pan. *International Patent Publication*. Number WO 1993/019494.

[404] S. H. Pan, E. W. Hudson, and J. C. Davis. 3he refrigerator based very low temperature scanning tunneling microscope. *Review of Scientific Instruments*, 70(2):1459–1463, 1999.

[405] Marvin L. Cohen. The existence of a superconducting state in semiconductors. *Reviews of Modern Physics*, 36(1):240–243, 1964.

[406] Lukas Kuerten, Christoph Richter, Narayan Mohanta, Thilo Kopp, Arno Kampf, Jochen Mannhart, and Hans Boschker. In-gap states in superconducting $LaAlO_3$-$SrTiO_3$ interfaces observed by tunneling spectroscopy. *Physical Review B*, 96(1):014513, 2017.

[407] D. Stornaiuolo, D. Massarotti, R. Di Capua, P. Lucignano, G. P. Pepe, M. Salluzzo, and F. Tafuri. Signatures of unconventional superconductivity in the $LaAlO_3/SrTiO_3$ two-dimensional system. *Physical Review B*, 95(14):140502, 2017.

[408] Pier Paolo Aurino, Alexey Kalabukhov, Nikolina Tuzla, Eva Olsson, Tord Claeson, and Dag Winkler. Nano-patterning of the electron gas at the $LaAlO_3/SrTiO_3$ interface using low-energy ion beam irradiation. *Applied Physics Letters*, 102(20):201610, 2013.

[409] C. W. Schneider, S. Thiel, G. Hammerl, C. Richter, and J. Mannhart. Microlithography of electron gases formed at interfaces in oxide heterostructures. *Applied Physics Letters*, 89(12):122101, 2006.

[410] A. Ron, E. Maniv, D. Graf, J. H. Park, and Y. Dagan. Anomalous magnetic ground state in an $LaAlO_3/SrTiO_3$ interface probed by transport through nanowires. *Physical Review Letters*, 113(21):216801, 2014.

[411] F. Altomare and A.M. Chang. *One-Dimensional Superconductivity in Nanowires*. Wiley, 2013.

[412] Mengchen Huang, Feng Bi, Sangwoo Ryu, Chang-Beom Eom, Patrick Irvin, and Jeremy Levy. Direct imaging of $LaAlO_3/SrTiO_3$ nanostructures using piezoresponse force microscopy. *APL Materials*, 1(5):052110, 2013.

[413] G. Catalan, J. Seidel, R. Ramesh, and J. F. Scott. Domain wall nanoelectronics. *Reviews of Modern Physics*, 84(1):119–156, 2012.

[414] P. W. Anderson. Model for electronic structure of amorphous semiconductors. *Physical Review Letters*, 34(15):953–955, 1975.

[415] Y. Matsushita, H. Bluhm, T. H. Geballe, and I. R. Fisher. Evidence for charge kondo effect in superconducting tl-doped pbte. *Physical Review Letters*, 94(15):157002, 2005.

[416] Nicholas J. Goble, Richard Akrobetu, Hicham Zaid, Sukrit Sucharitakul, Marie-Hlne Berger, Alp Sehirlioglu, and Xuan P. A. Gao. Anisotropic electrical resistance in mesoscopic $LaAlO_3/SrTiO_3$ devices with individual domain walls. *Scientific Reports*, 7:44361, 2017.

[417] A. Bezryadin. *Superconductivity in Nanowires: Fabrication and Quantum Transport*. Wiley, 2013.

[418] Roman M. Lutchyn, Jay D. Sau, and S. Das Sarma. Majorana fermions and a topological phase transition in semiconductor-superconductor heterostructures. *Physical Review Letters*, 105(7):077001, 2010.

[419] Manali Vivek, Mark O. Goerbig, and Marc Gabay. Topological states at the (001) surface of srtio$_3$. *Physical Review B*, 95(16):165117, 2017.

[420] A. B. Cawthorne, C. B. Whan, and C. J. Lobb. Complex dynamics of resistively and inductively shunted josephson junctions. *Journal of Applied Physics*, 84(2):1126–1132, 1998.

[421] D. Y. Vodolazov, F. M. Peeters, L. Piraux, S. Mátéfi-Tempfli, and S. Michotte. Current-voltage characteristics of quasi-one-dimensional superconductors: An *s*-shaped curve in the constant voltage regime. *Phys. Rev. Lett.*, 91:157001, Oct 2003.

[422] S. Hurand, A. Jouan, E. Lesne, G. Singh, C. Feuillet-Palma, M. Bibes, A. Barthélémy, J. Lesueur, and N. Bergeal. Josephson-like dynamics of the superconducting laalo$_3$/srtio$_3$ interface. *Phys. Rev. B*, 99:104515, Mar 2019.

[423] G. Venditti, J. Biscaras, S. Hurand, N. Bergeal, J. Lesueur, A. Dogra, R. C. Budhani, Mintu Mondal, John Jesudasan, Pratap Raychaudhuri, S. Caprara, and L. Benfatto. Non-linear *iv* characteristics in two-dimensional superconductors: Berezinskii-kosterlitz-thouless physics vs inhomogeneity. *arXiv:1905.01221*, 2019.

[424] Long-Qing Chen. Phase-field models for microstructure evolution. *Annual Review of Materials Research*, 32(1):113–140, 2002.

[425] S. Das, Y. L. Tang, Z. Hong, M. A. P. Gonalves, M. R. McCarter, C. Klewe, K. X. Nguyen, F. Gmez-Ortiz, P. Shafer, E. Arenholz, V. A. Stoica, S. L. Hsu, B. Wang, C. Ophus, J. F. Liu, C. T. Nelson, S. Saremi, B. Prasad, A. B. Mei, D. G. Schlom, J. iguez, P. Garca-Fernndez, D. A. Muller, L. Q. Chen, J. Junquera, L. W. Martin, and R. Ramesh. Observation of room-temperature polar skyrmions. *Nature*, 568(7752):368–372, 2019.

[426] Chaorui Qiu, Bo Wang, Nan Zhang, Shujun Zhang, Jinfeng Liu, David Walker, Yu Wang, Hao Tian, Thomas R. Shrout, Zhuo Xu, Long-Qing Chen, and Fei Li. Transparent ferroelectric crystals with ultrahigh piezoelectricity. *Nature*, 577(7790):350–354, 2020.

[427] L.Q. Chen and Jie Shen. Applications of semi-implicit fourier-spectral method to phase field equations. *Computer Physics Communications*, 108(2):147 – 158, 1998.

[428] Y. L. Li, S. Choudhury, J. H. Haeni, M. D. Biegalski, A. Vasudevarao, A. Sharan, H. Z. Ma, J. Levy, V. Gopalan, S. Trolier-McKinstry, D. G. Schlom, Q. X. Jia, and L. Q. Chen. Phase transitions and domain structures in strained pseudocubic (100) $SrTiO_3$ thin films. *Physical Review B*, 73(18):184112, 2006.

[429] G. Sheng, Y. L. Li, J. X. Zhang, S. Choudhury, Q. X. Jia, V. Gopalan, D. G. Schlom, Z. K. Liu, and L. Q. Chen. Phase transitions and domain stabilities in biaxially strained (001) $SrTiO_3$ epitaxial thin films. *Journal of Applied Physics*, 108(8):084113, 2010.

[430] John H. Barrett. Dielectric constant in perovskite type crystals. *Phys. Rev.*, 86:118–120, Apr 1952.

[431] Alexander K. Tagantsev, Eric Courtens, and Ludovic Arzel. Prediction of a low-temperature ferroelectric instability in antiphase domain boundaries of strontium titanate. *Physical Review B*, 64(22):224107, 2001.

[432] Anna N. Morozovska, Eugene A. Eliseev, Maya D. Glinchuk, Long-Qing Chen, and Venkatraman Gopalan. Interfacial polarization and pyroelectricity in antiferrodistortive structures induced by a flexoelectric effect and rotostriction. *Physical Review B*, 85(9):094107, 2012.

[433] Yijia Gu. *Phase-field Modeling of Flexoelectric Effect in Perovskite Ferroelectrics*. Doctoral thesis, Penn State University, PA, USA., 2014.

[434] Yijia Gu, Nan Wang, Fei Xue, and Long-Qing Chen. Origin of interfacial polar order in incipient ferroelectrics. *Phys. Rev. B*, 91:174103, May 2015.

[435] Atsutomo Nakamura, Kensuke Yasufuku, Yuho Furushima, Kazuaki Toyoura, K. Peter D. Lagerlf, and Katsuyuki Matsunaga. Room-temperature plastic deformation of strontium titanate crystals grown from different chemical compositions. *Crystals*, 7(11), 2017.

[436] Blai Casals, Andrea Schiaffino, Arianna Casiraghi, Sampo J. Hmlinen, Diego Lpez Gonzlez, Sebastiaan van Dijken, Massimiliano Stengel, and Gervasi Herranz. Low-temperature dielectric anisotropy driven by an antiferroelectric mode in $srtio_3$. *Physical Review Letters*, 120(21):217601, 2018.

[437] Blai Casals, Sebastiaan van Dijken, Gervasi Herranz, and Ekhard K. H. Salje. Electric-field-induced avalanches and glassiness of mobile ferroelastic twin domains in cryogenic $SrTiO_3$. *Phys. Rev. Research*, 1:032025, Nov 2019.

[438] Blai Casals, Sebastiaan van Dijken, Gervasi Herranz, and Ekhard K. H. Salje. Electric-field-induced avalanches and glassiness of mobile ferroelastic twin domains in cryogenic $SrTiO_3$. *Phys. Rev. Research*, 1:032025, Nov 2019.

[439] Per Bak, Chao Tang, and Kurt Wiesenfeld. Self-organized criticality: An explanation of the 1/f noise. *Phys. Rev. Lett.*, 59:381–384, Jul 1987.

[440] Fei Xue, Yijia Gu, Linyun Liang, Yi Wang, and Long-Qing Chen. Orientations of low-energy domain walls in perovskites with oxygen octahedral tilts. *Physical Review B*, 90(22):220101, 2014.